Imperial College London
Department of Mechanical Engineering, UK Research Centre in NDE

Calibration and Control of Advanced Ultrasonic Array Technology

David Duxbury

Submitted in part fulfilment of the requirements for the degree of
Engineering Doctorate in Non-Destructive Evaluation of Imperial College London

Declaration

I herewith certify that all material in this dissertation which is not my own work has been properly acknowledged.

David Duxbury

Copyright Statement

Abstract

Ultrasonic inspection is the primary method of Non-Destructive Evaluation (NDE) for the detection of planar flaws in engineering components. In recent years phased array technology has been adopted for use in NDE following success in related fields, such as medical and sonar applications. Phased array technology provides increased flexibility relative to single element monolithic transducers and the development of controlling hardware with large numbers of parallel channels has allowed the use of large phased arrays able to focus at long range, and offer increased performance.

Full Matrix Capture (FMC) is a method of recording data using a phased array transducer that allows image reconstruction to be performed for any inspection technique than could be deployed using delay laws applied to the transmit voltage pulses applied to the array and receiving amplifiers. FMC technology provides a step change in inspection flexibility, and also provides the opportunity to take advantage of imaging techniques that are not practical to implement using phased arrays in the conventional way. However, existing inspection calibration procedures defined in standards do not allow these benefits to be fully realised.

This thesis reports the development of a calibration framework designed for FMC based inspection for both rigid and conformable wedge mounted arrays. A large part of this work has been the development of acceptance limits on transducer performance variations. The developments of these limits have required a significant amount of modelling work, often using a Monte Carlo approach. To accommodate this, modelling tools have been developed to investigate the effect of array element directivity, sensitivity, and relative phase on system performance. For conformable phased arrays the effect of surface profile measurement accuracies has also been assessed. The developed calibration framework includes the tools necessary to monitor transducer performance throughout an inspection, with minimum impact on inspection duration. A means of calibrating imaging tools against known reflectors, in accordance with established industrial practice, has also been produced.

Acknowledgements

First and foremost I would like to thank my academic and industrial supervisors Mike Lowe and Jonathan Russell. Both have provided a fantastic level of support and have played a major part in shaping the direction of my work. Their efforts have made my doctorate a real enjoyment and without their mentoring I do not believe it would have been nearly as successful.

I am grateful to Rolls-Royce for supporting this work, and to EPSRC and MoD for funding it. I would like to the thank the NDE Research team at Rolls-Royce submarines for their help and also for creating a great place to work for the last four years. In particular, thanks is due to Martin Mienczakowski for listening to all my half baked ideas, and Chris Reed and Geoff Shand for patiently listening to and answering all my trivial coding questions!

Finally, I would like to thank my friends and family for their understanding and support. Particularly, I want to thank my wife Ruth for her continued support over the last four years. Without this support I could not have completed this thesis.

Contents

List of Figures

List of Tables

1 Introduction

Non-Destructive Evaluation (NDE) is a fundamental aspect of structural integrity assessment. In the nuclear industry the demonstration of the structural integrity of a plant component is completed on the basis of a safety case. The level of justification is based upon the safety classification of the component [1, 2]. The safety classification is based on the consequences of the failure of the safety functional requirements that the component provides. Regardless of the safety classification of the component it is likely that some form of NDE will be required, at some stage in the component's service life. Components that are designated a high safety classification are subject to a more rigorous analysis that must consider the expected service life of the component and predict tolerable start of life defects, produced in the manufacturing process. In service inspection may also be required for particular components. In the UK, inspections often must be carried out in accordance with the American Society of Mechanical Engineers (ASME) Boiler and Pressure Vessel Code, and in some cases to a higher standard [3]. Many applications require the use of ultrasonic inspection of welds, forgings, and castings. Often inspection must be automated to ensure consistent results, and to provide a permanent record of the inspection.

Rolls-Royce Submarines are the designated Technical Authority (TA) for the Nuclear Steam Raising Plant (NSRP) used by the Royal Navy in its various classes of nuclear submarines. As TA Rolls-Royce is responsible for the design, manufacture, and safety justification for the NSRP. This role requires the design, development, and completion of a range of automated ultrasonic inspections from manufacturing acceptance inspections at start of component life, to in-service inspections conducted on board the submarines. Many of these inspections involve inhomogeneous anisotropic materials, complex geometry, ionising radiation environments, and restricted access. As a result of these requirements Rolls-Royce have considerable interest in technologies that offer improved inspection performance, accuracy, flexibility, speed, or reduced user intervention.

For the past several years Rolls-Royce has been conducting a program of research into ultrasonic phased array inspections that record the full matrix of data, or simply Full Matrix Capture (FMC) [4]. This is a form of data capture that in principle records all possible transmit-receive element combinations in the array, and therefore contains the information to re-construct any result that could be produced using an algorithm, such as delay and sum beam forming. The work initially focused on the potential inspection improvements possible using phased array technology to adaptively beam form through an irregular surface, reported by Jonathan Russell [5]. FMC data capture was pursued as a means of capturing data such that it could be processed to measure the surface profile beneath a probe, and reprocessed to image the component volume beneath the irregular surface. FMC has since been pursued as a means to deliver a step change in array inspection performance and flexibility in its own right, with surface profile adaptive inspection as one of the potential benefits. Within Rolls-Royce a complete FMC software platform is nearing completion that allows FMC data collection and processing using a variety of conventional phased array and novel beam types. A calibration framework is a key requirement.

This thesis presents the development of a calibration framework for FMC based inspections. The framework covers the entire inspection process from initial probe checks to re-calibration throughout the inspection duration. The development of the calibration framework has required research into typical transducers variations and their effect on inspection performance. These studies have revealed the essential parameters that dictate inspection performance, as well as suitable limits on their variation. The results have been used to design the experimental procedures that make up the calibration framework.

1.1 Outline of thesis

One of the barriers to the deployment of FMC based inspection systems is the incompatibility of existing ultrasonic inspection system calibration frameworks with FMC. Existing means of calibration are based on manual ultrasonic inspection systems [6, 7], and their requirements do not provide the flexibility to fully benefit from FMC. The focus of this thesis is on the development of the tools required to calibrate FMC systems to a standard equivalent to that required by existing commercial standards, including inspections conducted through an irregular interface. This has required a thorough investigation into the essential parameters that govern array performance, typical variations observed experimentally, and the effect of their variation on a wide variety of inspection scenarios.

Chapter 2 begins with a review of the basic principles that describe ultrasonic inspection. A review is then conducted of currently state-of-the-art ultrasonic inspection, with a focus on phased array and FMC based techniques. This highlights the current focus of research in the NDE community on improved imaging capabilities and defect characterisation.

To develop a calibration routine a means of predicting the effect of various system parameters on inspection performance is required. Transducer modelling is able to provide this data in an efficient manner. Chapter 3 presents the review of a variety of methods used for modelling ultrasonic transducers, and discusses the relative merits and disadvantages of each technique. Based on this review a two dimensional array beam model based on Huygens-Fresnel theory of superposition is selected. The development and subsequent validation of this modelling tool against commercial modelling packages and experiment is presented.

The directivity function produced by an element directly influences the effective operating region of the array, and any variation in this parameter may affect performance. In order to decide if array element directivity must be considered as part of a calibration routine an investigation into the directivity pattern of piezo-composite array elements was conducted. Chapter 4 investigates the accuracy of models for directivity patterns based on piston source assumptions, and the variation in the directivity patterns of commercially available transducers.

Chapter 5 introduces the calibration frameworks used by conventional ultrasonic inspections and compares them to the requirements of FMC based inspections. A key requirement of inspection calibration is transducer checks. Chapter 5 reports the development of a transducer check that is decoupled from a particular imaging technique. The check is based on measurement of the performance of each array element. Monte Carlo simulations are used to investigate the effect of variation in element performance in order to define acceptable tolerances.

The element performance check is a straightforward method of ensuring array performance. The weakness of the technique is that measurement must be conducted with the array decoupled from

its wedge. This is not an attractive procedure industrially as the inspection must be stopped, the probe must be removed from the manipulator. All of these procedures require time and therefore the inspection duration is extended. If the operators are working in the presence of ionising radiation the extra time results in unnecessary radiation dose. Instead a combined probe check is developed that monitors element performance to a high accuracy using the reflections from the array's wedge. The required accuracy of measurement means that changes in wave velocity due to small temperature changes between measurements must be detected, and corrected. The development of this technique and a detailed analysis of its accuracy is reported in chapter 6.

Chapter 6 also reports the development of an automated data analysis algorithm that enables the sensitivity of FMC based inspections to be related to known calibration reflectors, from a detailed scan of a calibration block. Distance Amplitude Correction (DAC) curves are also implemented using the same data.

The inspection framework developed in chapters 5 and 6 is aimed at rigid wedge, or contact array, based inspections. Whilst the framework is applicable to inspection using conformable phased array, the technique introduces additional parameters into the array system that affect performance. Conformable phased arrays systems work on the basis of correcting delay laws such that adequate beam forming can be achieved through a given interface. For this process to achieve optimum performance the corrected delay laws must be as accurate as possible; this is controlled by the accuracy to which the geometry of the interface is known. Chapter 7 investigates the accuracy to which surface profiles formed by weld caps can be measured by an array in immersion. This review considers several imaging algorithms and assesses performance against profiles measured using a Co-ordinate Measuring Machine (CMM). The corresponding reduction in imaging performance associated with this typical measurement accuracy, and the effect of this on inspection performance, are also discussed.

1.2 Personal context

Since 2005 Rolls-Royce Submarines, on behalf of the UK Ministry of Defence, has been working with Imperial College London and the University of Bristol on the development of FMC based ultrasonic imaging systems for NDE, and hybrid modelling techniques. During this time Jonathan Russell and Rob Long, an Engineering Doctorate student and Researcher from Imperial College London supervised by Professor Peter Cawley, began the development of an inspection capability for un-dressed austenitic stainless steel pipe butt welds using FMC. Because of the nature of the application a means of surface profile adaptation was required. The selected solution was to image the component surface using an immersion array and image the component volume using delay laws adapted to the surface profile. The ultimate aim of this project was to develop a complete FMC inspection software package based on the prototypes developed at Imperial College.

My Engineering Doctorate began in 2008 when it became clear that in order to fully benefit from the flexibility FMC provides, the calibration of such a system would require a step change in the approach to calibration. I have been placed with the NDE group of Rolls-Royce Submarines for the duration of my doctorate under the supervision of Dr Jonathan Russell, with regular visits to Imperial College to visit my supervisor Professor Mike Lowe. I have benefited greatly from the research links between Rolls-Royce, Imperial College, and the University of Bristol.

Throughout my doctorate I have been responsible for managing the delivery of components of the

calibration routine to meet the requirements of the greater project, as well as the application of engineering governance within Rolls-Royce. For example, the presentation of methods and results at design reviews and Technology Readiness Level (TRL) gates.

2 Ultrasonic Inspection

Ultrasonic Testing (UT) is an important discipline for NDE and is used extensively around the world for the detection and characterisation of flaws, and the measurement of material properties [8]. This chapter will review the background of UT and discuss current state of the art technology with a focus on advancement of phased array based inspection.

2.1 Background

Ultrasonic inspection is commonly carried out using frequencies between one and five megahertz [9] across a range of industries. UT is commonly performed using piezoelectric crystals to generate low energy, high frequency stress waves in the component being tested. The stress waves generated are usually limited to normal compression waves and angled shear waves for manual inspection. The rationale for this approach is to make the interpretation of the time-amplitude plot (A-scan) displayed to the operator as easy as possible. Limiting the inspection to angled shear waves removes the majority of mode converted signals, and hence makes results interpretation less complicated as only one wave mode, and therefore wave velocity, must be considered by the operator.

The exception to this rule is the inspection of materials that are considered "ultrasonically noisy" or anisotropic materials. Common examples of "ultrasonically noisy" materials are large grain castings and welds. The variation in crystal orientation and stiffness between individual grains result in an inhomogeneous material. When an ultrasonic wave encounters a boundary between individual grains the variation in material properties causes low amplitude reflections from the boundary. These reflections are detected by the probe as standing noise that is commonly referred to as grain scatter. The variation in material properties, or crystal orientation, can also cause refractions of the ultrasonic wave that results in beam bending . For example, the inspection of austenitic stainless steel welds and castings.

Ultrasonically noisy materials are commonly inspected using low frequency angled twin crystal compression wave probes with a specific beam crossing depth. Compression waves are favoured as the slowness surface of the compression wave mode is significantly smoother compared to the vertically polarised transverse wave mode, and is therefore steered less [10, 11, 12]. For example, see Figure 2.1.1. Separate transmit and receive transducers are used to separate the two beam paths and reduce the amount of grain scatter recorded. The fixed beam crossing depth reduces the depth range over which the probes can be effectively used, and hence requires several probes to cover a given depth range. A common rule-of-thumb applied to this type of probe with beam crossing depth D, is to limit use to the depth range 0.5D - 1.5D.

Regardless of the chosen wave mode, angled wave probes use a Perspex shoe to angle the crystal relative to the surface of the component. When a wave is obliquely incident at an interface between two materials of different acoustic impedance the wave is refracted due to the different wave velocities; the result of this process is mathematically expressed by Snell's Law.

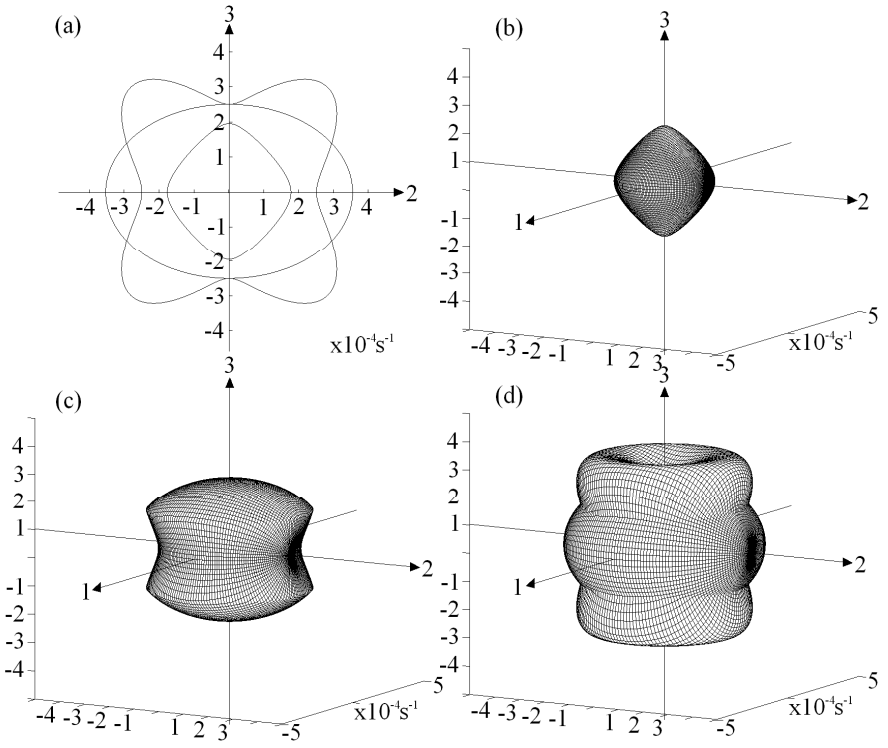

Figure 2.1.1: Predicted slowness surfaces for transversely isotropic stainless steel a) cross section in the 2-3 plane b) - d) longitudinal and transverse slowness surfaces [13]

2.1.1 Snell's Law

Snell's law can easily be derived using trigonometry from the geometry represented in Figure 2.1.2. If a plane wave propagates with a speed of c_1 toward the interface between materials one and two at an angle θ_1, a wave is transmitted into material two which propagates at angle θ_2 and with a speed of c_2. In time τ the wave in material one travels a distance BC and the transmitted wave in material two travels a distance AD. Therefore:

$$\tau = \frac{BC}{c_1} = \frac{AD}{c_2} \tag{2.1.1}$$

and via geometry

$$AC = \frac{AD}{\sin\theta_1} = \frac{BC}{\sin\theta_2} \tag{2.1.2}$$

rearranging and substituting equation (2.1.1) into (2.1.2) results in Snell's law:

$$\frac{c_1}{c_2} = \frac{\sin\theta_1}{\sin\theta_2} \tag{2.1.3}$$

An additional occurrence when a wave is obliquely incident upon an interface of an elastic material

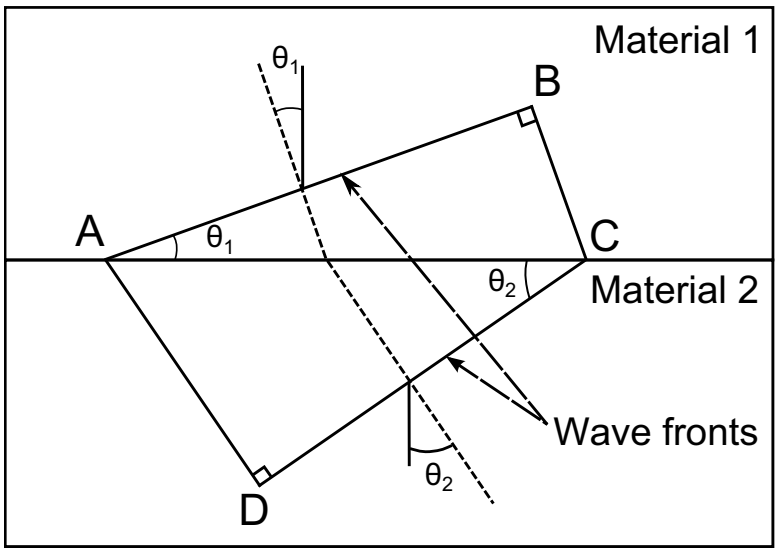

Figure 2.1.2: A diagram representing refractions as a plane compression wave passes from one material into a second (ignoring mode conversion) [14]

is mode conversion. This phenomenon results in a second transmitted wave mode becoming excited in the second (elastic) material. For example, a longitudinal wave incident on the interface between water and steel at an oblique angle would generate both a refracted longitudinal and shear wave in the steel [9]. This mechanism is actually taken advantage of in order to produce shear wave probes. These probes are designed to generate only shear waves in the specimen by generating a compression wave in a Perspex shoe at an angle relative to the specimen surface. When the longitudinal wave is incident on the surface the transmitted compression wave is refracted beyond ninety degrees, leaving only a mode converted shear wave in the specimen. This is known as total internal reflection of the longitudinal wave.

Equation (2.1.3) can be used to calculate the angle of refracted or mode converted wave modes by use of the appropriate wave speed and at least one wave angle. A common challenge encountered when carrying out ray tracing across an interface is how to solve the equation for an unknown wave angle. Equation (2.1.3) is not mathematically convenient to satisfy. A more attractive approach is to use Fermat's principle.

2.1.2 Fermat's Principle

Fermat's principle states that light rays of a given frequency will always follow the path of least time between two points [15]. Fermat's principle can be used to locate ray paths across an interface that results in wave refraction at a lower computational cost compared with solving Snell's law. It can be shown that Fermat's principle is equivalent to Snell's law. Consider the arrangement shown in Figure 2.1.3. A point source is located in material one at P_0. The ray path followed between points P_0 and P_2, located in material two, passes through point P_1 on the interface between the two materials. The travel time (t) of the waves can be described as:

$$t = \frac{L_1}{c_1} + \frac{L_2}{c_2} = \frac{\sqrt{(x_1 - x_0)^2 + (y_1 - y_0)^2}}{c_1} + \frac{\sqrt{(x_2 - x_1)^2 + (y_2 - y_1)^2}}{c_2} \tag{2.1.4}$$

where x and y are co-ordinates defined in Figure 2.1.3 and c is the wave speed in the material.

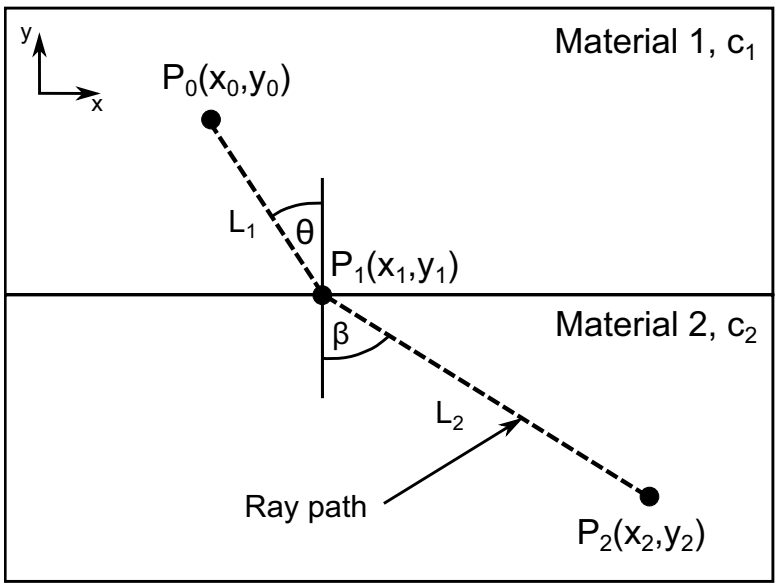

Figure 2.1.3: A diagram showing the ray path connecting a point source at P_0 to a point, P_2. The two locations are positioned in materials of a different acoustic impedance.

The minimum travel time can be found by differentiation of equation (2.1.4) *wrt* the location of the x co-ordinate of point P_1 and setting the equation to zero. The y co-ordinate is constant for a horizontal surface.

$$\frac{\partial t}{\partial x_1} = \frac{(x_1 - x_0)}{L_1 c_1} - \frac{(x_2 - x_1)}{L_2 c_2} = 0 \tag{2.1.5}$$

substituting x co-ordinates for expressions in terms of $\mathrm{L}_{1/2}$ (as defined in Figure 2.1.3) and the angles between the ray paths and the vertical leads to Snell's law:

$$\frac{L_1 \sin\theta}{L_1 c_1} = \frac{L_2 \sin\beta}{L_2 c_2} \tag{2.1.6}$$

Equation (2.1.5) can be solved to locate the transmission point on the interface, and therefore the refracted beam angle, in preference to Snell's law. This is particularly useful when calculating delay laws for phased array probes. The only disadvantage of this approach is that by solving equation (2.1.5) it is assumed that a solution to Snell's law exists. Equation (2.1.5) will always have a solution, but that solution will only satisfy Snell's law in some cases. For example, if scanning a component with an irregular surface in immersion it is possible that some fraction of the volume of the component cannot be reached by rays from a transducer with a fixed inclination. This is caused by changes in the surface normal that result in the wave mode of interest not being transmitted into the component.

2.1.3 Ultrasonic imagery

The A-scans produced using single element transducers can be used to build images by combining A-scans from successive probe locations. The resultant plot is referred to as a B-scan; an example is shown in Figure 2.1.4 a). Geometrically correct B-scan images can be formed by combining the stacked A-scans with the beam angle produced by the probe and positional information. This approach to imagery can be extended to C and D-scans when the probe is scanned along two perpendicular axis,

known as raster scanning. The C-scan is a projected top down view of stacked B-scans, and the D-scan a second projected view of successive B-scans. This approach allows a 3D volume of data to be displayed for interpretation. Diagrams demonstrating raster scanning and the produced B-scan views can be seen in Figure 2.1.4 b) and c).

The advantages of this form of data display, as opposed to simple A-scan display, is that a permanent record of the inspection can be stored. Whilst A-scans from a manual inspection can be stored, it is not practical to store all results from an inspection as the results are not normally encoded with positional data. Hence there is no means by which to link a particular A-scan to a component location. In comparison, this is easily achieved with an automated inspection. The results provide an auditable record of the inspection. A second benefit is the ability to analyse the results from an entire inspection at once, and even following data collection. The ability to view all the inspection data at once is particularly useful for applications on complex geometry or those containing materials which are inhomogeneous or anisotropic on an ultrasonic wavelength scale. The disadvantage of this approach is that probe manipulation must often be robotised and a higher degree of operator training is required, both of which increase the financial cost of the inspection significantly.

2.2 Phased arrays

A phased array is a single probe that contains many individual transducers known as elements [16]. An array transducer can be used to steer a plane wave or produce a focused beam by applying small time delays between the transmission and reception on each element in the array. These time delays are known as the delay law. This is possible as the array elements produce a very broad directivity pattern. The delay laws effectively optimise the inspection for a particular point on the directivity pattern, and in the case of a focused beam the inspection is also optimised for a point in time. Figure 2.2.1 demonstrates the differences in the delay law distribution across the array required to produce plane and focused beams.

Phased arrays can also be used to generate a B-scan scan image from a single position by using electronic scanning. This is possible if an aperture of elements is chosen which is smaller than the size of the array being used. This aperture is used to generate the desired beam and can be scanned electronically by moving the aperture along the array [16]. This procedure can be carried out in a very small period of time (tens of microseconds), so it is possible to fire and receive a number of different beams one after another and display the results graphically in real time. This method effectively allows an array to reproduce the raster scan shown in Figure 2.1.4 by physically scanning the array along a single axis and electronically scanning along the array.

Sectorial scans can also be produced using a phased array. A Sectorial scan is produced by sequentially firing a number of beam angles over a range of beam angles, with a defined step size. When plotted in space this produces a fan shaped plot, which is commonly associated with a foetal scan. The Sectorial scan can be composed of plane beams, or beams focused at a specific range or depth.

Phased array probes are designed to be more flexible than single element probes, and can be used in immersion, in direct contact, or with a wedge. Despite initial scepticism phased array technology is becoming increasingly popular for the purposes of NDE, due to recent developments in array controllers [17]. Improvements in array controllers are being driven by improvements in portable computer tech-

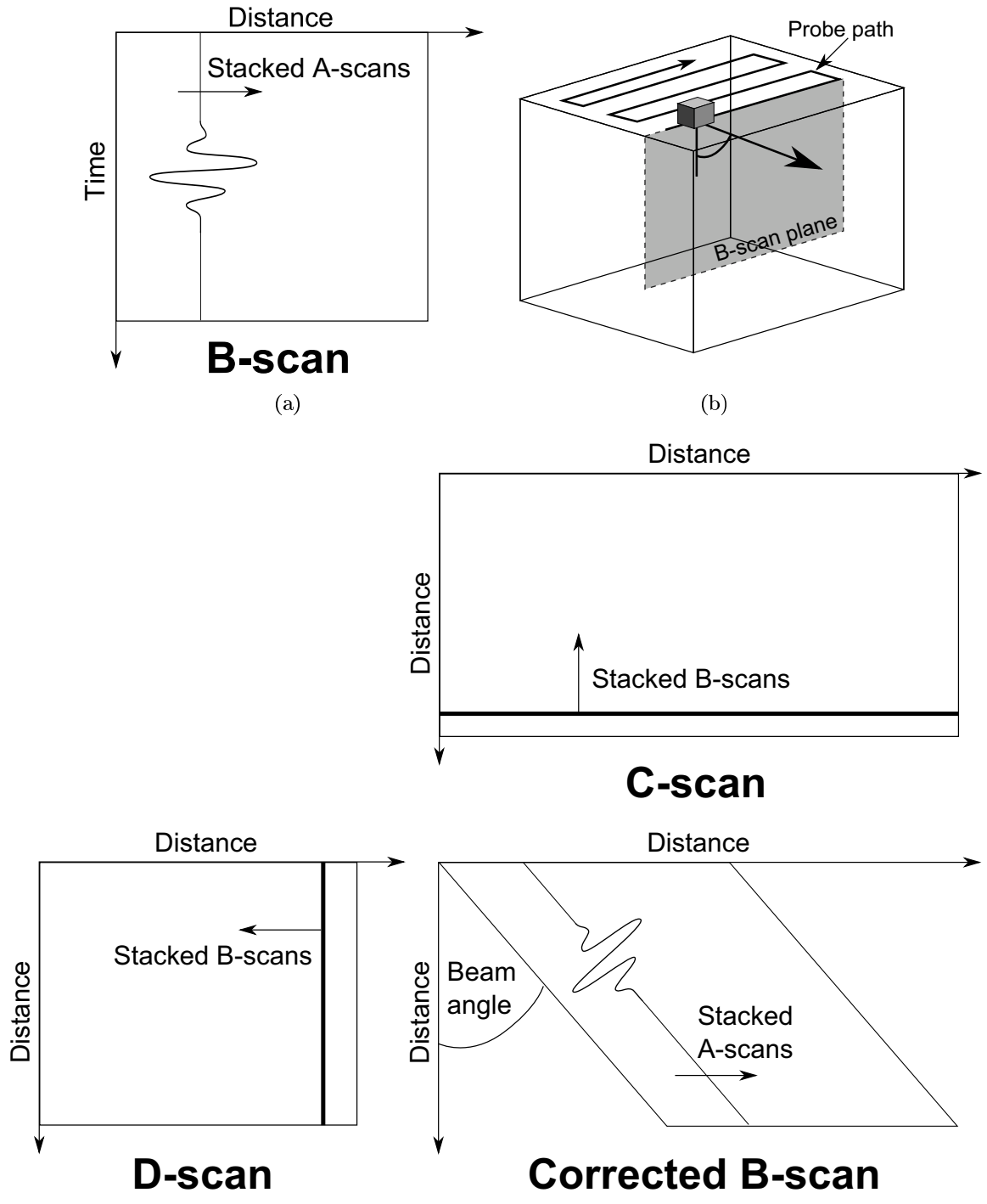

Figure 2.1.4: Diagrams demonstrating the concept of projected geometrically correct ultrasonic images, and the concept of raster scanning. Plot a) a standard B-scan constructed of stacked A-scans, b) a diagram representing the concept of raster scanning, c) diagrams demonstrating a geometrically corrected B-scan image, and projected views of stacked B-scan images.

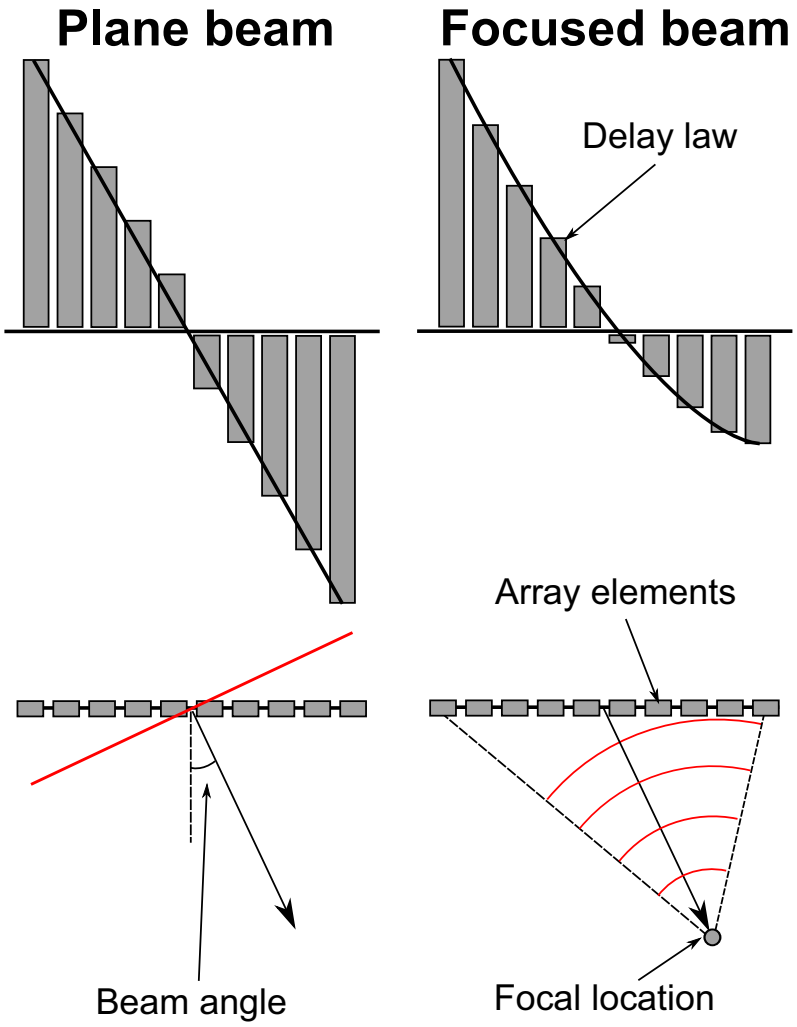

Figure 2.2.1: Diagrams demonstrating the principle of delay laws and the difference between a) a plane beam and b) a focused beam.

nology [18] as well as improvements in the maximum number of independent transmit-receive channels [19]. These improvements mean that array controllers are physically smaller and lighter, thus making them more attractive for manual inspections, whilst the higher number of independent channels means that arrays are more attractive to the high end of the market where the capability to use a large number of active elements, in order to produce beams without artefacts, is a requirement [17].

Ultrasonic phased arrays are now commonly used in NDE as a replacement for one or more monolithic transducers [20, 21, 4]. This is achieved by firing multiple elements with suitable delay laws in order to generate equivalent beams to those produced by monolithic devices. Reflections from the test piece are recorded (also using delay laws) and the response from every element is summed to produce a single A-scan . This approach to the use of phased array technology allows existing inspection procedures to be used whilst potentially speeding up inspection times, but fails to realise the full potential of phased array technology [22]. However this approach is especially attractive for qualified or performance demonstrated inspection, such as those used in the nuclear industry, as complete inspection redesign to take advantage of the benefits of arrays can be cost prohibitive due to the qualification process.

Phased arrays are a particularly attractive technology for manual ultrasonic inspection. Manual inspection is commonly applied using a zero degree compression wave probe and a small number of angled shear wave probes. Results are presented as an A-scan and the operator must have the knowledge and experience to match A-scan response to known defect response patterns in order to characterise any detected defects. In comparison a phased array can be use to generate the same beam types and produce a graphical output through the use of sectorial or electronic scanning. These types of images provide the operator with more information and arguably increase the probability of detecting a defect. Phased arrays also offer the ability to easily and relatively cheaply semi-automate inspections using a wheel encoder. This equipment can be used to record a line scan of the transducer and teh results later interpreted using graphical software. This allows all data to be assessed at once and also provides a permanent record of the inspection.

There are several types of arrays that are in common usage: linear arrays, annular arrays, and 2D arrays; all of these array types are shown in Figure 2.2.2. Linear arrays are most commonly used for NDE, and allow beam steering and focusing to be carried out in a single plane [19]. Linear arrays are also widely used within the medical industry; for example phased arrays are commonly used for foetal scanning [23, 24] and have also been used to manipulate detached retina using dynamic steering and focusing [25]. Annular arrays are only capable of generating focussed beam at different depths but one annular array can be used to replace a number of conventional focussed probes [26]. It is also possible to use a concave shape to provide some natural focussing in order to reduce the number of elements that are required [27].

Two dimensional arrays are rarely used by the NDE industry but are becoming more widespread in the medical industry [19]. Two dimensional arrays have the advantage of allowing beam steering in two dimensions. The beam forming performance of any array is governed by the size of the array aperture used to form a beam. 2D arrays are capable of forming an axially symmetric beam that can be focused and steered in three dimensions, improving the resolution of the beam. But the number of elements required are pushing the limits of current manufacturing capabilities [28]. The downside of 2D arrays is that for a fixed number of channels the maximum aperture size is limited by the maximum sampling size of the array, normally $\lambda/2$. For a rectangular grid, sampling sizes above this value produce grating lobes that corrupt the images produced using the array. A potential solution to this problem is the use

of larger element sampling sizes, different element layouts, and different transmit and receive apertures.

Smith et al [29] and Lockwood and Foster [30] used different transmit and receive apertures to reduce the effective transmit-receive amplitude of grating lobes. Smith et al used one design when an array aperture in the shape of a cross was used in transmit and receive, but rotated relative to each other. The cross aperture shape produces a grating lobe and a null sensitivity region in the beam pattern. The receive aperture was rotated such that the transmit grating lobe and receive null overlapped, thus producing an insensitivity to the grating lobes produced. For example, the Mills cross array configuration is commonly used in radar [31, 32] (See Figure 2.2.3).

Many researchers have investigated the design of sparse 2-D arrays using non-periodic element layouts to increase the inter element spacing. The non-periodic distribution of elements breaks up the formation of grating lobes at the cost of an increased level of background noise. Davidsen et al [33] investigated the design of an array which used a Gaussian distribution of elements, but secondary lobe formation was still an issue. Austeng and Holm [34] presented methods for designing arrays with axially or radially symmetric element distributions. However, this work focused on a medic application with element numbers often in excess of 500. This number of elements is still beyond the number of parallel channels available in array controllers designed for NDE.

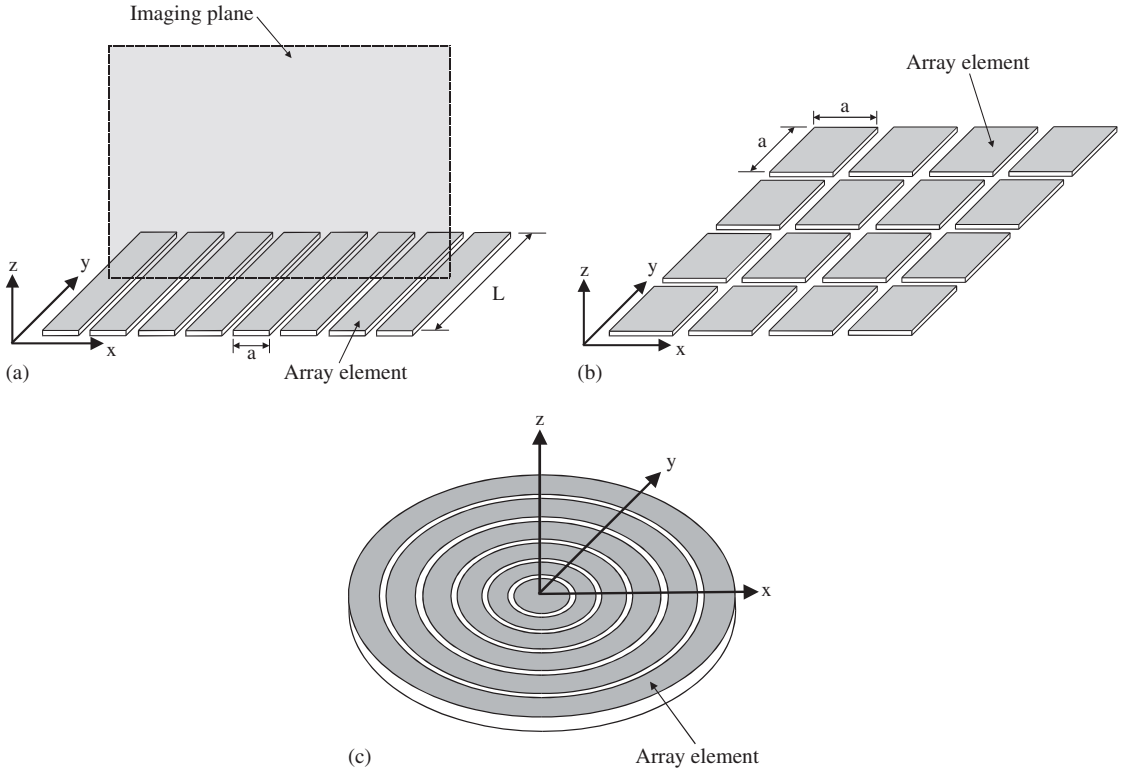

Figure 2.2.2: A selection of array types: a) linear array b) 2D array c) annular array [19]

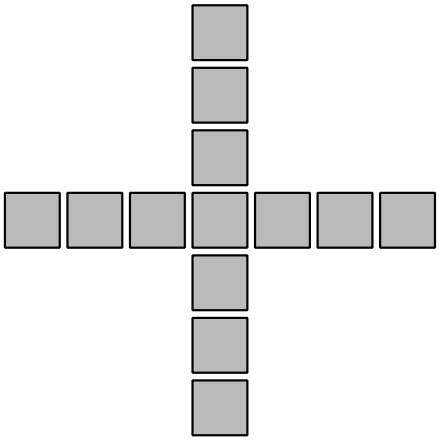

Figure 2.2.3: The Mills cross array configuration [19]

Recently work reported by Velichko and Wilcox [35, 36] compared the imaging performance of a periodic array using an hexagonal and an array using a Poisson disk distribution using only 128 channels. This work demonstrated good performance when using an hexagonal element layout with a spacing of $\lambda/\sqrt{3}$. However, the more promising result was that produced using a Poisson disk distribution. Figure 2.2.4 shows the results from a number of flat bottomed holes and a 1 mm notch in an aluminium block using a 3 MHz 11 x 11 array with a $\lambda/2$ rectangular element arrangement and a 128 element Poisson disk array with a maximum inter element spacing of ~0.9λ. The rectangular grid array has an effective aperture of 11 mm whilst the Poisson disk array has an aperture of 30 mm. The -30 dB isosurfaces clearly demonstrate the Poisson disk array out performs the rectangular grid array. These developments demonstrate that the focusing range of 2D arrays can be effectively extended whilst maintaining a practical number of elements.

The development of innovative solutions to 2D array design and beam forming presents a means by which 2D arrays be practically deployed in industry. However, sparse array manufacture for NDE applications is still at an early stage of development.

Phased arrays are also capable of generating beam types that a single element probe is not capable of. An example of such a technique is Dynamic Depth Focusing (DDF). DDF requires an unfocused beam, or several beams focused at different depths, to be fired, and varying reception delay laws are applied in order to improve sensitivity over an increased range of depths [37]. The reception delay laws can be changed in stages to represent a number of distinct focus depths or continuously varying delay laws can be used in reception that can extend the effective depth of field of the focused beam to the full thickness of the test piece. This capability allows a single phased array probe to replace a number of single element probes focused at different depths and to do so in a single scan. This type of processing is limited with conventional phased arrays due to a number of reasons:

- The speed of electronics required to implement complex delay laws in real time
- The increase in scan time if many transmit and receive combinations have to be used

Both of these factors can be overcome by the use of alternative data capture methods such as Full Matrix Capture (FMC).

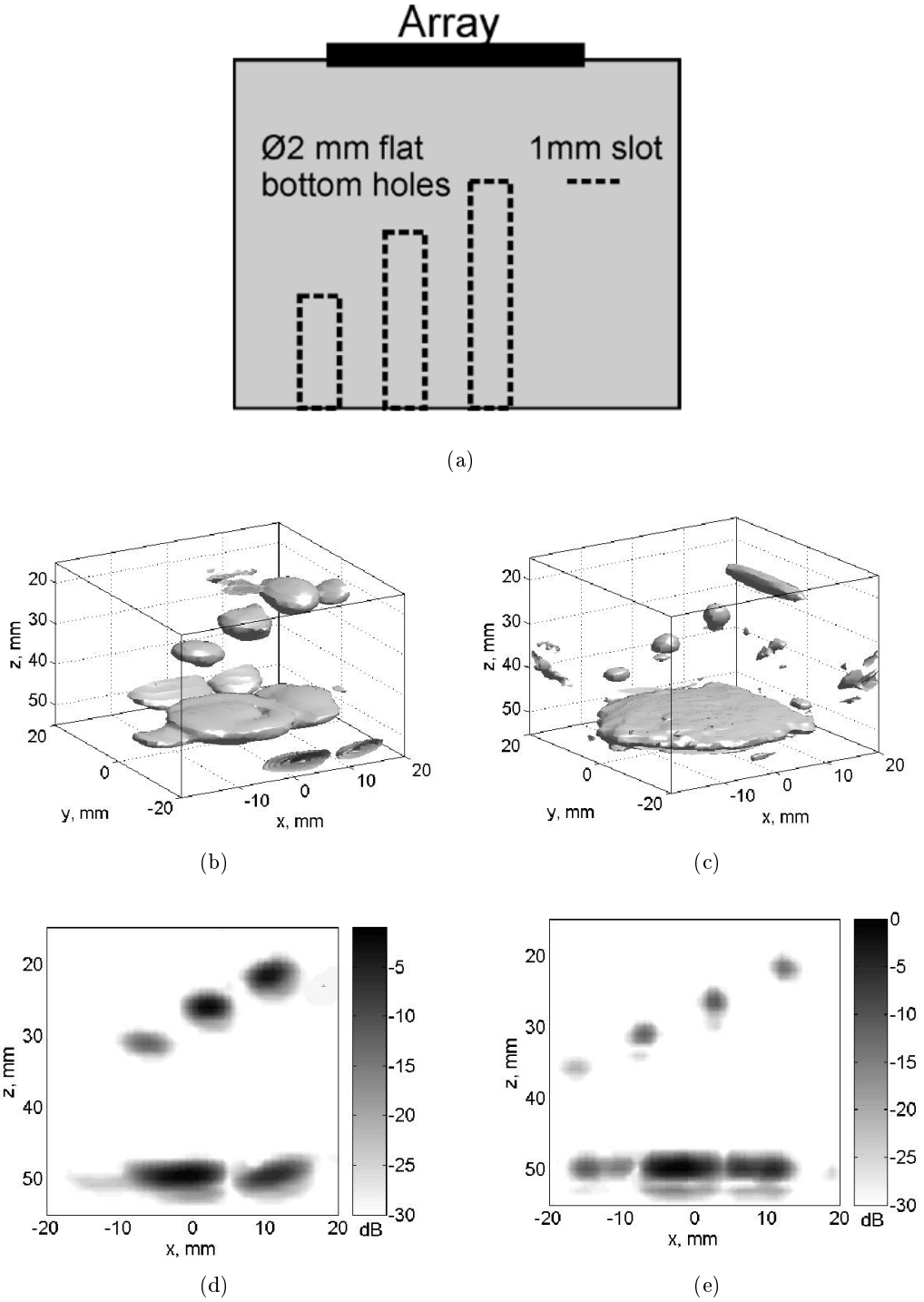

Figure 2.2.4: The comparison of a grid array and a Poisson disk array using 3D TFM imaging [36] a) test block diagram, b) - c) -30 dB isosurfaces for grid and Poisson disk array, d) - e) 2D TFM images along the array centreline for the matrix and Poisson disk arrays.

2.3 Full Matrix Capture (FMC)

Full Matrix Capture [4] is an alternative method of data capture to real-time beam forming that places the emphasis on the collection of raw unprocessed data. The full matrix of data is collected by pulsing a single element in the array and recording received signals on every element in the array; the process is then repeated for every element in the array. This produces a three dimensional matrix of data; two dimensions being equal in length to the number of elements in the array, and the third dimension containing the time domain data. This is demonstrated by the following equation:

$$FMC\left(T_i, R_j, t_k\right) = \begin{pmatrix} T_1R_1\left(t_k\right) & \ldots & T_1R_{n(t_k)} \\ \vdots & \ddots & \\ T_nR_1\left(t_k\right) & & T_nR_n\left(t_k\right) \end{pmatrix} \tag{2.3.1}$$

where T and R are the transmit and receive element number respectively, and t is the time sample.

FMC data must be collected with high levels of signal amplification as each A-scan only contains the signals produced via the excitation of a single array element. Accordingly the signal amplitude is relatively low in comparison to the same array using an aperture of elements to generate a certain beam. This requires high levels of gain and therefore high quality electronics in order to achieve low levels of electronic noise.

This form of data capture is time consuming relative to the conventional use of phased arrays. Although an inspection using conventional beam types easily exceeds the number of transmit receive combinations required by FMC, conventional inspections typically require a number of A-scans of the order of hundreds to be transferred from array controller to PC. In comparison, FMC datasets are composed of thousands of A-scans. This results in a significant data transfer burden when recording FMC data during large component inspections which may require thousands of probe firing locations. The size of the time burden this introduces is controlled by the achievable data transfer rate between array controller and PC. Current commercial array controllers often utilise Gigabit ethernet to deliver data transfer rates of approximately 50 mb/s, meaning typical FMC data transfer times of several seconds. This size of this burden will reduce if the adoption of FMC inspection results in array controllers offering faster data transfer interfaces. However, by collecting all possible data at a single probe position, any beam type that could be generated via delay and sum beam forming can be recreated in post processing. This flexibility is the main attraction of FMC as any number of inspection techniques could be applied retrospectively.

Examples of the types of algorithms that have been developed for FMC include conventional approaches that are widely used with phased arrays such as Sectorial scanning, Plane B-scan, and Focussed B-scan [4, 38]. Whilst these types of algorithms do not provide any more capability than the same type of algorithms employed in real time, they still offer the ability to change beam parameters retrospectively. For example, high integrity inspections such as nuclear power plant components are commonly performed using manipulators to automate the scanning of several single element probes at once [39, 40]. All the types of algorithms mentioned could be used in real time with a phased array probe; this would offer some time saving as only one probe has to be scanned over the component.

However, the use of FMC also provides the ability to apply new algorithms to old inspection data retrospectively as well as the ability to change beam parameters. Whilst this ability is at the cost of slower scanning times it is still attractive due to the flexibility it provides e.g. defect characterisation.

Much of the work done on the processing of FMC data has been on the development of algorithms that cannot be practically performed in real time due to the large number of transmit delay sequences required. Examples of these types of algorithms include the Total Focusing Method (TFM) [4], the Vector Total Focusing Method (VTFM) [41], the Almost Total Focusing Method (ATFM) [38], Diffraction Total Focusing Method (DTFM) [42], and the Wavenumber algorithm [43].

2.3.1 The Total Focusing Method (TFM)

The TFM algorithm is based on the premise of generating a B-scan image that is focused at every point in the image. This is achieved by discretising the target region into a grid of points; the entire array is then used to form a focus at each image point using the same method as a conventional focused beam. The amplitude of the received signal is then extracted at the time of flight corresponding to the imaging location and assigned to the image point. Repeating this process for each image point produces an image. Figure 2.3.1 a) demonstrates the principle of the TFM. The TFM algorithm has been demonstrated to outperform all other linear imaging algorithms when imaging point-like reflectors [4]. The disadvantage of this technique is the computation time required to form the image, particularly if a wedge mounted array is used as the ray path between each element and image location must be found using Fermat's principle. Figure 2.3.1 b) presents an example TFM image of three Ø3 mm Side Drilled Holes (SDHs) in a 30 mm thick stainless steel test block, using a 2 MHz 48 element array mounted on a Rexolite wedge. The reflection from the backwall of the test piece can clearly been seen at a depth of 30 mm, and the responses from the SDHs can be seen at a depth of 25 mm.

An alternative to the TFM algorithm is the Wavenumber algorithm. The Wavenumber algorithm performs a similar process as the TFM algorithm but uses Fourier-domain inversion of a forward model for the wave propagation and scattering process rather than the delay-and-sum beam forming used for TFM. The Wavenumber algorithm significantly decreases computation time compared with time domain processing [43, 44].

DTFM is another algorithm based on the TFM algorithm. The DTFM algorithm uses two arrays facing one another in a pitch catch configuration. One array acts as a transmitter and the second array as a receiver and the TFM algorithm is used to generate an image of the type shown in Figure 2.3.2. The diffraction from the end of the angled slot is clearly visible and located in the correct position. This would allow accurate sizing information to be extracted.

One of the disadvantages of the TFM is that point like scattering is assumed. Many ultrasonic inspections are primarily searching for planar defects. The ultrasonic response from a planar defect is highly dependent on the direction that the wave is incident upon the defect. If the TFM is used for such an application the experimental arrangement used dictates the range of beam angles that composes the imaging region. By careful selection of the imaging region the range of beam angles can be tailored for the application. For example, searching for lack of fusion defects in a weld with a 30 degree fusion face should be imaged with a range of beam angles centred on 60 degrees. Whilst this type of approach mitigates the assumed scattering behaviours associated with TFM a further problem is the interpretation of results. Defect characterisation using ultrasonic testing is performed on the basis of matching the amplitude variation across a defect with accepted defect response shapes, referred to as pattern types [45]. By using several different beam angles the data analyst can build a model of the defect that best fits the defect location, pattern type, and absolute amplitude. The TFM does not provide sufficient information to complete this process unless images are formed with the array in

several different locations. Instead an extension to the TFM method exists that aims to solve these issues.

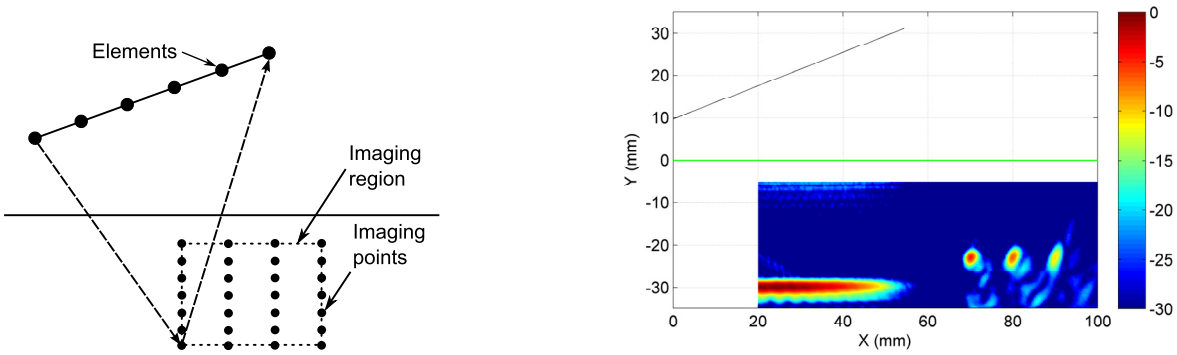

(a) (b)

Figure 2.3.1: The TFM a) diagram demonstrating the principles of the TFM b) a sample TFM image, three SDHs can clearly be seen. The colour scale is in decibels.

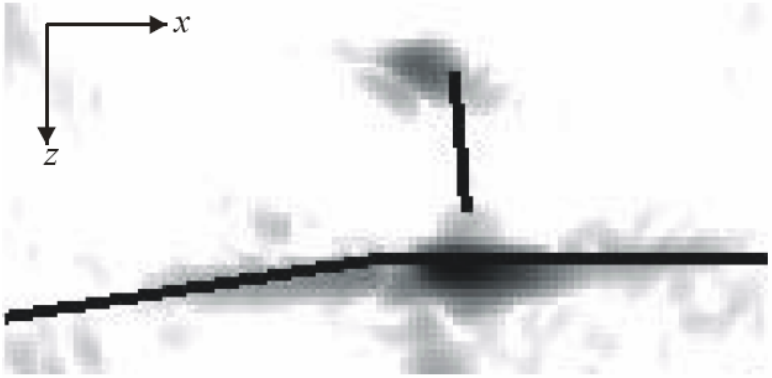

Figure 2.3.2: A DTFM image produced using one array as the transmitter and one as the receiver. The back of the specimen and an angled slot are represented by black lines [42]

2.3.2 The Vector Total Focusing Method (VTFM)

The VTFM [41, 22] algorithm uses the same methodology at the TFM algorithm but also seeks to extract more information from a reflector by attempting to measure the reflector orientation and specularity. The process for producing a VTFM image is as follows (this process is also demonstrated in Figure 2.3.3):

- The target area is discretised into a grid of points
- The array is divided into N equal sub-apertures
- n TFM images are produced using only one sub-aperture for each image
- Each image is used to calculate reflector orientation and specularity in order to generate a vector image. A more detailed description of the VTFM process can be found in [41].

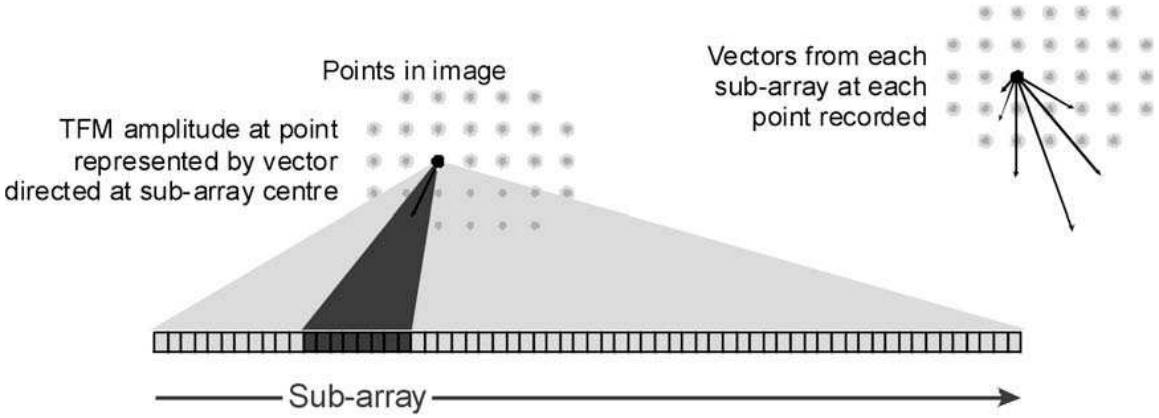

Figure 2.3.3: The operation of the VTFM algorithm: a) showing the selection of a sub-array and the inset diagram demonstrating the vectors produced by considering several sub-arrays [46]

The reflector orientation is calculated by summation of the vectors from each sub-aperture raised to a power [22]. This produces a result that is skewed toward the largest contribution. For example, a planar reflector would produce the largest reflection from the sub-aperture orientated closest to the normal to the plane. However, the result of this process can potentially be misleading. Consider the result of applying this process to an image containing the response from a side drilled hole. A side drilled hole has uniform response from all directions but the result from the process used to calculate a metric for reflector orientation would produce a vector pointing toward the centre of the array as not all angles have been probed [22]. As a result of this orientation alone cannot be relied upon. A second metric used to characterise the response from a reflector is its specularity. Reflector specularity is calculated from the standard deviation of vector lengths at a particular point[22]. The results of this can then be used to 'tune' an image by multiplying a TFM image by the specularity at every point. By raising the specularity parameter to increasing powers specular reflections in the image are emphasised.

The results of VTFM can then be applied to a TFM image in many ways. Orientation information can be displayed over the TFM image or the vectors can be coloured based on the image amplitude at that point. Both types of images are shown in Figure 2.3.4.

2.3.3 Scattering Matrices

Scattering matrices [48] could be described as an extension to the VTFM. Both techniques attempt to extract orientation information about a defect from experimental data. The VTFM method aims to add orientation and specularity information to the image produced by the TFM to communicate information on defect character. The scattering matrix approach is more closely related to the pattern matching approach that has been used in conventional ultrasonics for many years.

Scattering matrices are a graphical means of presenting the variation in reflection amplitude with incident angle. A reference scattering matrix for a given defect type must be formed by simulation,

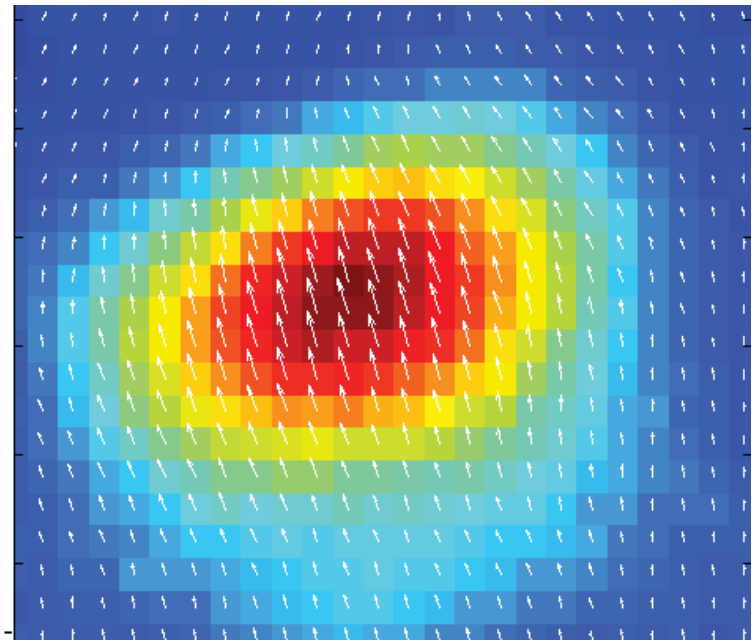

(a)

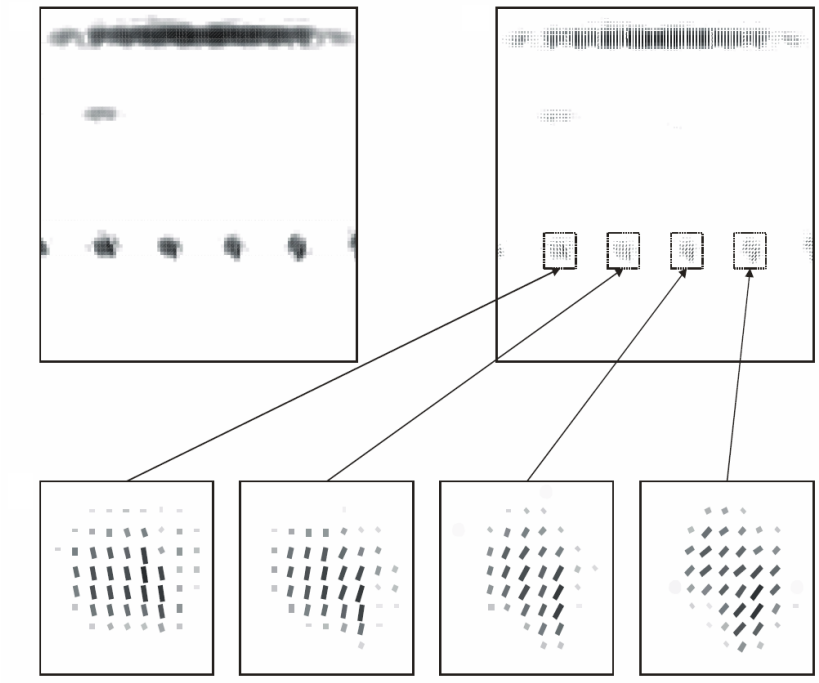

(b)

Figure 2.3.4: a) a TFM image overlaid with orientation information for a 30 degree slot [47] b) The TFM (left) VTFM (right) orientation vector field for a number of angled slots [22]

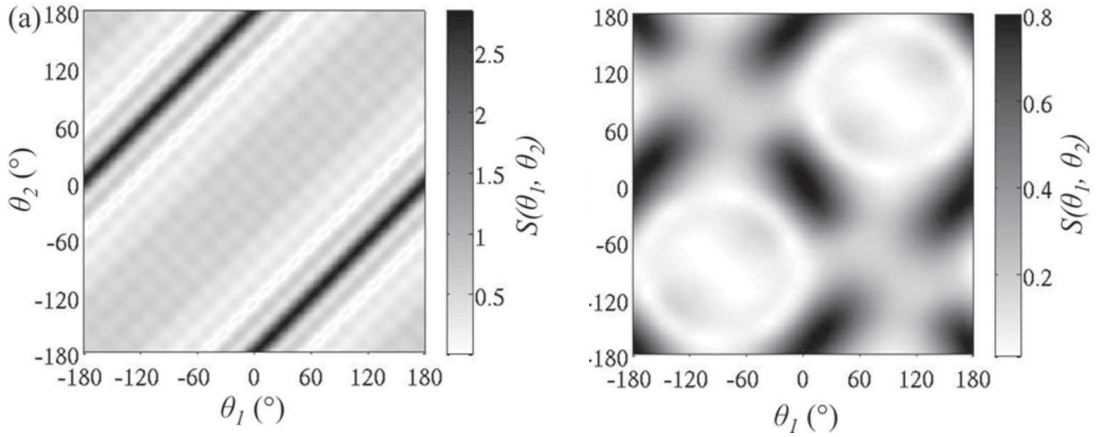

(a) (b)

Figure 2.3.5: Predicted scattering matrices for a a) 1 mm SDH b) 1 mm planar defect [48]

for example using the finite element method. Some examples taken from Zhang et al [48] for a Side Drilled Hole (SDH) and small planar defect can be seen in fig 2.3.5. Theta one on the x axis is the incident angle and theta two on the y axis is the receiving direction. The angles are measured from the horizontal in the anti-clockwise direction. The amplitude of the theta one and two combination is then plotted as a colour. As would be expected for a SDH there are two high amplitude lines across the matrix with a gradient of one, that correspond to a specular reflection that can occur at any theta position around the hole. The result from the planar defect is more complex. High amplitude regions that correspond to specular reflections can be seen as well as lower amplitude rectangular regions surrounded by circular shapes that are caused by tip diffracted signals.

Results such as these can be used to build a library of scattering matrices, against which experimentally recorded matrices can be compared . The challenge with this approach is that experimental data will typically only be able to populate a small region of the matrix due to the limited size of the array and geometric constraints etc. A further challenge with this approach is the variation in defect response due to small variations in defect shape and roughness. The existing approach to pattern recognition is much less specific than the scatter matrix approach and is more of a philosophy than a quantitative method. This places more reliance on the skill of the data analyst to correctly characterise complex defects, but makes the method more flexible. If the scattering matrix approach can be used to allow automated/semi-automated defect characterisation it may be possible to improve the accuracy of defect characterisation, or reduce the reliance on analyst experience. However, significantly more work is required before it could be used quantitatively for regulated inspections.

2.3.4 The Almost Total Focusing Method (ATFM)

The Almost Total Focusing Method (ATFM) [38, 49] is a variant of the TFM that is intended to maintain many of the benefits of TFM while producing results that are closer to those produced using conventional focused B-scan images. The advantage of this approach is that existing methods for data interpretation can be used. Where ATFM and TFM differ is the number of elements used to generate the image and the number of beam angles. As already mentioned TFM uses all the elements in the array

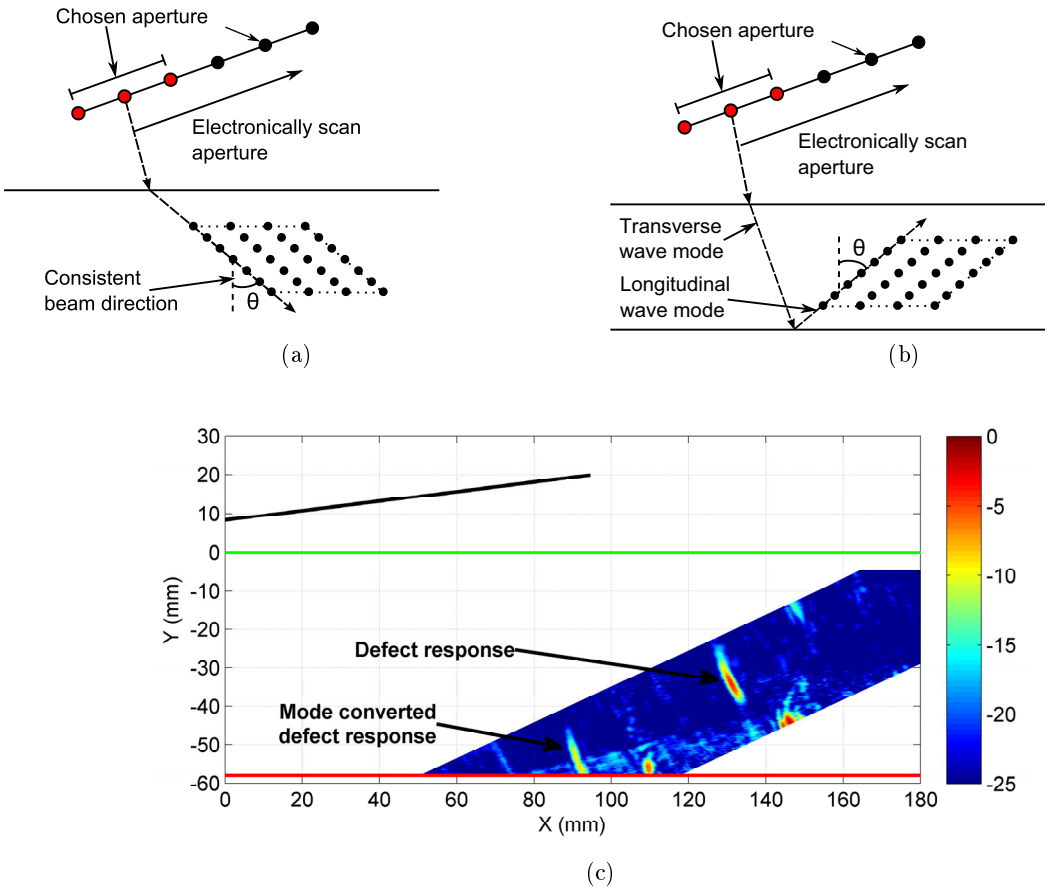

Figure 2.3.6: Diagrams demonstrating the methodology used by the ATFM a) the direct ATFM algorithm b) the mode converted ATFM algorithm c) an example mode converted ATFM image of a artificial planar defect.

and many different beam angles. ATFM uses a fixed beam angle and array sub-aperture to produce an image that is focused at every point along the ray path from the centre of the selected aperture up to the focus point. An image region is produced by electronically scanning the sub-aperture along the array. Figure 2.3.6 a) presents a diagram that highlights the differences between TFM and ATFM. This algorithm could be described as reduced aperture TFM and the FMC equivalent of dynamic depth focusing.

ATFM can also be used to generate mode converted focused beams. These techniques are commonly used during austenitic weld inspections to detect lower fusion face and vertically orientated defects. The technique requires a low angle shear wave incident on the backwall of the component which mode converts to a high angled compression wave . Long et al [38] discusses these techniques in some detail, and Russell et al [50] reports practical application of the methods. Figure 2.3.6 b) presents an example mode converted ATFM image. The data is plotted upwards from the backwall at ~60 mm and the defect can clearly be seen, along with other mode converted responses. A 128 element 2 MHz immersion array has been used to collect the FMC data.

2.3.5 Irregular surface adaptive inspection

An application of phased array technology that has generated considerable interest is adaptive surface profile inspection. In principle a phased array can beam-form through a smoothly varying surface by using delay laws that are adapted to the geometry of the interface. Clearly this method is not able adapt to any surface geometry, but smoothly varying surfaces can be accommodated with minimal loss of inspection performance [50]. This approach was first proposed by the Commissariat à l'Energie Atomique (CEA) [51, 52] using a flexible array that requires profilometers along the length of the array in order to measure the surface geometry. This type of approach has the benefit that each array element is in direct contact with the component so delay law calculation is straightforward. The drawback of this approach is that it requires a relatively expensive probe, that has been shown to be unable to conform to some geometries e.g. the weld toe at the edge of a domed weld cap [53]. This technique, and all the following techniques discussed in this section, assume isotropic material properties and ignore the inaccuracies introduced by the effect of anisotropic weld structures.

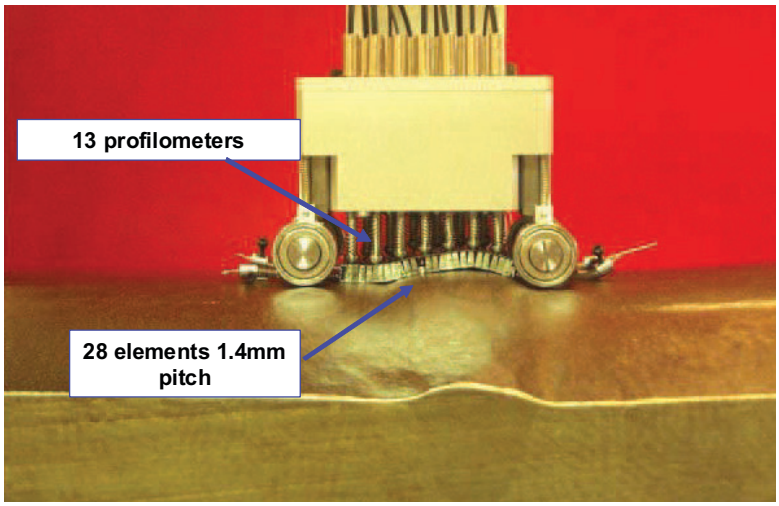

Figure 2.3.7: A photograph of a prototype flexible array produced by the CEA

An alternative approach initially developed by Imperial College London [54] and further developed by Rolls-Royce Submarines in collaboration with Imperial College London [5] uses a standard immersion array encased in hollow housing with a polyurethane membrane on the bottom surface. The housing can be filled with water and by raising the water pressure the membrane material is stretched and produces a "bulge" which allows the probe to conform to the geometry of a profile. This type of device is referred to as a membrane probe; a photograph can be seen in Figure 2.3.8. The drawback with this approach is that the probe can only conform to geometry that protrudes a distance of the same order as the "bulge", and therefore different housings may be required for different applications. This design also suffers from high amplitude parasitic echoes from the water-component interface due to the large acoustic impedance difference between the two materials [5].

The membrane probe requires that beam forming is first carried out in the water wedge to measure the surface profile beneath the probe; this step produces the same output as the profilometers used by the CEA device. FMC data collection is therefore attractive as a single data set can be used to measure the surface profile and subsequently inspect the component. Alternatively this step could be removed

if prior knowledge of the surface profile exists and the position of the probe relative to the surface is known accurately. This approach would allow surface profile adaptive inspection to be carried out using the array conventionally with real time delay laws. However, FMC allows this processing to be done without prior knowledge of the surface profile and probe location.

Some example results using a membrane probe can be seen in Figure 2.3.9. FMC data has been collected using a 128 element 2 MHz array on two test pieces. Each test-piece contains three SDHs. One test piece has a flat surface and the second has a artificial weld cap machined on the top surface. The figure shows the B-scans generated by electronically scanning a 60 element aperture along the full length of the array whilst generating a 60^{o} shear wave focused at the depth of the SDHs. The result provided in Figure 2.3.9 (a and b) have been generated using standard delay laws on both test pieces. The results show that the SDHs are not evident when the artificial weld cap test piece is used. Image b) shows the deterioration in inspection performance when using plane surface delay laws on the artificial weld cap test-piece. In this scenario, only one of the SDH targets is detected, and there is a high amplitude reflection from the weld cap. Image c) shows the results when the delay laws are updated to accommodate the surface profile. All three SDHs are reliably detected when using this technique.

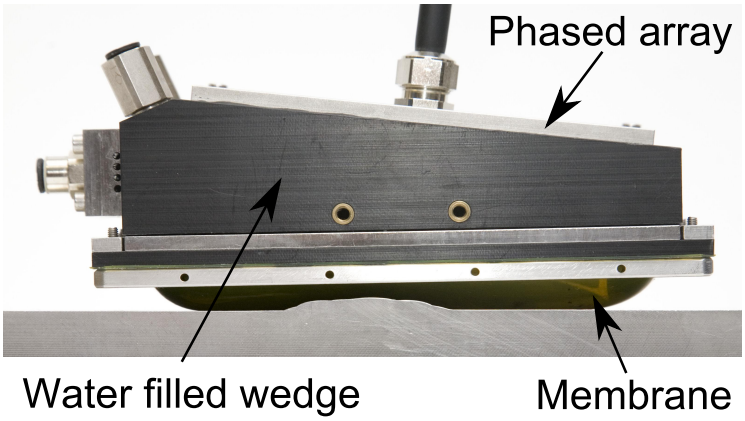

Figure 2.3.8: A photograph of the membrane probe assembly

An alternative approach developed by the University of Bristol, in association with Rolls-Royce Submarines, uses image based approaches to infer the surface profile of a component rather than a direct measurement. Two techniques have been developed, both based on the TFM [53, 55]. In each case an assumed surface profile is used and the component is imaged. The first technique is based on the extraction of an image contrast metric. A Monte Carlo based technique is then employed to search for the global maxima of image contrast via perturbation of the assumed surface profile. The disadvantage of this approach is the insensitivity of the image contrast metric to translation and rotation of the array profile [53]. Instead a second approach was developed that is based upon optimisation of a forward model of the experiment. Geometric features within the image are selected as known reference features and the time of flight error between the measured and modelled data are iteratively minimised using a least squares approach [55].

An example result from the model based technique is shown in Figure 2.3.10. The experimental arrangement is shown in a) and a reference result from a test piece with a flat surface is shown in image b). The autofocused result, shown in image c), was produced by using the backwall echo from the test piece as a known planar reflector in the forward model. The autofocused image demonstrates very similar performance to the reference result and shows the ability of the algorithm to accurately infer the surface profile of the test piece. In this example the flexible array developed by the CEA was used but there is no reason why the same approach could not be used with a conventional linear array, such as the membrane probe. The advantage of this approach is that complete coverage of the surface profile is not required in order to measure it, but the extent of the surface profile measured is still limited to the locations utilised to image the reference feature during autofocusing.

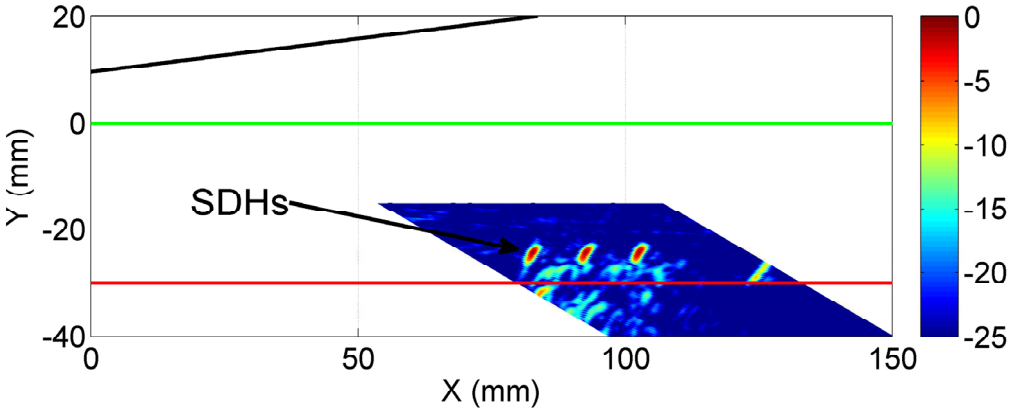

(a)

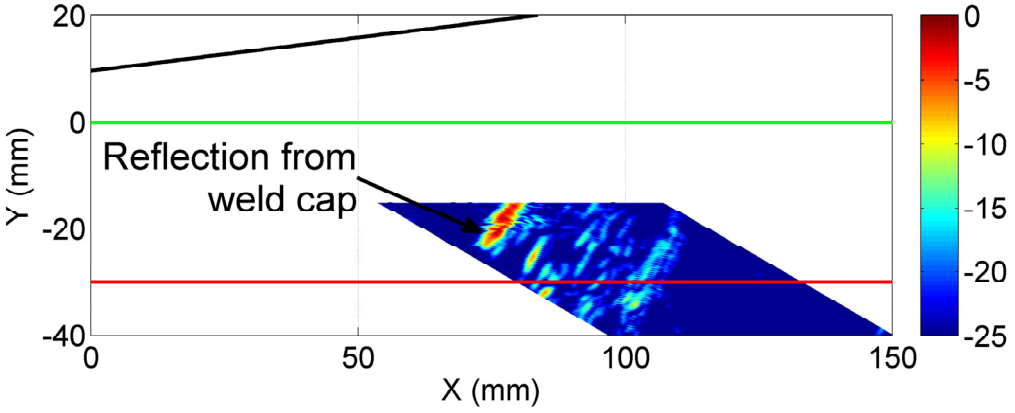

(b)

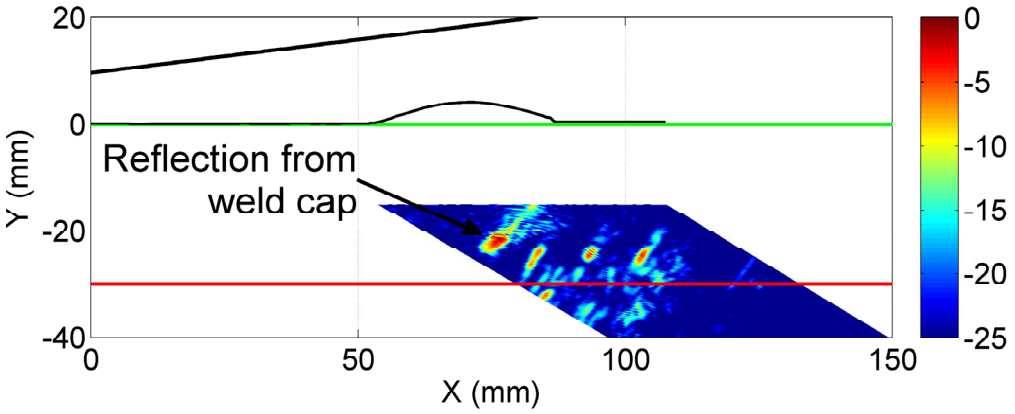

(c)

Figure 2.3.9: The results from experimental testing above a artificial weld cap with three Ø3 mm SDHs at 25 mm depth. The array location is represented by the black line, and the green and red lines show the location of the top and bottom surfaces of the test block: a) plane surface delay laws when no weld cap is present, b) plane surface delay laws when a weld cap is present c) updated delay laws applied when a weld cap is present. The additional black line shows the surface profile measured by the array, and used to update delay laws.

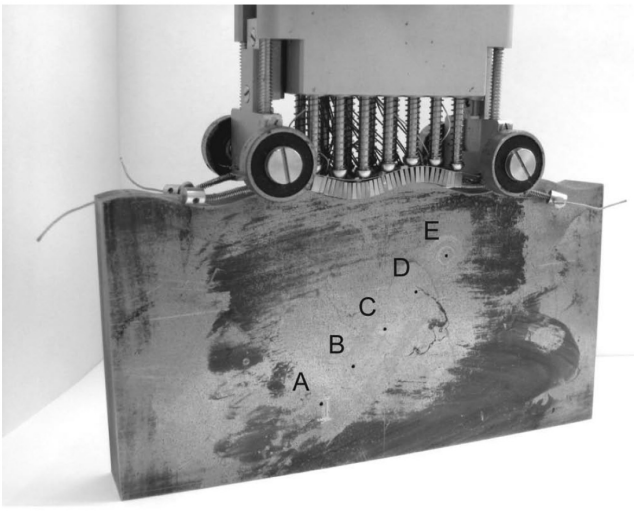

(a)

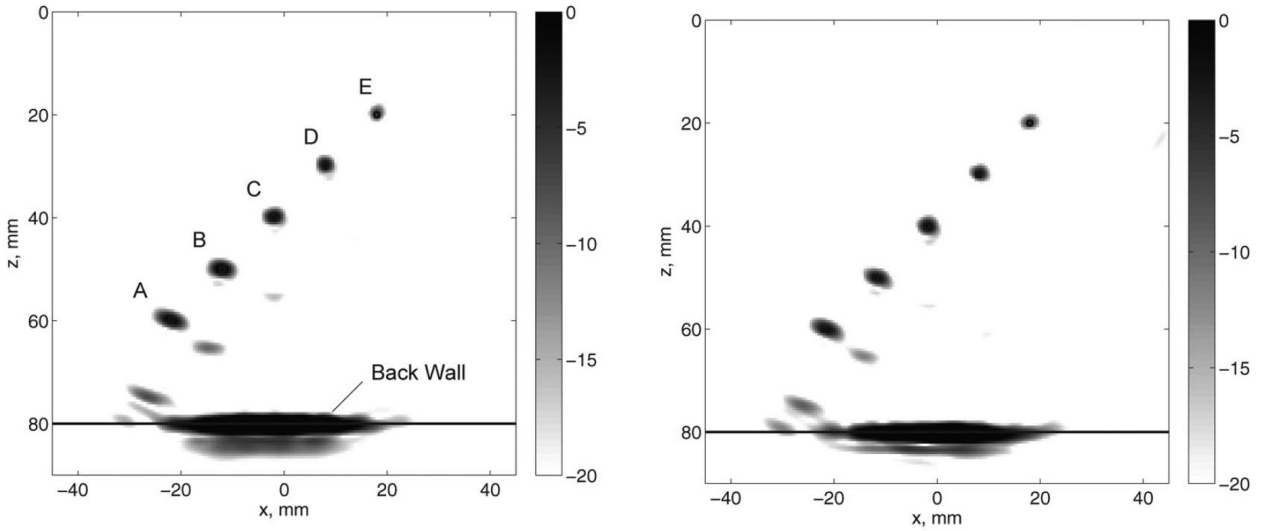

(b)

(c)

Figure 2.3.10: An example of the application of the model based autofocus algorithm a) a photograph of a flexible array mounted on a test piece containing a number of SDHs and a sinusoidally varying surface profile, b) the TFM image generated on an identical test piece with a flat surface, c) an autofocused image from the specimen with an irregular surface using the specular reflection from the backwall of the specimen as the geometric reference feature [55].

2.4 Summary

Ultrasonic inspection is extremely well established as one of the primary NDE methods for volumetric inspection, and is used extensively across many industries and the world. The use of ultrasonics is becoming increasingly popular in part due to a desire to reduce the amount of radiographic inspections carried out. The primary motivations for this are health and safety concerns and the disruption to sites that radiographic exclusion zones cause.

Phased arrays are increasingly being used across industries as a result of their flexibility, speed of inspection, and improved graphical data display. Phased arrays also offer the ability to record FMC data. This is attractive for industries that have a requirement for a high accuracy automated inspection capability due to the flexibility FMC provides, as well as the benefits of improved data processing. FMC provides a step change in how array data is processed. As a result existing methods for inspection calibration are not attractive, and new variables have been introduced that must be controlled and understood e.g. irregular surface characteristics.

3 Array beam model development

Many aspects of this project require transducer modelling. This chapter will review several methods of ultrasonic modelling and detail the development of an array beam model, including a program of validation against existing models and experiment.

3.1 Introduction

When planning an inspection utilising phased arrays it is important to understand the type of beam being produced by the array as this directly relates to the probability of detecting a defect. For example, when selecting a focussed beam the selection of aperture size and beam angle will control the size and location of the focus spot. If an aperture is selected where the focus depth is outside of the selected aperture's near field then there may be little or no focussing at the desired depth. If an aperture is selected that is very large then the depth of focus will be short, leading to poor sensitivity away from the desired focus depth. This problem is overcome through the use of beam models that allow the maximum amplitude field produced by the array to be visualised, thus enabling operators to check that the delay laws selected produce the desired result.

3.2 Methods of transducer modelling

Ultrasonic field modelling can be performed using a variety of methods. Models based on analytical solutions have been used to model single element transducers [56, 57]. These models are normally based on solutions to the wave equation, such as Kirchhoff theory or the Rayleigh-Sommerfeld theory of diffraction [58]. These models rely on the use of carefully selected Green's functions that satisfy the boundary conditions of the situation being modelled. The resulting integrals must then be solved analytically. This approach can be used for transducer field modelling as well as modelling the scattering of waves from defects [59, 60]. The challenge with this approach is that the Green's function selected to model a particular problem may not be suitable for a different scenario, for example changing from a circular transducer to a rectangular shaped transducer. The advantage of this approach is computation speed.

A widely used approach to overcome the limited flexibility of analytical models is to use numerical integration to solve the Rayleigh-Sommerfeld formulation of diffraction, or equivalent formulations [17, 61, 62, 63]. This approach is generally referred to as a semi-analytical method, and is commonly used to produce more generic models than a purely analytical approach.

An alternative approach to the semi-analytical method is the edge element approach [64]. This approach is based on dividing the surface of a transducer into a grid of smaller sections, the contribution of each of these can be evaluated analytically by solving a line integral over the perimeter of the section. The full field for the transducer can then be found by summation of the results from each section. This approach avoids the computationally expensive 2D numerical integration required for methods based

on the Rayleigh-Sommerfeld equation, and has been shown to provide computation times five times lower [64].

Another method that is commonly used in preference to semi-analytical methods is the use of multi-Gaussian beams. These models rely on the summation of a number of Gaussian beams to describe the field produced by a transducer [65, 66]. This method is less computationally expensive in comparison to methods that rely on numerical integration, but is less general due to the requirement to determine the expansion coefficients that define the Gaussian beams [66]. The method has been developed for several transducer shapes [67], and with modifications has been shown to accurately represent arrays [68, 69].

CIVA [70] and Simulus [17] are examples of commercial software packages based on semi-analytical methods. Both models are based on numerical solutions to the Rayleigh-Sommerfeld integral. CIVA uses a point source based model in conjunction with pencil based ray tracing [63] to predict the field, whilst Simulus uses a two stage approach based on the Huygens-Fresnel principle of superposition to model the propagation of ultrasound through the wedge to component interface. The first stage is to model the front face of the transducer and calculate the complex field at the interface between the array's wedge and the surface of the material to be inspected. The second stage is to use the amplitude and phase variation computed in stage one to model the field in the component.

CIVA uses a reduced number of point sources as each source has a 'pencil' beam associated with it. The 'pencil' beam is fired through the computation field and each time it interacts with a computation point the amplitude and phase due to the point source is assigned to that computation point. As the 'pencil' beam propagates through the computation field the effect of transmission coefficients and refraction is taken into account if the beam passes through an interface between two materials. Each 'pencil' beam fired is divergent so the beam has a finite width. A method developed in electromagnetics is then used to calculate the variation of the field due to the point source between the edge of the 'pencil' beam, known as the paraxial ray, and the centre of the beam, known as the axial ray [63] . It is this step that reduces the time CIVA takes to compute fields as less point sources have to be used than if the beam fired from each point source was simply a ray with no thickness. Both models compute particle displacement over the frequency spectrum covered by the transducer being modelled and multiply the field with the frequency response of the transducer. Time histories can then be obtained via Fourier synthesis.

This project requires an array beam model for several aspects that includes mode converted focused beam simulation, and Monte Carlo simulations to investigate the effect of variation in element performance, element directivity, and surface profile measurement accuracy. To achieve these goals a flexible model is required that can be altered to suit each task. A commercial package such as CIVA is not flexible enough to enable these goals to be achieved in an efficient manner. As a result of this limitation and often high computation times for both models when modelling pulsed operation a bespoke array beam model has been written rather than use a commercial package. The chosen method is based on the Huygens-Fresnel principle of superposition as the method is relatively simple, and offers more flexibility than analytical methods.

3.3 Beam model structure

An array beam model has been developed that utilises the Huygens-Fresnel principle of superposition combined with ray tracing to allow the effect of ultrasound passing through an interface between two materials to be modelled. This approach allows the field produced by an array to be modelled in a two dimensional space in plane strain such that each element in the array is an infinite line source coupled with a directivity function. This approach as well as others are discussed in more detail in [19]. The use of a directivity function reduces the computational requirements of the model compared with using many sources to model a transducer, but can only be used to model a transducer in the far field. This limitation is unlikely to pose a problem when modelling array elements as the near field of an individual element is small. The structure of the model is shown in Figure 3.3.1.

The displacement amplitude and phase of any point in material 2 can be calculated by carrying out the summation described by Equation 3.3.1.

$$A = \sum_{j=1}^{n} \frac{1}{\sqrt{R_E}} \exp^{-i(k(R_{1,j}+R_{2,j})+\omega\triangle t_j)} D_f\left(\varnothing_j, \omega\right) T\left(\beta_j\right) \tag{3.3.1}$$

where R_E is the effective propagation distance, R_1 and R_2 are the propagation distances in materials one and two respectively. D_f is the directivity function, T the transmission coefficient, k the wave number, $\triangle t$ the delay law, ω the angular frequency, and n the number of array elements. The effective propagation distance is required as equation 3.3.1 assumes that the wave front emitted by each line source is cylindrical and energy per unit area remains constant. Thus displacement amplitude can be described by assuming:

$$Energy \propto Amplitude^2 \tag{3.3.2}$$

However, refraction at the interface between materials one and two results in the wave fronts no longer being cylindrical in shape. Instead the decay in displacement amplitude can be modelled using an effective propagation distance based on an approximation derived by Johnson et al [71]:

$$R_E = R_1 \frac{cos\beta_2}{cos\beta} + R_2 \frac{C_2}{C_1} \frac{cos\beta}{cos\beta_2} \tag{3.3.3}$$

where β_2 is the angle between the material interface normal and the ray path in material two, and $C_{1/2}$ is the wave velocity in material 1/2. Equations 3.3.1 and 3.3.3 are calculated over a frequency range that covers the bandwidth of the transducer being modelled, and the result is multiplied with the transducer's frequency response. Time histories are then obtained by computing the inverse Fast Fourier Transform (FFT).

3.3.1 Speed Comparison

To quantify the speed of the completed model relative to CIVA an investigation has been completed by running an identical simulation in both models at different grid resolutions, and recording the computation time in each case.

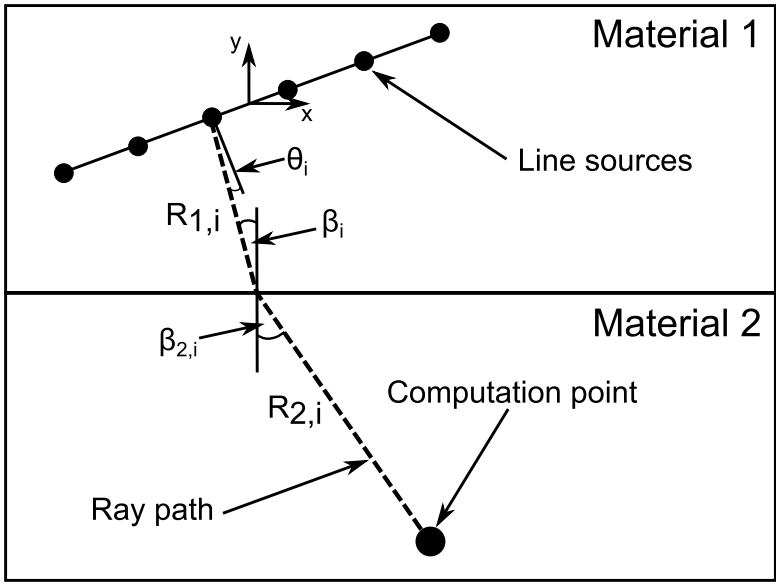

Figure 3.3.1: The structure of the beam model developed.

Both models have been configured to simulate a 40 element 2 MHz 50 % bandwidth array producing a 45 degree shear wave, focused at a depth of 30 mm. Computation times are compared when simulating a 1D computation field (a line of computation points) 40 mm long, located at the focal depth and perpendicular to the beam angle. The results for a variety of line resolutions can be seen in Table 3.3.1 a). The results show that the Huygens model offers similar performance at lower resolutions, and begins to fall behind as the resolution increases.

Table 3.3.1 b) presents the results when simulating a 100 by 100 mm 2D computation zone. The Huygens model again performs slower than CIVA, and the difference increases as the grid resolution increases. These results are thought to be due to the fact that Matlab is an interpretive scripting language while CIVA runs on compiled code, so Matlab would be expected to be slower. Matlab is also limited to single thread execution as the parallel computing tool box has not been used. Both applications are able to take advantage of multi-threading controlled by the operating system (Windows XP Professional 64 bit in this case) but observation of core loading shows that CIVA is consistently able to achieve higher values. This helps to explain the increasing advantage of CIVA as the field resolution increases as the computation is well suited to multi-thread execution. However, the computation time of the model is only significant when a large numbers of cases must be simulated e.g. Monte Carlo simulation. For these applications the model will be used to predict 1D fields and this is the regime where the two models exhibit similar performance.

3.4 Model Validation

An important first step in the development of any model is the validation of results against experimental results or another validated beam model. In order to investigate the relative accuracy of the array beam model a two stage validation program has been carried out. In the first stage beam profiles predicted by the model are validated against the CIVA beam model which has itself been validated in a large number of scenarios [72]. In the second stage, amplitude variation with increasing depth

Table 3.3.1: A comparison of computation times between CIVA and the array beam model developed from this project. The performance factor is the computation time of the Huygens model normalised by the time required by CIVA. a) 1D computation field b) 2D computation field.

Line resolution (pt/mm)	10	20	30
CIVA (Secs)	2.3	2.5	3.7
Huygens model (Secs)	2.0	3.6	5.2
Performance factor	**0.9**	**1.4**	**1.4**

(a)

Grid resolution (pt/mm)	0.5	1	2
CIVA (Secs)	9	28	92
Huygens model (Secs)	15	48	177
Performance factor	**1.7**	**1.7**	**1.9**

(b)

Table 3.4.1: Model settings used to generate results.

Parameter	Value
Array centre frequency (MHz)	2.0
-6 dB bandwidth (%)	50
Element pitch (mm)	0.75
Element gap (mm)	0.20
Matching layer	Water

into the modelled medium are compared with both CIVA and experimental results. All the test cases modelled have been based on the arrays used in the membrane probe project [5]. The array parameters and the test cases modelled are listed in Table 3.4.1.

3.4.1 Beam profile comparisons

The comparison of beam profiles has been carried out by configuring both models as closely as possible. In some cases there are model parameters with are not common between the two models, e.g. the CIVA accuracy parameter which controls point source density. In these cases a value has been chosen that reflects how the model would normally be configured. The only exception to this approach is delay laws. Rather than use the CIVA delay calculator the delay law values used by the Huygens model have been imported into CIVA.

3.4.1.1 Plane beams

The first set of beam profile validation results focus on the production of plane beams. The test cases modelled all use an aperture of 20 elements to produce a zero and 60 degree longitudinal beam. Further

details of the model configuration can be seen in Figure 3.4.1 a), and the corresponding simulation results are shown in plots b) to d). Test case one is very simple as no delay laws are used and simulations are performed with the echodynamic placed parallel and perpendicular to the beam axis. The results clearly show that the two models are in very good agreement along the whole width of the echodynamic. The only disagreement between the two models is that the Huygens model predicts two side lobes approximately 10 mm either side of the beam centreline to be of larger amplitude than CIVA, although the disagreement is $<$1 dB.

Test case two uses the same aperture size, but an array angle is introduced and delay laws are used to steer the beam around to 60 degrees. Figure 3.4.1 plot d) demonstrates that the models are in overall excellent agreement. Both models predict very similar maxima locations and the decay of the beam with increasing depth also agrees well. As the depth decreases from the maximum amplitude at the centre of the echodynamic the two models gradually diverge; at 20mm from the echodynamic centre CIVA predicts the amplitude is approximately 3 dB lower in amplitude. This difference is thought to arise from differences in transmission coefficient close to the critical angle. The Huygens model uses tabulated values at a fixed resolution that results in small errors.

3.4.1.2 Focused beams

The ability of the model to correctly predict the ultrasonic field produced by a focused beam is tested by simulation of three cases: a zero degree longitudinal and 45 degree transverse wave using an aperture of 40 elements, and a 60 degree transverse wave using an aperture of 60 elements. Further details of the model configuration can be seen in Figure 3.4.1 a), and the corresponding simulation results are shown in plots b) to d). All of the results exhibit excellent agreement in the vicinity of the beam axis; amplitudes are very similar with differences generally less than 1 dB, and there is good agreement on feature location. Away from the beam axis there are small discrepancies in side lobe amplitude in cases one and three. In all cases CIVA predicts that the amplitude decays at a higher rate with increasing distance from the beam axis, but the difference is small and the amplitude difference is approximately 2-3 dB in the worst cases.

3.4.1.3 Mode Converted focused beams

The final test case is a focused mode converted longitudinal wave, generated via the mode conversion of a low angled transverse wave at the backwall of a component. Details of the model configuration can be seen in Figure 3.4.3 a), and the predicted echodynamics can be seen in plot b). As with previous results the models are in excellent agreement around the beam axis, including a side lobe present at approximately -10 mm on the echodynamic. There are some discrepancies for echodynamics locations above 0 mm (the beam axis). Again this is thought to be due to variation in transmission coefficients close to the interface where the mode conversion occurs. Errors introduced due to this effect are insignificant as the beam axis is of primary interest.

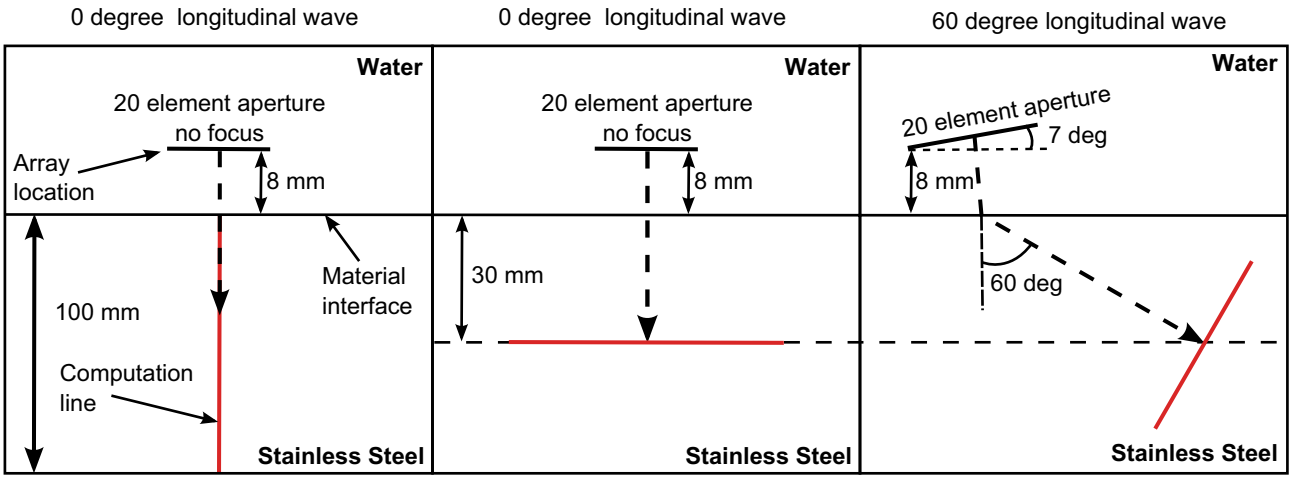

(a)

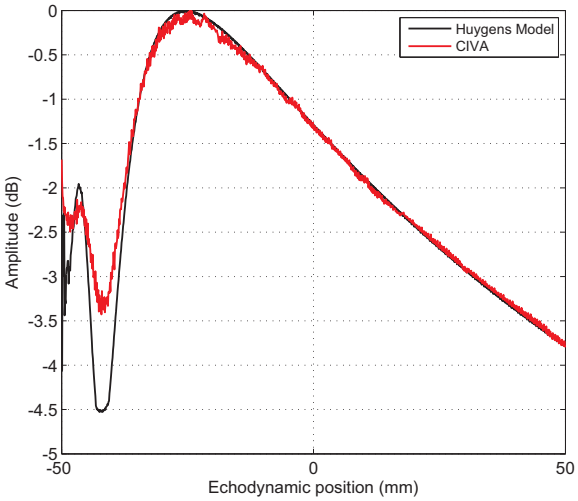

(b)

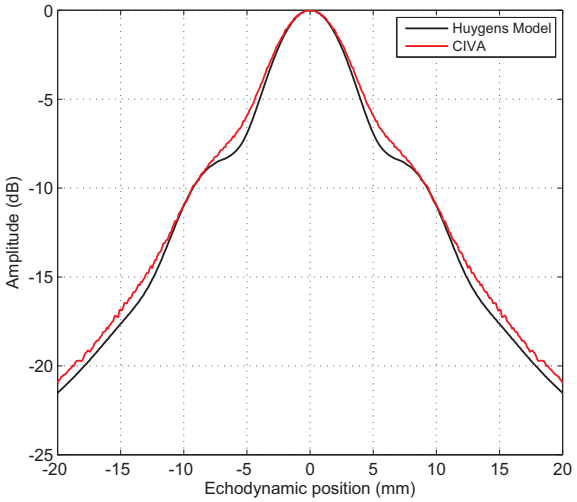

(c)

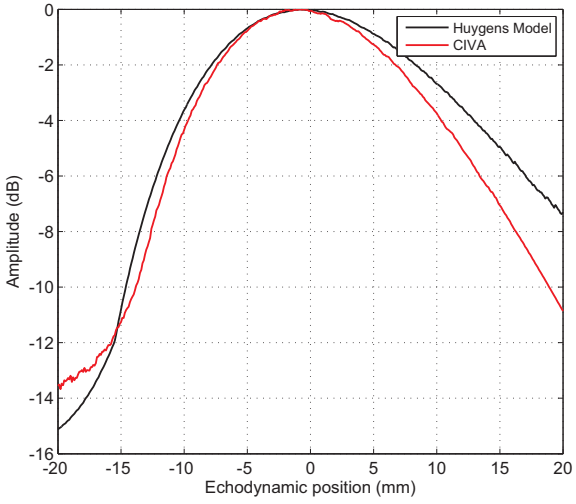

(d)

Figure 3.4.1: A comparison of echodynamics between CIVA and Huygens beam model for plane beams a) model configurations b) plane zero degree, vertical echodynamic c) horizontal echodynamic d) plane 60 degree longitudinal wave.

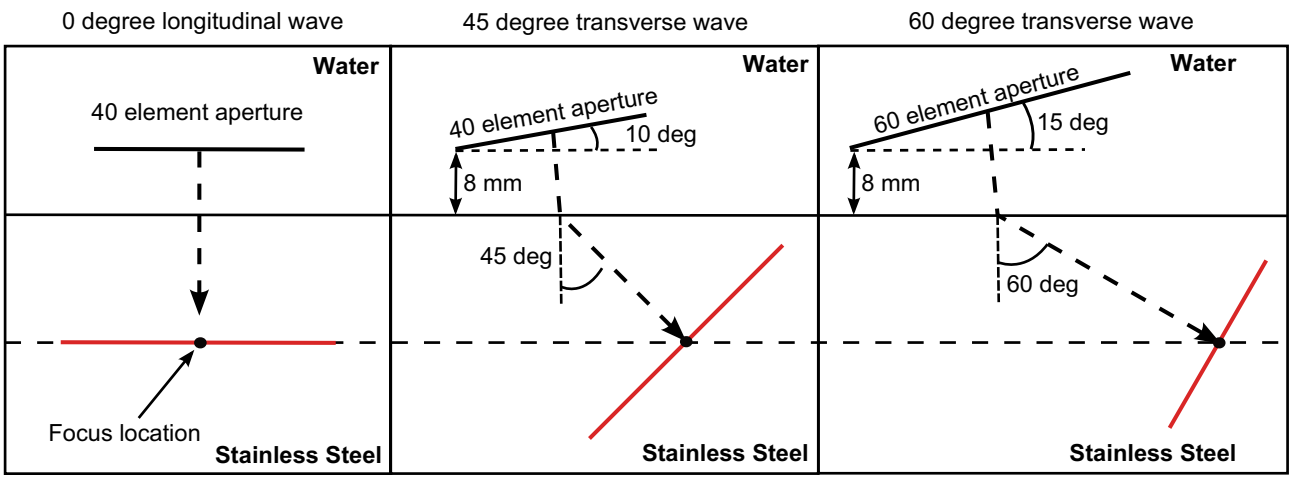

(a)

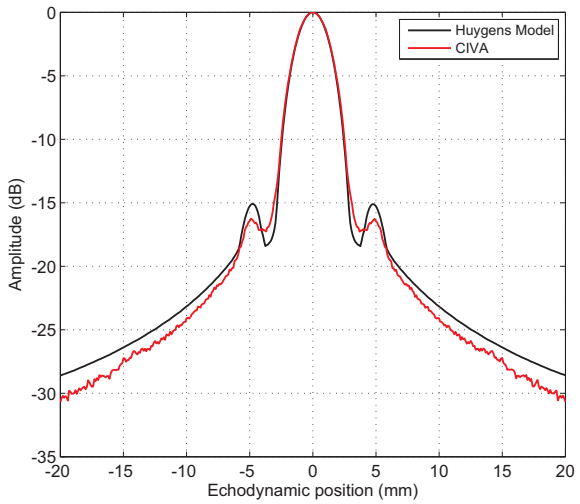

(b)

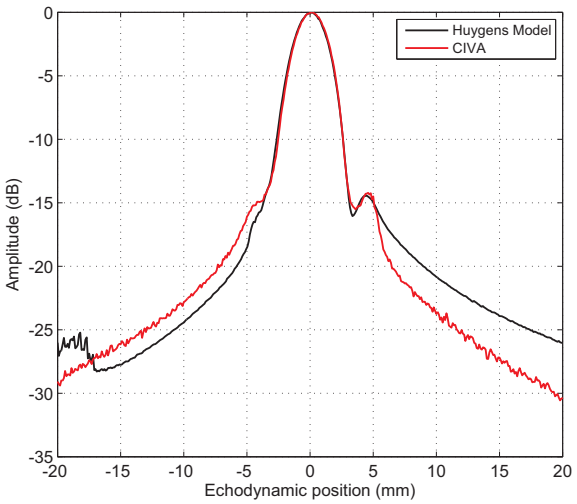

(c)

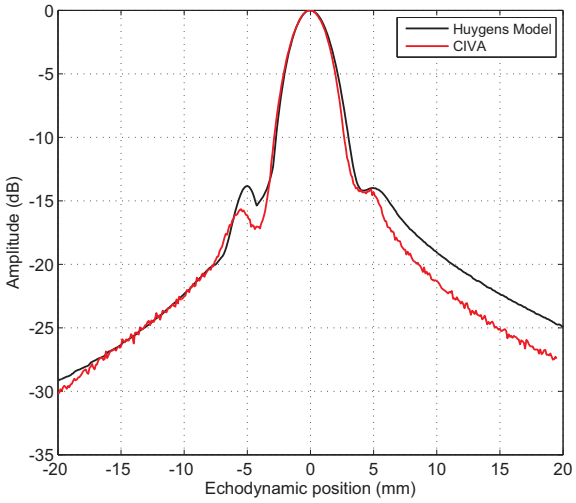

(d)

Figure 3.4.2: A comparison of echodynamics between CIVA and Huygens beam model for focused beams a) model configurations b) zero degree, c) 45 degree transverse wave d) 60 degree transverse wave.

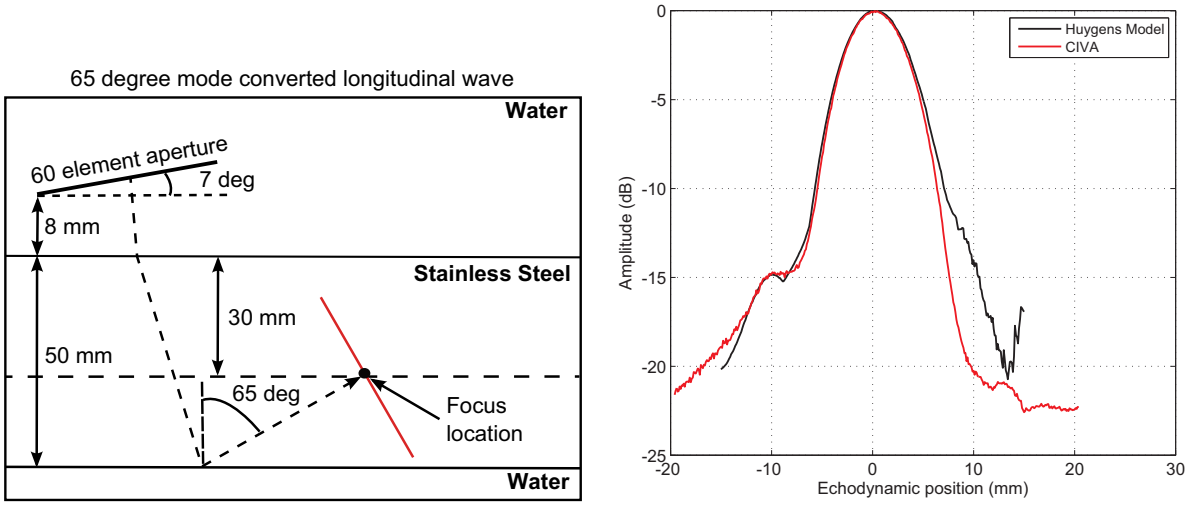

(a) (b)

Figure 3.4.3: A comparison of echodynamics between CIVA and Huygens beam model for a focused mode converted longitudinal beam a) model configuration b) comparison of echodynamics. Increasing echodynamic positions correspond with increasing depth.

3.4.2 Amplitude comparisons

The second stage of the validation program is amplitude comparisons between both the Huygens model and CIVA against experimentally measured amplitude variations. The same specification array as the previous section has been used, and experimental results have collected using a calibration block containing Ø3 mm SDHs. The block has been mechanically scanned with the array in immersion (with a first element stand-off of 8 mm and an inclination of 7 degrees) and frames of FMC data have been recorded at 1 mm intervals. A processed A-scan has been produced at each scan location using a single aperture location in the array, and the results combined to produce a B-scan. The data interpretation has been completed in the British Energy/EDF software called Graphical User Interface Data Evaluation (GUIDE). This program is limited to a resolution of 1 dB steps and the experimental results have been converted to equivalent free field values, there is therefore a ±0.25 dB tolerance on the experimental results. The amplitude errors associated with the 1 mm scan step is predicted to be at least ±1 dB.

A variety of plane and focused wave types have been compared, and in each case an aperture size of 20 or 40 elements has been used for plane and focused waves types respectively. In the case of the focused beams, at each measurement depth the beam has been re-focused at the depth of each SDH. The results are presented in Figure 3.4.4. Additional cases can also be seen in section 9.1 Appendix. In all cases there is excellent agreement between the Huygens model and CIVA 2D. The agreement between the modelled results and experiment is not as good. For the plane beams and the focused 45 degree transverse wave there are errors up to approximately 2-3 dB. This is thought to be a result of the 2D nature of the modelled results as the first two measurement depths are likely to be in the near field of the aperture in both the active and passive array planes. The CIVA model can be used to predict the ultrasonic field using a 3D simulation.

CIVA 2D means that a 2D representation of the transducer has been used. As with the Huygens based model developed for this project, the array elements are effectively assumed to act as a line

source. The transducer can be more accurately represented by applying the Huygens-Frenel theory of superposition in 3D. This requires the surface of the transducers to be represented by a number of evenly distributed point sources. The advantage of this approach is that the finite length of the array elements is taken into consideration, rather than just the element width , and therefore the diffraction pattern and corresponding near-field effects are modelled. This means that the model should provide more accurate results at small depths where near-field effects due to the length of the elements are significant. The disadvantage of this approach is that the computational cost of the simulation is significantly higher.

CIVA predictions when simulating the 3D field have been included for some results, and better match the experimental profile variation but produce similar errors to the 2D predictions. Taking into account the known experimental tolerances the results of the comparison show that the 2D models produce acceptable agreement with experiment, but care should be taken to ensure that the 2D approximation is valid.

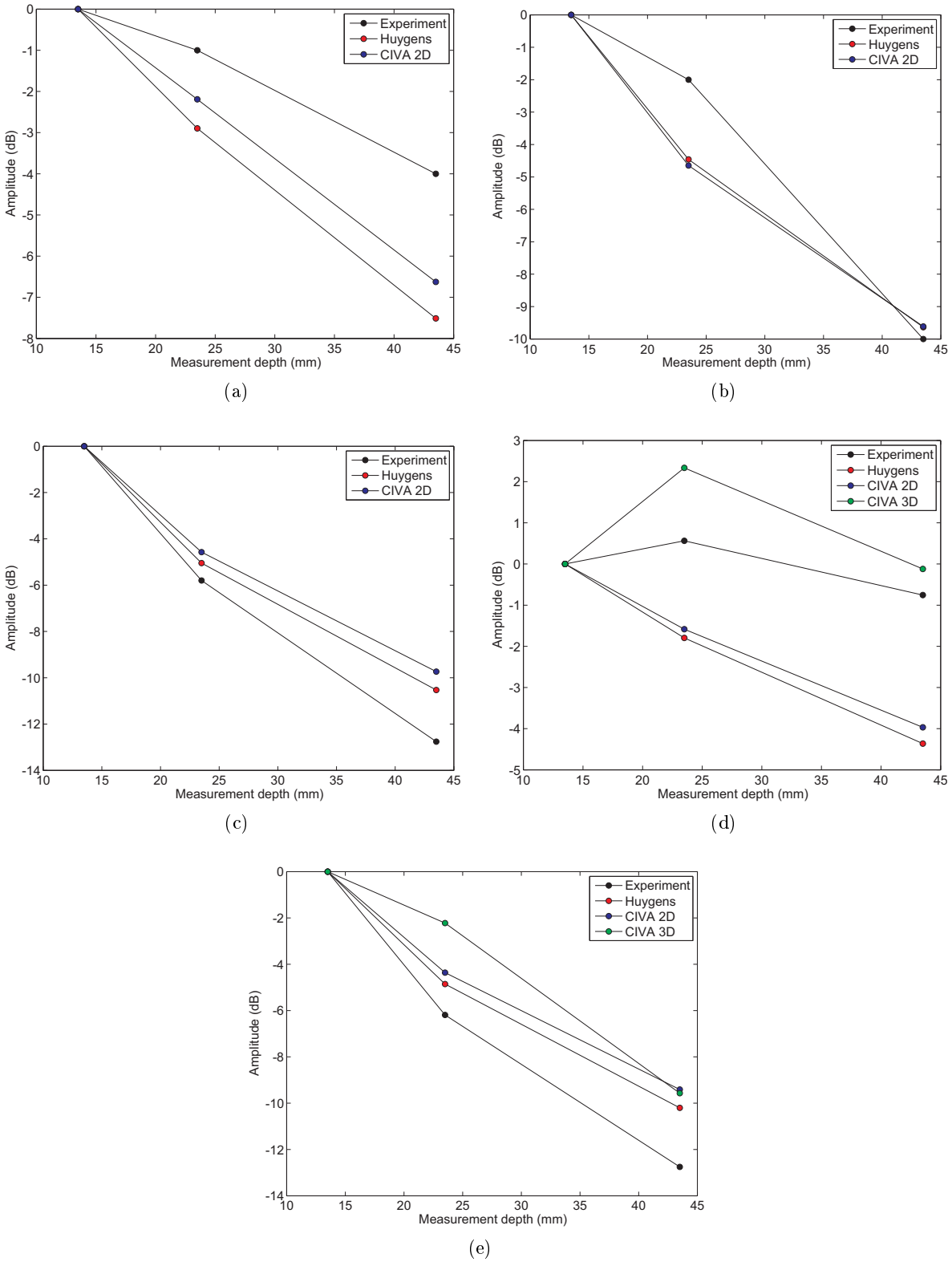

Figure 3.4.4: A comparison of predicted amplitude variations of CIVA and the Huygens model against experimentally measured values a) plane 45 degree transverse wave b) plane 60 degree transverse wave c) focused 60 degree longitudinal wave d) focused 45 degree transverse wave e) focused 60 degree transverse wave.

3.5 Summary

An array beam model has been produced under the assumption of plane strain conditions using the Huygens-Fresnel theory of superposition. The model has been validated against the commercial package CIVA and has been shown to produce typical amplitude differences around the beam axis of less than 2-3 dB for a variety of different beam types. The model has also been compared against experiment and shown to produce acceptable agreement, but the inclusion of CIVA predictions has also shown that the model produces very similar results to other two dimensional models. However, the results do highlight that care must be taken to ensure that the 2D approximation used in the model is valid.

A comparison of computation times has shown that the model produces similar computation times to CIVA for small computation fields, but the advantages of compiled software and superior multi-threading ability allow CIVA to offer advantages for larger fields. However, the primary motivation for producing a bespoke model is the flexibility to carry out studies not suited to commercial software.

4 Accurate Two Dimensional Modelling of Piezo-composite Array Transducer Elements

In the previous chapter the development and validation of an array beam model was presented. A fundamental aspect of this model is the array element directivity model chosen to describe the behaviour of the array elements. This chapter will investigate the accuracy of various methods of modelling the array elements via experiment, using both ultrasonic and optical measurement of element behaviour. The results are used to validate the use of established ultrasonic modelling techniques for small transducers, and also demonstrate that element-to-element variation in directivity pattern is sufficiently small that it may be excluded from the calibration framework for arrays.

4.1 Introduction

Ultrasonic phased arrays are now routinely used for Non-Destructive Evaluation (NDE) [73, 21, 20], medical diagnosis [74, 23] and sonar [75] to generate a variety of different beam types. Due to the complex nature of the ultrasonic fields produced by phased arrays it is common practice to use modelling tools to predict transducer performance.

Regardless of the mathematical framework selected to model an ultrasonic array an important decision is the selection of an assumed variation in the surface displacement, or pressure, across the face of the array elements. A common approximation used when modelling ultrasonic transducers is the assumption of uniform pressure across the face of the transducer [76], also known as the assumption of piston-like behaviour. When applied to narrow transducers, such as array elements, the accuracy of this assumption has previously been called into question [77, 61], but has been shown to be an accurate approximation for larger piezo-composite transducers [78].

In the following section the accuracy of the assumption of piston-like behaviour will be investigated by comparison of models based on this assumption with experimental results. The experimental results have been collected using a number of modern piezo-composite array transducers, thus enabling the validity of the models to be established over a range of element sizes.

4.2 Modelling the directivity pattern of array elements

If an array element operating into a liquid is modelled using the Huygens-Fresnel principle of superposition the following directivity function results, assuming that the observation point is in the far field and pressure is uniform across the surface of the element [76]:

$$D\left(k,\Theta,\alpha\right) = sinc\left(\frac{kd_1 sin\Theta cos\alpha}{2}\right) sinc\left(\frac{kd_2 sin\Theta sin\alpha}{2}\right) \tag{4.2.1}$$

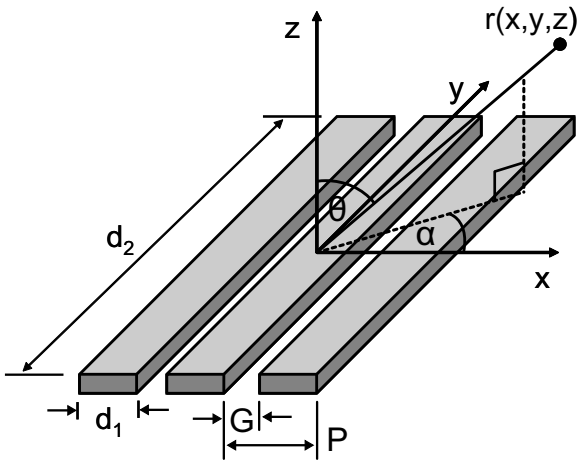

Figure 4.2.1: The coordinate system used to model the array element.

where d_1 is the width and d_2 is the length of the aperture, k is the wave number, and Θ and α are defined by Figure 4.2.1.

If it is assumed that the observation point is located on the x-z plane and $d_2 \gg d_1$ then equation (4.2.1) can be reduced to the following [76, 79, 80, 19]:

$$D_f(k, \Theta) = sinc\left(\frac{kW sin\Theta}{2}\right) \tag{4.2.2}$$

where W is the width of the aperture (P - G using the notation of figure 4.2.1).

4.2.1 Ultrasonically measured directivity patterns

The validity of the function expressed in equation (4.2.2) can be investigated by comparison with experimentally measured directivity patterns of a number of elements from several different array probes. To perform these measurements a two axis manipulator has been designed and manufactured that allows all the elements in an array to be measured automatically; the manipulator is shown in Figure 4.2.2. The rotary axis allows a target to be moved around an element at a constant radius, and the linear axis moves the array to allow each element to be measured. Measurements were made by placing the entire rig in a water bath and moving a Ø2mm steel rod in a circular path around each element, and recording pulse-echo signals. The manipulator has been designed such that the centre of the circle described by the movement of the target is located on the front face of the array. The directivity pattern is recorded by extracting the maximum amplitude of the first reflection from the rod in each location. The results are normalised by the amplitude of the reflection with the target directly in front of the array. The square root of the values are then taken to convert the combined transmit-receive directivity pattern recorded by the pulse-echo measurement method into a transmit directivity pattern. The directivity pattern of the array elements are assumed to be identical in transmit and receive.

The results from measuring several different commercially available arrays manufactured from 1-3 piezo-composite are presented in Figure 4.2.3, and the specifications of these arrays can be seen in Table 4.2.1. A measurement radius of 30 mm was used to ensure that the target is in the far field of the elements. The plotted profiles are the averaged result from the measurement of several different elements in the same array. The mean standard deviation of the results over all the angular positions

Table 4.2.1: Specifications of the arrays measured using the directivity manipulator. The bandwidth is defined as the frequency range of the transducer where the amplitude is within 50% of the amplitude generated at the centre frequency. The value is expressed as a percentage of the centre frequency of the probe. Element dimensions are as defined in Figure 4.2.1. The wavelength (λ) is that at the array centre frequency in water.

Array	Centre frequency (MHz)	Bandwidth (%)	Pitch, P (mm)	Inter element gap, G (mm)	Element width, d_1 (mm)	Element length, d_2 (mm)	Element width (λ)
A	2	60	0.75	0.20	0.55	15.0	0.7
B	2	60	0.78	0.25	0.53	15.0	0.7
C	2	60	1.25	0.25	1.00	15.0	1.4
D	2	60	1.60	0.25	1.35	20.0	1.8
E	4	60	1.00	0.15	0.85	10.0	2.3

measured was below 0.01. This demonstrates that for the arrays measured there is very little variation in directivity patterns for elements within the same array; it also shows that the agreement with a Fourier synthesis of equation (4.2.2) over a frequency range representative of the measured arrays is poor for array types A and B, which are the thinnest elements.

The relative sensitivity of each element in the arrays used to generate the results presented in Figure 4.2.3 has also been measured. Relative sensitivity is defined as the combined transmit-receive sensitivity of each element relative to the mean value of the array. The element sensitivity results show that there is typically a variation of less than 2 dB in the relative sensitivity across the arrays, with a small number of outlying elements. This variation does not appear to have affected the directivity pattern produced by the elements. Based on this finding it can be concluded that directivity is not coupled to element properties, besides element dimensions and the integrity of the piezo-composite structure. Element dimensions are controlled to within a high tolerance during manufacture (approximately +/-

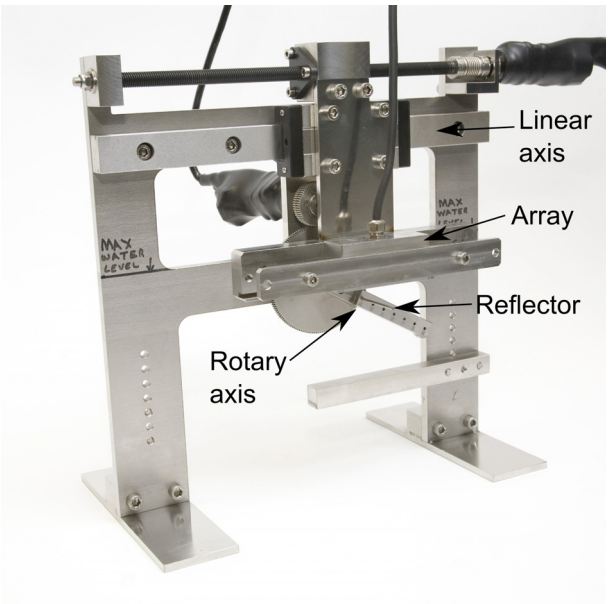

Figure 4.2.2: The manipulator used to measure the directivity patterns of array elements.

10 μm), and significant changes to the structure of the element would be detected as a large change in element sensitivity. However, the experimental results demonstrate that a Fourier synthesis of the model used for element directivity, described by equation (4.2.2), is not valid for some element sizes, and should be investigated further.

4.2.2 Existing modelling methodology

Commonly applied models for the directivity pattern of ultrasonic transducers operating into an acoustic medium are derived from work originally performed on an optical application [58]. Consider the disturbance field produced by an aperture in an infinite opaque screen diffracting a single wave from a point source, see Figure 4.2.4. The pressure at P0 can be found by solving the scalar wave equation. This is commonly done using Kirchhoff's theory or the Rayleigh-Sommerfeld formulation of diffraction [58]. Both of these methods use Green's theory to solve the wave equation, but differ on the selection of the boundary conditions imposed on the Green's function.

If P2 is located such that normally incident plane waves illuminate the aperture, then the following integral describes the displacement at P0 [58]:

$$U(P_0) = \frac{A}{i\lambda} \int \int_{\Sigma} \frac{e^{ik(r_{21}+r_{10})}}{r_{21}r_{10}} \Lambda ds \tag{4.2.3}$$

where Σ is the area occupied by the aperture, A is the amplitude and phase of the point source P_2, λ is the wavelength, and ψ are the *obliquity factors* that results from the boundary conditions that are used to solve the wave equation. The *obliquity factors* and how they originate are as follows:

$$\Lambda = \begin{cases} \frac{1}{2}\left[1 + cos\Theta\right] & Kirchhoff\ theory \\ cos\Theta & 1st\ Rayleigh - Sommerfeld\ solution \\ 1 & 2nd\ Rayleigh - Sommerfeld\ solution \end{cases}$$

where Θ is the angle between r_{10} and n.

When the arrangement is changed to an ultrasonic transducer operating into a liquid the same approach can be used to solve for the ultrasonic field, but the arrangement is slightly different. The diffracting aperture now represents the ultrasonic transducer, and A now represents the amplitude and phase variation across the aperture. The calculation is simplified by the removal of r_{21}. The co-ordinate system used for the calculation is demonstrated in Figure 4.2.5, and the resulting integral is [77]:

$$U(P) = \frac{1}{i\lambda} \iint_{\Sigma} A(x,y) \frac{e^{ikR}}{R} cos\Theta' dxdy \tag{4.2.4}$$

where the y dimension is the out of plane direction and Σ is the area occupied by the transducer. If the amplitude and phase of the array element does not vary over the surface of the element, the calculation point is in the far field ($\Theta \approx \Theta'$, $R \approx r$, and $R \approx r - xsin\Theta$ for the phase variation), there is no variation in the Y direction, and kR $>>$ 1, and equation (4.2.4) can be simplified to [77]:

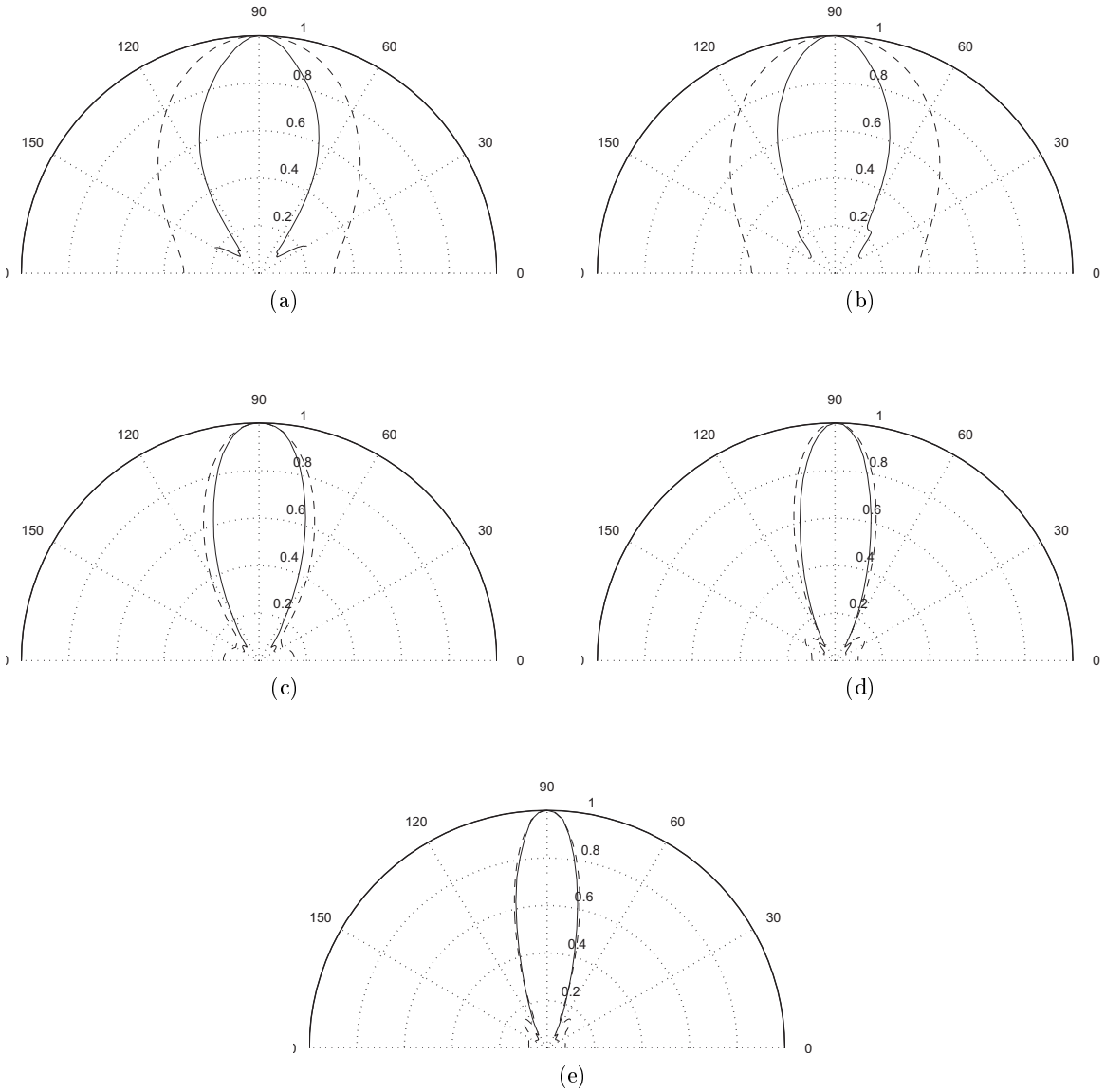

Figure 4.2.3: Experimentally measured directivity patterns. The solid lines are the measured patterns averaged over the number of element measured, and the dashed lines have been generated using a Fourier synthesis of equation (4.2.2). In each case the array type and number of experimental results are listed: a) A, 22 b) B, 32 c) C, 24, d) D, 16 e) E, 16. The radius of the plot represents the amplitude. In each case the mean standard deviation of the results over all the angular positions measured was below 0.01.

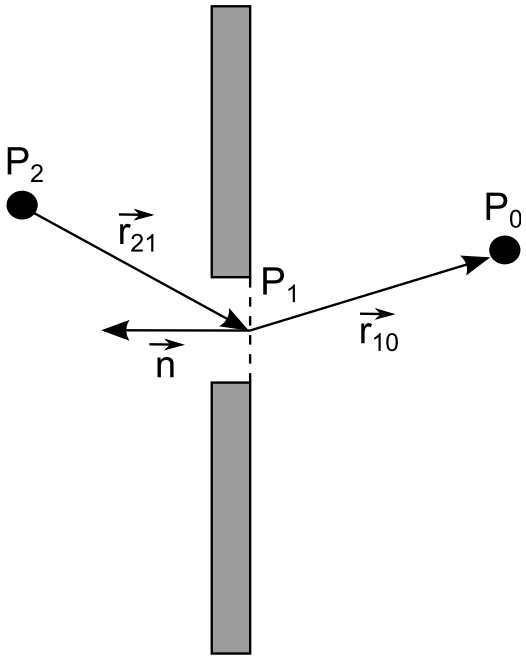

Figure 4.2.4: An aperture in an infinite opaque screen illuminated by a single point source P2 [58].

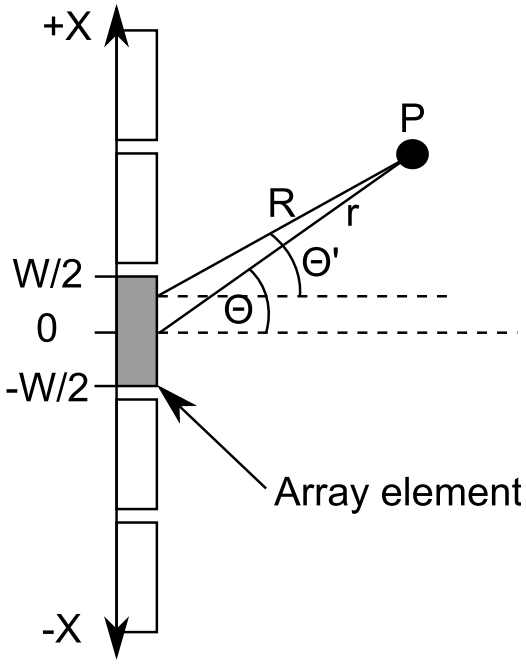

Figure 4.2.5: The co-ordinate system used to calculate the pressure field in the liquid, resulting from the excitation of a single array element [77].

$$U(P) = \frac{A}{i\lambda^{1/2}} \int_{-W/2}^{W/2} \frac{e^{ik(r - xsin\Theta)}}{r^{\frac{1}{2}}} cos\Theta dx \tag{4.2.5}$$

where W is the width of the transducer. Equation (4.2.5) is very similar to the result given in equation (4.2.3) when using the first Rayleigh-Sommerfeld solution. If the integral is solved the following result is true:

$$U(P) = \frac{AW}{i\lambda^{1/2}} \frac{e^{ikr}}{r^{\frac{1}{2}}} \frac{sin\left(\frac{kWsin(\Theta)}{2}\right)}{\frac{kWsin(\Theta)}{2}} cos\Theta \tag{4.2.6}$$

This result yields the following directivity function:

$$D_f(\Theta) = sinc\left(\frac{kWsin(\Theta)}{2}\right) cos\Theta \tag{4.2.7}$$

This function was proposed by Selfridge [77] and Delannoy [61] for transducers mounted in an acoustically soft baffle. The same function without the cosine term was proposed by Delannoy for transducers mounted in an acoustically hard baffle [61], i.e. piston like behaviour; this function has also been used by other authors in the past for modelling phased array elements [4][19]. However, as demonstrated in the previous section these functions are found not to be valid for small element sizes. This is thought to be a consequence of the pressure variation across the face of the element diverging from a constant value as the width of the element approaches the wavelength. The accuracy of this assumption can be investigated further via experimental measurement.

4.2.3 Experimental verification

The accuracy of the assumption of constant pressure across the element can be investigated by calculation of the pressure field generated by the transducer from the displacement of the surface of the array. This method has been reported previously by Jensen and Svendsen [62], and is based on the formulation of the Rayleigh-Sommerfeld integral reported by Tupholme [81] and Stephanishen [82, 56]. This approach is based upon the calculation of the transient field produced by an array of arbitrarily shaped and apodized transducers mounted in an infinite rigid baffle. The velocity potential at a point P can be calculated from the normal surface velocity via [61]:

$$\psi(\overrightarrow{r}, t) = \frac{1}{2\pi} \int_S \frac{v_n(t) \otimes \delta\left(t - |\overrightarrow{r_s}|/c\right)}{|\overrightarrow{r_s}|} \cos\beta dS \tag{4.2.8}$$

where S is the excited surface, v_n is the normal velocity of the surface, $\overrightarrow{r_s}$ is the vector from the point on the radiating surface to the observation point defined by the vector $\overrightarrow{r}$, and β is the angle between $\overrightarrow{r_s}$ and the surface normal. Figure 4.2.6 a) presents a graphical representation of the modelled system. The pressure field can then be calculated by solving the wave equation, which leads to the following [62]:

$$p(\overrightarrow{r}, t) = \rho \frac{\partial \psi(\overrightarrow{r}, t)}{\partial t} \tag{4.2.9}$$

where ρ is the density of the modelled medium. Felix et al. [83, 84] have previously used this approach to model the transient pressure field produced by an array element using measurements of the array surface when excited.

A Polytec OFV-5000 laser vibrometer with OFV-505 laser head and OFV-MR lens [85] has been used to measure the displacement of the surface of an array along a line perpendicular to the long axis of the elements when a single array element is excited in air. The details of the experimental arrangement can be seen in Figures 4.2.6 b). The laser vibrometer used to collect the experimental results can accurately record measurements at frequencies up to 1.5 MHz. Since the arrays under measurement produce frequency content above this value, the arrays were excited by a voltage pulse of length equal to half a cycle at 1.3 MHz. At this operating frequency the array will be producing significant frequency content not recorded by the vibrometer, but it is assumed that the surface displacement in the frequency range recorded will be approximately representative of the behaviour at 2 MHz. This assumes that the width of the array's surface that is excited when an element is pulsed is not strongly influenced by the operating frequency of the element. It has also been assumed that the sensitivity drop off of the laser with increasing frequency is sufficient to prevent significant aliasing. Due to the limited bandwidth of the laser, array type E has been excluded. The element width for array E is 2.3λ at the centre frequency of the transducer. As the element is very wide the proportion of the surface excited outside of the nominal region occupied by the element is relatively small, hence the element is tending toward piston source behaviour. This explains why the ultrasonically measured directivity patterns are in good agreement with the piston approximation.

The laser head and lens combination used to record the data produces a spot size of 25 - 54 microns over the range 200 - 500 mm from the lens [85]. The measurements were taken at a range of approximately 300 mm, hence a spot size of approximately 35 microns can be expected. As the width of the smallest array element considered is 530 microns, averaging effects due to the finite spot size have been considered insignificant.

The surface displacement time histories have been used to numerically solve equation (4.2.8) whilst assuming that the measured surface displacement does not vary in the direction parallel to the long axis of the element (d_2 using the notation of Figure 4.2.1). The results from equation (4.2.8) have then been numerically differentiated and normalised by the peak value to obtain the pressure variation. The results in Figure 4.2.7 present for all array types the displacement variation across the array elements at a time T, where T is the time after excitation at which the first positive peak in surface displacement occurs when the laser is positioned on the centre of the element. The associated pressure variations across the element are also shown for each array type, at the time of peak pressure. In each case a single element was measured for each array. Repeat measurements produced very similar results in each case.

The results clearly demonstrate that the approximation of constant pressure across the array element, i.e. piston like behaviour, is not representative. To prove that this simplification is the cause of the inaccuracies observed in section 4.2.1 directivity patterns are simulated using a Fourier synthesis of equation (4.2.5), using an obliquity factor of one. The equation has been numerically solved for observation points along a 30mm radius centred at the centre of the element face. The pressure time histories calculated from the optical measurement have been used to set the amplitude apodization and phase variation of each frequency component simulated. Figure 4.2.8 demonstrates the model configuration used. The simulation results can be directly compared to the ultrasonic results presented

in section 4.2.1 as these model and experimental configurations are identical.

The directivity patterns simulated using the surface displacement time histories are presented in Figure 4.2.9. The results show that for all array types considered the modelled results are in excellent agreement with the experimental results. In each plot the results using a Fourier synthesis of the piston source approximation are also included. For the two smaller element sizes the modelled results based on the calculated pressure fields are in significantly better agreement with the ultrasonically measured results than in the other cases. This suggests that it was reasonable to assume two dimensional behaviour and that the surface profile measurements recorded at a centre frequency of 1.3 MHz are approximately representative of the behaviour at 2 MHz. The modelled results predict the presence of side lobes centred at approximately 90 degrees for array types A and B, and 50 degrees for types C and D. In each of the ultrasonic experimental results there are side lobes present in very similar locations to the predicted results. Differences between the two results are unknown, but could be due to the reduced array operating frequency used when recording the surface displacements, and the limited bandwidth of the laser.

The side lobes for the 0.55 mm wide element are noticeably larger than those for other sizes. Element type B is very similar to type A, the only differences being a slightly larger element gap and a matching layer for Rexolite rather than water. The larger side lobes could be caused by increased electronic and acoustic cross coupling between array elements, caused by a combination of the smaller gap and matching layer material. Electronic cross coupling between elements in piezo-composite arrays has been shown to cause adjacent elements to become excited in phase with one another [86], and effectively increase the size of the element. Acoustic cross coupling is caused by the generation of a surface wave on the array surface that sheds energy into the liquid as it propagates [87]. This behaviour introduces an ultrasonic component that is phase shifted relative to the component generated by the excited element. Cross talk with neighbouring elements has not been directly included in the modelled directivity patterns. Despite this omission the results predicted by the model are remarkably accurate. Significant electronic cross talk would likely appear as extra peaks in the profiles presented in Figure 4.2.7, separated by the element pitch. There is no obvious sign of electronic cross talk in this result, but a surface wave can clearly be seen propagating in each direction away from the centre of the element in the full laser vibrometry results, this data is not presented here. Turnbull [88, 89] has suggested a directivity model that includes the effect of both coupling mechanisms. This method has not been investigated as the results suggest that the effect of cross coupling in the arrays considered is small enough to ignore. The measured arrays exhibit cross-coupling between neighbouring elements of the order of -40 dB, whilst work in the past that has found cross-coupling to be an important factor in global diffraction behaviour with cross-coupling values of the order of -10 to -20 dB [88, 89, 86, 87]. The difference in cross-coupling levels is thought to be due to improved piezo-composite design and manufacturing since the previous papers were published over a decade ago.

The use of measured surface displacement as a means to model the ultrasonic field produced by array elements has been shown to produce excellent results. However, this method is not attractive as it requires the surface displacement of the array to be measured before it can be simulated. A more attractive approach would be to use an assumed pressure displacement. This approach should produce more accurate results than assuming piston like behaviour, provided that a suitable function is selected for the pressure variation.

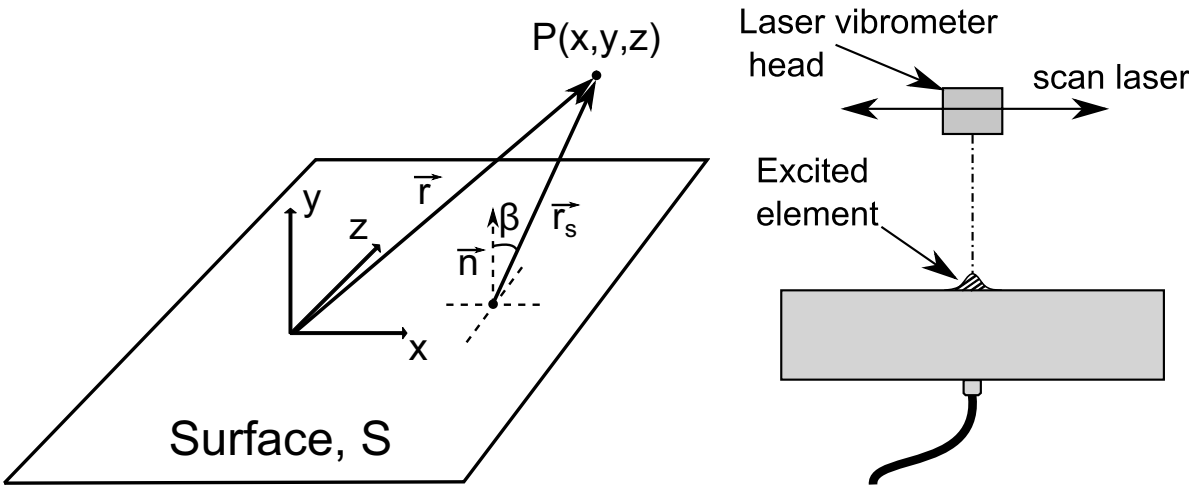

(a) (b)

Figure 4.2.6: The experimental arrangement used to record the surface displacement of arrays

4.3 An updated model for element directivity

The diffraction behaviour of array elements can be more accurately modelled by replacement of the piston approximation with an alternative pressure variation. A Hanning window has been selected to approximate the pressure distribution across the surface of the array element and beyond it. A Hanning window is a commonly used window defined as follows:

$$W(n) = 0.5\left(1 + \cos\left(2\pi\frac{n}{(N-1)}\right)\right) \tag{4.3.1}$$

where N is the window length. Using a Hanning window to describe the pressure variation has been used previously [90], but in this case the window is larger than the physical size of the array elements. Equation (4.2.5) has been numerically solved by assuming that the Hanning window describes the amplitude variation over the element. An obliquity factor resulting from the second solution to the Rayleigh-Sommerfeld equation has been used. This process has been performed over a range of Hanning window widths, and the results have been compared with the mean ultrasonically measured directivity pattern for that element size. The fitting process could have been performed iteratively to locate the optimum window width, instead a large number of increasing window sizes were fitted as the computation time was low enough to avoid the necessity of producing a more advanced algorithm.

The results of following this modelling approach are presented in Figure 4.3.1. The results show excellent agreement with the experimental results for the main lobe, especially for the two smaller elements. The side lobes are not present in the modelled results, but they make no significant contribution to the pressure field generated due to their angular position. The results from the function based upon an assumption of piston like behaviour, described by equation (4.2.2), provides acceptable agreement for the two larger element sizes but the agreement breaks down for the smaller sizes. Analysis of the size of the best fit windows has shown that there is some correlation between the window width and the element size. The results shown in Table 4.3.1 show that the ratio of the 50 % Hanning width to the physical element width is 1.5 for the two smaller elements and approximately 1.0 for the larger ele-

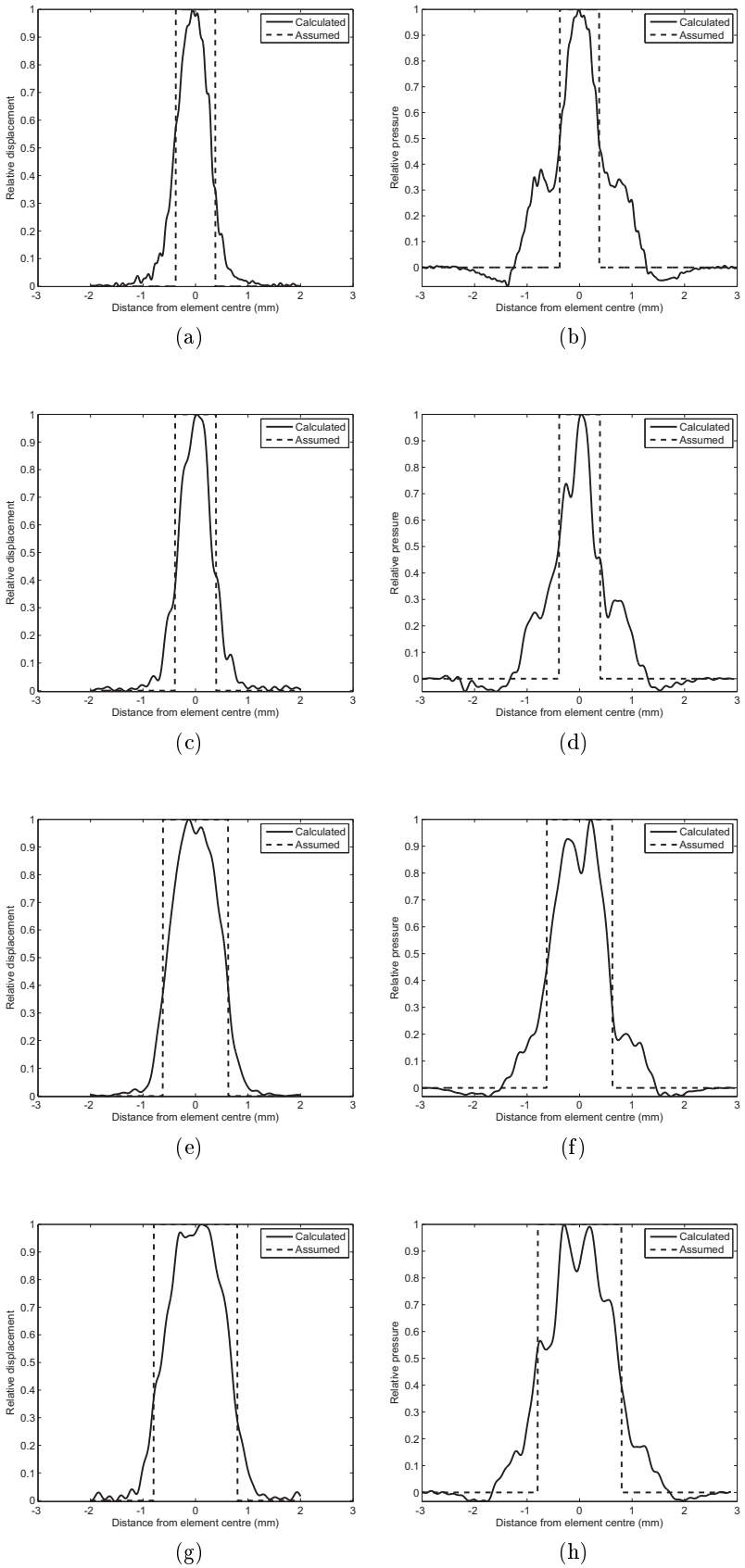

Figure 4.2.7: Plots of the surface profile, and calculated maximum pressure profile in water, of a single array element when excited with a -100 V voltage pulse in air, for array types A-D. The assumed profiles are based on the width of the element as specified by the probe manufacturer. a) - b) displacement and pressure for array type A, as per Table 4.2.1, c) - d) type B, e) - f) type C, and g) - h) type D

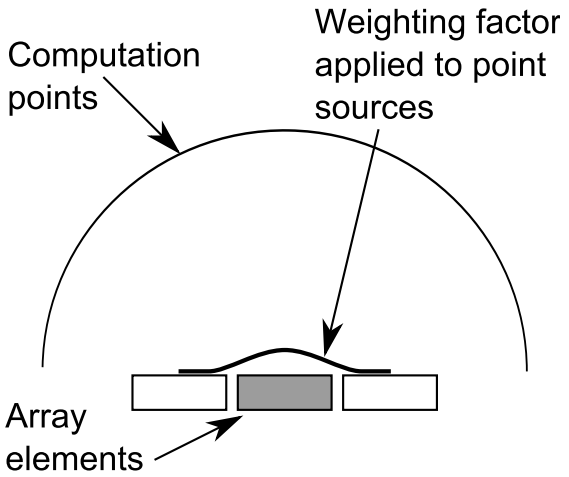

Figure 4.2.8: The structure of the model used to extract directivity patterns from the surface displacement measurements.

Table 4.3.1: Details of the best fit Hanning windows for several element sizes. The array types are in line with Table 4.2.1.

Array	Element width, W (mm)	50% Hanning window width, H (mm)	H/W
A	0.55	0.84	1.5
B	0.53	0.82	1.5
C	1.00	1.04	1.0
D	1.35	1.28	0.9

ments. Clearly there is not sufficient data to draw any general rules, but this method has the potential to significantly improve on the accuracy of either of the functions based upon an assumption of piston like behaviour. It should also be possible to solve equation (4.2.5) for the general case assuming the pressure across the element varies as a Hanning window. To take this model further significantly more experimental data points are required to understand the transition in behaviour observed.

It may be possible to provide the extra data using the finite element method rather than experiment. A detailed model that accurately represents the piezo-composite structure and material properties could be used to validate the assumption that surface displacement profiles measured in air accurately represent the displacement under water loading. The model could then be used to provide data for changes in element sizes and composite structure. This would reveal the correlation between the ratio of H and W for different element sizes, and it could also be used to discover the element size at which the assumption of piston like behaviour is accurate. However, it is not clear what effect the inaccuracies in the directivity pattern have on the beam forming performance of an aperture of elements, which is of primary interest to the NDE community. Before a generalised solution is developed it is first important to understand the modelling errors introduced by the assumption of piston like behaviour.

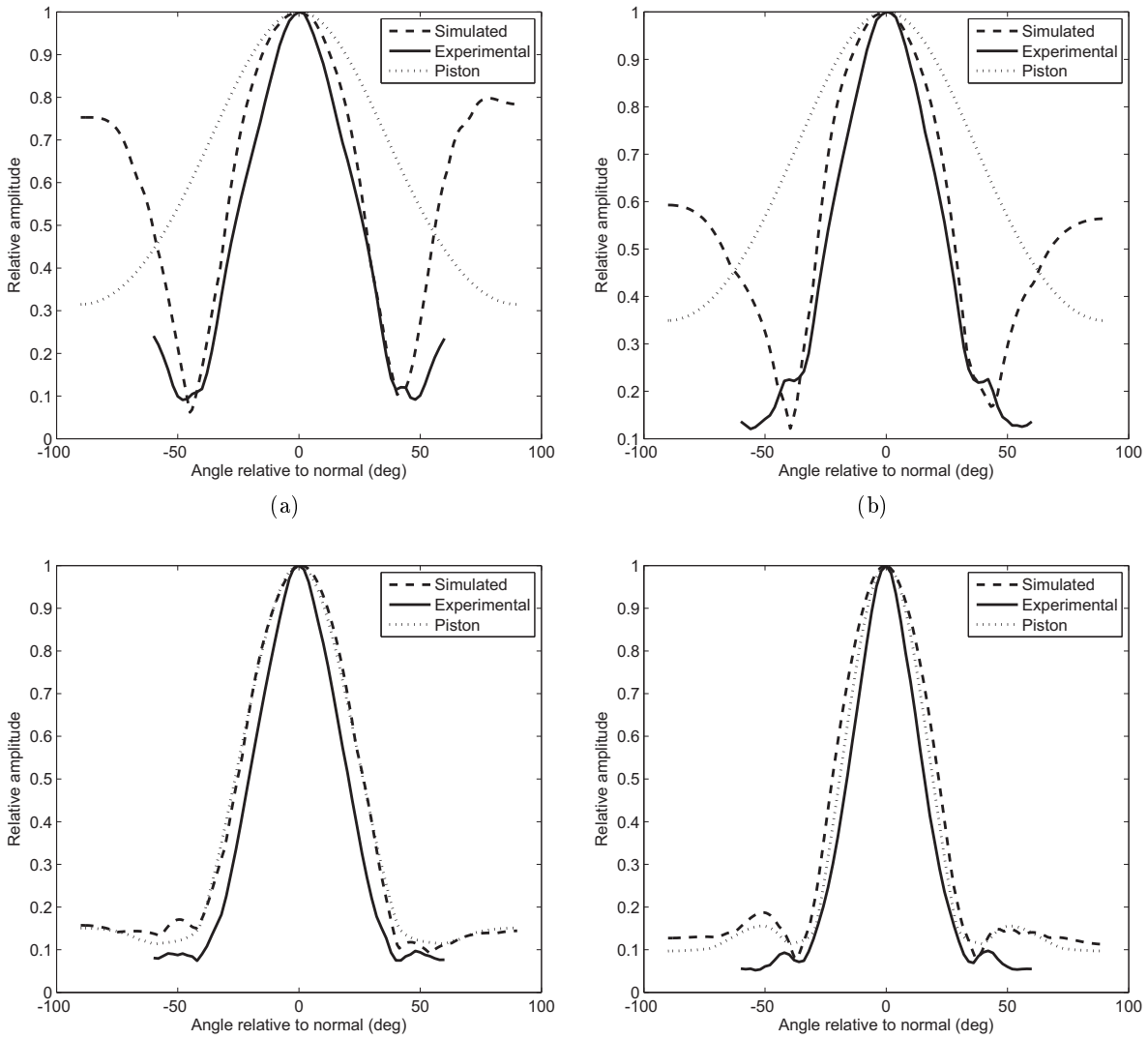

Figure 4.2.9: The results of simulating the directivity pattern of array elements of different sizes. The simulated results are those using the calculated pressure fields, the experimental results are those measured ultrasonically, and the Piston results are those calculated using a Fourier synthesis of equation (4.2.2). Element width: a) 0.55 mm width element (type A, as per Table 4.2.1), b) 0.53 mm (type B), c) 1 mm (type C), d) 1.35 mm (type D).

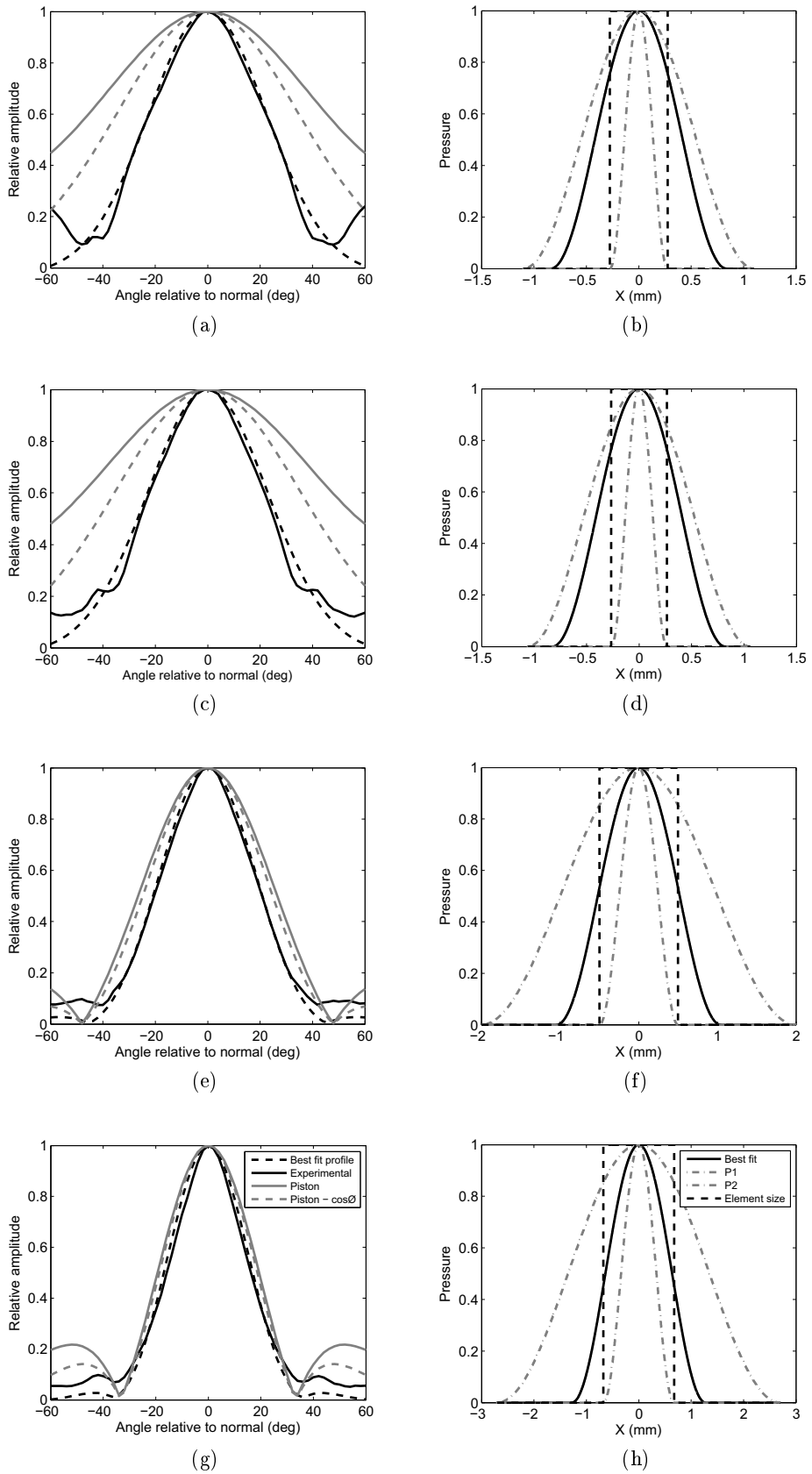

Figure 4.3.1: The results of fitting a Hanning window to the pressure distribution over an array element. In each case the modelled directivity pattern is presented , the model expressed in equation (4.2.2) with and without the cosine obliquity factor (labelled piston), and the ultrasonically measured result. The best fit Hanning window pressure distribution are range considered are also plotted, P1-P2. Plot a) - b) element type A, c) - d) type B, e) - f) type C, and g) - h) type D.

4.4 The impact of an inaccurate model for directivity

Modelling is often used to predict the performance of ultrasonic inspections so it is important to understand the consequences of directivity model inaccuracies. To quantify the modelling inaccuracies a number of simulations have been carried out using array type A, as listed in Table 4.2.1. Arrays sharing these properties were experimentally measured in the previous section. The 2D pulsed array beam model presented in chapter 3 has been used to model an array of elements. Each element is modelled as a single line source coupled with a directivity function. The model utilises ray tracing based upon Fermat's principle, that waves of a given frequency will always follow the path of least propagation time. Refraction effects are modelled using an effective propagation technique proposed by Johnson [71]. The arrays were modelled in immersion and simulations were carried out twice, once using the function described by equation (4.2.2), and a second time using the fitted pressure distribution based on a Hanning window, presented in Table 4.3.1.

Array A has relatively small elements (0.74λ wide) and the results in Figure 4.2.3 demonstrate that array A is poorly described by the model expressed by equation (4.2.2). The model arrangement used to investigate beam performance is described by Figure 4.4.1. The model has been used to simulate a 0 degree longitudinal beam using a 20 degree array angle, and a 45 degree shear wave using a zero degree array angle. In both cases focused and plane beams have been simulated, using aperture sizes of 40 and 20 elements respectively. The results of the simulations have been analysed by extracting the 6 dB beam width, amplitude, and beam angle. This analysis has shown that all three parameters are practically unaffected by the change in directivity model. A selection of the results can be seen in Figure 4.4.2. These results should be the worst case as array angles well above the first critical angle have been used to generate the longitudinal beams, and a zero degree wedge angle has been used to generate the transverse beams. This approach results in array elements relying on the extremes of their directivity pattern and this is the region where the two models disagree the most.

However, the simulations in Figure 4.4.2 have only considered two example beam angles in isolation. The effect of changing directivity pattern is most likely to affect the amplitude observed over a range of different beam angles. In order to test this hypothesis the model has been modified to simulate several different beams, all focused at 30 mm range in steel. Again an extreme case has been chosen, transverse waves generated using a zero degree wedge angle. The results of this process are presented in Figure 4.4.3 and show that the errors in relative amplitude between beam angles are much more significant than previously thought. In the worst cases maximum errors are approximately 3 dB, this translates to a pulse-echo difference of 6 dB. This level of error is clearly unacceptable but is practically outside of the normal operating range of an array e.g. generating a 70 degree transverse wave with a zero degree array angle. In the normal operating range of an array errors are limited to $<$1 dB, or $<$2 dB pulse-echo.

Ultrasonic array inspections typically use a number of wedge angles to generate longitudinal and transverse waves. This approach limits the amount of steering that the array is required to perform, and thus improves beam quality. As a result, arrays are very rarely required to steer a beam more than 10-15 degrees in the wedge. In this operating range the amplitude errors introduced by assuming the elements act as piston sources are in the region of 2 dB in pulse-echo. When using modelling tools where the directivity model cannot be changed e.g. CIVA [70] these errors should be acknowledged. Alternatively, errors can be avoided by normalising results from different beam angles by the response from calibration reflectors positioned at the same location as the point of interest. By removing the

direct comparison of absolute amplitude errors can be significantly reduced.

In summary, provided that the array is not required to steer over large angles (e.g. $>$ 10 degrees) the use of the piston source approximation is justified, and there is limited benefit in the development of a generalised model for elements with a width in the region of the wavelength. Amplitude errors up to 2 dB will only be produced if the absolute amplitudes from significantly different beam angles are related.

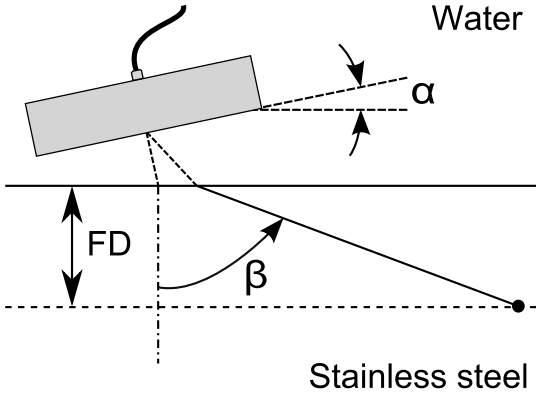

Figure 4.4.1: A diagram of the beam model arrangement used to investigate the effects of directivity. β is the beam angle simulated, α is the array angle, and FD is the focus depth. Measurement locations correspond to the focus depths.

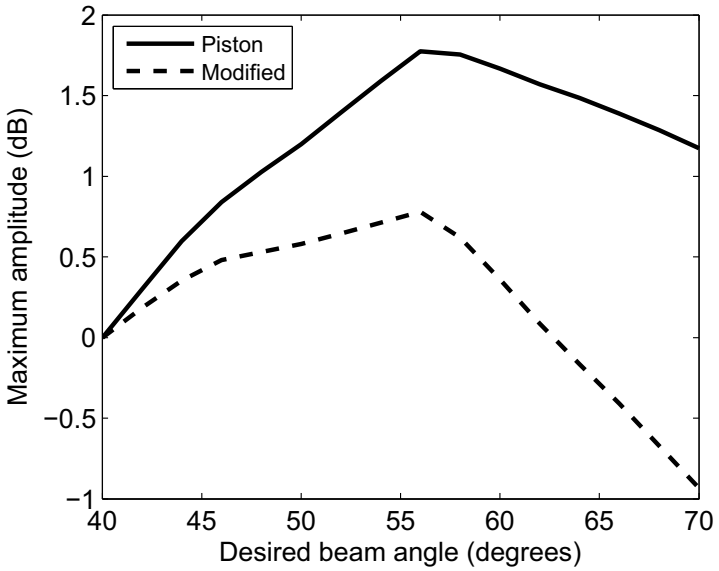

Figure 4.4.3: The results of simulating the effect of array element directivity pattern. Transverse beams focused at 30 mm range in steel, using a zero degree array angle. The results labelled as piston are using the directivity function described by equation (4.2.5), and the modified results are those using the fitted Hanning window for the pressure distribution. The amplitude scale is relative to the amplitude for a 40 degree beam angle.

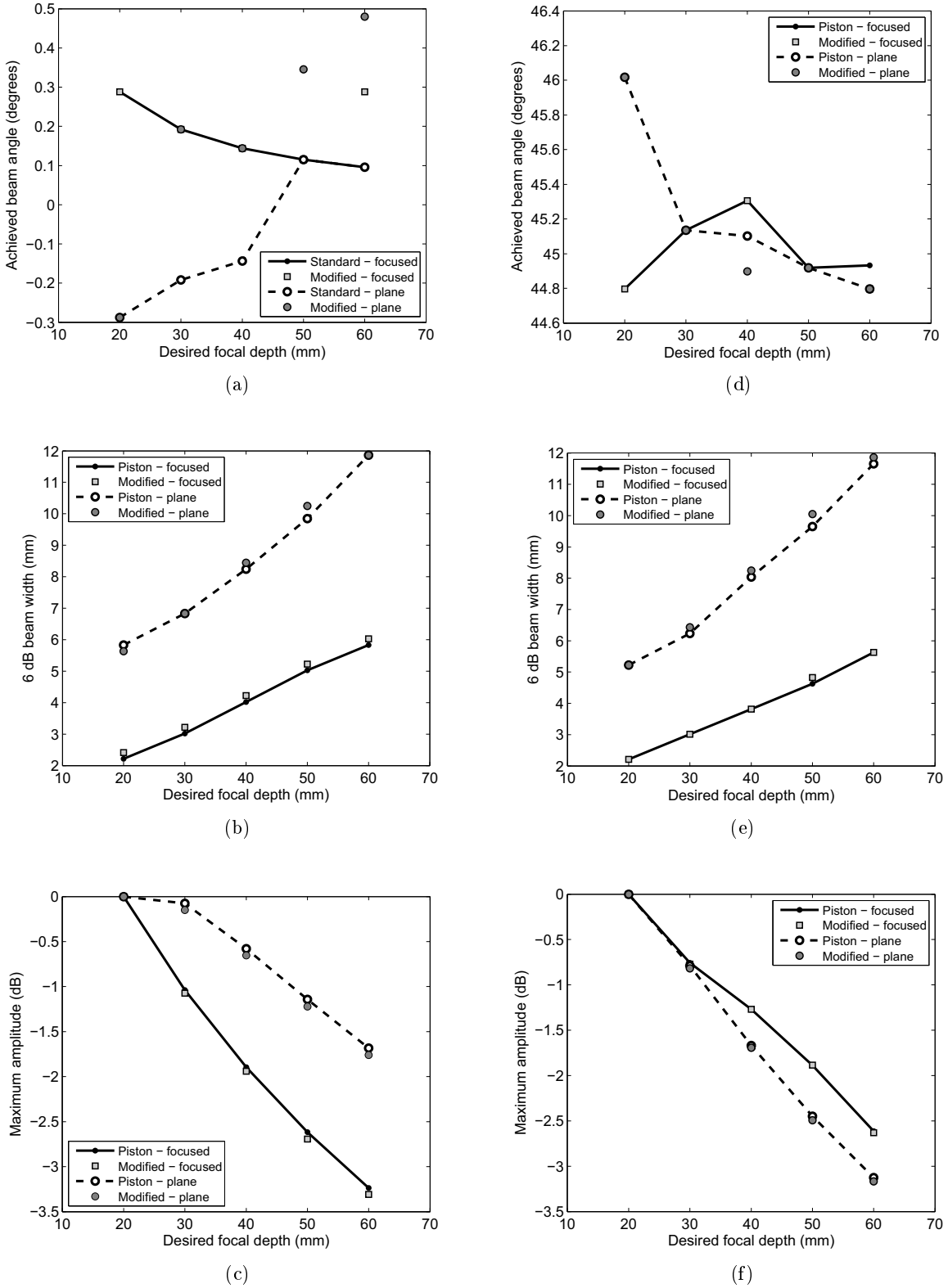

Figure 4.4.2: The results of simulating the effect of array element directivity pattern. Plots a) - c) are the results for a plane and focused zero degree longitudinal beam generated using a 20 degree array angle. Plots d) - f) are the results for a plane and focused 45 degree transverse beam generated using a 0 degree array angle. The results labelled as piston are using the directivity function described by equation (4.2.5), and the modified results are those using a best fit Hanning window for the pressure distribution.

4.5 Summary

Investigation into the accuracy of modelling array elements as piston-like sources has shown, by experimental measurement, that the assumption introduces significant errors into predicted directivity patterns. An improved directivity model for array elements has been developed. The fundamental difference between this model and existing models is that the elements are not assumed to act as pistons. Instead the pressure acting across the array element is assumed to vary as a Hanning window, and the area over which this pressure acts is larger than the nominal size of the element. This approach has been shown to produce excellent results via validation against experimental results for both ultrasonically measured directivity patterns, and modelled results using experimentally measured array surface displacements.

The development of this model into a generalised solution will require more experimental data points to verify the link between element size and pressure distribution. However, modelling the pressure field generated by an aperture of array elements has shown that the error introduced when using the piston source approximation is limited to small amplitude errors, provided the array is not required to steer the beam a large amount, e.g. $>$15 deg in water. These results provide the justification for assuming piston like behaviour in the normal operating range of an array.

5 A Calibration Routine for Full Matrix Capture (FMC)

Inspection calibration is an important part of any inspection system. It provides a means of ensuring every component of the inspection system is functioning within acceptable tolerance bands. This provides the system user with confidence that the results of an inspection are accurate. The second requirement of calibration is to relate the output of the inspection system to a known input. Calibration frameworks are well established for ultrasonic inspections utilising single element, fixed beam angle, transducers. Whilst compatible to a certain degree, existing calibration frameworks are ill suited to phased array transducers and even less so to FMC data capture. To fully benefit from the benefits of FMC based phased array technology a bespoke calibration routine must be developed.

5.1 Calibration framework requirements

Ultrasonic phased arrays are now routinely used for Non-Destructive Evaluation (NDE) [21, 20, 73], yet array specific calibration procedures to control inspection performance do not exist.

If overall transduction efficiency is ignored the performance of phased array probes is principally governed by the array design, and the relative uniformity of each element in the array in respect to one another; where performance is referring to the efficiency of an array at steering and focusing ultrasound. On the other hand the practical consequence of non-uniformity in element performance is the generation or amplification of existing artefacts in the beam such as side lobes, increased beam width, or increased energy levels away from the main beam. The impact of these artefacts when the array is being used could be the unsuccessful detection of a defect in a critical component in the field of NDE, the failure to detect a life threatening cancer in the field of medicine, or the failure to detect a sub-surface hazard in the field of sonar. As a result of the potentially fatal consequences of using poor quality or defective array transducers it is vital to carry out sufficient equipment checks to ensure an array is fit for purpose.

In the field of NDE it is currently standard practice to use arrays to emulate the performance of a number of monolithic transducers. Calibration is performed by carrying out direct measurement on the beams produced by an array using standard reflectors to ensure beam integrity. These procedures have been inherited from standards written for monolithic transducers, such as BSEN12668-2:2010 [6], as there are currently no completed standards for the calibration of array probes agreed by the British, European, or American national standards committees. As there are no centrally agreed standards in place the calibration procedures used for arrays vary from operator to operator and may include the calibration of a single beam for each array, the calibration of the lowest and highest angled beams the array is required to produce, or the calibration of every beam. In accordance with British and European standards a complete calibration procedure consists of several parts:

- Transducer checks - this consists of measurements of probe angle, beam width, and bandwidth

(although the last item would rarely be checked). These items are measured conventionally using calibration reflectors.

- Combined equipment checks - this step requires that the electronics of the flaw detector are tested to ensure that the time base and amplifiers behave linearly in response to known inputs. Again, this is performed using calibration reflectors.
- Distance Amplitude Correction (DAC) - this item is implemented in automated inspection using calibration reflectors to record range-amplitude curves for every probe/beam that is used. These curves can then be used to vary amplifier gain such that the recorded calibration reflector amplitude is independent of range.
- Setting of inspection sensitivity - Reporting criteria for pulse-echo ultrasonic inspections are commonly amplitude based. Hence it is normal practice to specify the required inspection sensitivity in relation to DAC curves. For example, a weld inspection designed to detect porosity in the weld metal may require a scanning sensitivity of DAC + 20 dB. Specifying the required sensitivity in this way means that the inspection can be performed with any combination of probe and flaw detector.

The development of Full Matrix Capture (FMC) technology [4] makes this approach impractical as one of the main benefits of FMC is that data can be processed at any time after data has been collected. Using the existing approach would mean the usable results from an inspection would be limited to those beams calibrated at the beginning of an inspection. Instead a calibration procedure is proposed that is based on the transducer rather than the beams produced by it. This can be achieved using the following steps:

- Transducer checks - This requirement can be split into two steps. The first step is the measurement of the essential parameters that define array performance and subsequent comparison against acceptable tolerances. By ensuring each element is functioning within specification you can then guarantee inspection performance when beam forming is subsequently carried out. This approach decouples the checks from a specific beam and instead ensures that the array is capable of producing any beam that are appropriate for the array specification and application. The second step is a combined probe check. The first step required accurate measurements to be made with the array detached from any wedge in immersion to ensure even coupling. The second step is designed to be carried out with the array attached to any wedge, and uses the reflection from the wedge component interface to monitor element performance without removing the probe from the component under inspection.
- Combined equipment checks - this step would be performed as it is for conventional inspections for items such as amplifier linearity (e.g. BSEN12668-3 [7]) , but would also include a further check. A calibration block containing a range of reflectors would be imaged and analysed in terms of response locations and amplitudes. This provides a final check that the combination of transducer, wedge, and flaw detector are all correctly configured and functioning. This step would also be repeated at regular intervals throughout the inspection, but at a lower frequency than the combined probe check, and successive results compared to ensure no drift in probe performance. The change in performance could be caused by changes in array performance, coupling efficiency between array and wedge, severe wear to the wedge, or array controller fault.

- Setting of inspection sensitivity and Distance Amplitude Correction (DAC) - a method of recording DAC curves has been devised that uses FMC technology to scan a calibration block and thereby allows DAC reconstruction and amplitude normalisation at any point in the future.

Each aspect of the proposed calibration routine for FMC based inspections will be detailed in this, and the following, chapter.

5.2 Array Integrity Testing

As discussed in the previous section a key component of the calibration of an ultrasonic inspection system is transducer checks. This chapter will discuss the developments of transducer check that is not coupled to any particular beam type. The essence of this approach is to ensure transducer performance rather than demonstrate that a transducer can produce specific beam types.

To accommodate such a general transducer check acceptable variations in transducer performance must be defined. The development of such criteria are reported in this chapter via the use of the array beam model, reported in chapter 3, to conduct Monte Carlo modelling.

5.2.1 The essential parameters of phased array elements

The performance of an array element can be defined using the following parameters:

- Sensitivity - this refers to the amplitude of the ultrasound produced by an element for a given electrical input. In practical terms this parameter is used to refer to the combined transmit-receive sensitivity of the element relative to the mean value of the array. A reduction of element sensitivity to zero simulates a faulty element, referred to as a dead element.

- The relative phase of the element - this refers to any difference in the time it takes for an element to begin generating ultrasound after a voltage pulse has been sent by the controlling hardware from the mean value for the array. This is referred to as element firing delay.

- The directivity pattern of an element - this parameter directly influences the types of beams that the array is capable of producing [79]. In theory this parameter is simply governed by the geometry of the piezo-ceramic composite that make up the elements in modern phased array probes [19]. In practice this parameter is also influenced by the matching layer used between the piezo-ceramic composite and the test material, as well as any mechanical and electronic cross talk present within the array [84, 88, 89, 77].

- The pulse shape and length produced by the element - this parameter is governed by the array construction and driving conditions used to operate the transducer.

By measuring each of these parameters it is possible to ensure that the array is functioning correctly without time consuming beam measurements being carried out. For this approach to be adopted acceptance criteria need to be decided upon based on evidence of the effects that each parameter has on the ultrasonic field produced by an array. This chapter presents the process used to select tolerances on each parameter based on the results from Monte Carlo simulations using an array beam model. Element directivity and pulse length will not be included in this chapter as these parameters are separable from the effects from sensitivity and phase, and are not thought to vary between elements.

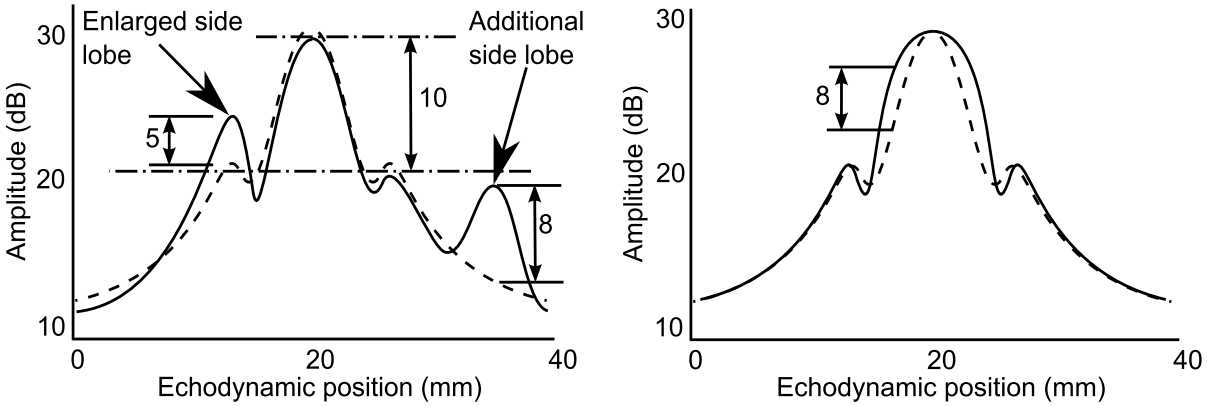

Figure 5.2.1: Examples of the type of changes observed in echodynamics. The dashed line is produced using a uniform sensitivity profile, and the solid line is produced by varying element sensitivity a) enlarged side lobe plus an extra side lobe b) increase in main beam width.

Element directivity is discussed in detail in chapter 4, and results demonstrate that directivity is very consistent in modern arrays.

Variations in performance between elements cause changes to the ultrasonic field produced by the array. These changes can be the formation of areas of higher or lower amplitude, or simply alterations to existing features. It is common practice to present ultrasonic fields as one or two dimensional plots of maximum amplitude. The advantage of this approach is that results can be visualised without considering the time dependent nature of ultrasonic fields. A one dimensional plot of maximum amplitude across an ultrasonic field allows the locations of the main beam and any additional features to be observed. This type of plot is refered to as an echodynamic [91]. Figure 5.2.1 presents some examples of echodynamics with and without features that have been introduced as a result of element inhomogeneity.

Plot a) demonstrates how the echodynamic can change by the enlargement of a small side lobe, a small change in the peak amplitude of the main beam, and the introduction of a separate side lobe. Plot b) demonstrates a more subtle change to the echodynamic, an increase in main beam width. It is proposed that beam artefacts be categorised as the following:

- Changes to peak amplitude
- The enlargement or introduction of side lobes
- Broadening of the main beam
- Changes to the intended propagation direction of the ultrasonic wave

All of these beam artefacts can lead to significant changes to the image produced by a beam as ultrasonic imagery is formed on the basis of *a priori* knowledge of the characteristics of an ultrasonic wave. Changes to these characteristics cause reflected wave signals to be plotted in the incorrect location, or the shape of the response to change. Both of these pieces of information are used to postulate the cause of the reflection and its potential significance, so minimisation of errors is important.

5.3 Modelling approach

The modelling approach selected for this chapter has been used by previous authors [92, 93, 94, 95] to investigate the effect of variations in element performance. Steinberg [96] has also carried out a broadly similar study based on an analytical approximation of the ultrasound scattered by a point reflector. Steinberg's study actually aimed to quantify the effect of phase errors introduced by the finite sample period inherent with digital systems. Regardless of the fact that the aim and methods of Steinberg's study are quite different to those selected for this chapter the conclusions drawn are applicable to this study and comparisons can be made between the results.

The studies carried out by Lancee et al [92, 94] were targeted at a medical application so focused on the modelling of the acoustic case, whilst the study by Nageswaran [93] focused on the elastic case but relied on the results from a small number of simulations. The limitation placed on Nageswaran was that a commercial modelling package was used and its performance was such that parametric studies using large data sets were impractical to carry out. For these reasons the model developed for this present chapter has been written to allow Monte Carlo simulations using large data sets to be carried out in a short amount of time. The model uses a uniformly distributed random number generator to automatically apply variations to a single parameter at a time, within set limitations. A uniformly random distribution has been chosen to ensure the limits suggested by this study are conservative. In each case a thousand simulations have been carried out plus the same simulation using a uniform array to allow for a baseline comparison to be made. The randomly generated profiles used by the model have been made extreme relative to experimental measurements made on arrays, this is demonstrated by Figure 5.3.1. The dashed line in the plot shows that a typical array exhibits small variations of the majority of elements, and a small number of elements within the array have much larger variations. In comparison, the solid line, which represents the type of variation used in the model, has a much larger standard deviation. This approach has been adopted so that any conclusions drawn on the basis of the results of this study will be conservative. This approach is very similar to that taken by Zhang et al [95], but that paper focused on the effect of transducer inconsistencies on images produced by the Total Focusing Method (TFM) [4] rather than on the ultrasonic beam.

The model parameters used for the simulations can be seen in Table 5.3.1, and details of the beam types modelled can be seen in Figure 5.3.2. These values have been selected as the beam types are commonly used in the field of NDE, and the broad range of settings should help to guard against the formation of conclusions that are true for a particular model configuration rather than generally. To support the modelling results a number of experimental measurements of element sensitivity and firing delay have been made on eight different arrays. These profiles have then been used as an input to the beam model and the results have been analysed using the same method as applied to the results from the randomly generated profiles.

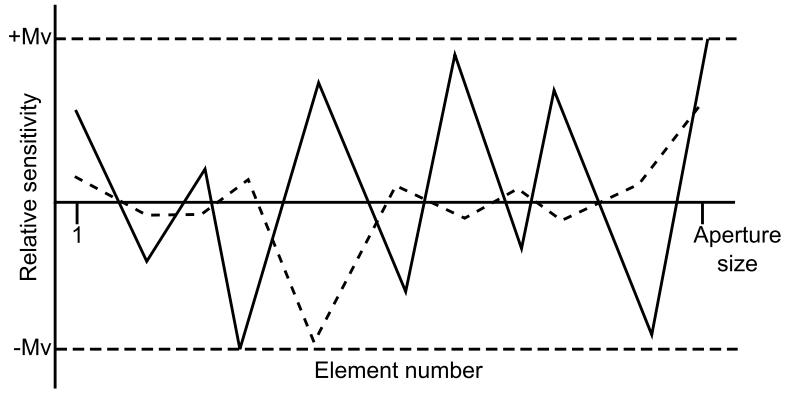

Figure 5.3.1: An example of the type of randomly generated profiles used by the model. The solid line is the type of profile used by the model, and the dashed line represents an example of the type of variation measured in real arrays. Mv defines the maximum variation present in the profile.

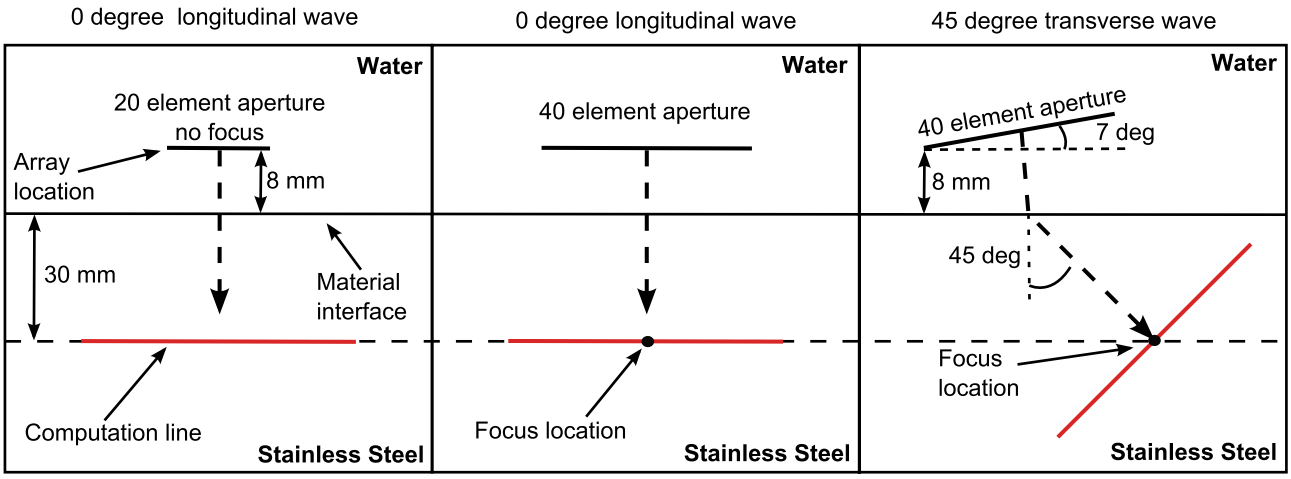

Figure 5.3.2: The details of the three different beam types modelled.

Table 5.3.1: Simulated array parameters.

Parameter	Value		
Array centre frequency (MHz)	2.0	5.0	7.5
-6 dB bandwidth (%)	50	50	50
Element pitch (mm)	0.75	0.6	0.4
Element gap (mm)	0.20	0.1	0.1

5.3.1 Beam model structure

The beam model discussed in chapter 3 has been used. Recall that the model computes the amplitude and phase of any point in a material and can be calculated by carrying out the summation described by equation (5.3.1).

$$A = \sum_{j=1}^{n} \frac{1}{\sqrt{R_E}} \exp^{-i(k(R_{1,j}+R_{2,j})+\omega \triangle t_j)} D_f\left(\varnothing_j, \omega\right) T\left(\beta_j\right) \tag{5.3.1}$$

where symbols retain their previous meanings.

The model described by equation 5.3.1 has been used for the Monte Carlo study by the introduction of, and subsequent variation of, element sensitivity and firing delay. Dead elements are simulated by setting element sensitivity to zero. Equation 5.3.1 is then modified into the following:

$$A = \sum_{j=1}^{n} \frac{1}{\sqrt{R_E}} \exp^{-i(k(R_{1,j}+R_{2,j})+\omega(\triangle t_j + FD_j))} D_f\left(\varnothing_j, \omega\right) T\left(\beta_j\right) S_j \tag{5.3.2}$$

where FD is the firing delay (s) that has been applied, and S is the sensitivity of the element relative to the mean value for the array.

5.4 Data Analysis

Analysis of the results generated by the Monte Carlo simulations has shown that the effects of changes in sensitivity are not frequency dependent, and the largest changes are observed in maximum amplitude and beam artefacts, whilst other parameters vary on much smaller scales. The results from changes in element firing delay exhibit a strong frequency dependence.

A change in maximum beam amplitude is found by calculating the difference in the maximum amplitude generated when modelling an array composed of identical elements and one composed of elements with varying properties. The same method is used to give a quantitative measure to the severity of beam artefacts, but this is done by finding the maximum difference between the whole echodynamics rather than limiting the search to only the peak.

The severity of any beam artefact is subjective as the location of the artefact and its relative amplitude must be taken into account. The echodynamics shown in Figure 5.2.1 are good examples of the subjective nature of beam artefacts. The echodynamic shown in plot a) contains two beam artefacts that are 5 and 8 dB higher in amplitude than the amplitude generated using an array of identical elements. In this case the beam artefact that is only 5 dB higher in amplitude is arguably the worse as it is much closer to the main beam. As a result of outcomes such as this it has been decided to search

for beam artefacts only in the part of the echodynamic whose amplitude is within 12 dB of the peak of the main beam. This filtering does not exclude results where beam artefacts are initially below the 12 dB threshold but are increased in amplitude, via variation in element performance, such that they break the threshold. Thus this process cannot exclude relevant results, but only exclude changes to the beam whose absolute amplitude relative to the peak value is very low. From this point forward the numerical measure of beam artefacts will be referred to as changes in background level.

The example echodynamic shown in Figure 5.2.1 plot b) demonstrates a case when the chosen method for quantifying the severity of beam artefacts produces a misleading result. In plot b) a large difference in amplitude is caused by an increase in the width of the main beam. From an NDE perspective this type of beam artefact is much less of a problem in comparison to the type of artefacts shown in plot a), so the numerical measure is misleading.

Analysis of results from simulations has shown that results are well separated if the standard deviation of the element performance parameter is plotted against the change in background level. As the Mv value is increased the standard deviation of element performance parameter increases, as does the mean and standard deviation of change in background level. A line of best fit must then be added to the plot to enable the standard deviation of measurement error that results in a certain change in background level to be predicted.

A sample result is shown in Figure 5.4.1 a). The fitted profile can be used to locate the maximum change in background level that will occur for a given standard deviation of standard deviation. Figure Figure 5.4.1 b) demonstrates how linear interpolation can be used to locate the value of standard deviation of measurement error (X) that results in 2 dB changes in background level. The standard deviation of element sensitivity is not a useful parameter, instead the variation in background level for changes in the maximum parameter change is preferable. The transformation in parameter can be achieved by assuming that the mean standard deviation of element sensitivity is proportional to the maximum measurement error (Mv value) used for that simulation group. For example, in Figure 5.4.1b SD_1 is assumed to be proportional to $M_v = 0.1$. This approximation appears to be valid by inspection of the results, see Figure 5.4.1 a). Using this method of parameter transformation the maximum allowable parameter variation can be calculated from the best fit profiles.

5.4.1 Acceptance criteria

To use the Monte Carlo based modelling approach to suggest limitations on acceptable variations in element performance it is first necessary to decide upon an acceptance criterion for the beam profile produced by a given array. The approach taken for this study has been to use the method described in a standard that has been in use for many years, BSEN12668-2 [6]. BSEN12668-2 is a standard written for the evaluation of single element probes rather than arrays, but the procedures are also applicable to arrays. This standard mandates that a 10 dB amplitude separation should exist in the free field (20 dB for the pulse-echo case) between the main lobe and any side lobes.

A potential disadvantage of this approach is that beam profile modelling does not predict the effect of a beam artefact on the response from, or image produced of, a scatterer present in the region insonified by the array. However, the predicted transmit beam profile must be multiplied by the associated receive beam profile, which is often the identical profile for NDE applications [4, 38], and the scattering function

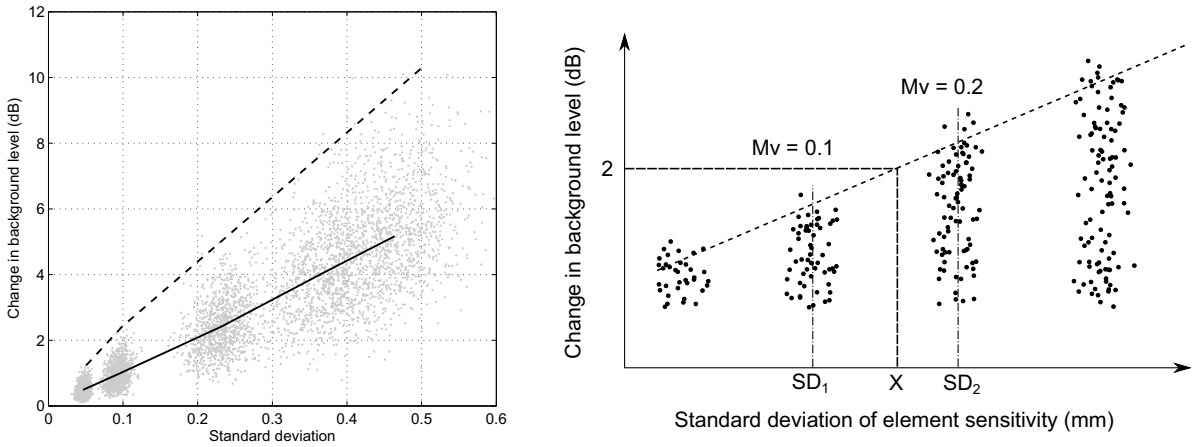

(a) (b)

Figure 5.4.1: The process used to extract results profiles. a) The dashed and solid lines represent the maximum and mean changes respectively, and the scatter plot is the raw data. b) A sketch demonstrating the method used to interpolate the results. $SD_{1/2}$ are the mean standard deviation values for simulation groups using a maximum variation (M_V) of element sensitivity of 0.1 and 0.2 .

of the defect. This often results in the response from the defect being dominated by the main lobe of the beam, even for very high amplitude artefacts. For example, the plane and focused zero beams used in this study have been simulated at 2 MHz in the commercial modelling package CIVA [70], version 10.1. In each case the beam has been simulated with the delay laws calculated by CIVA, and a second time with an extreme variation in element firing delay added to the delay laws. A maximum variation value of 50 and 100 ns has been applied to the plane and focused beam respectively. The predicted transmit beam profiles can be seen in Figure 5.4.2, and show that the second simulation results include side lobes that are within approximately 4 and 8 dB of the main lobe peak for the two beam types. The two results have an associated change in background level of approximately 4 and 6 dB respectively for the plane and focused beams.

Clearly both beam profiles are badly degraded by the effect of the firing delay, but the effect of beam artefacts on the defect response produced by the array should also be considered. The defect response from a 2 mm diameter Side Drilled Hole (SDH) at a depth of 30 mm can also be simulated by CIVA using a Kirchhoff model to predict the response from the reflector. The firing delay variation has been applied in both transmission and reception, and the array has been mechanically scanned in 0.5 mm steps. The predicted B-scans are presented for both beam types in Figure 5.4.3. The response from the SDH is not significantly different in either case, despite the extreme variation in firing delay applied. The levels of element performance variation considered in this study will be smaller that those considered in this example, and hence the approach mandated by the selected standard is considered justified.

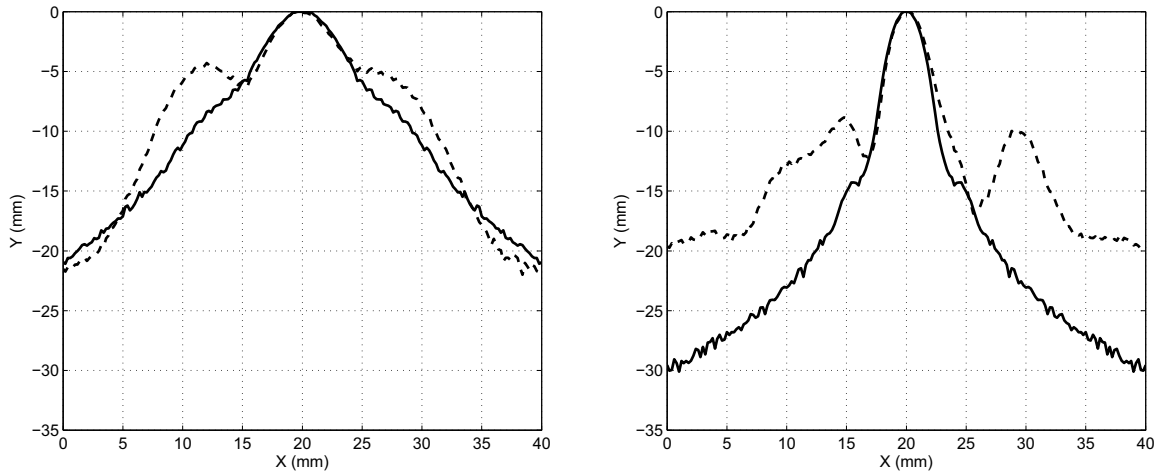

(a) (b)

Figure 5.4.2: Beam profiles predicted by the modelling package CIVA with and without variation in element firing delay; the dashed beam profiles include variation a) 2 MHz zero degree plane beam with 50 ns maximum variation b) 2 MHz zero degree focused beam with 100 ns maximum variation. Details of the array and beams can be found in section 5.3.

5.4.2 Element sensitivity

The results from variation in element sensitivity will also be analysed using a second parameter called the Second Central Moment (SCM), defined in equation (5.4.1). The parameter SCM has been used by Lancee et al [92] to investigate the effect of element sensitivity. SCM is simply a measure of the distribution of a two dimensional profile about from the centre of gravity of the profile, which is calculated as the mean of the second moment of the distribution about the centre of gravity of the distribution.

$$SCM = \frac{\sum_{i=1}^{n} a_i \left(x_i - x_o\right)^2}{\sum_{i=1}^{n} a_i} \tag{5.4.1}$$

where a is the parameter being measured, n is the number of elements in the aperture, and x_i and x_o are the co-ordinates of the value a_i and the centre of gravity of the distribution respectively. x_o is calculated via the following equation:

$$x_o = \frac{\sum_{i=1}^{n} a_i x_i}{\sum_{i=1}^{n} a_i} \tag{5.4.2}$$

For example, a uniform parameter distribution would have an SCM value of one. The difference between SCM and standard deviation is that SCM takes into account the spatial distribution of a parameter, whilst standard deviation is only a function of variation in the amplitude of the parameter. For example, a distribution could exist that has a large standard deviation value and a SCM value of approximately one. Consideration of SCM will reveal any spatial dependence of the effect of changes in element sensitivity.

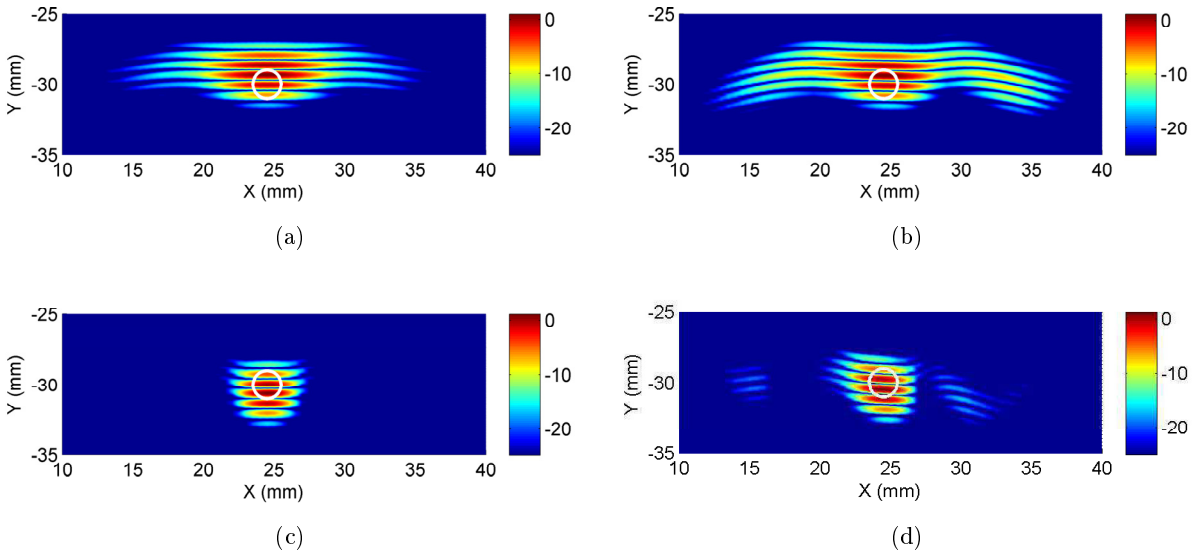

Figure 5.4.3: The B-scan images predicted by CIVA for the beam profiles shown in Figure 5.4.2 for a 2 mm diameter SDH. The location of the SDH has been superimposed on the image. a) plane zero degree beam b) plane zero degree beam with variation c) focused zero degree beam d) focused zero degree beam with variation. The colour scale is in decibels.

The results considering the maximum change in background level will be presented as line plots composed of the mean and maximum change from each data set. The plot in Figure 5.4.1 demonstrates how the profiles have been extracted from the analysed data.

The conclusion of Lancee et al was that when the SCM of an array's sensitivity profile is normalised by the SCM value of an identical array of uniform sensitivity it effectively becomes a measure of the beam width. A normalised SCM value > 1 represents a bias of the distribution toward the edges of the array and tends to indicate the enlargement, or introduction, of side lobes into a beam. A normalised SCM value < 1 represents a bias of the distribution toward the centre of the array and tends to indicate an increase in the main beam width, but also indicates that the beam amplitude is reducing more sharply with distance from the beam centre. These results would be expected as a normalised SCM < 1 suggest the sensitivity distribution is biased toward the centre of the array, this is equivalent to an array centre biased apodization function which have been shown to reduce beam width and suppress side lobes [19].

5.4.2.1 Echodynamic categorisation

An automated means of echodynamic characterisation has been used to better understand how normalised SCM can be used to predict the likely beam artefact that a given sensitivity distribution will produce. Least Mean Squares (LMS) signal decomposition has been used to classify the dominant artefact in each echodynamic using examples of each type of beam artefact. This method is based on least squares curve fitting, which is commonly used [97]. LMS signal decomposition can be explained by assuming that each echodynamic is a signal made up of a number of basis functions with corresponding coefficients:

$$y(f) = a_1 + a_2 F_2(f) + a_3 F_3(f) \tag{5.4.3}$$

The sum squared error between the assumed function, $y(f)$, and the real signal, $y_r(f)$ can be described by equation (5.4.4):

$$SSE = \sum_{i=1}^{n} \left(y(f_i) - y_r(f_i) \right)^2 \tag{5.4.4}$$

The best fit between the real signal and the assumed signal can be found by taking the partial differential with respect to each coefficient and setting the result to zero. The result of this process expressed in matrix notation can be seen in equation (5.4.5). This can be easily solved for the basis function coefficients by matrix inversion:

$$\begin{bmatrix} \sum y_r(f_i) \\ \sum y_2(f_i)\, y_r(f_i) \\ \sum y_3(f_i)\, y_r(f_i) \end{bmatrix} = \begin{bmatrix} n & \sum y_2(f_i) & \sum y_3(f_i) \\ \sum y_2(f_i) & \sum y_2(f_i)^2 & \sum y_2(f_i)\, y_3(f_i) \\ \sum y_3(f_i) & \sum y_2(f_i)\, y_3(f_i) & \sum y_3(f_i)^2 \end{bmatrix} \begin{bmatrix} a_1 \\ a_2 \\ a_3 \end{bmatrix} \tag{5.4.5}$$

This process allows the basis function coefficients to be found that result in the best fit between the assumed function and the real function. This can be applied to an echodynamic by using a series of basis functions based on the type of beam artefacts that need to be identified. For example, analysis of a number of echodynamics produced for a focused zero degree beam beam suggests that the defects can be separated into three groups:

- enlarged side lobes
- the introduction of extra side lobes in addition to the pair normally present
- a general increase in the amplitude level in the echodynamic away from the main beam

Figure 5.4.4 demonstrates the type of basis functions that could be used for a 0L beam using the least mean square signal decomposition method. The coefficients that result from this process then need to be calibrated against echodynamics exhibiting typical artefacts in order to gain an understanding of what the magnitude of each coefficient means. An important part of this process is ensuring that the chosen basis functions result in coefficients that vary on the same scales. The aim of this process is to clearly categorise each echodynamic. Using the examples given in Figure 5.4.4 would result in seven coefficients corresponding to the following:

- the DC component of the echodynamic; this value is not used
- a general increase in background amplitude
- an increase in side lobes
- three coefficients corresponding to the appearance of extra side lobes
- the similarity to the echodynamic for the beam produced using an array of uniform elements

If the echodynamic being analysed contained enlarged side lobes one would expect the corresponding coefficient to be the largest, and similarly for any other type of beam artefact. It should be noted that by its nature this process is largely qualitative but testing has shown it to be accurate at the categorising of echodynamics provided sufficient time is invested in calibration of the basis functions.

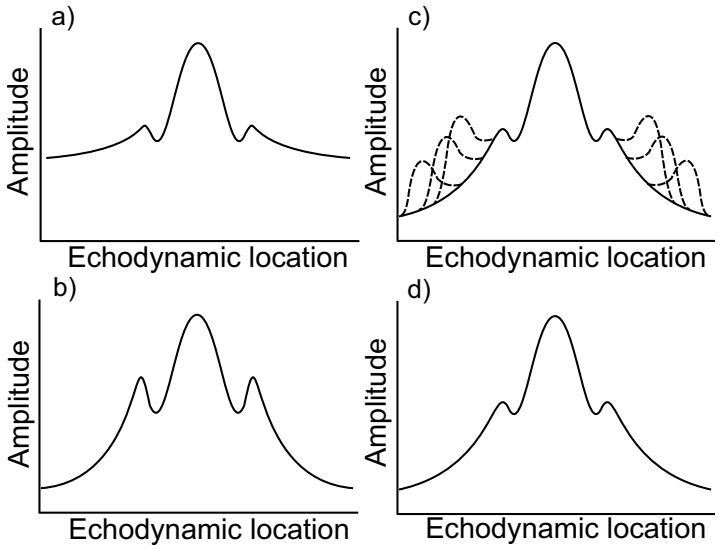

Figure 5.4.4: Examples of the type of basis functions used for a zero degree focused longitudinal beam: a) a general increase in background level b) enlarged side lobes c) an additional pair of side lobes in different locations d) the echodynamic produced using a uniform sensitivity profile.

5.4.2.2 Basis function generation and application

To demonstrate how basis functions are created , the process used to generate the basis functions for the 0L beam will be presented.

The first step in generating the basis functions is to review the echodynamics produced via the variation of element properties. This will identify the number, or type, of beam artefacts that are introduced. The LMS signal decomposition process will only produce reliable results providing that the basis function are capable of describing every possible beam artefact. In reality, it is not possible to account for every possible beam artefact, and indeed attempting to do so by using large numbers of basis functions is counter productive. If there are a sufficiently high number of basis functions any echodynamic can be accurately decomposed in to the basis functions, regardless of the agreement between the echodynamic and basis functions. Hence, the number of basis functions must be limited to the main types of echodynamic artefacts.

As discussed in the previous sub-section, the main types of beam artefacts observed for the 0L beam are:

- A general increase in the echodynamic amplitude away from the main lobe
- The enlargement of the pre-existing side lobes
- The addition of a second set of side lobes in a variety of positions

To allow decomposition of the echodynamics basis functions have to be produced. In most cases these basis functions are based on the echodynamic produced using a uniform array of elements. This is refered to as the standard echodynamic.

Plots of the basis functions used for LMS signal decomposition for the 0L beam are shown in Figure 5.4.5. In plot a) the basis function used for an increase in background amplitude is shown. This was produced by artificially setting the amplitude of the standard echodynamic to a constant value beyond the side lobes. In plot b) the basis function for increase side lobe amplitude is presented.

This was generated by artificially increasing the amplitude of the side lobes present in the standard echodynamic. In this case a Hanning window was used to prevent the introduction of amplitude discontinuities. Finally, in plot c) the three basis functions used to represent extra side lobes are shown. The extra side lobes were added to the standard echodynamic by adding Hanning windows at three symmetric locations either side of the main lobe.

Once the basis functions have been created the logic used to categorise the echodynamics must be defined. The only reliable method found for this stage was to manually categorise a selection of results containing a range of artefacts, and record the basis function coefficients from the LMS decomposition process. If the chosen basis functions are able to distinguish the beam artefacts of interest the coefficient corresponding to the basis function matching the beam artefact present in the echodynamic will have the largest value. If this is not the case then different basis functions must be used, and the process repeated.

An example of basis function coefficient variation for a focused zero degree longitudinal beam is presented in Figure 5.4.6. Three sample echodynamics have been produced by variation of element sensitivity up to 0.5, and are shown in plots a) to c). The major artefact present in each echodynamic is increased side lobe amplitude. Plot c) shows the basis function coefficient amplitudes for the three echodynamics, using the basis function shown in Figure 5.4.5. In each case the amplitude of the basis function corresponding to increased side lobe amplitude is the largest value. For echodynamic three there is also a significant increase in background energy. Accordingly the amplitude of the background energy basis function is only slightly lower in amplitude than the side lobe basis function. This demonstrates that the LMS method applied will only select the largest echodynamic artefact, despite the presence of other artefacts. Experience has shown that in the vast majority of cases the artefact selected is the artefact of primary concern. However, this method is used to highlight statistical trends and for this purpose it is considered appropriate.

5.4.3 Element firing delay

The same methods used to analyse the results from element sensitivity will be used for element firing delay, and data will be presented by plotting the change in background level or peak amplitude against the standard deviation of the firing delay profile across the array. However, as the results from changes in firing delay are frequency dependent the allowable firing delay variations will be presented as a function of transducer bandwidth. This approach was used by Steinberg [96] to investigate the effect of phase errors on the average side lobe level produced by an array. He assumed that the echodynamic produced by the array was a single peak that asymptotically decays away to zero amplitude, and defined side lobes as any feature that interrupted this behaviour. As previously mentioned, Steinberg's work investigated the effect of delay law quantization error resulting from the application of delay laws at the sample frequency of the system. The conclusion of this work was that the tolerance of an array to phase errors is governed by the bandwidth and centre frequency of the transducer. He found that so long as the product of -6 dB bandwidth (B) and time sample period (t_0), or sampling interval, were in the range 0.1-0.25 then the mean level of side lobes would be sufficiently suppressed. Table 5.4.1

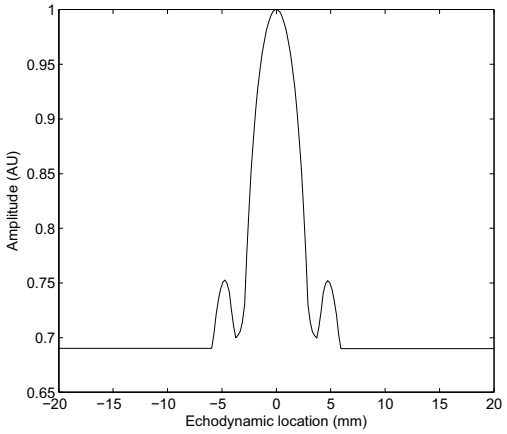

(a)

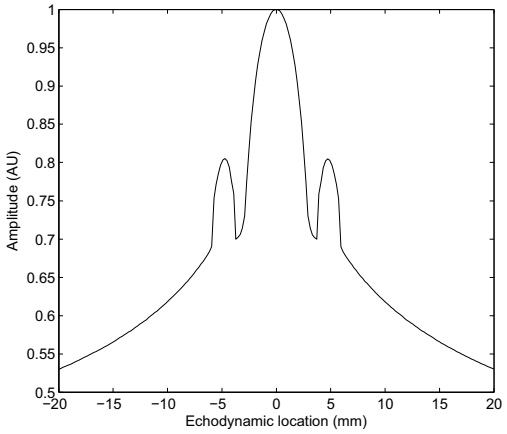

(b)

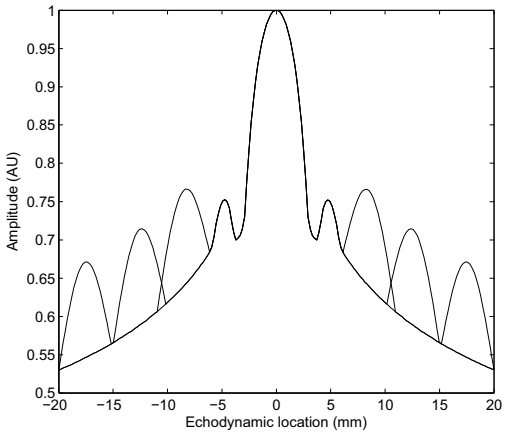

(c)

Figure 5.4.5: The basis functions used to categorise the zero degree focused beam. In each case the plot contains a different echodynamic artefact: a) an increase in background amplitude, b) enlarged side lobes, c) additional side lobes in three locations.

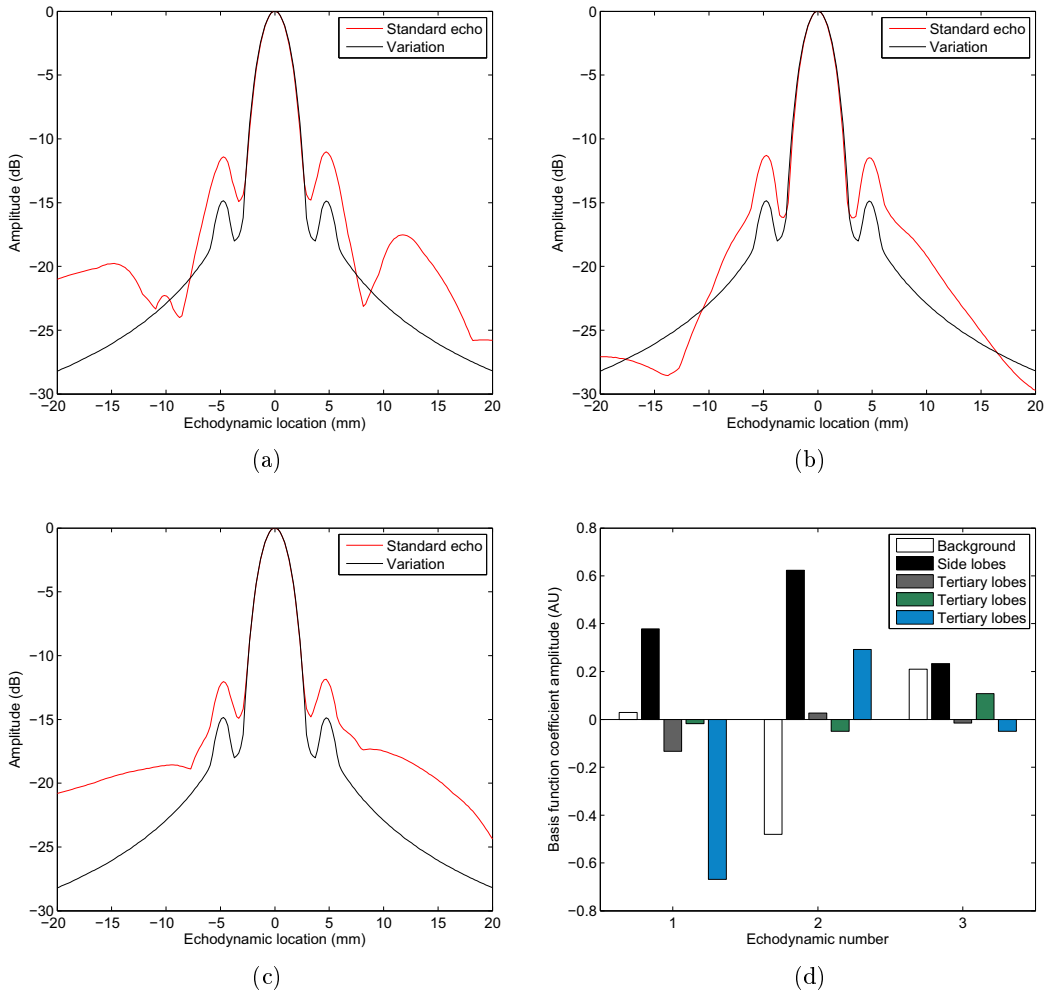

Figure 5.4.6: An example of the application of the echodynamic categorisation method for a zero degree focused longitudinal beam a) to c) three example echodynamic produced via application of element sensitivity variation up to 0.5, d) basis function coefficient amplitudes results from the LMS minimisation process associated with the three echodynamics.

Table 5.4.1: The limits on maximum possible phase error suggested by Steinberg [96].

Centre Frequency (MHz)	$Bt_0 = 0.1$		$Bt_0 = 0.25$	
	t_0 (ns)	Max error (ns)	t_0 (ns)	Max error (ns)
2.0	100	50	250	125
5.0	40	20	100	50
7.5	27	14	67	34

expresses the results of Steinberg's study for a number of typical probe centre frequencies, and the maximum tolerable phase error that follows.

Steinberg [96] also considered the effect of phase errors on the peak amplitude produced by an array, and proposed the following equation to describe it:

$$Y = exp\left(-\sigma_\phi^2\right) \tag{5.4.6}$$

where Y is the reduction in peak amplitude, and σ_ϕ is the standard deviation of the phase error (radians).

The results from this study will be compared to the values in Table 5.4.1 and equation (5.4.6), as each method provides a useful tool for predicting changes in array performance.

5.4.4 Dead elements

The effect of dead elements within an array has been investigated using the same methodology as previously, but a two staged approach has been selected. The first stage was to carry out simulations that only consider contiguous groups of dead elements but vary the group size, group location, and the size of the aperture the group is within. The aim of this is to reveal the maximum proportion of dead elements that can be tolerated within an aperture. The second stage was to repeat one of the simulations carried out in stage one, but use a random distribution of dead elements to support the hypothesis that a group of dead elements will always be the worst possible case.

Results will be presented by plotting the change in background level or peak amplitude against the percentage of dead elements in the aperture.

5.5 Results

5.5.1 Element sensitivity

The results from element sensitivity were found to be frequency independent, and as a consequence only the results at a centre frequency of 2 MHz will be discussed. The results presented will also be limited to changes in background level as the changes in peak beam amplitude are much less significant when caused by changes in element sensitivity, rather than changes in element firign delay. The profiles generated by varying element sensitivity can be seen in Figure 5.5.1. Each data set here is based on different limits on the maximum variation in element sensitivity. For example a maximum variation of 0.1 means each simulation in that group had element sensitivities varying between 0.9 and 1.1. In Figure 5.5.1 this corresponds to the data points with a standard deviation of approximately 0.05. The experimentally measured profiles are marked as stars on the figure (Md). The results for the zero degree focused longitudinal beam (0L), plane zero degree longitudinal beam (0LP) and the focused 45 degree transverse beam (45T) can been seen in plot a) in Figure 5.5.1. This plot presents the mean and maximum change profiles extracted from the simulation results when no limitation is placed on the search for changes in background level. From these results one can see that the experimentally measured profiles are always below the artificial profiles.

Plot b) shows the profiles when changes in background level are limited to beam artefacts that are not more than 12 dB lower in amplitude than the peak of the main beam. A value of 12 dB has been chosen as 10 dB is the limit mandated in BSEN12668-2:2010 [6] for the smallest acceptable difference in amplitude between the main lobe and side lobe in an ultrasonic field. Therefore it would be acceptable to have changes up to 2 dB when using the 12 dB search limit. The results clearly demonstrate a strong link between the standard deviation of the sensitivity distribution and the maximum change in background level. As the standard deviation increases, both the mean and maximum change in background level for each group of simulations increase approximately linearly. The magnitude of changes in background level is also reduced when the search extent is limited to 12 dB.

The most apparent difference between the results from the three beams is that the 0LP beam appears to be more sensitive to changes in element sensitivity than the two focused beams. The most likely explanation for this behaviour is that by limiting the search extent to 12 dB the results from both of the focused beams are reduced to mainly changes in main beam width, and those with gross side lobe artefacts. When limiting the search extent for the 0LP beam to 12 dB the same reduction in gross beam artefacts is not seen because the maximum beam amplitude is much lower than the focused beams, as it is a result of the superposition of the ultrasound generated by a much smaller number of elements. This means that it is much easier for side lobe amplitude to be a significant fraction of the main beam's amplitude.

From plot b) in Figure 5.5.1 it is not possible to separate the type of beam artefacts demonstrated in Figure 5.2.1 from one another, although plot c) does show that the vast majority of results for the 0L beam have normalised SCM value below one when the search is limited to 12 dB. As previously stated, Lancee et al found than a normalised SCM value below one generally indicates an increase in the main beam width. This suggests that the majority of results in plot b) are actually due to increased beam width rather than more serious artefacts such as side lobes. In order to confirm this hypothesis the main artefact in each echodynamic needs to be categorised. The LMS based echodynamic categorisation method discussed previously will be employed.

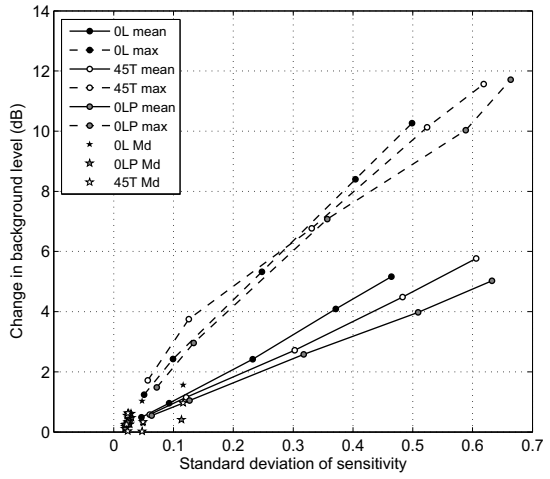

(a)

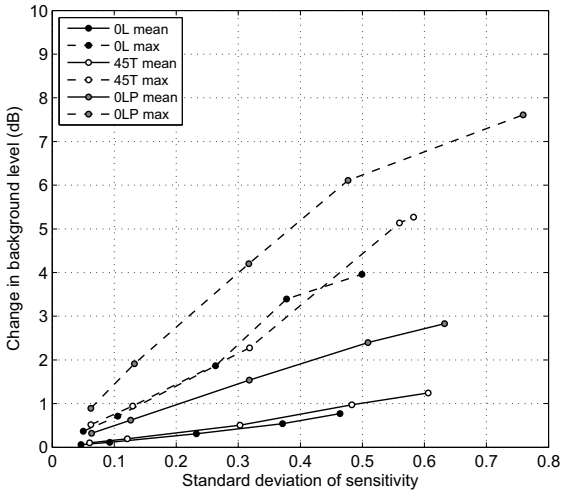

(b)

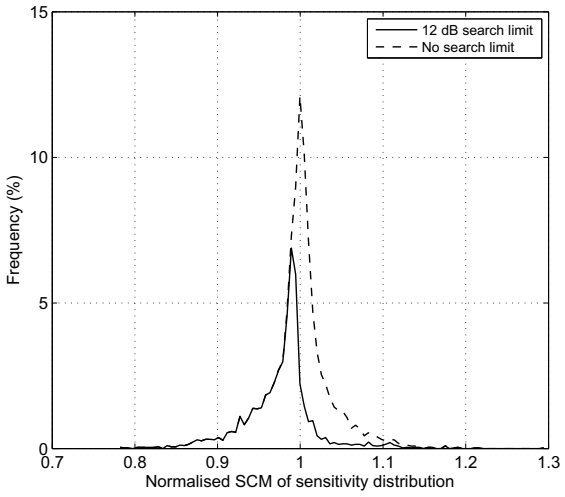

(c)

Figure 5.5.1: The results from simulations varying element sensitivity a) plot of maximum change in background level for the 0L, 0LP, and 45T beam types. The stars included in the plot represent the results from experimentally measured sensitivity profiles, Md b) plot of maximum change in background level with the comparison limited to within 12 dB of main beam b) the distribution of results from the 0L beam based upon normalized SCM of sensitivity.

5.5.1.1 Echodynamic categorisation

The results of applying LMS signal decomposition to the echodynamics produced from the 0L beam are presented in Figure 5.5.2. Plot a) shows that standard deviation values <0.2 do not result in the enlargement of existing, or the formation of additional, side lobes. This result supports the theory that many of the large changes recorded are actually due to broadening of the main beams. Plot b) shows that side lobe artefacts that come within 12 dB of the main beam account for a small fraction of the total number of realisations made of this beam type.

It also demonstrates that in the vast majority of cases enlarged side lobes are generated with a normalized SCM greater than one. This finding agrees with earlier discussion on the connection between main beam broadening and SCM values less than one as the LMS signal decomposition process would classify these types of echodynamics as a change in background energy. Figure 5.5.3 demonstrates the changes resulting from increasing levels of sensitivity variation.

Figure 5.5.2 plot c) shows that maximum variations of element sensitivity up to 0.2 do not result in a significant number of enlarged side lobes, and it also shows that barely any additional side lobes are formed at this level of maximum variation.

The LMS signal decomposition process has also been applied to the results from the focused 45 degree shear wave and the plane zero degree longitudinal beam; the results for these beams can be seen in Figure 5.5.4, and examples of the changes in echodynamics can be seen in Figure 5.5.3. The main conclusions that can be drawn from this data is that the 0LP beam appears to be equally resistant to the formation of side lobes as the 0L beam. This conclusion is supported by plot a) which shows that a maximum variation of 0.5 is required to cause the formation of side lobes, and at this level of variation they account for a similar number of results as the 0L beam. However, the 0LP beam differs from the other beam types as the model predicts that no side lobes are present for the beam generated with a uniform sensitivity profile.

In contrast both of the other beams have small side lobes present when a uniform sensitivity profile is used. The side lobes increase in size as the maximum variation, and therefore standard deviation, of the sensitivity profile increase. As there are no side lobes to begin with for the 0LP beam a larger increase in sensitivity variation is required to form defined side lobes, but when the side lobes appear they are more of a problem as the peak amplitude of the main beam is relatively low.

The results from the 45T beam are presented in plot b) in Figure 5.5.4. These results reveal that this beam does not exhibit the same resistance to the enlargement and formation of side lobes as the 0L beam. This is probably caused by the fact that the array is required to steer the beam a relatively large amount to produce the shear wave. The plot shows that as the maximum variation increases, enlargement of side lobes is a more common outcome than the formation of additional side lobes. With a maximum variation of 0.2 and below, the results from the 0L beam are predominantly limited to changes in background level, and main beam broadening, whilst significantly more results for the 45T beam have been classified as containing side lobe enlargement. Despite this the results in Figure 5.5.2 plot b) shows that the 0LP beam is the limiting factor due to its low peak amplitude.

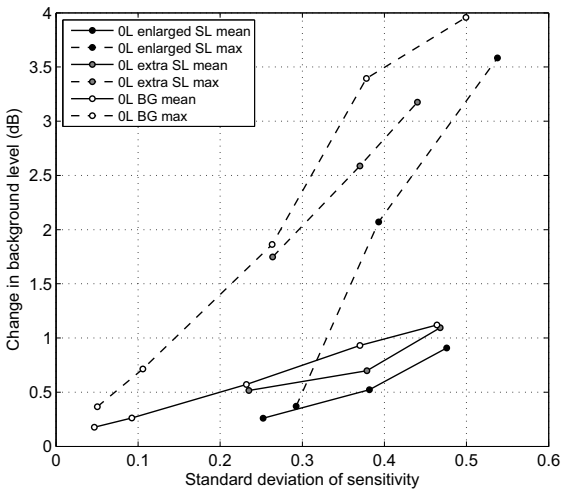

(a)

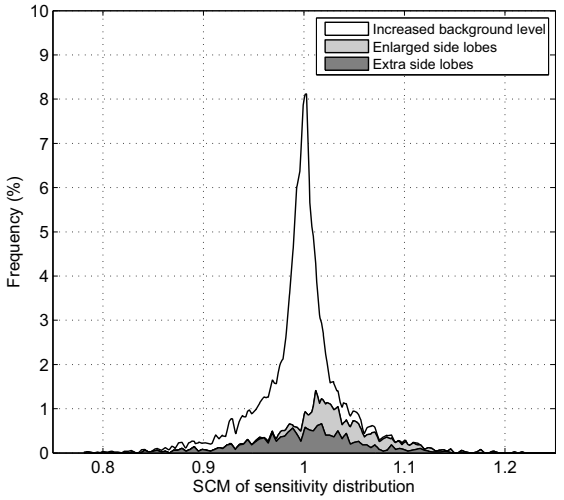

(b)

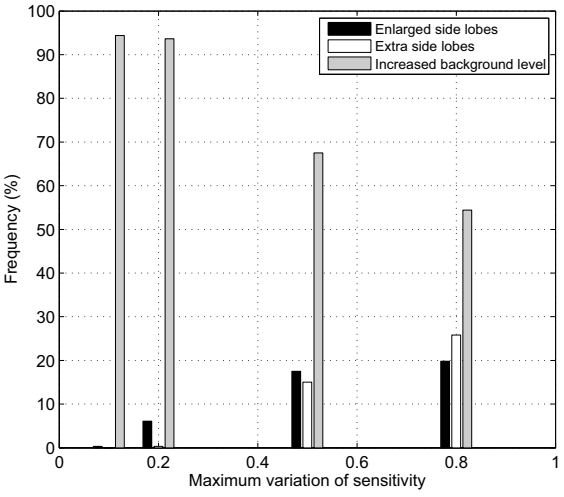

(c)

Figure 5.5.2: The result of applying LMS signal decomposition to the results from the 0L beam a) change in background level with the 12 dB search limit applied b) the distribution of results classified as containing enlarged side lobes (SL), extra side lobes (SL), and increased background levels (BG). The frequency axis is relative to the total number of simulations for that beam. c) the distribution of beam artefacts within each variation group. The frequency axis is relative to an individual simulation group of 1000 results.

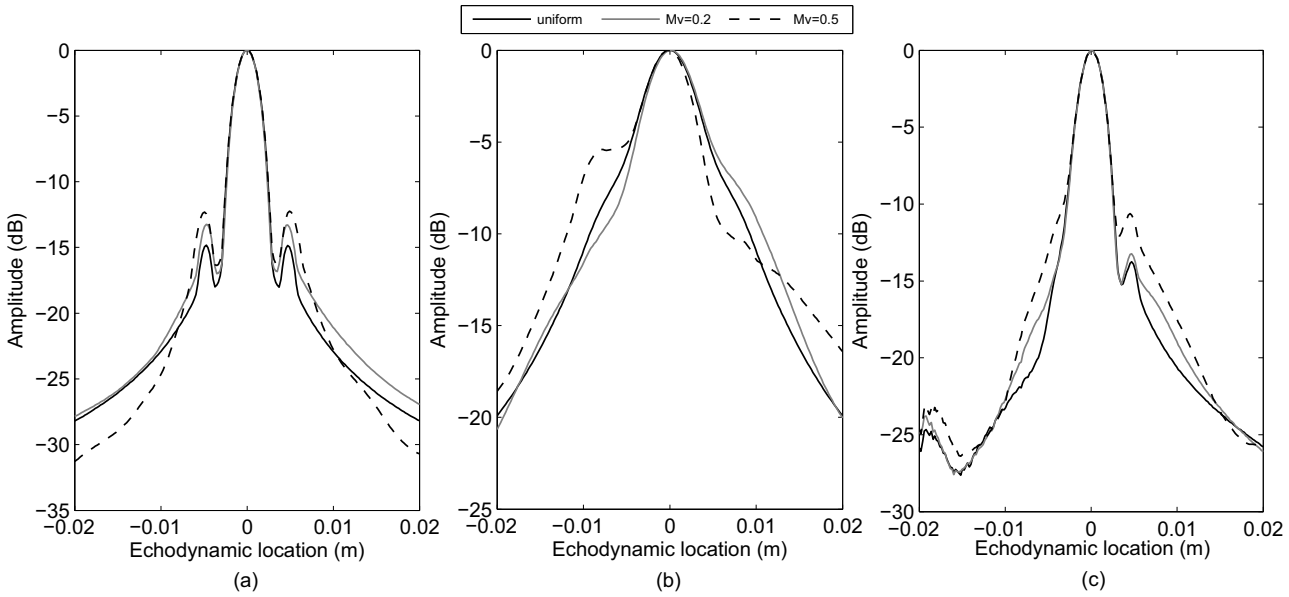

Figure 5.5.3: A comparison of the echodynamics produced by the sensitivity profiles that cause the largest changes in background level a) 0L b) 0LP c) 45T.

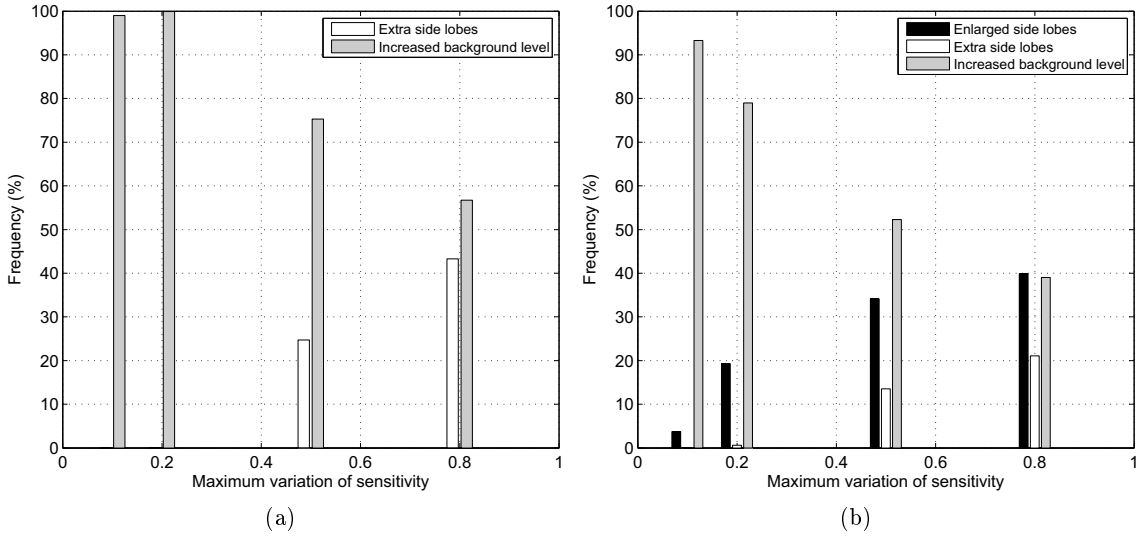

Figure 5.5.4: The result of applying LMS signal decomposition a) the distribution of beam artefacts within each variation group for the 0LP beam b) the distribution of beam artefacts within each variation group for the 45T beam. The frequency axis is relative to an individual simulation group of 1000 results.

5.5.2 Element firing delay

The results from variation of element firing delay on the three test beams selected can be seen in Figure 5.5.5. The plots present the changes in background level and peak amplitude, and suggest that the standard deviation of the firing delay is a good measure of the size of the change in background level, or peak amplitude, that will result. The experimentally measured profiles are plotted as stars in plots a) and c), and always result in a smaller change than the worst result using artificially generated profiles. This suggests that the simulations carried out cover a sufficiently broad region that any conclusions drawn from them will be conservative.

The reduction in peak amplitude due to firing delay is presented in plot c). There is a strong non-linear correlation between the reduction in peak amplitude and the standard deviation of the firing delay distribution. The link between peak amplitude and the standard deviation of the phase distribution of elements is more pronounced, as there is much less variation between the mean and maximum change for the focused beams. The plot shows that the maximum change in peak amplitude is larger for the 0LP beam than for the focused beams. The same behaviour is also seen in the change in background level shown in plots a) and b). The results in plot b) have been limited to changes within 12 dB of the peak amplitude in order to show the most significant results.

The main difference between plots a) and b) for the focused beams is a reduction in the size of beam artefacts as the results are effectively limited to only gross beam artefacts and broadening of the main beam. The change from a) to b) for the 0LP beam is similar to that for the focused beams for the mean value, but the maximum change reduces far less. This demonstrates that this beam is much more susceptible to large beam artefacts than the two focused beams, as previously discussed.

The reduction in peak amplitude observed in this study has been compared with the model suggested by Steinberg, introduced in section 5.4.3. Plot c) demonstrates that equation (5.4.6) is overly conservative, but the replacement of σ_ϕ with $0.75\sigma_\phi$ has been found to produce excellent agreement with the results from this study for the focused beams. The factor of 0.75 has been arrived at by best fit with the results. The effect of changes in peak amplitude is relatively insignificant in comparison to changes in background level as the worst possible result only reduces the peak amplitude by approximately 6 dB, and realistic firing delay variations are more likely to produce a reduction of the order of 2 dB.

The results suggest that the main deciding factor on the suitability of an array for use is the introduction of beam artefacts. Table 5.5.1 contains the maximum variation values for each beam type before the 10 dB criterion is broken for several different centre frequencies. For 2 MHz probes this suggests that a maximum firing delay of 14 and 25 ns can be tolerated by the plane and focused beams respectively before a change above 2 dB is possible. An acceptance criterion this low is not practical as it is the author's experience that it is not uncommon for arrays to contain elements with up to 25 ns of firing delay, and sometimes as high as 50 ns. This result can be compared with limiting values suggested by Steinberg of 50-125 ns at 2 MHz, expressed in table 5.4.1. This result shows that the limits proposed by Steinberg are significantly less stringent than those suggested in this study. The reason for this is that this study is attempting to place limits on phase error based on the worst possible reduction in beam quality, whilst Steinberg was interested in the mean result.

If the results in Figures 5.5.5 plot b) are reduced to those that are not caused by the main lobe, i.e. not results caused by beam broadening, the number of results that break the 2 dB threshold with a

maximum variation of 50 nanoseconds is reduced to 0 % for the 0L beam, and 0.03 % for the 45 T beam. Unfortunately the same type of filtering cannot be applied to the results from the 0LP beam as the main lobe is so wide that gross beam artefacts, such as side lobes, appear within the main lobe rather than to one side as happens with focused beams. From the simulations of the 0LP beam 43.3 % break the 2 dB limit when using a maximum variation of 50 nanoseconds.

Table 5.5.1: The maximum tolerable firing delay values before beam artefacts come within 10 dB of the main lobe peak amplitude. Linear interpolation has been used to to calculate the values for maximum variation.

Centre frequency (MHz)	2.0	5.0	7.5
Beam	Mv (ns)		
0L	25	10	6
0LP	14	7	5
45T	25	-	-

5.5.3 Dead elements

The results from the simulation of the 0L and 0LP beams for several aperture sizes at a centre frequency of 2 MHz can be seen in Figure 5.5.6. These plots contain the worst case result from the simulations of each aperture size with the group of dead elements in every possible location. The results from the focused beam exhibit very similar behaviour for both reduction in peak amplitude and change in background level. The reduction in peak amplitude appears to be in proportion to the reduction in the active area of the aperture for the 0L beam, although there is some non-linearity in the profile. The profiles extracted from the 45T beam (not presented) exhibit a larger shift from a linear relationship that increases as the aperture size increases. However, assuming a linear reduction in peak amplitude in proportion to the reduction in active area is a good approximation.

The 0LP beam follows similar behaviour for small apertures, but as the aperture gets larger the peak amplitude begins to increase with the number of dead elements. This behaviour appears to be due to the dead elements resulting in some unintended focusing of the beam.

The effect on peak amplitude is also governed by the location of dead elements in the aperture, but behaviour is different for each of the three beams simulated. The only common feature in the behaviour is that there is always a greater reduction in amplitude if the group is at the centre of the aperture rather than at the edges, and the difference between the two locations increases as the aperture size increases.

The effect of dead elements on background level is broadly similar for the three beams simulated. The two focused beams exhibit a non-linear increase in changes in background level with an increasing number of dead elements, and the 0LP beam shows similar behaviour until an aperture size of approximately 20 elements. As the aperture size increases further a shift in behaviour is seen that results in smaller changes in background level. The shift in behaviour begins at approximately the same aperture size as the change in behaviour for peak amplitude begins, but does not significantly affect change in background level until 20 % of the aperture is dead.

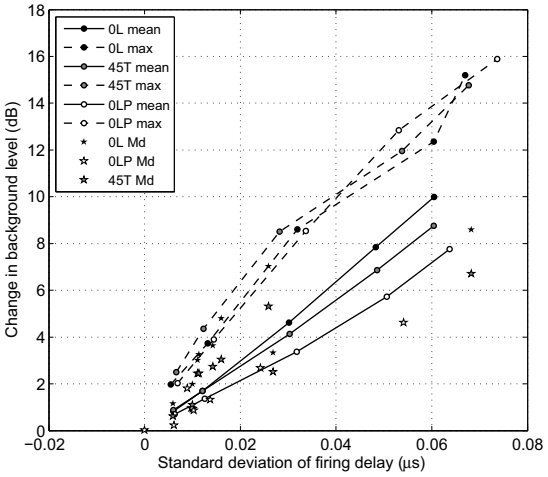

(a)

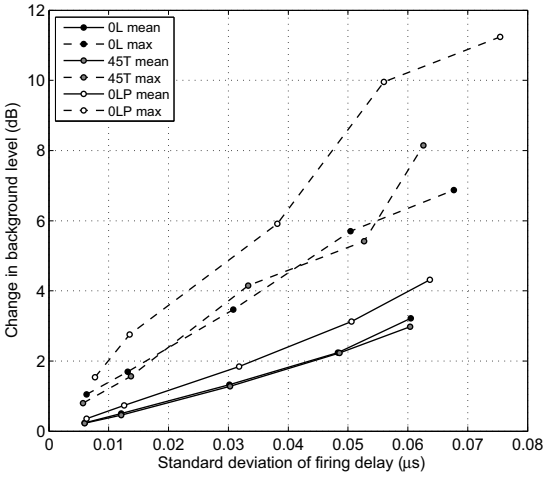

(b)

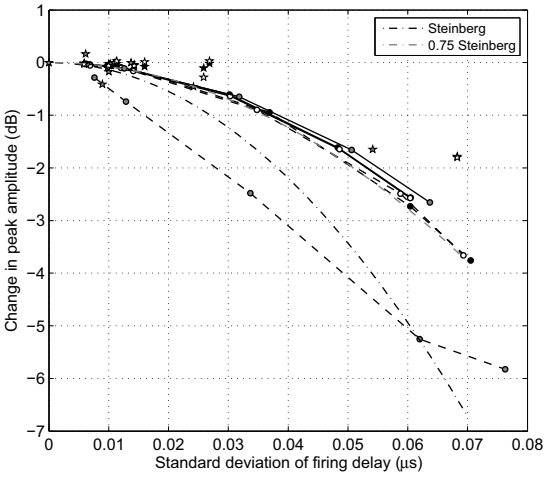

(c)

Figure 5.5.5: The results of simulations varying firing delay at a centre frequency of 2 MHz a) maximum change in background level b) maximum change in background level with comparison limited to within 12 dB of main beam c) reduction in peak amplitude (legend as plot a). The stars included in the plot represent the results from experimentally measured firing delay profiles.

The second stage of simulations has been carried out for the 0L beam using an aperture size of 30 elements and allowing a random distribution of 10 % of the elements in the aperture to be dead. The results from this set of simulations have shown that the maximum change in background level, out of the 1000 simulations carried out, is below or equal to the maximum change when using a contiguous group of dead elements. Based on this finding the results from the simulations of contiguous groups of dead elements can be assumed to be the worst case.

If the 10 dB criterion for changes in background level is applied to the results, the 0L, 0LP, and 45T beams would be limited to a maximum of 7 %, 4 %, and 5 % dead elements respectively. With these numbers of dead elements the reduction in peak amplitude is less than 1 dB, and is considered to be negligible. Applying any of these criteria to phased arrays does not pose the same problems as sensitivity and firing delay because the number of dead elements in an array is governed by damage done to the array in use rather than a limitation of the current manufacturing methods. That is to say it would be possible to implement a 4 % limitation on the number of dead elements in an aperture, but it is highly unattractive due to the financial cost of arrays. In addition to this, phased arrays have been used for a number of years to successfully detect and size defects in the field of NDE without such stringent limitations.

For example, Nageswaran [93] proposed to allow up to 12.5 % of an aperture to be dead before the aperture was deemed to be unsuitable for use. A study has been carried out by the Electric Power Research Institute (EPRI) using a 2D array with up to 20 % dead elements to investigate changes in defect response. The study found that the worst changes were an amplitude error of 5 dB and a location error of 2mm [98]. Clearly the criteria used thus far in this study appear to be too conservative and the results from the simulation of dead elements also show, as for both sensitivity and firing delay, that plane beams are more sensitive than focused beams to dead elements.

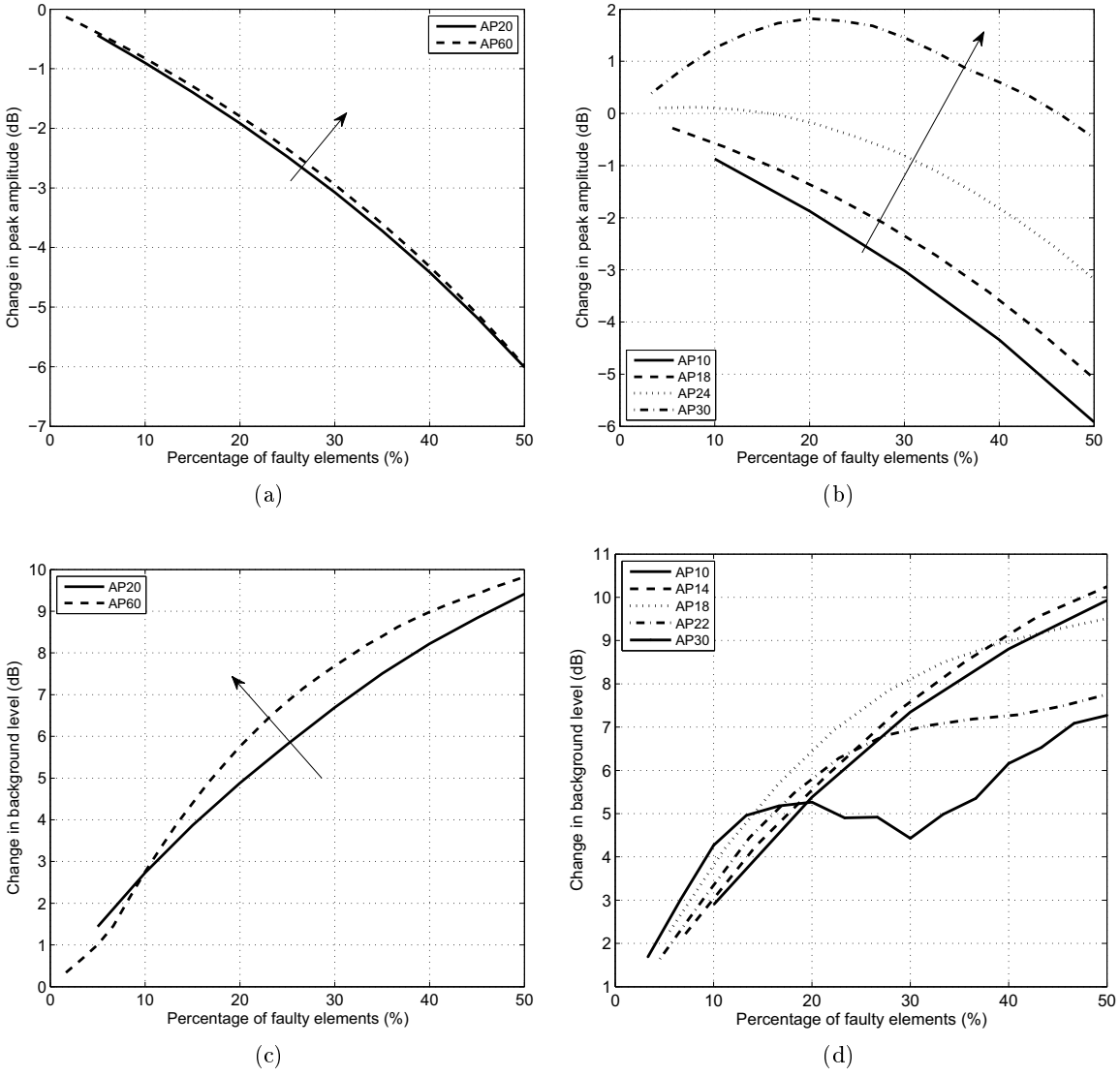

Figure 5.5.6: Plots of maximum change in background level, and peak amplitude, versus the percentage of dead elements in the active aperture. The reduction in peak amplitude for the a) 0L beam b) 0LP beam. The change in background level when using the 12 dB search limit for the c) 0L beam d) the 0LP beam.

5.6 Discussion

The analysis of results from the independent simulation of the effect of element sensitivity, firing delay, and dead elements have shown that the dominant effect on performance is changes in the background level of the ultrasonic field. Changes in peak amplitude have been shown to be very similar for all three beams, but the magnitude of change is insignificant in comparison to changes in background level. The analysis of results has focused on an acceptance criterion of a minimum of 10 dB difference between the amplitude of the main beam and the amplitude of any beam artefacts; this is based on the intent of BSEN12668 part 2 [6] but using acceptance criteria that better reflect the realities of using phased arrays. Application of this approach results in an impractical limit on firing delay of 14 ns difference between any element and the mean for its aperture, and a limit of 3.8 % dead elements. It is the authors' experience that pulse-echo sensitivity variations of +/-2 dB, and +/- 25 ns of firing delay is not uncommon with a modern phased array. The British and European standard that has been used for the acceptance criteria is designed for use with single element probes that are only likely to cause the generation of beam artefacts that break the 10 dB limit if the probe has been damaged or if the probe design is on the limit of suitability. The ultrasonic fields produced by phased arrays are by their nature far more complex than those of a single element probe, and the generation of side or grating lobes is an additional problem [79, 99, 80]. In a like-for-like comparison a purpose designed single element probe will always outperform a phased array, as the array is designed for flexibility and speed, at the cost of small compromises on performance.

Phased arrays have been used in the field of NDE for the inspection of critical components for more than a decade, including performance demonstrated inspections of pressurised components [20, 100, 73]. During all of this time no official calibration procedures have existed and to the authors' knowledge little work has been performed on the effect of variations in element sensitivity and firing delay, only the effect of dead elements has been investigated quantitatively. Nageswaran [93] concluded that up to 10 % of an aperture could be accepted to be dead, but suggested that contiguous groups of dead elements should be investigated further on a case-by-case basis using an array beam model. A white paper produced by the Electric Power Research Institute (EPRI) [98] has also shown that a 2D array with 20 % dead elements was still able to detect defects. These two studies as well as the collective experience of the NDE community demonstrate that the 10 dB criterion is too conservative and based on this assertion a reduction of the acceptance criterion to 8 dB is proposed. A 2 dB reduction has been chosen as it is a smallest change from the 10 dB criterion which is likely to affect the limits on element performance variation significantly. Table 5.6.1 and 5.6.2 includes the results of applying the 8 dB criterion and shows that the tolerable limits would be reduced to a pulse-echo sensitivity range of +/- 0.5 (+7 dB and -12 dB), +/-32 ns for firing delay at 2 MHz, and 9 % for dead elements. It is more practical to impose these limits on arrays, and they better reflect the realities of ultrasonic fields produced by arrays.

Steinberg's conclusion that the maximum tolerable phase error can be found by ensuring that the product of transducer bandwidth and sample period (Bt_0) is in the range 0.1-0.25 has been applied to the results from this study by substituting sample period with maximum variation. The results of this can be seen in Table 5.6.2 and demonstrates that Bt_0 remains approximately constant regardless of the beam angle and centre frequency. The results from a plane 45 degree shear wave using a zero degree array angle and an aperture of 30 elements have also been included to demonstrate that the

Table 5.6.1: Results summary for sensitivity and firing delay at a probe centre frequency of 2 MHz when allowing a minimum of 8dB between the amplitude of beam artefacts and the main lobe.

Beam	Sensitivity		Dead elements
	Std dev	Mv	Percentage of aperture
0L	0.5	1.0	13.5
0LP	0.3	0.5	9.0
45T	0.46	0.7	11.7

Table 5.6.2: Bt_0 values for several centre frequencies when allowing a minimum of 8dB between the amplitude of beam artefacts and the main lobe.

Centre frequency (MHz)	2.0		5.0		7.5	
Beam	Mv (ns)	Bt_0	Mv (ns)	Bt_0	Mv (ns)	Bt_0
0L	57	0.057	19.9	0.050	13.3	0.050
45T	48	0.048	-	-	-	-
0LP	32	0.032	14.6	0.037	8.7	0.033
45TP	-	-	14.8	0.037	-	-

results are independent of the model configuration. The average value for the focused beams is 0.051, and 0.035 for the plane beams. If the value for the focused beams is converted to a Bt_0 value that uses sample rate, the average value rises to 0.104, as the maximum error for a sample period of T is T/2. This value agrees with the minimum value suggested by Steinberg of 0.1, and suggests that this rule could be applied universally.

The 32 ns limit of firing delay for an array with a 2 MHz centre frequency and 50 % bandwidth appears to be quite small relative to the experimental measurements of firing delay of up to 50 ns. It can be argued that experimental measurement of firing delay using pulse-echo signals, as used in this study, is actually measuring differences in phase twice. This assumes that differences in transduction times between elements occur equally in transmit and receive. If this is the case then the maximum experimental measurements are actually 25 ns, so the 34 ns limit is quite conservative. However, as the bandwidth or centre frequency of the transducer increases, the limit decreases. If this limit is found to be too low one solution would be to limit the array to producing focused beams as this raises the criterion by a factor of 1.5.

5.7 Experimental measurements of element non-uniformity

The limits on element performance predicted via modelling can be compared to experimental measurements of typical variations in element parameters to reveal how stringent the limits are. Experimental measurements of element sensitivity and firing delay can be recorded using a simple immersion arrangement shown in Figure 5.7.1. Each element in the array can be pulsed and the echo from the granite surface recorded at a time T, and with an amplitude of A. The variation in amplitude and arrival time can then be used to record element sensitivity (S) and relative firing delay (FD) using equations (5.7.1) and (5.7.2).

$$S = \frac{A}{\overline{A}} \tag{5.7.1}$$

$$FD = T - \overline{T} \tag{5.7.2}$$

where bar denotes the arithmetic mean taken over all measured elements.

This method has been used to measure eight different arrays with centre frequencies between 2 and 4 MHz. The arrival time (T) has been calculated via detection of the first positive to negative zero crossing point within the toneburst generated by each element. The results can be seen in Figure 5.7.2, and shows that the vast majority of results are within the sensitivity and firing delay ranges of 0.9 to 1.1 and -10 to 15 ns respectively. The experimental results also demonstrate that the distribution is bell shaped in each case, although the relative firing delay values are skewed toward positive values. The Monte Carlo simulations discussed in previous chapters use a uniformly distributed random number generator to vary element performance. Based on the experimental results it appears that a normally distributed random number generator would be a better representation of parameter variation. This change would make a significant difference to the maximum acceptable parameter variations as the limit is dictated by outlying results, which would be far less likely to occur when using a normal distribution.

The measurement accuracy of the experimental system can be predicted by consideration of known sources of error in the experiment. The arrangement uses a granite measurement plate that is flat to within 2 µm and steel setting blocks that are of equal length within 3 µm. Variation in setting block length will be ignored as the effect of the error will vary along the array and is considered small.

The arrival time of the surface echo (T) is a function of the length of the steel setting blocks (D), variation in flatness of the granite plate (μ) and wave speed (δ), and data sample period (P).

$$T = \frac{2\,(D \pm \mu)}{c \pm \delta} \pm \frac{P}{2} \tag{5.7.3}$$

Assuming that wave velocity is does not vary locally and mean variation in granite plate flatness is zero over the array length , $\overline{T}$ can be approximated as:

$$\overline{T} = \frac{2D}{c \pm \delta} \tag{5.7.4}$$

Maximum error in relative firing delay can be calculated as:

$$E = \frac{1}{2}\left(\frac{2\mu}{c-\delta} - \frac{-2\mu}{c+\delta}\right) + \frac{T}{2} \tag{5.7.5}$$

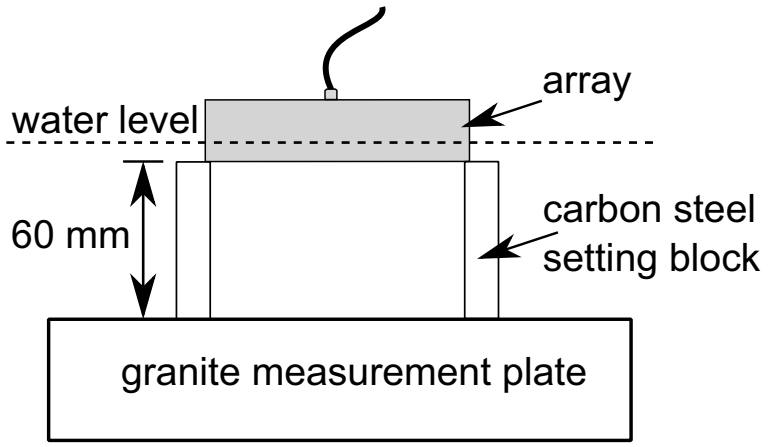

Figure 5.7.1: The experimental arrangement used to measure element sensitivity and phase.

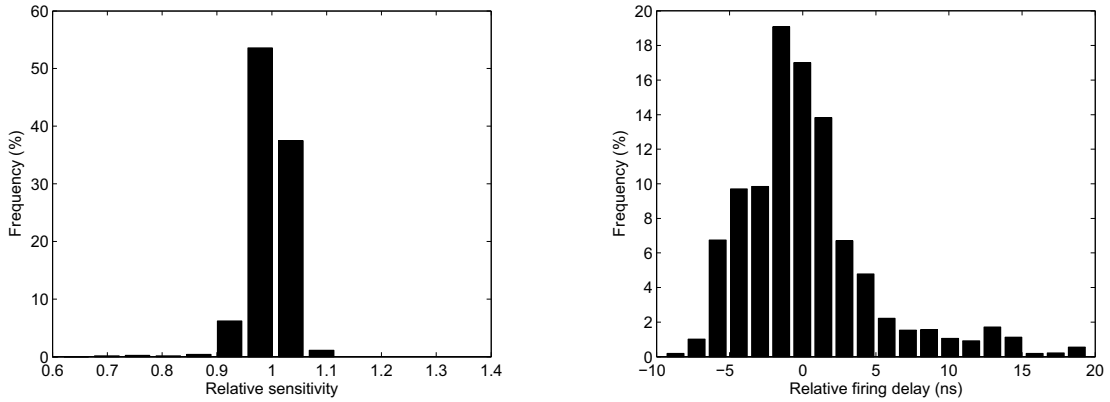

(a) (b)

Figure 5.7.2: The distribution of measured element a) sensitivity and b) phase.

which simplifies to:

$$E = \frac{2\mu c}{(c-\delta)(c+\delta)} + \frac{T}{2} \tag{5.7.6}$$

Equation (5.7.6) results in measurement error of 7.7 ns assuming a sample rate of 100 MHz and a maximum variation in water temperature of 2 degrees. The change in the wave velocity in water has been calculated using the 148 point equation suggested by Bilaniuk and Wong [101].

To quantify the systematic measurement error achieved in the experiment two of the arrays were measured 20 times each. Analysis of the results reveals that the achieved systematic error was less than 5 ns. Although this error is a significant proportion of the values that the experiment is attempting to record, it is low enough to allow the range of relative firing delay values exhibited by commercial arrays to be quantified.

5.8 Extension to multi-dimensional Monte Carlo method

The modelling methods and results reported have considered the effect of element parameters independently. Whilst this approach is useful to understand the dependence of array systems on each parameter, a better approach to decide upon parameter limits is to model all variations in parallel. The disadvantage of this approach is that the number of required simulations to cover a meaningful amount of the multi-dimensional space described by the considered parameters increases significantly. However, the simulation and experimental results presented in previous sections have demonstrated that the most significant parameter is firing delay. The limits for firing delay are close enough to values experimentally measured in commercial arrays that the combination of all variations in element performance may result in unpractical limits on element performance. This may ultimately require optimisation, for example delay laws modified to account for firing delay. Commercial arrays have been shown to exhibit relative sensitivity variations in the region of ± 0.1, and dead elements are sufficiently uncommon that placing more stringent limits on the number of dead elements than those presented previously would not be unpractical to implement. Therefore, by placing prescribed limits on element sensitivity and dead elements that are lower than those previously predicted, larger variations in firing delay can be accommodated. This approach also has the benefit that only a single parameter requires simulation over a range of values, thereby reducing computation requirements. The Monte Carlo simulations have been completed using a normally distributed random number generator to better reflect the parameter variations that will be encountered experimentally.

5.8.1 Data analysis

The method of results analysis remains largely unchanged from section 5.4, the only change is the method used to add a best fit profile to the raw Monte Carlo simulation results. Previously the profile has simply been added to the results by plotting the maximum result against the mean standard deviation of the varied parameter. This method is extremely conservative as the profile is controlled by the outlying simulation results. Instead a method of selecting a profile that excludes a very small fraction of the outlying simulation results will be used.

A line of best fit is added to the results based on an empirical Cumulative Distribution Function (CDF) calculated using the Kaplan-Meier estimate of the CDF [102, 103]. The Kaplan-Meier estimate is commonly used to produce life tables that predicted the number, or proportion, of failed items at a specified time. For this study the Kaplan-Meier estimate will be used to predict the probability of a given change in background level being exceeded.

The Kaplan-Meier estimate has been used to calculate the CDF for each simulation group based on the change in background level introduced as a result of the variation in element performance; recall that each simulation group is composed of the results from many realisations of the echodynamic produced by the array after the random application of element performance variation in the range $\pm$Mv. For each simulation group an eCDF is produced that estimates the probability of a given change in background level being exceeded. The method of adding a line of best fit previously used always selected the worst possible result for each simulation group, i.e. the probability of a smaller change background level being observed, for a fixed Mv value, is close to one assuming sufficient realisations are considered. By selecting a smaller probability outlying simulation results are excluded which otherwise has a significant effect of the maximum change is background level, but are extremely

unlikely to occur.

The CDF function is based on an incomplete data set so it is good practice to estimate the variance of the function, and use this variance as an estimate of the confidence bound for the eCDF. Greenwood's formula [104] is a common estimator used for this purpose. The variance estimate produced using Greenwood's formula is used as a confidence bound for the CDF, calculated using the Kaplan-Meier estimate. For each simulation group the 99% confidence interval has been located on the CDF, with the confidence bound included. This method results in less than 1 % of the outlying simulation results being excluded from each simulation group. An example CDF function is shown in Figure 5.8.1, plot a).

In summary, a line of best fit is added to the results by plotting the mean standard deviation of the varied parameter against the maximum change in background level estimated to a probability of 0.99, i.e. in 1 % of cases the chosen level of background level has been exceeded. This significantly reduces the Mv value required before changes in background level above 2 dB are observed. This profile describes the relationship between the change in background level and the standard deviation of the element performance parameter, an example is shown in Figure 5.8.1, plot b). This result is much closer to a linear profile than those previously shown.

Previous simulations have only allowed one parameter to vary, for which results presentation was straightforward. The results produced when allowing all aspects of element performance to vary can be presented using a three dimensional plot described by the standard deviations of element sensitivity and firing delay against the change in background level. The introduction of dead elements to the simulations is taken into account by settings the sensitivity of dead elements to zero. Hence the variation of all three aspects of elements performance can be represented by considering only element sensitivity and firing delay.

An example result is shown in figure 5.8.2. A three dimensional plot is shown in figure 5.8.2 a). From the results it is clear than although there is significant spread due to the effect of element sensitivity, the limit on maximum firing delay variation is not a function of element sensitivity for a fixed maximum variation value. As with the 1D Monte Carlo results the standard deviation in element firing delay and change in background level can be used to separate the simulation groups. This means that it is possible to interpolate between the results from increasing maximum firing delay variations using the same methodology as the results from the 1D Monte Carlo simulations. This is demonstrated by the 2D plots shown in figure 5.8.2 plot b) and c).

5.8.2 Results

Multi-dimension Monte Carlo simulations have been performed for the plane and focused zero degree longitudinal and 45 degree shear waves at three different centre frequencies. The model configuration is the same as that described in figure 5.3.2 and table 5.3.1, and again aperture sizes of 20 and 40 elements have been used for the plane and focused beams respectively. The model has been configured to use maximum variations in element sensitivity of 0.2 and four/one randomly distributed dead elements for the focused and plane beams respectively. Several simulations groups using increasing levels of

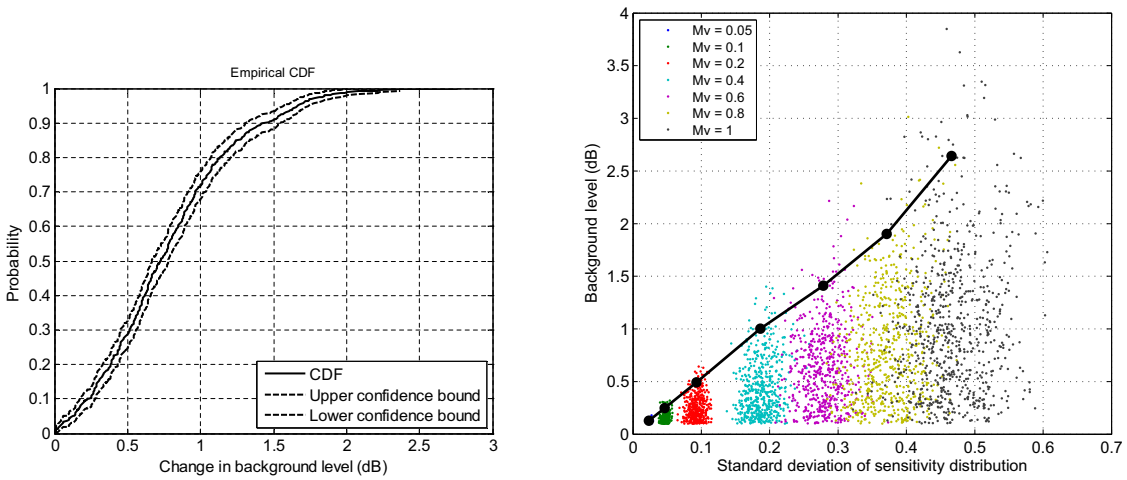

(a) (b)

Figure 5.8.1: A plot of an example a) CDF and associated confidence bounds b) a profile based on CDFs overlaid on the original data points.

element firing delay have been simulated, and a profile has been added to the results as described in the previous section.

The predicted maximum levels of firing delay variation are presented in Table 5.8.1, along with the associated Bt_0 values. The results show that the Bt_0 values remain approximately constant across the simulated centre frequencies, and the limits for the plane beams are approximately half of those for the focused beams. This demonstrates that the parameter Bt_0 can be used to predict limits for variation in element performance for transducers of different centre frequencies and bandwidths. The results suggest a limit of 30 ns on relative element firing delay, and a single dead element (5 % of aperture), for the model configurations considered. However, further data is required to prove that this is applicable to other combinations of element and aperture sizes.

Further plane beams have been simulated using different element and aperture sizes, and a variety of longitudinal and transverse beam angles. Details of the model configuration can be found in Table 5.8.2 and the associated predicted maximum variation values are presented in Table 5.8.3. Again a fixed maximum variation in element sensitivity of 0.2 has been used, and a number of randomly located dead elements equal to 5 % of the aperture size down to a minimum of one.

The results from the different element sizes are plotted against aperture sizes in Figure 5.8.3. The mean results, across the different beam types have been plotted, and vertical error bars are shown using the minimum and maximum results for each aperture size. Linear lines of best fit have also been included for the two element sizes using a least squares approach. There is a clear linear correlation between the increasing maximum firing delay values and increasing aperture size. The profiles for the two element sizes are vertically offset with the profile for the smaller element size above the larger element size; the two profiles are also converging and intersect the Y axis within 5 ns of one another. This is an intuitive result as the smaller the number of elements that make up an aperture the greater the contribution each element has to the beam produced. Thus for a given physical aperture size the aperture will be more resilient to variation in element performance for smaller element sizes.

The results show that a limit of 30 ns and 5 % dead elements appears applicable across the transducers, aperture sizes, and beam types considered, and hence a Bt_0 value of 0.03 is recommended. As

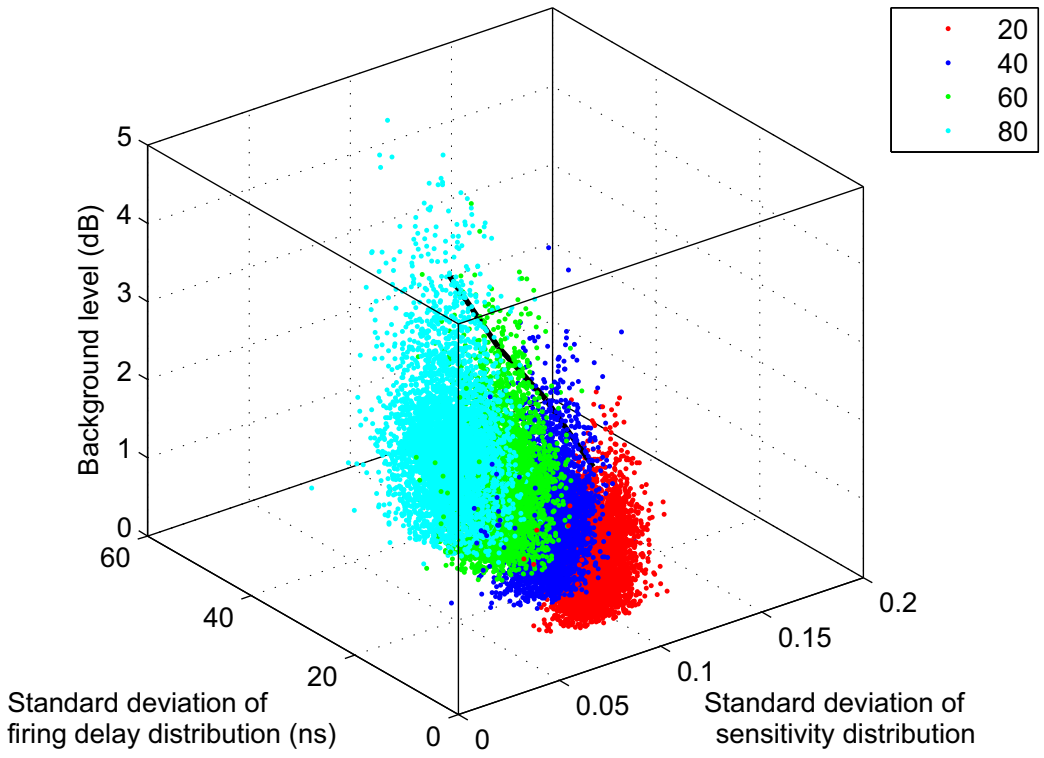

again

(a)

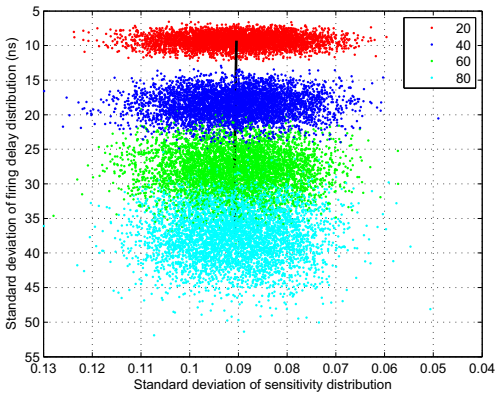

(b)

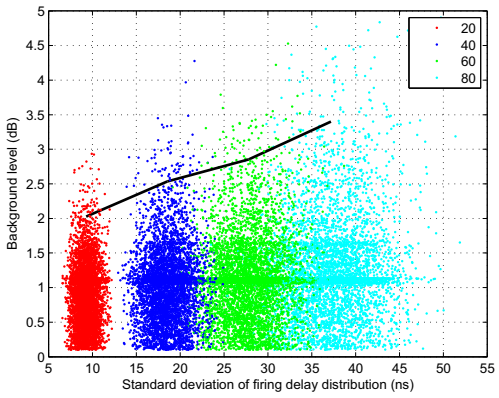

(c)

Figure 5.8.2: Example result from multi-dimensional Monte Carlo simulations. This result is for a plane zero degree longitudinal beam simulated with the following maximum parameter variations: 5 % dead elements, and 0.2 relative sensitivity. a) a 3D plot of the results b) a 2D plot of the standard deviations of element sensitivity against firing delay c) a 2D plot of the standard deviation of element firing delay against background level. The legend describes the maximum firing delay variation (ns).

a result of the correlation between aperture size and maximum firing delay, aperture sizes below 10 elements are not recommended.

The exception to this recommendation on the number of dead elements is when the dead element is located at the end of the aperture. In this situation the effect of the dead element is only to introduce an error in probe index point, and therefore a plotting error of the order of the element pitch. In most applications this could be tolerated.

For focused beams a higher limit on dead elements of 10 % of the aperture is recommended. This is a more practical limit for focused beams as aperture sizes are likely to be larger than those used to generate plane beams, and the recommended limit on firing delay of $0.03Bt_0$ is significantly below the tolerable limit for focused beams.

Table 5.8.1: Limiting values for maximum firing delay variation and associated Bt_0 values when varying all parameters in parallel. In all cases a maximum variation in element sensitivity of 0.2 has been used. For the focused beam four dead elements have been randomly distributed, and one element for the plane beams.

Centre frequency (MHz)	2.0		5.0		7.5		
Beam	M_v	Bt_0 $(\times 10^{-3})$	M_v	Bt_0 $(\times 10^{-3})$	M_v	Bt_0 $(\times 10^{-3})$	$\overline{Bt_0}$ $(\times 10^{-3})$
0L	74	74	28	70	21	79	74
45T	70	70	29	73	18	68	70
0LP	35	35	11	28	-	-	32
45TP	39	39	13	33	-	-	36

Table 5.8.2: Modelled element sizes and beams for extra plane beam simulations a) element specifications b) simulated beams.

Parameter	Value	
Array Type	A	B
Centre frequency (MHz)	2.0	2.0
-6 dB bandwidth (%)	50	50
Element pitch (mm)	0.75	1.0
Element gap (mm)	0.20	0.25

(a)

Beam angle (degrees)	Array angle (degrees)	Wave mode (L/T)
0	0	L
60	4	L
45	7	T
60	15	T

(b)

Table 5.8.3: Limiting values for maximum firing delay variation (M_v) when varying all parameters in parallel. In all cases a maximum variation in element sensitivity of 0.2 has been used, and 5 % dead elements (rounding down).

Aperture	10		20		30		40	
Element type	A	B	A	B	A	B	A	B
Beam	M_v (ns)							
0LP	32	31	40	32	62	58	>80*	>80*
60LP	34	32	44	40	60	56	67	66
45TP	36	36	41	41	59	55	76	>80*
60TP	32	32	43	37	57	50	59	62
$\overline{M_v}$	34	32	42	38	60	55	72	75

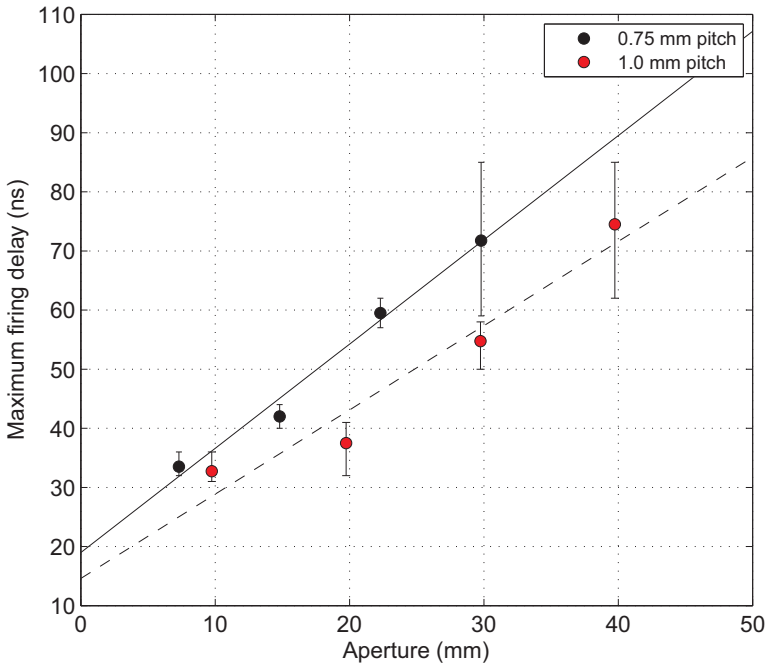

Figure 5.8.3: A plot of the mean maximum tolerable firing delay values for the two element sizes and plane beam types displayed in table 5.8.3. Error bars indicate the maximum and minimum results, and the plotted lines are fitted to the results using minimisation of least square errors.

5.9 Summary

The effect of element sensitivity, phase, and faulty elements has been investigated using a 2D array beam model to carry out Monte Carlo simulations. The results from these studies have shown that the two parameters most affected by changes to element properties are the peak amplitude of the ultrasound produced by the array, and the presence of beam artefacts. These two parameters have been investigated and beam artefacts have been found to be the dominant feature.

The results have been analysed by finding the largest level of variation in each property that results in beam artefacts that have an amplitude that is within 8 dB of the peak amplitude of the beam. This has led to a limit on element sensitivity of +/- 50 % relative to the mean level of sensitivity for that aperture, and a limit on the number of dead elements of up to 9 % of the aperture size. The effect of element firing delay has been shown to be frequency dependent, but provided that the product of probe bandwidth and maximum phase error is below 0.035 then beam artefacts will be at least 8 dB lower in amplitude than the main beam.

The results have been further extended by considering the effect all three aspects of element performance in parallel have on beam forming performance. To facilitate this change the distribution in element property variation has been altered from a uniform to a normal distribution. This change is supported by empirical observation of variation in element properties. These changes have resulted in a recommendation of limits on element performance presented in table 5.9.1. It is proposed that the limitations can be used as acceptance criteria for probe integrity testing. This approach provides a means of replacing probe check procedures required by calibration routines currently used by industry for pulse-echo ultrasonic inspection, but less well suited to FMC based inspections.

Table 5.9.1: The proposed limits of variation in element performance.

Element property	Plane beam	Focused beam
Relative sensitivity	±0.2	
Relative firing delay (Bt_0)	±0.03	
Dead elements (%)	5	10

6 A Calibration Routine for FMC: Combined probe checks and inspection sensitivity

The previous chapter presented a methodology and associated results for determining the maximum variation in element performance that can be tolerated prior to deterioration in beam quality to the point where the array is no longer fit for purpose. These limits are essential for the first stage of inspection calibration, the array integrity check. The next stage for array calibration is to perform a baseline set of measurements that can be used to monitor transducer performance and set the inspection sensitivity, and finally combined equipment checks. These requirements can be split into three stages: a baseline set of measurements used to monitor element performance known as the combined probe check, a check of combined system performance (e.g. amplifier linearity) known as the combined equipment check, and a calibration scan that is used to relate the results of an FMC inspection to the response from known calibration reflectors.

6.1 Combined probe checks

An important part of inspection calibration is re-calibration throughout the inspection duration. This is particularly important for automated inspections as the inspection duration is often several days. The array integrity check procedure developed for FMC requires that the array be removed from its wedge and measurements made in immersion. Repeating the probe checks in immersion is not an attractive option as this requires that the probe be removed from the manipulator and have its wedge removed. A more attractive approach is to monitor transducer performance whilst the array is still mounted on its wedge and attached to the manipulator. This would allow probe performance to be monitored at regular intervals throughout the inspection with little impact on inspection duration, and the process could be automated.

Changes in element performance can be detected by monitoring the amplitude and arrival time of any consistent signal that can be reacquired repeatably. One of the most reliable signals to monitor is the echo from the array's wedge bottom surface, or in the case of an immersion inspection, the echo from the top surface of the component at a specific location. These reflectors are independent provided that the wedge is not worn significantly during the inspection, or the probe location is accurately controlled in the immersion case. If a contact array was to be used then a signal from the component geometry, e.g. back wall echo, could be used. However, this type of signal is much more susceptible to errors due to changes in coupling layer thickness and efficiency, and any variation in component geometry.

6.1.1 Methodology

Element performance can be can be measured and subsequently monitored using the following steps:

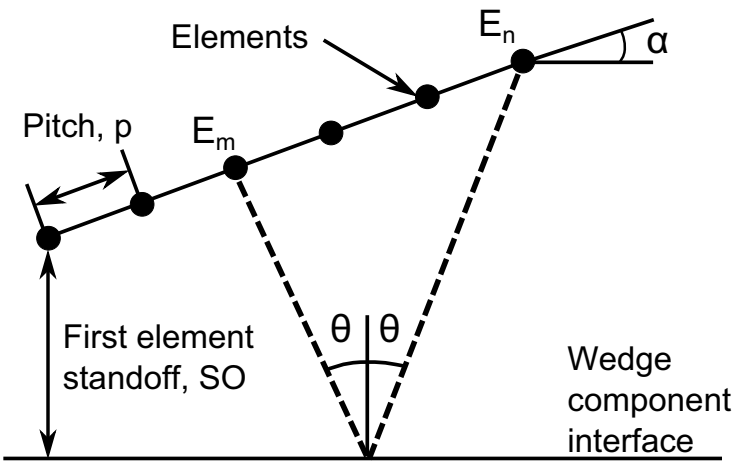

Figure 6.1.1: A diagram of the co-ordinate system used to calculate the expected time of arrival of an echo from the wedge-component interface.

- Perform an array integrity check in immersion using a constant range reflector to record relative element sensitivity and relative firing delay (FD).
- Compare recorded sensitivity and FD with limiting values proposed in chapter 5.2. If the array meets the requirements it is eligible to be used to conduct the inspection. If any elements have a sensitivity value outside of the required range the elements are classified as 'dead'. These elements should not be excluded from the inspection as they will still contribute to the beam produced by the aperture. However, any FD values outside of the prescribed range are classified as 'dead' and should not be used to beam form, as the delay law error is more likely to cause beam artefacts than variation in element sensitivity.
- The array should be attached to the wedge that will be used during the inspection.
- To obtain a set of baseline echoes from the array's wedge a frame of FMC data should be recorded at the highest possible sample rate directly following the array integrity check. From the FMC data pitch-catch reflections from one element, to the bottom surface of the wedge, to a second element can be extracted. Many such signals should be selected such that each element is used as a transmitter.
- The previous step can be repeated at regular intervals throughout the inspection and the amplitude and arrival times compared to the baseline data set.
- If any of the amplitudes or times change then the changes should be added to the value recorded in the array integrity check, and the total value compared to the limiting values.
- If the element is now classed as dead the inspection can only continue if the total number of dead elements is not prohibitive.

For this approach to be employed, a method of selecting and analysing the pitch-catch signals that is robust to any electrical noise must be developed. The first step is to select the pitch-catch combinations and calculate the time of arrival of the reflection. Consider the arrangement shown in Figure 6.1.1.

The angle between the vertical and ray path (θ) between elements can be calculated as follows:

$$\theta = \arctan\left(\frac{(m-n)\,p\cos\alpha}{2SO + (m+n-2)\,p\sin\alpha}\right) \tag{6.1.1}$$

The travel time between the two elements can then be calculated:

$$T = \frac{1}{c\cos\theta}\left(2SO + (m+n-2)\,p\sin\alpha\right) \tag{6.1.2}$$

where all symbols are described in Figure 6.1.1, c is the longitudinal wave speed in the wedge material, and T is the travel time in the wedge.

The accuracy of this method of monitoring element performance has been quantified using the commercial modelling package CIVA [70] to predict the scattering of the ultrasonic waves generated by a single element and received by a second element. Array elements with the same properties as the first entry in table 5.3.1 in chapter 5.2 have been modelled. A Rexolite wedge with a 25 degree inclination is also included in the simulation. The defect response module of CIVA does not support the calculation of surface echoes alone, a defect must be present in the model e.g. SDH or rectangular planar flaw. Instead the model has been configured such that the "component" in the model is the same material as the array's wedge and a large rectangular flaw has been placed in the horizontal plane where the bottom surface of the wedge should be located. Figure 6.1.2 presents a diagram showing the model configuration used. The response from the rectangular flaw is then predicted using Kirchoff theory. Edge effects from the flaw have been omitted from the model by including a probe sensitivity region that excludes the defect edges. The defect is also wider than the array element in the plane orthogonal to the active plane of the array.

The CIVA model has been used to predict the reflection from the bottom of the wedge for pitch catch reflections between elements 1-2 and 55-56. Changes in element performance have been added by introducing small time delays to the elements, and reducing the amplitude of the elements. The A-scans are then analysed by calculating the sum of the rectified time history and recording the location of the first negative to positive zero crossing point. The change in element FD is simply the change in zero crossing arrival time, and change in sensitivity is the ratio of the A-scan sums. This method has been selected as it effectively measures the change in average element amplitude and thus makes the result less sensitive to quantisation and time sampling errors. The results of analysing the A-scans predicted by CIVA are shown in Figure 6.1.3. The results show that in both cases there is zero error in the extracted change in sensitivity and FD. The time histories produced by CIVA are produced with a sample rate of 100 MHz, the same value as will be used experimentally.

The sensitivity of measurements to noise in the time histories can be assessed by artificially adding random noise to the simulation results. A uniformly random number generator has been used to produced a random number history of a prescribed Root Mean Squared (RMS) value. The noise is superimposed on the CIVA time histories, and the effect on the accuracy on the recording of element sensitivity and timing can be assessed against the RMS level of noise. This is expressed as a signal to noise ratio (S/N) defined as the ratio of the maximum amplitude in the toneburst to the RMS noise level.

A simple Monte Carlo simulation has been used to investigate a range of S/N values, with 1000 realisations at each S/N value. The results have been analysed by extracting the mean and 5 and 95 % confidence intervals using the Kaplan-Meier estimate for an empirical cumulative distribution

function [102]. The results are shown in Figure 6.1.4 for the extracted changes in sensitivity and FD, and demonstrate that there is little difference between the two pitch-catch element combinations. Measurement of relative sensitivity is extremely robust to noise but FD less so. In order to ensure the error in FD measurement is below +/- 5 ns the time history S/N must be at least 50 dB. However, initial experimental trials have shown that a second parameter dominates the accuracy of the technique, variation in wave velocity due to temperature change.

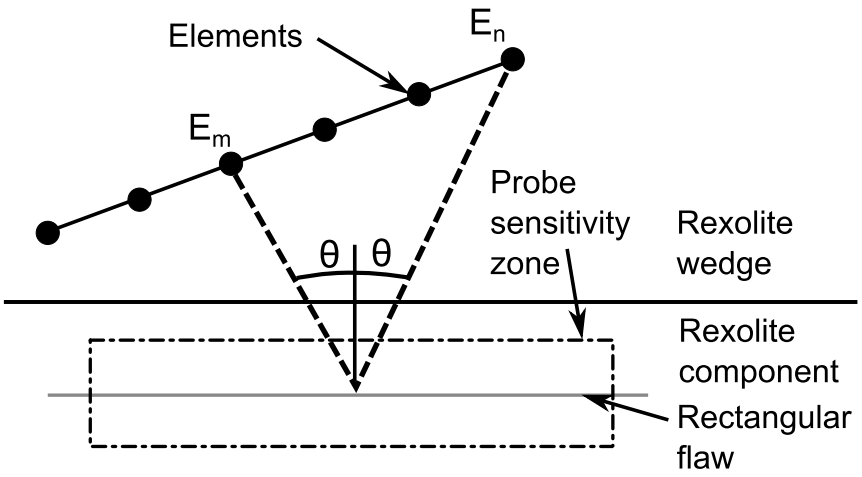

Figure 6.1.2: A diagram of the CIVA model configuration used to predict time histories for the reflection of a wave generated by one element within an array and received by a second.

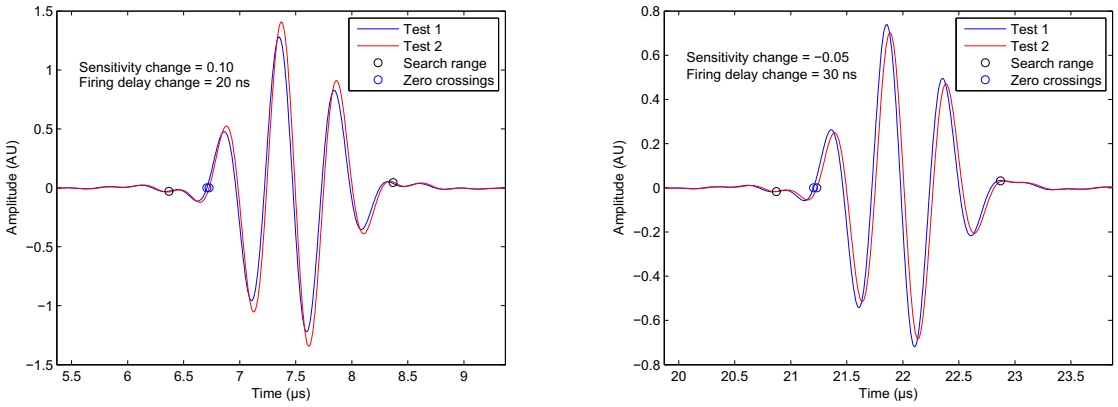

(a) (b)

Figure 6.1.3: The surface echoes predicted by CIVA for pitch-catch element combinations, with and without variation in element performance. a) elements one and two. Test 2 included a 0.1 variation in sensitivity and 20 ns FD. b) elements 55 and 56. Test 2 included a -0.05 variation in sensitivity and 30 ns FD. The changes in element performance detected from the A-scans are displayed in the plots.

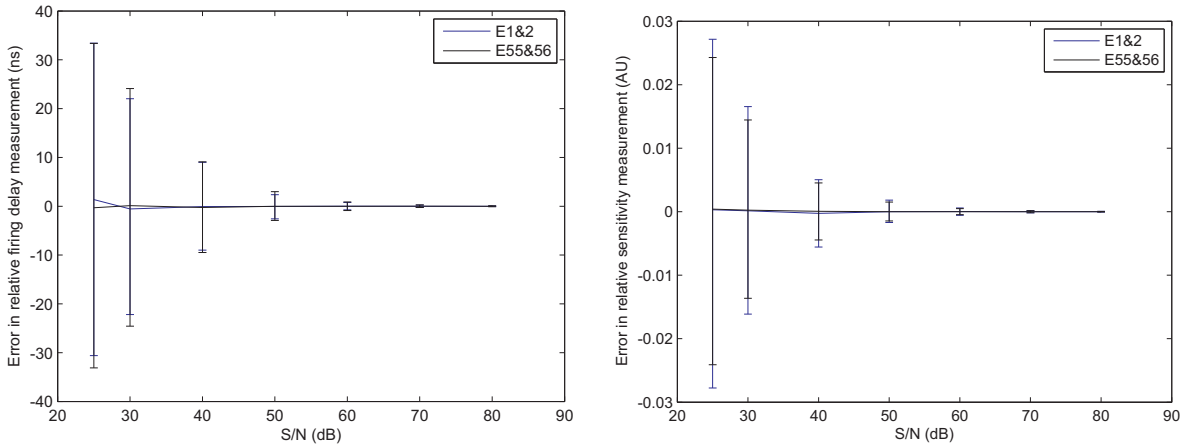

(a) (b)

Figure 6.1.4: The results of adding uniformly random noise with a defined RMS value to the time histories predicted by CIVA. The effect of the noise is expressed as the S/N of the time history. The plot includes the mean and 5 and 95 % confidence intervals after 1000 realisations. a) FD b) Sensitivity.

6.1.2 Temperature insensitive firing delay shift measurement

The previous section demonstrated that provided that the S/N is sufficiently high a combined probe check can be used to accurately measure any change in element performance. However, in practice the experimental results are dominated by any shift in wave velocity due to changes in temperature. Consider a wave emitted from an array element that propagates a distance d with a velocity of c, and is detected by a second transducer with an arrival time of t. If the experiment is repeated after a change in temperature the arrival time shifts:

$$t = \frac{d}{c + \triangle c} + \triangle FD \tag{6.1.3}$$

where Δc is the velocity shift, and ΔFD is the combined change in the FD of the transmitting and receiving elements. For a Rexolite wedge a typical distance could be 50 mm, and a temperature shift of 5 degrees from room temperature would result in a velocity shift of approximately 10 m/s from 2337 m/s using the formula reported by Greenwood et al. [105]. This results in a change in arrival time of over 91 ns. In order for any change in element timing to be accurately recorded a means of detecting and correcting for the velocity shift must be used.

An algorithm has been developed that aims to detect and correct the effects of velocity shift from FMC data sets F1 and F2, recorded before and after a temperature change respectively. The rationale behind the algorithm is that the FMC data contains sufficient pitch-catch combinations between elements that groups can be selected that have have similar travel times. Providing that the element group is large enough that the introduction of firing delay to some elements will not significantly alter the mean arrival time of the group, the change in mean arrival time of the group can be used to calculate the velocity change. The algorithm is based on the assumption that the propagation distances between two elements within the array is temperature independent:

$$d = t_1 c = t_2 \left(c + \Delta c\right) \tag{6.1.4}$$

where $t_{1/2}$ are the recorded arrival times from F1 and F2, and $\triangle c$ is the wave velocity shift. This process can be made more robust by using several groups of elements. Using this approach, the velocity shift can be measured using the following steps:

- Equation (6.1.2) is used to calculate arrival times for all TXRX combinations in the array.
- The calculated arrival times are used to gate the FMC data and record measured arrival times for F1 and F2.
- Locate and group arrival times within 100 ns of one another. These groups are termed arrival groups.
- Limit the arrival groups to transmit-receive element combinations within 40 elements of one another - this helps to ensure that the S/N is high enough to accurately measure arrival time.
- Record the mean arrival time of each element group.
- Split the array into n regions of equal size, and select the largest arrival group within each region.
- Equation 6.1.4 is used to calculate n changes in velocity from the change in the n mean arrival times between F1 and F2.
- The mean change in velocity across all n groups is used to correct the arrival times recorded from F2.
- Change in element FD is measured using a single TXRX combination for each element.

The accuracy of this algorithm is driven by the errors arising from the fact that arrival groups are formed of TXRX combinations that produce arrival times within a range, rather than a fixed value. Errors are also introduced into the velocity change by any changes in element FD affecting the mean arrival time of the element group. However, the arrival groups always contain at least 20 elements so the mean change in element FD for the group should be close to zero.

To quantify the accuracy of this method for a range of input variables a simple model has been used to simulate the FMC files. The model is based on the model reported in chapter 3, and has been adapted to use the configuration shown in Figure 6.1.1. The time history recorded by element n following the excitation of element m is calculated by performing a Fourier synthesis of the following equation over the frequency bandwidth of the modelled transducer:

$$A = \frac{1}{\sqrt{R}} \exp^{-i(kR+\omega(FD_m+FD_n))} D_f\left(\varnothing_m, \omega\right) D_f\left(\varnothing_n, \omega\right) \tag{6.1.5}$$

where symbols retain their previous meanings. This model assumes perfect reflection from the bottom surface of the wedge. This approach allows the full matrix of data to be simulated.

Figure 6.1.5 presents the results of applying the algorithm described above to a set of simulated FMC data. The model has been used to simulate two datasets, F1 and F2, one using a normal FD variation across the array with a maximum value of 25 ns, and a second set using the same FD distribution but with an additional normally distributed FD shift applied over a random 10 % of the array elements.

The maximum size of the FD shift is 15 ns, and the velocity has also increased by 10 m/s. This results in the first run of the model having a normal distributed FD variation between -25 and 25 ns. The second run of the model uses the same distribution but a randomly distributed 10 % of the elements exhibit a FD shift up to 15 ns.

The array modelled is of the following specification: 2.25 MHz, 80 element, 1.25 mm pitch, and 0.25 mm gap. Plot a) displays the extracted time of arrivals for dataset F1, for all TXRX combinations in the array. Plot b) shows the results of analysing the data in plot a) to locate the number of arrival times within 100 ns of one another, whilst limiting TXRX separation to 40 elements. The colour scale indicates the number of elements with similar arrival times. The next step is to form element groups and calculate the velocity shift for each group. Six element groups are presented in plot c), and plot d) shows the calculated velocity shifts. The final stage of the combined probe check is to calculate the FD shifts for all elements. The mean value of plot d) is used to correct the arrival times of elements in F2, and the resulting variation in arrival times for TXRX separations of 10 elements are displayed in plot e) along with the values applied by the model. The results show that the algorithm is able to predict the mean change in wave velocity to within 0.25 m/s, and this allows the element FD shift to be measured to within less than 3 ns. Had the velocity correction not been applied the measured values of FD shift would have been in the range 35 - 120 ns.

6.1.3 Accuracy analysis

To use the chosen method of monitoring element FD the accuracy of the algorithm must be quantified over the desired operating region. This has been achieved by using the modelling approach described in the previous section to perform a Monte Carlo analysis. The array and model parameters used are displayed in Table 6.1.1. Two arrays have been modelled, a 128 element 2 MHz array with a high angled shear wave wedge and a 64 element 4 MHz array with a lower angled compression wave wedge. The two configurations cover two extremes that must be accommodated: a large pitch high angle wedge that results in a large range of travel times, and a smaller pitch low angle wedge that results in a smaller range of travel times.

The simulation results have been analysed by calculating the error in measured FD shift for each simulation. The results for array specification A are shown in Figure 6.1.6 by calculating the mean, and maximum and minimum errors using the 95 % confidence interval. As in previous chapters the confidence interval has been calculated using the Kaplan-Meier estimate for an empirical cumulative distribution function [102]. The plots reveal that as the number of element groups increases the range of measurement errors decrease. This would be expected as more TXRX combinations are included in the calculation of mean velocity shift.

The results presented in Figure 6.1.7 are the results from simulations completed using array specification B. This probe configuration produced a smaller range of time errors compared to specification A. The measurement error is always below 5 ns for 10 or more element groups across all the model configurations considered.

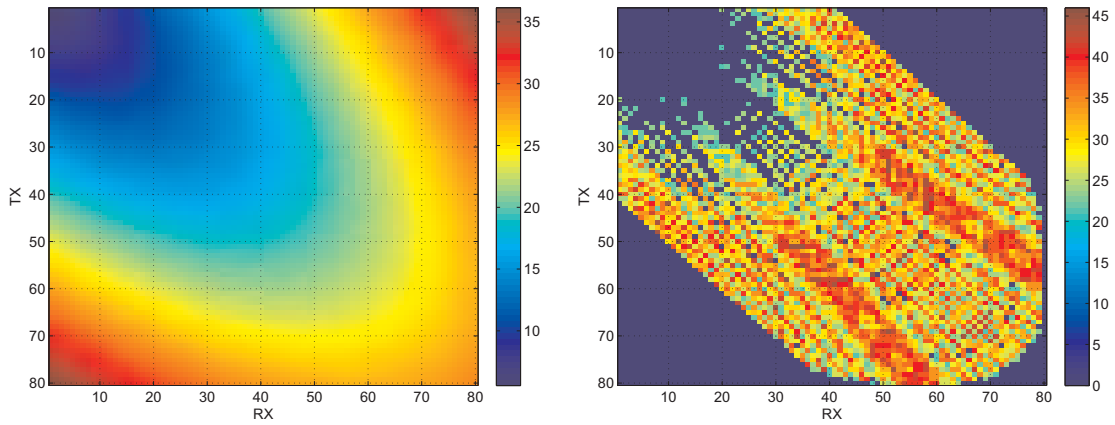

(a)

(b)

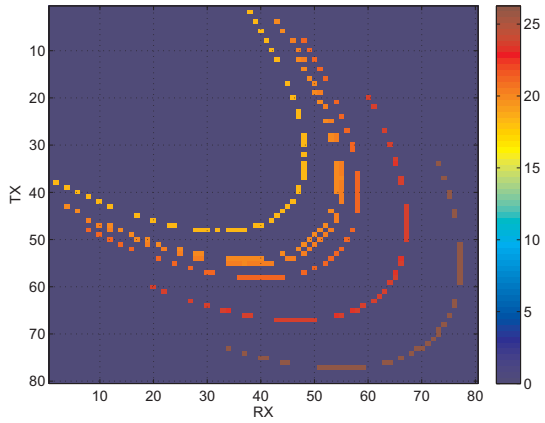

(c)

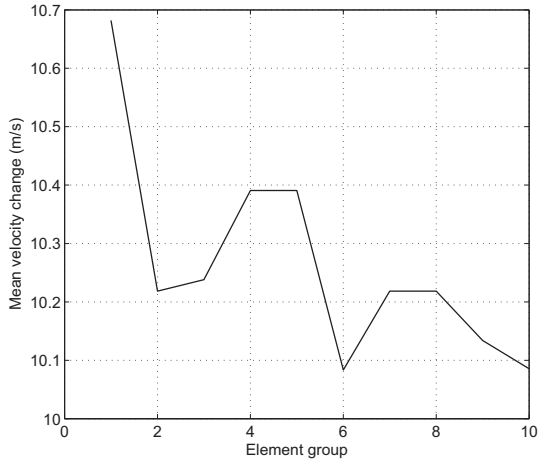

(d)

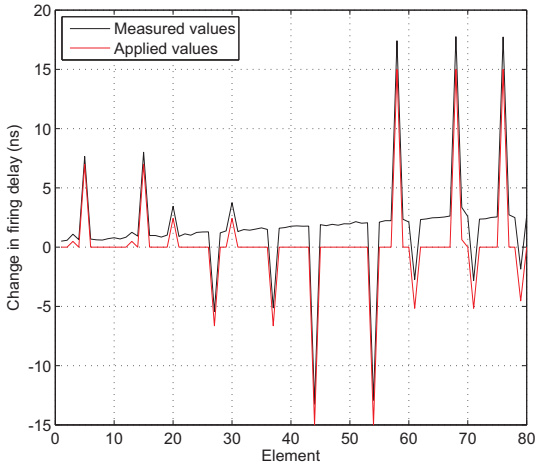

(e)

Figure 6.1.5: The results from several stages of the velocity correction algorithm when run on simulated FMC data. The array modelled is of the following specification: 2.25 MHz, 80 element, 1.25 mm pitch, and 0.25 mm gap. The array is mounted on a 20 degree Rexolite wedge with a first element stand off value of 6.6 mm. a) The recorded time of arrivals in microseconds, b) A graphical display of the number of elements that have an arrival time within 100 ns, when the 40 element TXRX separation limit is applied, c) the selected arrival groups and their arrival times d) the velocity shift measured by each element group, e) measured FD change after velocity compensation using a TXRX separation of 10 elements.

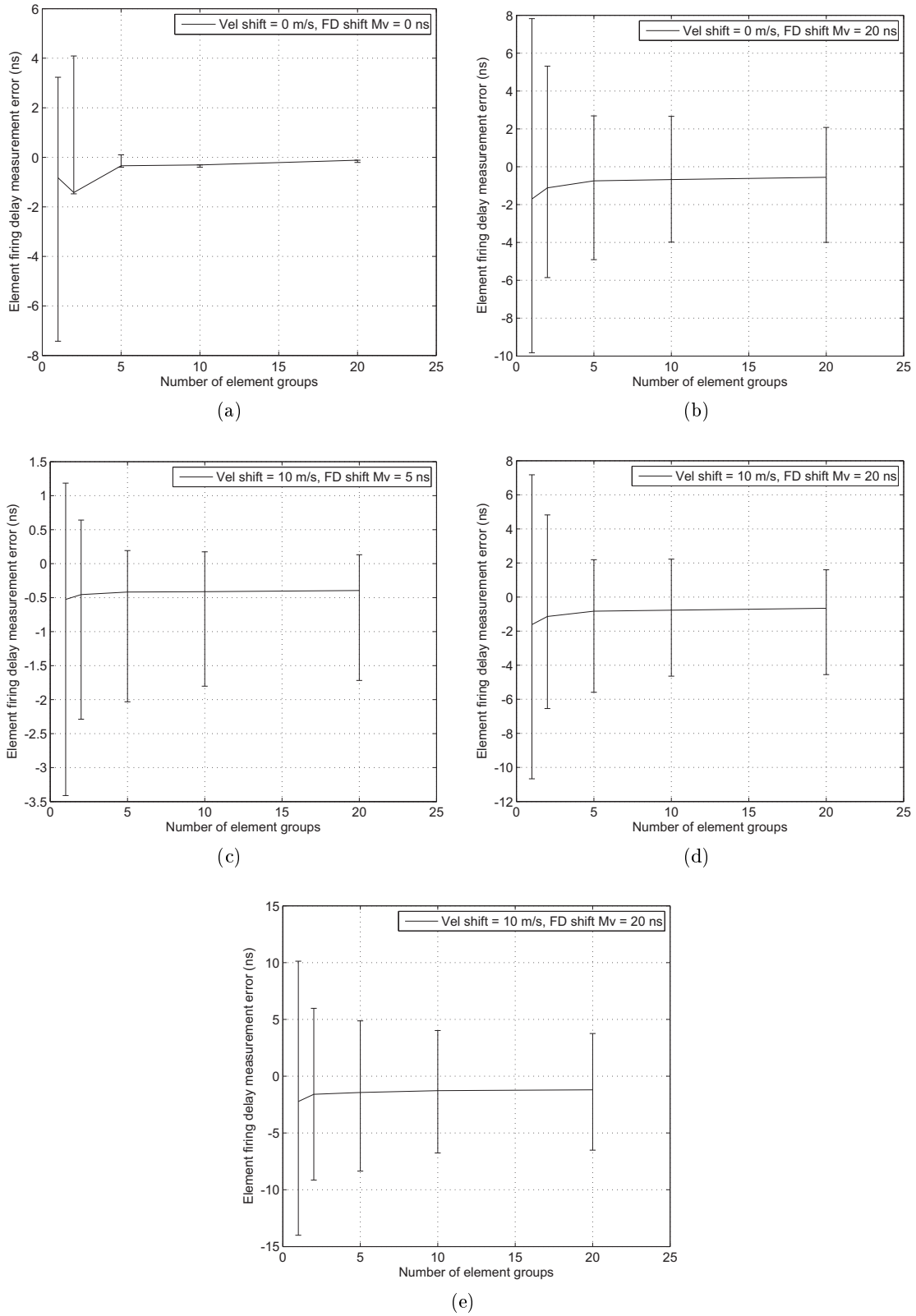

Figure 6.1.6: The error in FD shift measurement predicted via Monte Carlo simulation using array specification A: a) velocity shift = 0 m/s, FD shift Mv = 0 ns, b) velocity shift = 0 m/s, FD shift Mv = 20 ns, c) velocity shift = 10 m/s, FD shift Mv = 5 ns, d) velocity shift = 10 m/s, FD shift Mv = 20 ns, e)velocity shift = 10 m/s, FD shift Mv = 20 ns. In results a) - d) 10 % of the array is affected by FD shift, in case e) 20 % is affected. In all cases a maximum FD value of 25 ns has been applied, and the FD shift have been measured using a TXRX separation of 10 elements. In each case 300 simulations have been completed for each element group size.

Table 6.1.1: The model configurations used to perform the Monte Carlo simulations a) the simulated array and wedge specifications, b) the velocity and FD shift distributions modelled.

Array specification	Value	
	A	B
Array centre frequency (MHz)	2.0	4.0
Number of elements	128	64
-6 dB bandwidth (%)	50	50
Element pitch (mm)	1.0	1.0
Element gap (mm)	0.25	0.15
Wedge velocity (m/s)	2330	2330
Wedge angle (deg)	31	20
First element stand-off (mm)	6.6	6.6

(a)

Array specification	A	A	A	A	A	B	B
Velocity shift (m/s)	0	0	10	10	10	10	10
Firing delay shift (ns)	0	20	5	20	20	20	20
Fraction of array affected	0.1	0.1	0.1	0.1	0.2	0.1	0.2

(b)

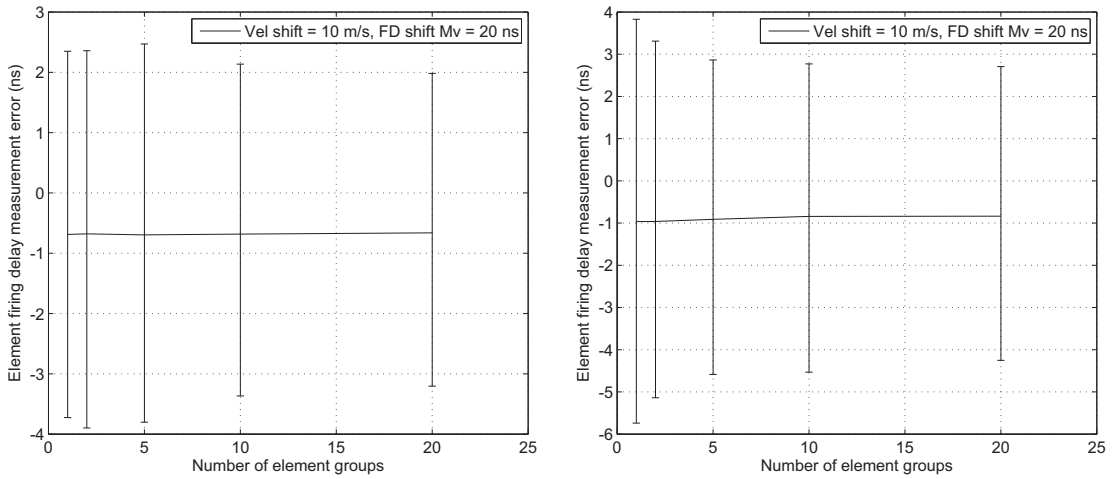

(a) (b)

Figure 6.1.7: The error in FD shift measurement predicted via Monte Carlo simulation using array specification B, velocity shift = 10 m/s, FD shift Mv = 20 ns. a) 10 % of elements effected by FD shift, b) 20 % of elements effected by FD shift. In all cases a maximum FD value of 25 ns has been applied, and the FD shift have been measured using a TXRX separation of 10 elements. In each case 300 simulations have been completed for each element group size.

6.1.4 Experimental testing

The achievable experimental accuracy of this method of monitoring element timing has been measured experimentally using array specification A, as listed in Table 6.1.1. The experiment was performed by assembling the array and Rexolite wedge using Glycerol as the coupling agent. The Glycerol was carefully applied such that no air bubbles were visible through the wedge, and a calibrated digital thermometer [106] was taped to the side of the wedge to monitor temperature. The thermometer is accurate to 0.03 degrees Celsius. The probe assembly was then left to reach a stable temperature and a FMC file was recorded at 100 MHz. The probe was then covered with foam insulation to minimise the effects of convective heat transfer and the temperature of the room was lowered using an air conditioning system. FMC files were regularly recorded until the thermometer had dropped by approximately one degree.

The results of analysing the experimental data can be seen in Figure 6.1.8. Plot a) displays the variation in wedge temperature, and also shows the times at which data was recorded. Plot b) presents the measurements of FD shift at increasing times during the experiment, in each case T1 is used as the baseline. It is assumed that the echoes recorded by the array from the wedge are stationary in time, hence FD shift values of zero would be expected. There is no reason to suspect that a change in element performance could conceivably have taken place. The results show that the algorithm is able to accurately measure FD shift between times T1 and T2 to approximately 1-2 ns, but despite correction the temperature shift betweens T1 and T4 have introduced errors up to approximately 8 ns in magnitude for some elements. The error increases with the transmit element number. This is expected as the arrival time correction error is proportional to propagation distance, which is proportional to transmit element number due to the wedge angle. Had velocity correction not been applied the measured FD shift would have varied between -10 and -50 ns.

The measured velocity change by each element group can be seen in Figure 6.1.8 plot c). Using the formula reported by Greenwood et al. [105] for the variation in wave velocity in Rexolite with temperature, the measured temperature values T1 and T4 result in a velocity change of 2.1 m/s, and 1.7 m/s between T1 and T3. The mean velocity change measured by the algorithm (using plot c) was 2.3 m/s between T1 and T4, and 1.9 m/s between T1 and T3, in both cases a difference of 0.2 m/s relative to the calculated values based on the temperature change. The range of measured velocity errors associated with the Monte Carlo results for FD shift shown in Figure 6.1.6 are typically up to 0.1 m/s; detailed results can be seen in Appendix 9.2 Figure 9.2.1. This demonstrates that the experimental error is approximately twice that predicted by simulation. The discrepancy is thought to be due to non-uniform variation in temperature across the wedge. This hypothesis is supported by the temperature variation measured from the FMC data shown in Figure 6.1.8 c).

The experimental data has been reprocessed using individual velocity values, measured by individual element groups, rather than the mean value. The velocity values are selected on the basis of the closest element group to the TXRX combination used to measure change in element FD. Results of using this method on the experimental data at T1 and T4 are presented in Figure 6.1.9 plot a). The error in FD shift is significantly reduced for the higher transmit element numbers. However, Monte Carlo simulations have been performed using this method, and the model previously discussed, and results for the error in FD shift measurement are presented in Figure 6.1.9 plot b). The results show that the maximum measurement error is larger compared to using the mean velocity change. This is thought to be caused by cases where the velocity change predicted by one element group has a large error,

due to a large number of elements being assigned a FD shift in that group. As this method relies on individual measurements of velocity change, a large error in FD shift is then introduced. Thus, using the mean velocity change is a more robust approach.

Element sensitivity has also been measured using the same experimental data. As previously discussed the change in element sensitivity is measured by comparison of the sum of the rectified A-scan. Figure 6.1.10 displays the shift in element sensitivity between T1 and T4, and the S/N of the A-scans used. The relative sensitivity measurements appear accurate to approximately 0.02, and show a small mean reduction in element sensitivity. The S/N ratio is in excess of 50 dB for the majority of the cases, but drops to approximately 30 dB for transmit elements below 25. This result is caused by low propagation times resulting in the toneburst becoming superimposed upon low frequency content generated by the voltage applied when firing the element. Modelling reported in the previous section suggests a S/N in excess of 50 dB is required to ensure that FD measurement accuracy is within 5 ns. Despite the reduction in S/N both sensitivity and FD appear to have been reliably measured. This is thought to be due to the smoothly varying nature of low frequency A-scan content not adversely affecting location of the zero crossing point, but lowering the S/N. The artificial noise added to the data in section 6.1.1 is random and therefore has a greater impact on locating the zero crossing point.

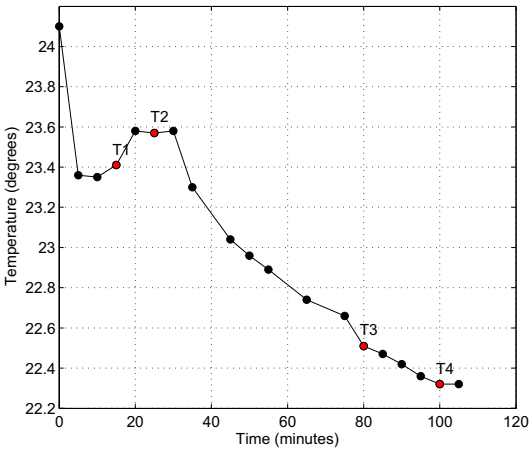

(a)

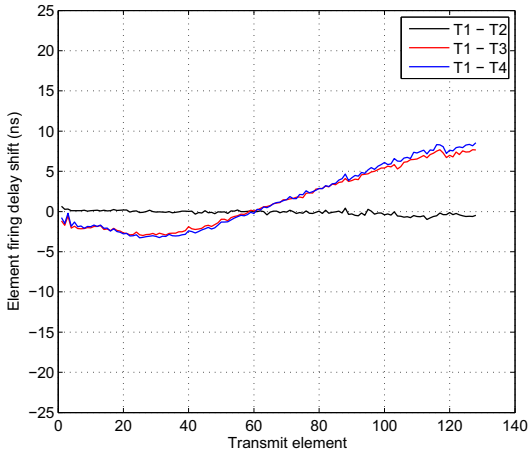

(b)

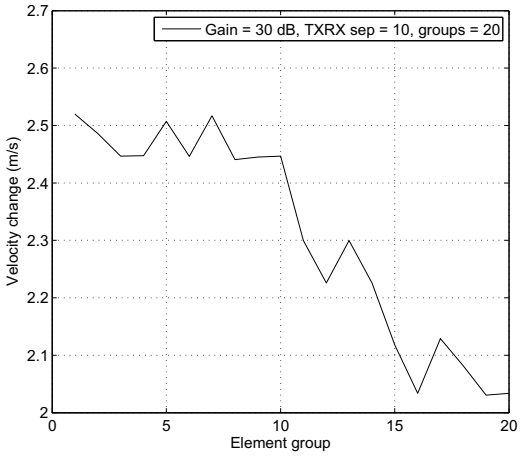

(c)

Figure 6.1.8: The results of measuring FD shift under temperature variation. a) the temperature variation against time. Points T1 to T4 represent the times at which FMC data was recorded. b) Measurements of FD shift. T1 is used as the baseline in each case. c) The velocity change measured by each element group between T1 and T4.

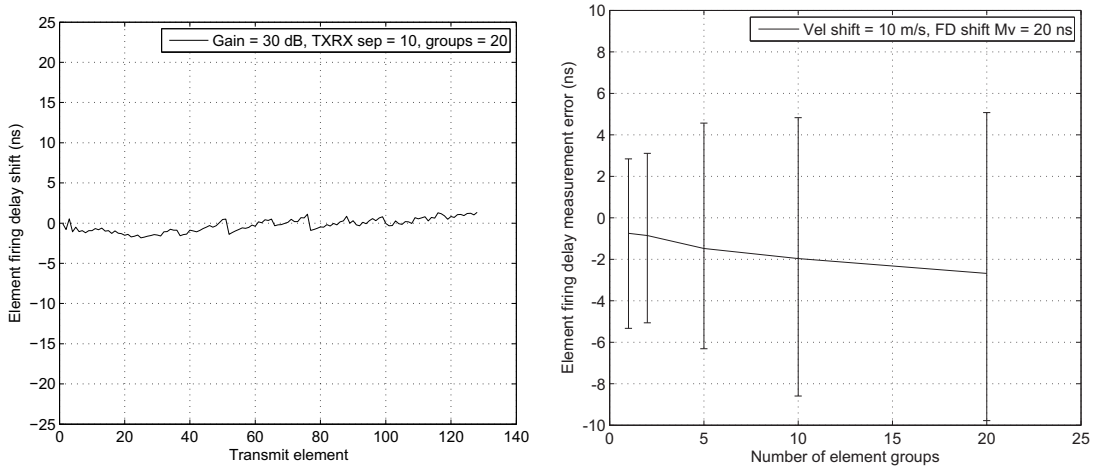

(a) (b)

Figure 6.1.9: The results of measuring FD shift between point T1 and T4 using individual values of velocity shift, rather than the mean. a) the FD shift variation with transmit element number, when using a TXRX separation of 10 elements, b) the results of Monte Carlo simulation using individual velocity shift values for array configuration A. The methodology employed in section 6.1.3 has been used.

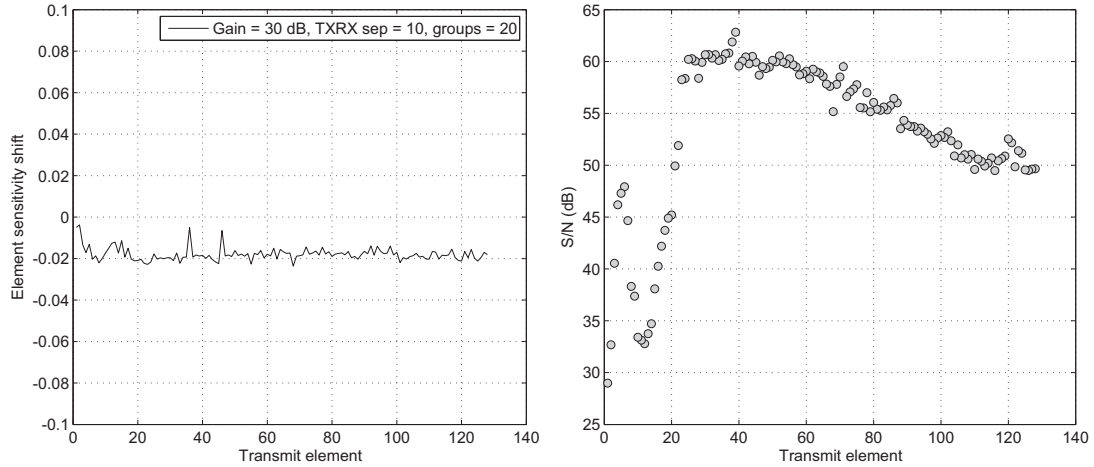

(a) (b)

Figure 6.1.10: The results of measuring element relative sensitivity shift from the experimental FMC data recorded at T1 and T4: a) the shift in element sensitivity when using a TXRX separation of 10 elements, and 20 element groups to correct velocity variation, b) the S/N of the A-scans used to record sensitivity shift using the definition given in section 6.1.1.

6.1.5 Discussion

The experimental results have shown that it is possible to measure shift in element FD to an accuracy of 10 ns. The magnitude of this time error is a good estimate of the largest likely measurement error as the error is proportional to propagation distance used to measure the time difference. As the array is of a relatively large pitch (1 mm), a high number of elements (128), and a high wedge angle (31 degrees) the propagation distance for the elements at the top of the array is very high. Despite the limited accuracy of the measurement method it is probable that smaller changes in element FD could be reliably detected.

The measurement error introduced as a result of small errors in the calculation of velocity change causes a smoothly varying change in element FD. Change to element FD caused by array damage would appear as spikes in the variation. To demonstrate this point artificial FD has been applied to the FMC data recorded at T4. The FD shift has been applied in the frequency domain as a complex phase shift as described for the modelled data in equation (6.1.5). A Fast Fourier Transform (FFT) has been used to transform the FMC data to and from the frequency domain, along with a suitable window. The results of measuring the FD shift from the FMC data collected at T4 after application of 10 ns of FD to element 54 are presented in Figure 6.1.11 plot a). The plot show the measured FD shift, two peaks are visible as element 54 is used as the receiver for element 44. Plot b) displays the associated velocity shift values calculated for all element groups. The effect of the FD shift on group three is clearly visible, despite the fact that a delay of 10 ns only represents a single time sample at 100 MHz. A cubic polynomial fitted to the FD shift profile is also plotted, along with versions at +/- 10 ns. The peaks in FD shift have little effect on the polynomial so it can be considered as a measure of the shift in the Y axis due to temperature variation. The result demonstrates that the polynomial can be used as a tool to detect shifts in FD of the order of 10 ns.

To investigate the accuracy of this approach, a parametric study has been performed to record the range of detected FD shift values for a range of artificial changes, using the method described above, applied to all possible transmit elements. The results of this study are shown in Figure 6.1.11 plot c). The plot shows that the value of the FD shift superimposed on the variation due to temperature shift can be measured to an accuracy better than 0.5 ns. It should be noted that these results are not based on a fitted cubic. Instead the measured value is calculated based on the difference between the FMC data with and without the artificial FD shift. This method should produce similar results as using a cubic fit to FD shift profile. This approach provides a means of monitoring element timing to an accuracy better than 10 ns.

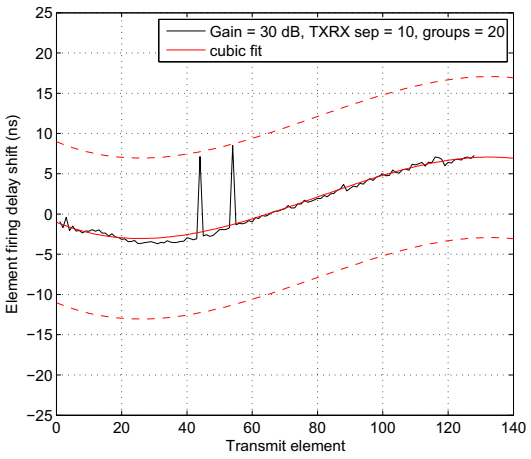

(a)

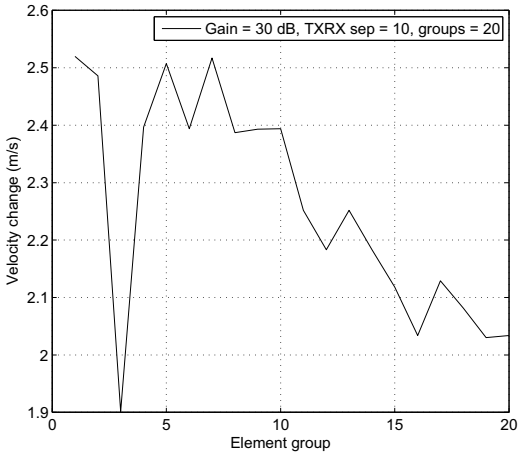

(b)

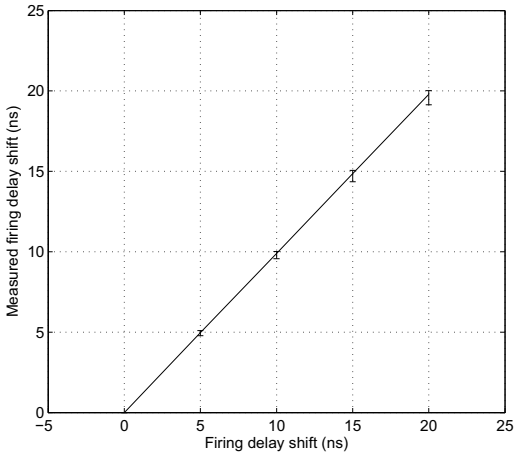

(c)

Figure 6.1.11: The results of artificially adding FD shift to the FMC data collected at T4. a) The measured shift in FD between T1 and T4 when 10 ns of FD is added to element 54. The dashed lines represents the fitted profile +/- 10 ns, b) the measured shift in wedge velocity associated with the results in plot a), c) a plot of the range of measured FD shift values, when considering all possible transmit elements, against the value of artificial FD introduced.

6.1.6 Summary

In summary a method of monitoring element sensitivity and FD using the echo from the wedge interface has been demonstrated. A means of correcting the effects of temperature variation has been developed that assumes temperature variation will be uniform across the wedge. Modelling and experiment have been used to demonstrate the accuracy of the technique. Results show that relative element sensitivity can be recorded to an accuracy in the region of 0.02, and FD to within 10 ns following correction for velocity variation. Application of artificial FD to experimental data has demonstrated that FD shifts of 10 ns can easily be detected, but the absolute accuracy will vary between experiments. The evidence provided suggests that an accuracy better than 10 ns can be achieved.

This technique can be used industrially to monitor variation in probe performance throughout an inspection. Ideally results from the measurement of element sensitivity and FD, recorded using a granite measurement plate without a wedge attached, would be recorded and stored at the beginning of an inspection. Changes in element performance detected via analysis of the echoes from the wedge could then be added to the saved data and compared with the limits given in chapter 5. This method can be used for element sensitivity. However, the accuracy achieved for element FD is not sufficiently high to allow this approach. Instead element timing must be monitored using the technique outlined in this section. To be conservative, if any change in element timing above 10 ns is observed the array should be removed from the wedge and re-analysed using a granite surface plate. If at any point a shift in performance is detected the inspection must be stopped and the array integrity check repeated.

6.2 Combined equipment checks

Combined equipment checks are a vital component of inspection calibration, used to demonstrate the combined performance of probe, cables, and array controller. In industry this stage of calibration is carried out in accordance with BSEN12668-3 [7]. This standard is written with single element transducers in mind but is applicable to phased array systems. The standard requires that the following items must be checked:

- Linearity of timebase
- Linearity of equipment gain (combined probe and amplifier)
- Probe index and beam angle
- Sensitivity and S/N
- Pulse duration produced by the system

Fulfilling the requirements of this standard for FMC based inspections presents all of the challenges associated with probe checks discussed in the previous chapter, due to the flexibility FMC provides. The timebase and amplifier linearity, sensitivity and pulse duration checks are performed prior to the start of the inspection and do not present a problem for FMC based inspections. The array integrity check effectively demonstrates that the array is capable of producing the correct beam angle and therefore index point provided that the array controller is functioning correctly. The combined probe check then monitors the combined performance of the array and array controller, but not all aspects of the combined equipment check are fulfilled. For automated ultrasonic inspections it is considered best practice to monitor system performance. This is achieved by a process of re-calibration.

Re-calibration is achieved by comparison of the response from a calibration reflector before and after the inspection. The amplitudes and times of arrival of the peak responses are compared. The same type of calibration reflector used for DAC curve measurement is used, so peak response should be at the calibration amplitude of the inspection, e.g. 80 % of the system's dynamic range. Standard practice in the UK nuclear industry is to re-calibrate with a +/- 10 % tolerance on amplitude and +/- 2 mm on arrival time . An equivalent procedure for FMC must be developed, this will be referred to as the combined equipment check.

For FMC based systems, prior to each inspection the array performance could be checked using the array integrity check. The combined probe check discussed in section 6.1 can be used to monitor element performance at regular intervals throughout an inspection, without removing the probe from the manipulator and with little time cost. A further check must also be carried out in addition to the monitoring of the interface echo, but at a reduced frequency compared to the combined probe check. For example, when inspecting a large pressure vessel where a probe is fired axially and scanned circumferentially, a combined probe check could be performed at four points around the circumference of the vessel. A combined equipment check could then be performed after every complete circumferential scan. The premise is that the time between successive combined probe checks is hours, and the time between combined equipment checks is tens of hours.

The combined equipment check will provide a more complete test of system performance than the combined probe check, as well as a more tangible output for the system operator. A calibration block that is designed to provide a number of small calibration reflectors over a range of angular positions

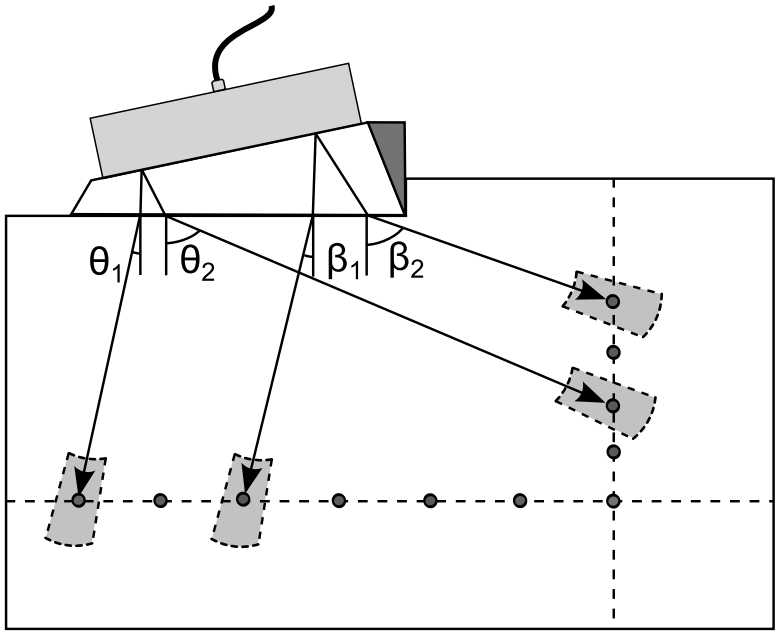

Figure 6.2.1: A sketch of a concept for a calibration block used to complete the combined equipment check.

requiring the probe to produce a range of beam angles could be used. Imaging of these reflectors will provide a complete test of system performance. As discussed in chapter 5.2 plane beams have been found to be the most susceptible to variation in element performance, hence the combined equipment check will use plane beams to check performance.

A concept for such a calibration block is presented in Figure 6.2.1. The calibration block contains a horizontal and vertical line of SDHs, and a machined step is used to ensure that repeatable probe location is easily achieved. The diagram shows an aperture at the top and bottom of the array generating small sectorial scan regions. The number of SDHs means that several aperture locations along the array can be used to image two or three targets that are spread over a similar angular range. The advantage of using a small aperture is increased sensitivity to element performance. The analysis of the timing and amplitude of the response from each SDH, for each aperture location, can be automated and the operator presented with a composite image of all the SDHs and given a simple pass fail result. The acceptance criteria for repeat calibration, discussed above, can be used when analysing the responses from calibration reflectors.

This combined equipment check can also be used for arrays with a permanently attached wedge provided that the uniformity of element timing and sensitivity across the array is measured (eg by the probe manufacturer) before the wedge is attached. The combined equipment check can then be used to demonstrate the system performance. If this check is successful the wedge interface echoes can be used to establish a baseline level of performance via the combined probe check. This enables probe performance to be monitored throughout the inspection.

6.3 The Setting of Inspection sensitivity

Reporting criteria for pulse-echo ultrasonic inspections are commonly amplitude based, and it is normal practice to specify the required inspection sensitivity in relation to DAC curves. The reasoning behind this approach is that by using relative amplitude criteria any combination of probe and flaw detector, of the correct specification, can be used to carry out an inspection. The expected response amplitude for a given defect type is also normally known in relation to a calibration reflector, via experience or modelling. As a result, inspection sensitivity is conventionally set using calibration reflectors to record the relative amplitude of each probe/beam at a specific depth, and if some form of Distance Amplitude Correction (DAC) will be used, the variation of beam amplitude with increasing depth is also recorded use identical reflectors. DAC is commonly applied to manual inspections by variation of the reporting criteria with increasing depth, and for automated inspections it is more common to increase receiving amplifier gain with increasing time. This results in depth independent amplitude, which is known as Time Corrected Gain (TGC). Neither of these approaches is attractive for FMC for the same reasons discussed in the previous chapter on probe integrity testing. Ideally FMC requires a method of setting sensitivity, and if necessary applying DAC, that does not require the prior measurement of individual beams produced by the array. To maintain the flexibility of FMC inspection it is necessary to adopt an alternative approach to inspection calibration.

6.3.1 Distance Amplitude Correction (DAC) methodology

FMC data is normally collected at a fixed level of gain in order to maximise the S/N of the time histories that compose the FMC data set, and make use of the maximum dynamic range of the hardware. Hence the gain level would normally be set at the maximum level supported by the array controller before the amplitude of electronic noise is raised to the point that significant averaging is required. As a result, TGC applied in hardware is not an attractive option as the hardware is already being used at the maximum possible gain. Instead a fixed gain is used to record data and artificial gain is applied in post processing to produce DAC.

For FMC based inspections it is desirable to have the ability to record DAC curves, or calibration reflector amplitude at a given depth, for any beam type that the FMC data could conceivably be processed to produce. One solution to this problem is to record sufficient FMC data on a calibration block that the inherent flexibility of FMC data capture can be used to produce the necessary data for calibration. This approach effectively fully characterises the transducer prior to the inspection, and allows calibration in post-processing. This process allows all of the standard phased array and single element inspection techniques typically used to be reproduced using FMC data acquisition. It also allows appropriate calibration of more novel inspection techniques to be completed.

The calibration scan is practically performed by recording a high resolution scan along the length of a calibration block containing reflectors over a depth range suitable for the inspected component. The line scan should be automated for consistency and to provide location encoded data. The length and resolution of the scan is dictated by the range of beams that must be supported. For example, the ability to calibrate a 70 degree transverse wave at full skip would require a particularly long scan, as data must be recorded such that every element in the array can produce a wave incident on the shallowest reflector. The resolution of the data must be high enough that the processed data contains probe locations that produce the maximised, or close to maximised, amplitude response from each

reflector. Therefore data must be collected at the same resolution that would be used to raster scan conventional phased array or single element probes for the same application. A scan resolution of 1 mm has been found to produce adequate results. This method can be used to record DAC curves for direct beams, and beams reflected or mode converted at the backwall.

Following the collection of the calibration scan, DAC curves are produced by first processing the data using the selected imaging algorithm. The resulting amplitude data is then processed using the following steps:

- The user provides the co-ordinates, size, and nature of the calibration reflectors, e.g. SDH or Flat Bottomed Hole (FBH). For the SDH case the radius has an impact on the location of the recorded response.
- Acceptable tolerances on the time/range and amplitude of the responses from reflectors, and probe location, must be input by the user.
- The data on reflector location and tolerances are used to calculate a search region for each aperture location in the array that should contain the maximised response from each target.
- The amplitude and co-ordinate data produced from the processed calibration scan is searched using the regions selected in the previous step.
- The maximum response amplitude is selected in each search region.
- For each aperture location in the array the maximum response amplitudes are combined to produce the DAC curve.
- The DAC curves from all aperture locations are normalised by the response from a single reflector using the most sensitive aperture. The user selects which target to be used for amplitude normalisation.
- The DAC curves are inverted to produce artificial TGC curves, and applied to the FMC data from the component inspection.

Figure 6.3.1 presents a diagram explaining the method used to extract the response from each calibration reflector. The array is mechanically scanned and the search region for a single target is shown. Two example DAC curves are shown in plot b). The curves have been produced using a 20 element aperture of a 0.75 mm pitch 2 MHz immersion array and a 60 mm thick calibration block containing Ø3 mm SDHs. The FMC data was processed to produce a 65 degree longitudinal beam and a 65 degree mode converted longitudinal beam at the backwall. The two results averaged over all aperture locations are shown in the plot as the solid lines, and the dashed lines represent the range of amplitudes when considering all aperture locations.

The complete DAC capability is demonstrated by the results provided in Figure 6.3.2. This data has been produced using a 48 element, 1.25 mm pitch, 2 MHz array mounted on a ~22º Rexolite wedge. A 10 element aperture generating a 45º plane shear wave has been mechanically scanned along the top surface of a stainless steel calibration block containing 4 Side Drilled Holes (SDHs) at different depths. The data is displayed in the British Energy/EDF software Graphical Ultrasonic Inspection Data Evaluation (GUIDE) [107], and the SDH locations have been superimposed on the data. The four direct shear wave responses from the SDH targets are labelled in Figure 6.3.2, along with a fifth signal

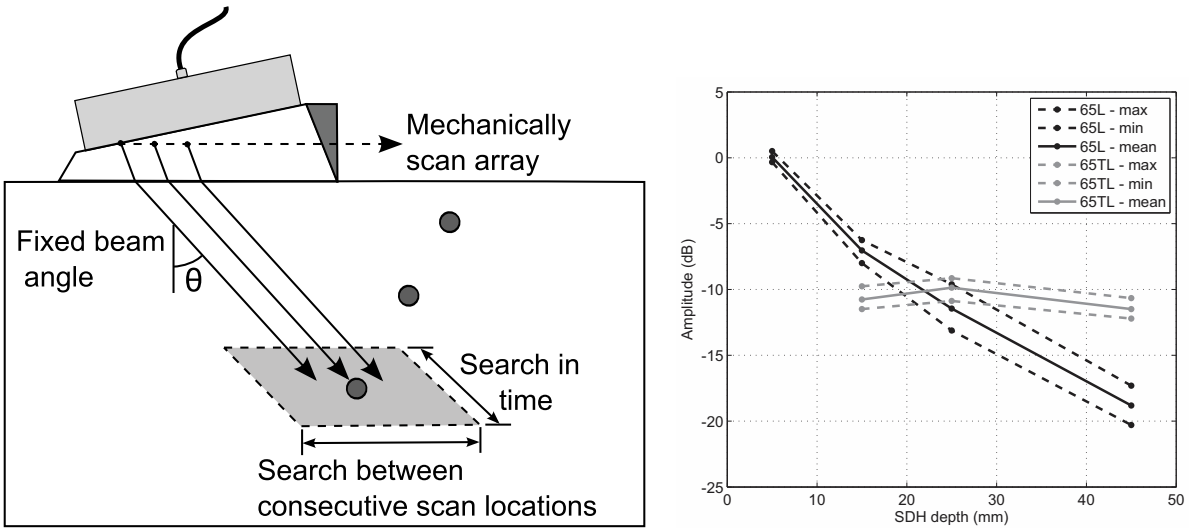

(a) (b)

Figure 6.3.1: The automated DAC algorithm used for FMC data a) The method used to record the response from each reflector, b) example DAC curves for direct and mode converted 65 degree longitudinal beams (65L and 65TL respectively). The DAC curves were recorded using 3 mm SDHs and a 2 MHz 128 element array in immersion, utilising 20 elements.

which is due to a skip shear-shear wave reflection from the underside of the deepest hole. In Figure 6.3.2 a) signals from all four SDH targets are clearly observed, but the amplitude of the individual responses varies with depth. In Figure 6.3.2 b) DAC is applied to the data and the three SDH responses appear at the same amplitude; the signal from the first SDH is partially masked by the front wall echo. This method is entirely automated and allows a separate DAC curve to be recorded for each aperture location in the array. This allows B-scans formed via the use of electronic scanning to be presented at constant sensitivity. The amplitude of the SDH reflections is also used to set inspection sensitivity. In the image presented in plot b) the colour scale is plotted relative to the amplitude of the shallowest SDH response.

6.3.2 Example experimental result

A worked example will be presented to demonstrate how a calibrated FMC inspection could be carried out. A common inspection problem encountered in the nuclear industry is the detection and subsequent sizing of lack of fusion weld defects. Many of the components in a typical nuclear steam raising plant are manufactured from austenitic stainless steel. When welded, this type of material can exhibit epitaxial grain growth and produce columnar dendritic grain structures in the weld metal that cause significant scattering and steering of ultrasound, and consequently make it challenging to inspect using ultrasonic methods [108]. The microstructure means that the inspection of welds for lack of fusion defects on the lower half of the fusion face is challenging. The most obvious detection technique is a direct specular reflection from a longitudinal wave travelling through the weld, but the anisotropy in the weld make this technique unattractive. An alternative detection method is to use a transverse wave that mode converts to a longitudinal wave, at the back face of the component, and reflects off the under side of the defect. The beam type is known as a TL beam. Figure 6.3.3 demonstrates each of these methods.

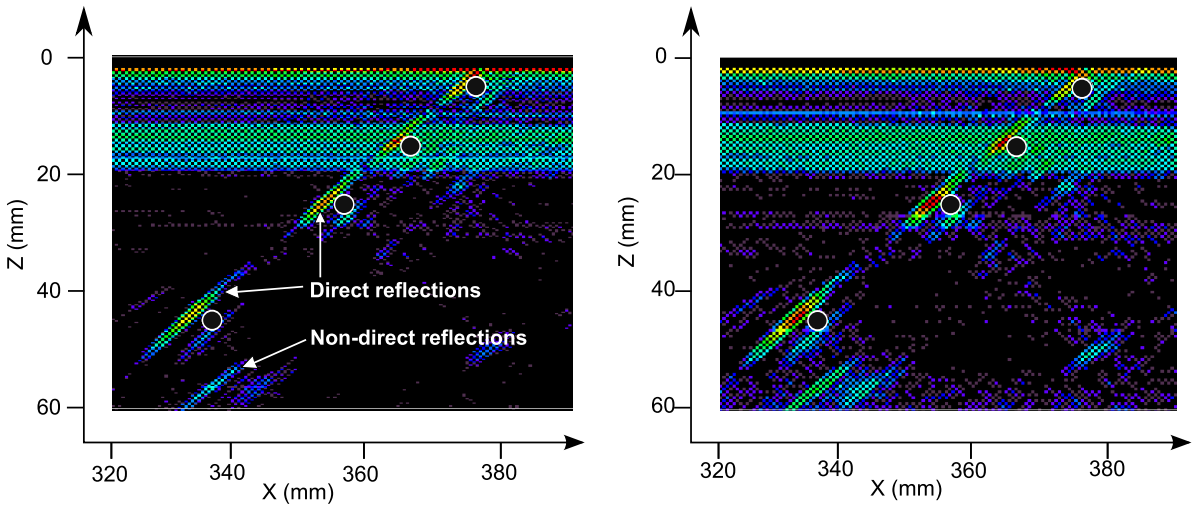

Figure 6.3.2: FMC inspection of a calibration block containing four SDH defects using a conventional 48 element array generating a plane 45º shear wave. A 10 element aperture has been mechanically scanned along the calibration block (left to right in the images), (a) without DAC, and (b) with DAC applied. All data is plotted by GUIDE [107] using a RGB colour scale with a 26 dB dynamic range.

The advantage of the TL method is that the waves only propagate through parent material, so are unaffected by anisotropy in the weld metal. Large phased arrays also allow the use of focused mode converted waves.

FMC data has been captured on a test piece containing an austenitic stainless steel weld and an embedded artificial lack of fusion defect, located at the bottom of the upper fusion face. Figure 6.3.4 shows a photograph of the test piece and details of the techniques used to detect the defect. Practically this type of defect is detected using low frequency, high angle longitudinal wave probes. The high angle longitudinal wave is used to scan the weld volume and far fusion face. A transverse wave is also generated that mode converts to a longitudinal wave at the backwall of the component, and can be used to scan the near fusion face of the weld. If a DAC curve can be recorded for both the direct and mode converted longitudinal waves, both waves can be imaged at equal sensitivity. The example DAC curves previously shown in Figure 6.3.1 are results generated using this technique.

The defect is nominally 12 × 8 mm (length × through wall extent). Scanned FMC data has also been collected on a calibration block, and DACs recorded in line with the method described in the previous section. FMC data has been collected using a 2 MHz 0.75 mm pitch 128 element array in immersion, positioned with the first element 8 mm above the top surface of the test piece with the array inclined at 7 degrees. The data has been processed to produce a plane longitudinal wave at 65 degrees (65L) using an aperture of 20 elements, and an aperture of 40 elements has been used to generate the 65L and 65TL beams using the Almost Total Focusing Method (ATFM) [38]. This method focuses the beam in transmit and receive at a number of depths in the image, thus allowing the advantages of a focused beam without the reduced sensitivity away from the depth of focus. Electronic scanning has also been used to generate a fully focused B-scan with fixed beam angle.

Figure 6.3.5 displays the B-scan images generated from the FMC data after processing for the direct and mode converted beams. Plot a) shows the results for a plane 65L wave generated using a 20 element

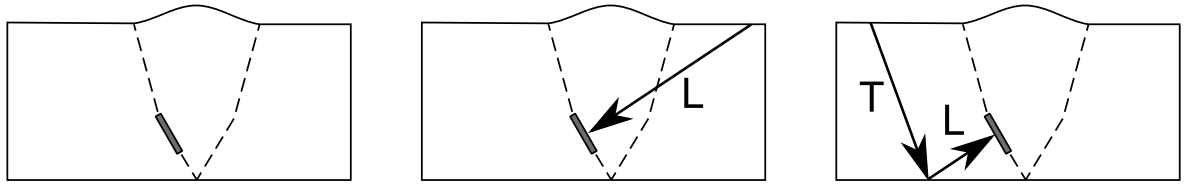

(a) (b) (c)

Figure 6.3.3: Diagrams demonstrating the type of inspection methods: a) an example defect location, b) an inspection using a direct longitudinal (L) wave, c) an inspection using a mode converted longitudinal (TL) wave.

aperture, after the application of DAC. The response from the defect is visible above material noise, and has a peak amplitude of approximately 12 dB above Ø3 mm SDH sensitivity (6 dB signal-to-noise ratio ignoring the probe echo). However, the response is distorted and appears to originate at the bottom of the fusion face rather than the top. Material noise due to the austenitic weld is displayed around Ø3 mm SDH sensitivity, and a strong internal probe echo is visible. The ATFM result for the direct longitudinal wave is shown in plot b). The specular response from the fusion face defect can clearly be seen at Ø3 mm SDH sensitivity + 15 dB (15 dB signal-to-noise ratio ignoring the probe echo). The grain scatter from the weld is at a slightly lower amplitude, probably due to the increased spatial averaging due to the larger aperture size. As a result the S/N is appreciably improved, and the defect response is more obvious.

The result from the mode converted beam is displayed in plot c). The TL data has been plotted upwards after the mode conversion at the backwall, and DAC has been applied. The response from the 65TL beam is 4 dB above Ø3 mm SDH sensitivity (35 dB signal-to-noise ratio). There is little noise in the image as the wave propagates only in the parent plate. The specular TL response is correctly plotted on the weld preparation lines superimposed on the image, and other mode converted signals can be seen in the image.

The second requirement of the inspection is to size the defect. Current practice for sizing a defect of this type is to use tip diffractions to locate each end of the defect [9]. The TFM will be used to image the tip diffractions from the defect using transverse waves reflected from the backwall of the component. However, in this case the large array allows the defect to be sized using a focused TL beam, and the 6 dB drop technique as a secondary method. In order for the 6 dB drop sizing technique to yield accurate results, the 6 dB beam width must be smaller than the size of the defect. At this point a beam model is required to predict the beam width and inform the operator of the best aperture size to select in order to accurately size the defect. This process has been performed using the beam model reported in chapter 3.

The model is used to simulate the beam width of a focused TL beam for the configuration used experimentally. The selected aperture size is progressively increased until the predicted beam width is smaller than the defect size obtained via the 6 dB drop method. The results of this process are shown in Figure 6.3.6 plot a). The red line added to the plot at 7.4 mm is the result from sizing the defect from its tip diffractions. The TFM image used to measure the distance between the tip diffractions is

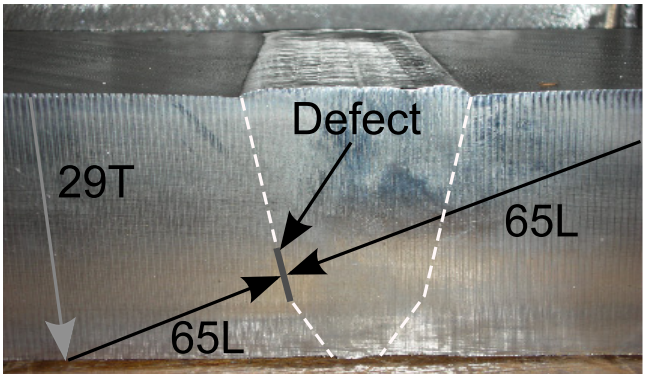

Figure 6.3.4: The test piece used to collect the experimental data. The dashed white lines represent the approximate location of the weld fusion faces. The arrows represent the beam angles used to detect the defect, using transverse (T) or longitudinal (L) waves.

displayed in plot b), the signals are clearly visible in the image. The results from the 6 dB drop sizing technique include the error bars due to the limited resolution available with electronic scanning. The errors introduced by inaccuracies in phase velocities and probe geometry have not been included. The predicted beam widths suggest that the defect can be accurately sized when an aperture of at least 80 elements is used. When using this aperture size experimentally the measured defect size is 6.1 mm, and increasing the aperture size further causes little difference. The nominal size of the defect is 8mm. Including the error bars the two methods produce results within 1.0 mm of one another. The TFM result is likely to be more accurate, as the 6 dB drop technique assumes that the defect is rectangular in shape. In this case the defect has been introduced by welding a patch onto the weld fusion face; as the technique is proprietary the variation in completed defect shape is unknown. It is likely that the shape of the unfused area is not rectangular, but this would also be expected with real defects. Despite the limitations of the 6 dB drop method the agreement in results is impressive.

The combination of the two inspection directions and sizing techniques demonstrate that this type of defect is easily detected and sized with redundancy, despite the challenging weld microstructure. The benefits of setting inspection sensitivity and the application of DAC in terms of the comparison of results from different FMC imaging algorithms are also demonstrated. The worked example shows the benefits that FMC technology provides. The data can be reprocessed many times to characterise the defect, and novel algorithms such as the ATFM and TFM can be used to improve performance.

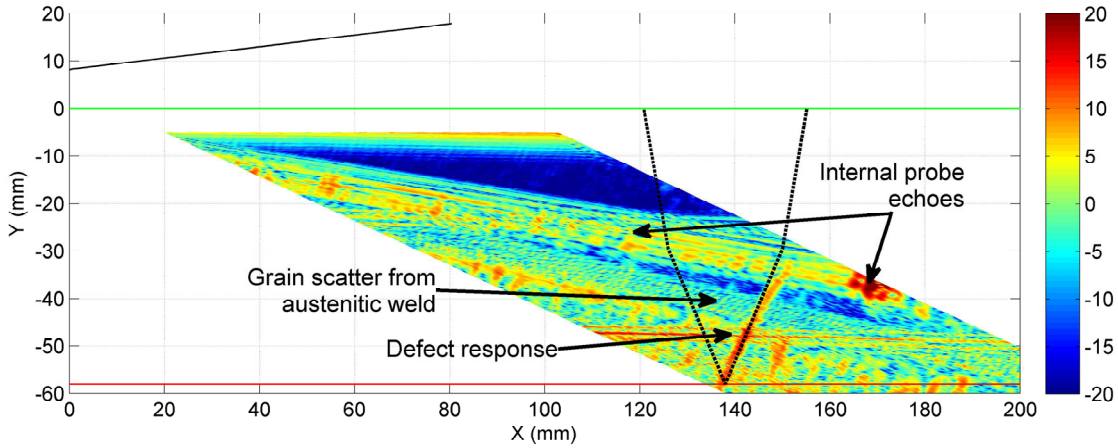

(a)

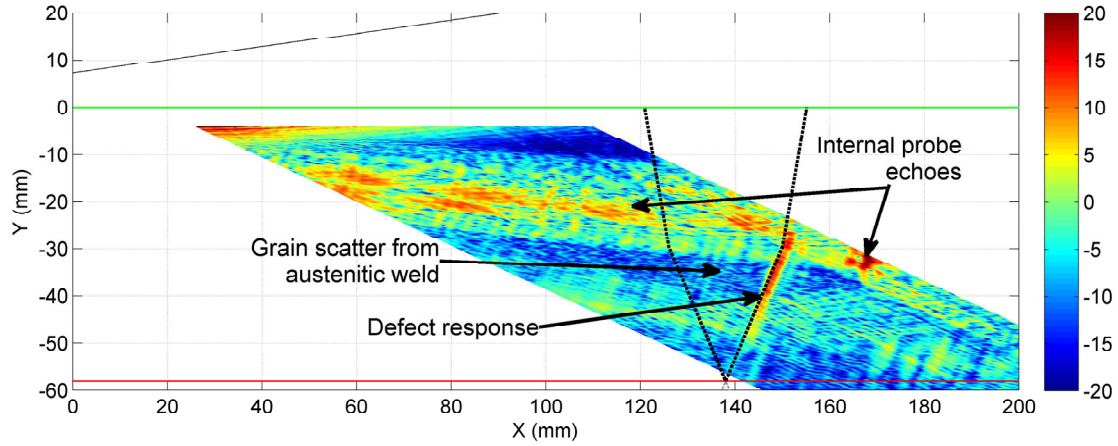

(b)

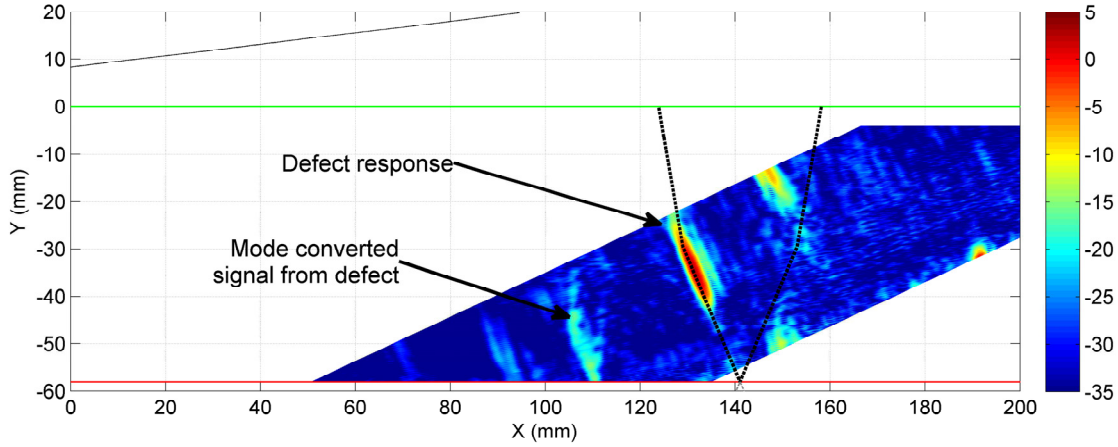

(c)

Figure 6.3.5: The processed FMC data collected on the test piece shown in figure 6.3.4. In the first two results the beams are fired right to left in the photograph of the test piece, and in the third result the beam is fired left to right. a) The image produced using a 65L wave focused at the depth of the defect with DAC applied, b) the image produced from the 65L ATFM results after the application of DAC, c) the 65TL ATFM results after the application of DAC. The colour scale is in decibels, and 0 dB represents Ø3 mm SDH sensitivity.

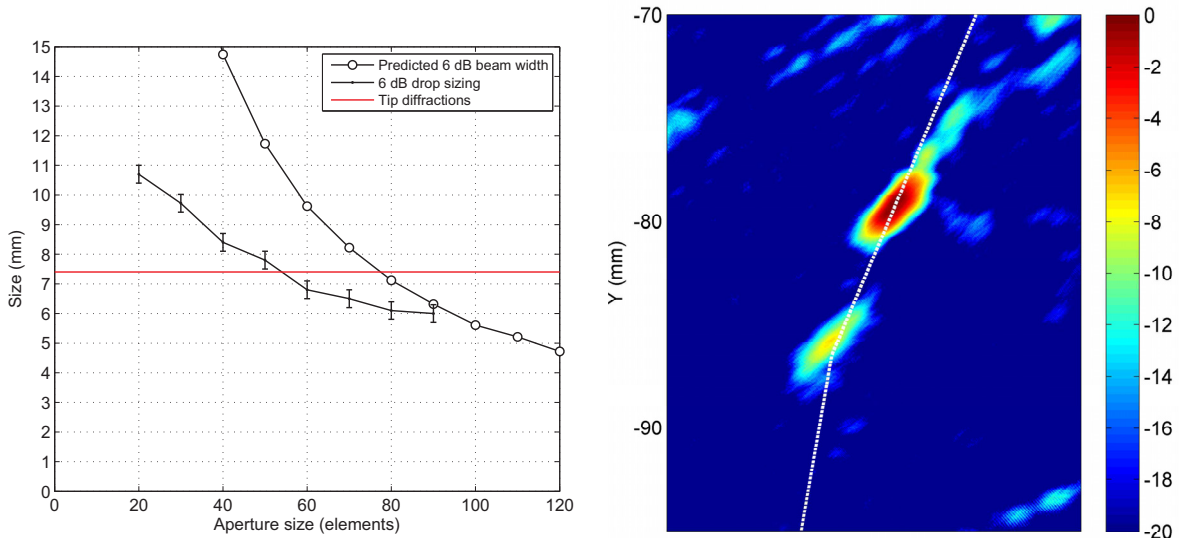

(a) (b)

Figure 6.3.6: The results of sizing the defect a) The results using the 6 dB drop technique with a focused TL beam, tip diffractions using the TFM, and the predicted 6 dB beam widths. The error bars show the potential error in the results due to electronic scanning. b) the TFM image of the tip diffractions from the defect.

6.4 Summary: FMC calibration

Chapters 5 to 6 have discussed the development of the tools required to industrially implement a calibration routine for FMC based phased array inspections. The proposed calibration routine involves three main steps:

- Transducer integrity check
- Monitoring of element performance throughout the inspection
- Calibration scan

Chapter 5.2 has detailed the development of a transducer integrity check based on simple pulse-echo A-scans on each array element. This check is designed to be straightforward to carry out with simple pass-fail criteria. The criteria used have been developed via Monte Carlo study on the effect of the essential parameters that dictate element performance. The criteria are designed to be conservative in nature, but offer the potential to replace time consuming probe checks with a simple automated means of ensuring transducer performance.

A means of monitoring element performance has been developed using the echo from the array's wedge to component interface; referred to as the combined probe check. In principle this check is trivial to perform. However, the accuracy with which element timing must be monitored results in temperature variations in the region of 0.1 degree becoming significant. An algorithm has been reported that utilises the redundant pitch-catch signals recorded between elements within the array to detect and correct changes in the wedge velocity. The accuracy of this approach has been shown to be affected by changes in element timing, but simulation has been used to demonstrate that the algorithm can detect timing shift to an accuracy of the order of 10 ns. Further, it has been shown that a simple cubic fit enables changes in element timing to be extracted to a higher accuracy, via artificial time shifts added to experiment data.

The combined probe check enables array performance to be monitored at regular intervals throughout an inspection without the need to remove the wedge from the array, or remove the probe from the component. The combined probe check is supported by the combined equipment check. The combined equipment check is designed to provide the operator with a more tangible image based output, but at reduced frequency. A specific calibration block is used to provide the probe with a number of identical targets that are imaged using plane sectorial scans covering a large angular range. Plane beams should be used, as chapter 5.2 has shown that this beam type is the most susceptible to changes in element performance. This check will provide a quick and automated means of demonstrating probe performance once the probe is removed from the component. The combined equipment check also allows conventional limits for changes in probe performance to be used, as well as a route for using arrays with permanently attached wedges.

The final aspect of inspection calibration is the setting of inspection sensitivity. For FMC a high resolution scan is recorded on a calibration block prior to the inspection, using the same data collection parameters used during the inspection. This scan is then processed after the inspection and DAC curves and normalisation amplitudes are extracted from the data. This provides a tool for relating results to calibration reflectors, comparing relative amplitude between imaging algorithms, and correcting for the effects of beam spread and attenuation with increasing depth.

The combination of all the tools developed for FMC calibration provide a structured route for the measurement and monitoring of both element and system performance, and finally normalisation of results by a known sensitivity level.

7 The effect of surface profile measurement inaccuracies

The extension of inspection calibration to a conformable array device introduces additional essential parameters that must be controlled in order to guarantee that inspection performance is adequate. This chapter reports the investigation into the effect of surface profile measurement accuracies on beam forming performance. The investigation is two staged: the first stage is to demonstrate the accuracy to which typical irregular surfaces can be ultrasonically measured using a membrane type device, and the effect of parameters such as imaging algorithm, aperture size etc. The second stage of the investigation is to predict via Monte Carlo modelling what size of measurement error can be accommodated before beam forming performance drops to an unacceptable level.

The two sets of results presented demonstrate that for smoothly varying surface profiles a focused beam is able to measure the surface profile accurately enough to allow inspection through the interface. The exception to this conclusion is interfaces with regions of very surface high gradient.

7.1 Introduction

An application of array technology that is of interest to Rolls-Royce is beam forming in a component with an irregular surface profile. This is practically achieved by using a conventional immersion array with a water filled wedge. A polyurethane membrane is used on the bottom of the wedge to contain the water, and allow the device to conform to the irregular surface geometry. This probe is referred to as the membrane probe, details of the device development can be found in Russell [5] and a photograph can be seen in Chapter 2, Figure 2.3.8. The membrane probe itself can be used to measure the surface profile under it, and this information can then be used to calculate the delay laws necessary to beam form in the component [54]. The accuracy of the surface profile measurement is limited by the ultrasonic technique used to measure it, thus errors are introduced into the calculated delay laws. Delay law errors have been shown to degrade the beam produced by the array [109, 54], and ultimately degrade the accuracy of the inspection.

A series of experimental trials have been performed to understand the accuracy to which it is possible to measure an irregular surface profile using the peak detection algorithm chosen for this study. Many different strategies for range measurements using ultrasonic transducers exist in the literature. The method chosen has been incorporated into the FMC inspection platform under development at Rolls-Royce and is therefore the focus.

FMC data has been collected on a number of test pieces with irregular surface profiles. The FMC data has been processed using a selection of different imaging algorithms in order to assess the relative performance of each algorithm. This has been achieved by comparison with surface profiles measured using a Coordinate Measurement Machine (CMM).

A second aspect of the experimental trials is the investigation of the effect of amplifier saturation

during data collection. Ideally a single set of FMC data should be collected to allow surface profile measurement and inspection below the component surface. This approach reduces the number of scans of a component that must be recorded and therefore reduces inspection time and cost. To use this approach the FMC data should be recorded at high gain in order to maximise the dynamic range of the data recorded below the surface of the component, but this inevitably leads to saturation of the surface echo due to the large impedance difference between water and steel. The effect of the amplifier saturation on surface profile measurement accuracy will be quantified.

The final aspect of this chapter is an investigation into the effect of surface profile measurement inaccuracies on beam forming performance in the component. This has been investigated by using a 2D array beam model to simulate the effect of small delay law errors introduced into the inspection as a result of errors in the surface profile used to calculate delay laws. The assessment of the degradation of inspection performance is based on the introduction of artefacts into the beam produced by the array. This task has been completed by using the model to carry out Monte Carlo simulations, and using the results to suggest acceptable limits on surface profile measurement accuracy.

7.2 Surface profile measurement accuracy

A series of trials have been performed on two test pieces to investigate the measurement accuracy that can be achieved using the membrane probe. A variety of beam forming methods has been evaluated for the measurement of surface profile. These include: plane and focused zero degree longitudinal waves, and a variety of methods based around the Total Focusing Method [4]. Ultrasonic data has been collected in immersion using two test pieces. The first test piece is a 30 mm thick stainless steel block with a 4 mm tall artificial weld cap on the top surface. The artificial weld cap has been formed by machining the top surface of the block. The second test piece is a 58 mm thick stainless steel block that contains a butt weld and an un-dressed weld cap. Figures 7.2.1 and 7.2.2 show sketches of the two test pieces, and each contains details of the surface profile geometry. All the methods assessed have been compared to results collected using a Coordinate Measurement Machine (CMM) on the two test pieces.

The comparison of the ultrasonically measured profiles and the CMM results has required the profiles to be overlaid on top of one another. The comparison of results must be completed to a resolution of at least 0.1 mm. Encoded ultrasonic and CMM results were collected at the same locations on the test piece to enable a direct comparison of the raw results. Analysis of the results has shown that the test pieces were in slightly different orientations when the measurements were taken, as it was not possible to record both sets of data without moving the test pieces. To solve this problem several methods of automatically overlaying the CMM and ultrasonic profiles were attempted, however none was found to be sufficiently robust. Instead 2D profiles have been compared at one location on the machined test block and at four locations on the welded test piece by manually translating and rotating the ultrasonic profiles such that they appear to match the orientation of the CMM results. The error introduced by this process is estimated to be less than 0.05 mm.

The accuracy of the various ultrasonic approaches, and the effect of parameters such as aperture size have been investigated. Experimental data has been recorded at 25 MHz using a 128 element 2 MHz array detailed in table 3.4.1. The array was centred over the weld centre line and a 10 mm water path was set using slip gauges. A 0 degree array angle was used to collected data on the welded test

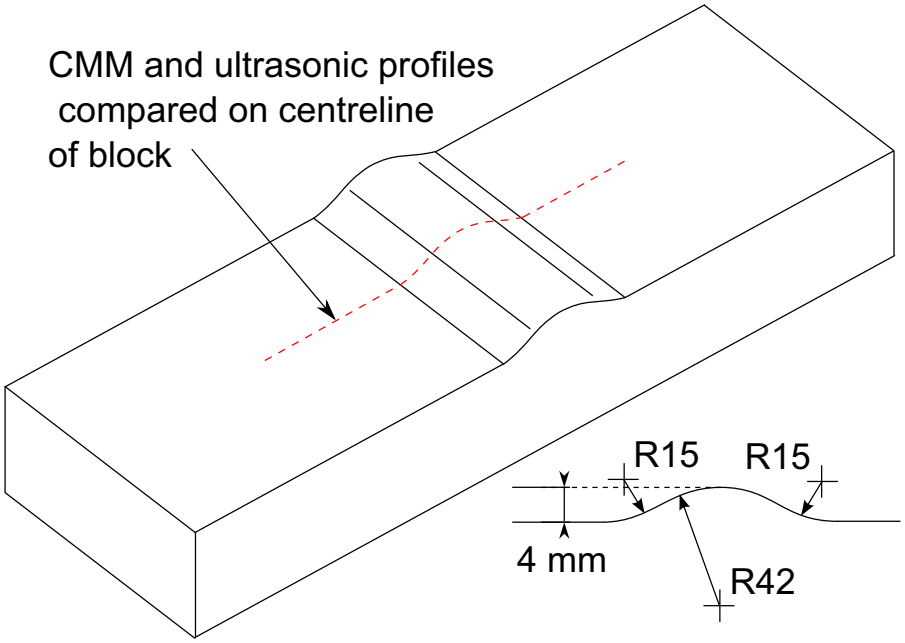

Figure 7.2.1: A diagram showing a sketch of the test block with a artificial weld cap. The location on the test piece used for the comparison of ultrasonic and CMM results is shown by the red dashed line. Approximate details of the weld cap geometry are also shown.

piece, and a 0 and 7 degree array angle was used on the artificial weld cap test piece. The mean firing delay of the array was measured before the data was collected. This information was used to correct the time base reported by the array controller.

7.2.1 Peak selection methodology

The ultrasonic method of surface profile measurement is based on assuming that the arrival time of the peak of the tone burst reflected from the water-steel interface can be combined with *a priori* knowledge of the beam angle to locate the interface. Surface profiles have been extracted from the experimental results by generating a zero degree beam with an aperture, A, and electronically scanning the aperture along the array. The A-scan from each aperture location is then extracted, a Hilbert transform is performed to obtain the envelope, and the surface location is determined using the centroid of the maximum amplitude signal in the envelope. The centroid is calculated over locations of the envelope within 50 % of the maximum amplitude of the peak. For a discrete signal $Y(X)$, the centroid is estimated using equation (7.2.1):

$$Centroid = \frac{\sum Y(X).X}{\sum Y(X)} \tag{7.2.1}$$

where Y is the signal amplitude, and X is the range of the A-scan. In practice this process is complicated by the presence of multiple echoes in the gate, and in some cases amplifier saturation. To ensure that the surface profile extracted from the ultrasonic data is robust, a series of signal processing steps have been implemented:

1. Calculate the range of the maximum amplitude in the A-scan, R.

2. Calculate the mean value of the previous three R values, Rm.

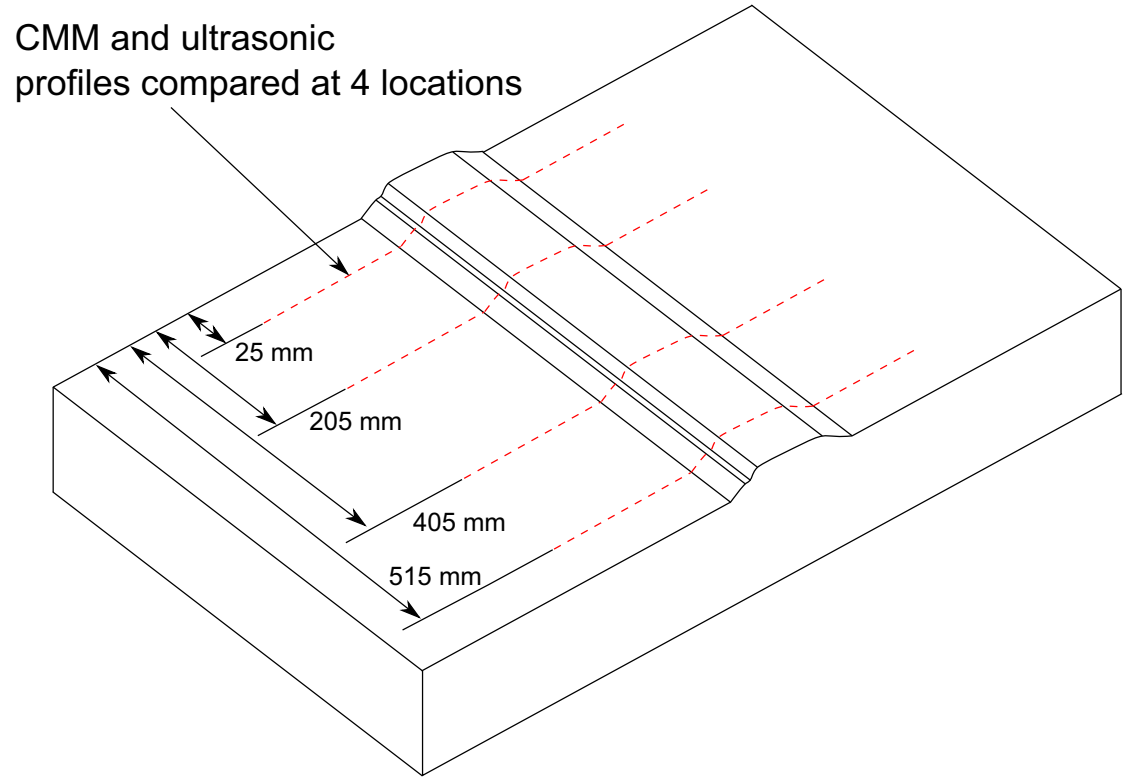

(a)

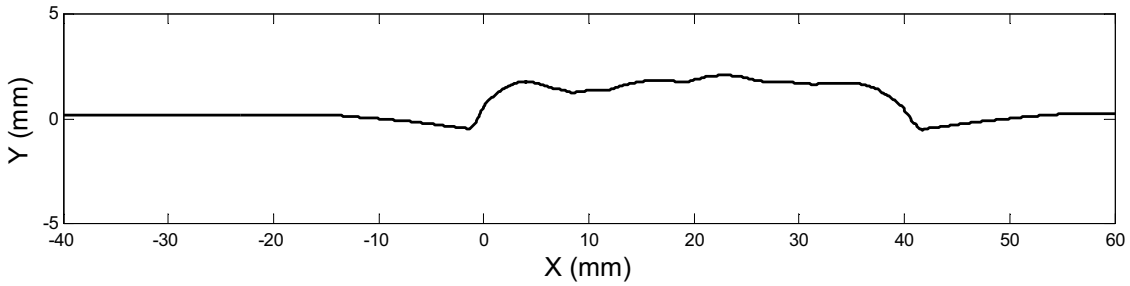

(b)

Figure 7.2.2: a) A diagram showing a sketch of the test block containing a butt weld. The locations on the test piece used for the comparison of ultrasonic and CMM results are shown by the red dashed lines. b) An example of the weld cap geometry extracted from the CMM results.

3. Calculate the search limit, S. This is either the standard deviation of the last three R values, or 1 mm if the standard deviation is less than 1mm.

4. If R is not in the range Rm $\pm$ S then R is set to the maximum value in that range, R2.

5. If the difference between R2 and R is less than 0.5 mm or R2 $<$ R, then R is re-set to the value determined in step 1.

6. Linear interpolation is applied to the A-scans to increase the resolution by a factor of 5.

The motivation behind these processing steps is to guard against the selection of high amplitude signals that can occur before the Front Wall Echo (FWE). In these cases a large jump in R is normally observed compared to neighbouring aperture locations. The process is demonstrated by Figure 7.2.3, and an experimental example is shown in Figure 7.2.4.

The checks outlined in step 5 are designed to detect cases where the change in R is relatively small, which this algorithm is not intended to achieve. Further, step 5 prevents a change in the R value if the new value is at closer range. The rationale for this approach is that the FWE will always be higher in amplitude than subsequent signals as the transmission co-efficient between water and steel is very low; therefore this function should only guard against erroneous signals that occur before the FWE.

Finally, step 6 is designed to increase the accuracy of the centroid that is calculated following peak selection. The centroid is only calculated using the A-scan points that are within 50 % of the maximum amplitude of the selected peak. In most cases the gradient of the envelope in the vicinity of the peak is very high, so increasing the A-scan resolution allows points much closer to 50 % to be selected; this allows the centroid to be calculated over a more symmetrical section of the A-scan. This step is particularly important when focused beams are used, as the focusing causes the length of time that echoes occur over to tend toward the toneburst length generated by each element. Hence the echoes are short and high amplitude, which causes the envelope to have a high gradient. In the case of techniques based on the TFM, the A-scan would be a line of image points down the TFM image.

The signal processing steps can be employed on a group of A-scans from any imaging technique. The described steps have been found to be robust against erroneous signals in the A-scan, however predefined logic will not always produce the correct answer. Therefore to produce the best possible surface profile results it is important to provide the highest quality A-scan to the algorithm. The next section discusses a number of imaging methods that can be used for surface profile measurement, and investigates their accuracy when coupled with the algorithm discussed in this section.

7.2.2 Imaging algorithms

The data from the two test pieces has been analysed using a variety of imaging methods, the most simple of which is beam steering. When imaging in a single medium the delay between the firing and reception of ultrasound on the ith element in an aperture can be calculated directly [80]:

$$\alpha = \frac{sin\theta_s.p.i}{c.T} \tag{7.2.2}$$

where α is the time delay expressed in time steps, p is the inter-element pitch (m), i is the element number, c is the longitudinal wave velocity (m/s), and T is the sample period (s). If the full matrix of data is visualised as a three dimensional matrix $FMC_{i,j,k}$, when i and j are the transmit and receive element numbers and k represents the temporal axis in steps of the sample period, then the α value can

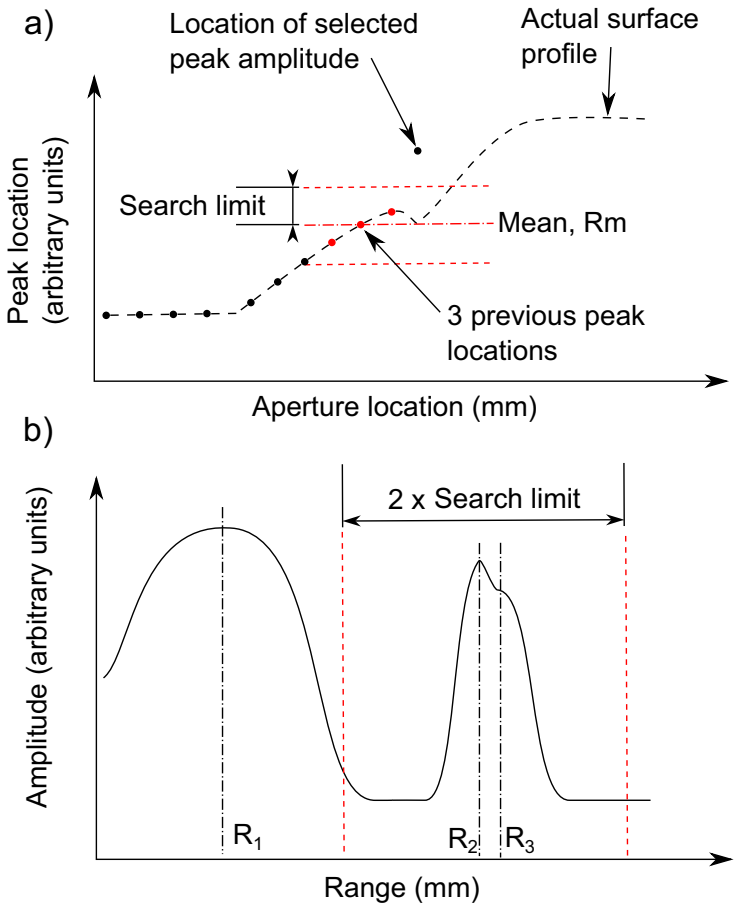

Figure 7.2.3: Diagrams demonstrating the processing performed during surface profile extraction a) a comparison is made between the range of the selected peak and a moving average b) R1 is the maximum amplitude in the A-scan, R2 would then be selected due to the large change in R (as shown in a)). R3 is the range of the envelope centroid.

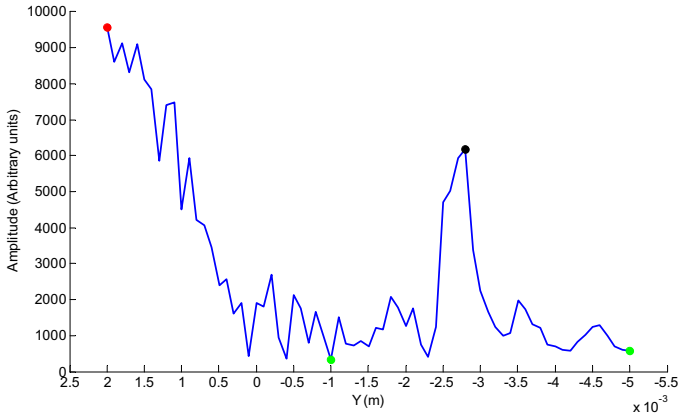

Figure 7.2.4: A plot down a vertical line of image points in a TFM grid using an aperture of 30 elements and a grid resolution of 0.1 mm. The plot demonstrates an example of when a high amplitude signal before the FWE has been selected. The red dot is the highest amplitude signal, and the black dot is the highest amplitude signal that occurs within the search range (the green dots) resulting from the previous three results.

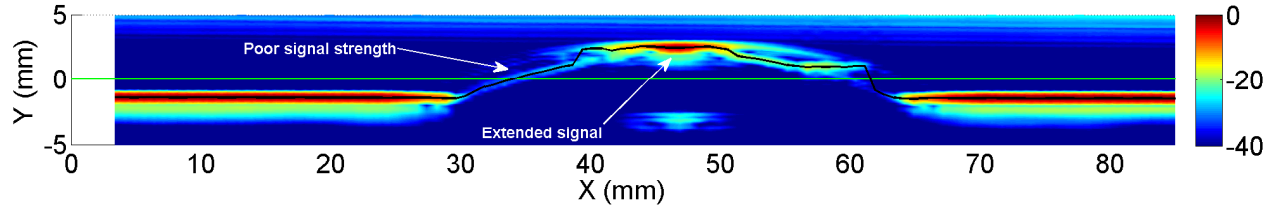

(a)

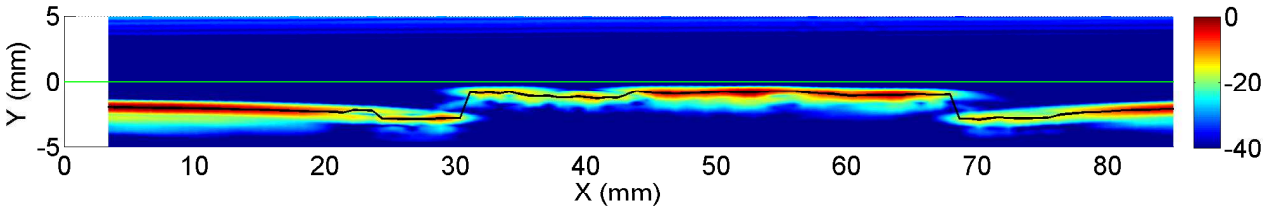

(b)

Figure 7.2.5: A sample image generated using a zero degree plane beam, and an aperture of 10 elements a) artificial weld cap b) real weld cap. The black line represents the surface profile extracted from the results. The colour scale is in decibels.

be used to generate a time history for the steered beam. The time history is commonly referred to as an amplitude scan, or A-scan. The values in the A-scan are calculated using the following expression:

$$A_k = \sum_{i,j=1}^{AP} FMC_{i,j,k+\left(\alpha_{i+}\alpha_j - 2\alpha_{\frac{AP}{2}}\right)} \tag{7.2.3}$$

where i, j, and k retain their previous meaning, and AP is the number of elements in the aperture. When used for the measurement of a surface profile a zero degree beam is used. The beam steering method is disadvantaged by the fact that the ultrasound is not resolved at a particular point. This means that when the beam strikes the interface and is reflected back to the probe, received echoes from different parts of the beam are not in phase with one another. This leads to the reflected toneburst recorded by the aperture being much longer than the tone burst generated by each element. The effects of this mechanism increase with increasing aperture size, and also complicate surface profile extraction as there are multiple peaks in the gate. These effects can be seen in the sample B-scan shown in Figure 7.2.5.

These problems can be resolved by instead using a focused beam. Figure 7.2.6 a) shows an array imaging in a single medium at point p, and transmitting and receiving ultrasound on elements i and j. Plot b) shows the same system but imaging from a point located at the centre of the aperture. The time (τ) required for a wave to travel the round trip from element i to j is described by equation (7.2.4). The time is expressed in multiplies of the sample period used to discretise the data. Equation (7.2.5) calculates the time required to travel the return journey from the aperture centre to the imaging point.

$$\tau = \frac{\sqrt{(x_p - x_i)^2 + (y_i - y_p)^2} + \sqrt{(x_p - x_j)^2 + (y_j - y_p)^2}}{c.T} \tag{7.2.4}$$

$$\tau_{AC} = \frac{2\sqrt{(x_p - x_{AC})^2 + (y_{AC} - y_p)^2}}{c.T} \tag{7.2.5}$$

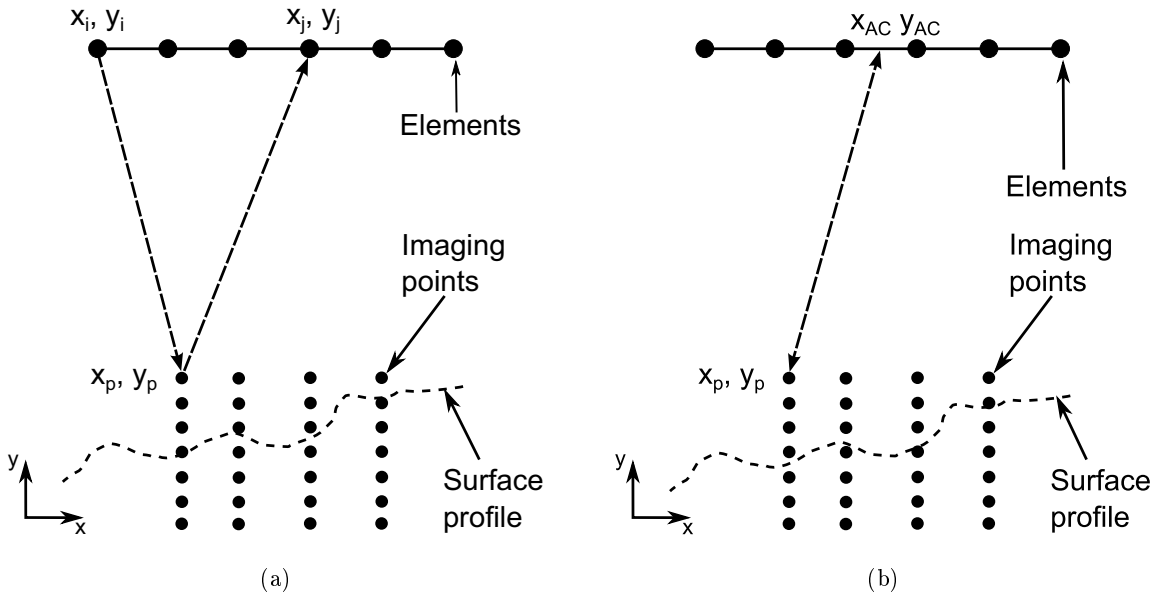

Figure 7.2.6: An array imaging in a single medium a) the ray paths between two elements in the array and the imaging point b) the ray path from the aperture centre.

where x and y are the coordinates using the Cartesian system expressed in Figure 7.2.6. The A-scan for the focused beam can be computed using the same convention as previously:

$$A_k = \sum_{i,j=1}^{AP} FMC_{i,j,k+\tau-\tau_{AC}} \tag{7.2.6}$$

This method is an improvement over the plane beam as the ultrasound is now resolved at a particular point in space. If this point coincides with the top surface of the component being measured, any echoes recorded by the array aperture will be in phase with one another, resulting in a higher amplitude signal and a shorter received toneburst. Focused beams also allow the use of larger aperture sizes which results in smaller beam widths, and therefore greater spatial resolution.

A problem resulting from the use of a larger aperture size to generate a focused beam is the presence of unwanted echoes in the time trace recorded from each element. Figure 7.2.7 a) demonstrates a case where a large array aperture is focusing at the interface between two materials. As the array elements have a wide directivity pattern, echoes will be recorded from a significant portion of the surface profile for each element. The delay laws used to process the data will phase the A-scans from each element such that the echoes of interest are in phase when the processed A-scans are formed, in-line with 7.2.6. Echoes from regions of the surface profile not at the focal point will not be in phase with one another, leading to destructive interference when the processed A-scan is formed. The degree of destructive interference will increase with the aperture size. However, the recorded normal reflection (shown in the figure) will be much higher in amplitude that the reflection at the focal point, as it is closer to normal incidence on the interface and the array element's directivity pattern is maximum at normal incidence. The normal reflection will be present in the A-scans from most of the transmit-receive combinations within the right hand side of the aperture. When the processed A-scans are formed the normal reflections will not be in phase, but the difference in phase will not be large relative to the length of the tone burst emitted by a 2 MHz array. Hence there will be constructive interference of

these signals, leading to a high amplitude signal being present in the processed A-scan earlier in the time base than the echo from the focal point. The A-scans presented in Figures 7.2.3 b) and 7.2.4 are caused by the type of situation discussed here. Example B-scans that contain these signals from a variety of imaging methods are also shown in Figure 7.2.7.

A further problem with using larger aperture sizes is that the aperture becomes less sensitive to reflectors not at the focal point, as the degree of focusing achieved by the array increases with aperture size. For this application the location of the interface, and therefore the desired location of the focal point is not known. A method which mitigates against this problem is the Total Focusing Method (TFM) [4]. This method uses the array to focus at points in a uniform grid. If the grid is positioned in the region where the interface is known to be located, then a fine grid will result in a focus location within a fraction of a millimetre of the interface across the whole width of the imaging grid. The TFM uses the same delay laws as the focused beam but rather than producing delays relative to the aperture centre, the round trip flight time is used to extract the appropriate amplitude from the FMC data for every transmit receive combination in the aperture. The summation of all these values results in an amplitude value that is assigned to a pixel centred at the focus location. Using this convention, the amplitude of any imaging point, P, in a TFM image can be described by equation (7.2.7).

$$P = \sum_{i,j=1}^{AP} FMC_{j,j,\tau} \tag{7.2.7}$$

Repeating this process for the entire imaging grid results in an image of the focusing grid. The TFM is normally applied using an aperture size equal to the number of elements in the array. This relies on the array elements maintaining sensitivity as the angle between the element normal and the line intersecting the centre of the element and the imaging point increases. Results presented in chapter 4 have shown that modern piezo-composite array elements with a width of the order of a wavelength at the centre frequency of the transducer exhibit a directivity pattern in water that is not well modelled by the assumption of piston like behaviour. Experimental measurements have shown that transmit-receive sensitivity typically decreases rapidly as the angle from normal exceeds 30 degrees. When arrays are utilised for angle beam inspection a wedge is normally employed of a material with a wave speed below that of the material being inspected. This is done to reduce the amount of steering required by the array to generate high angle compression and shear waves, as ultrasound is refracted at the interface between the wedge and the component. For the measurement of surface profile a wedge is not used and a water path of the order of 20 mm or less would be expected. Limiting the maximum angle between element normal and focal point to 30 degrees for a zero degree array angle results in a maximum aperture size of approximately 23 mm, or 30 elements of the 2 MHz 0.75 mm pitch array used to collect the experimental data. This could be increased by increasing the water path, but this will also decrease the degree of focusing achieved by the array. For this reason a TFM algorithm has been produced which also utilises electronic scanning of the aperture to enable a larger length of surface profile to be measured whilst limiting the angular operating range of the elements.

Figure 7.2.8 a) describes a TFM algorithm using an array sub-aperture to generate a zero degree beam, and electronically scanning the aperture. The imaging grid is then spaced in X by the array pitch; this method is effectively the same as the Almost Total Focusing Method (ATFM) [49]. Plot b) demonstrates the same arrangement but with a smaller spacing between the imaging points in X, resulting in a small range of beam angles centred about zero degrees. This method is intended to provide

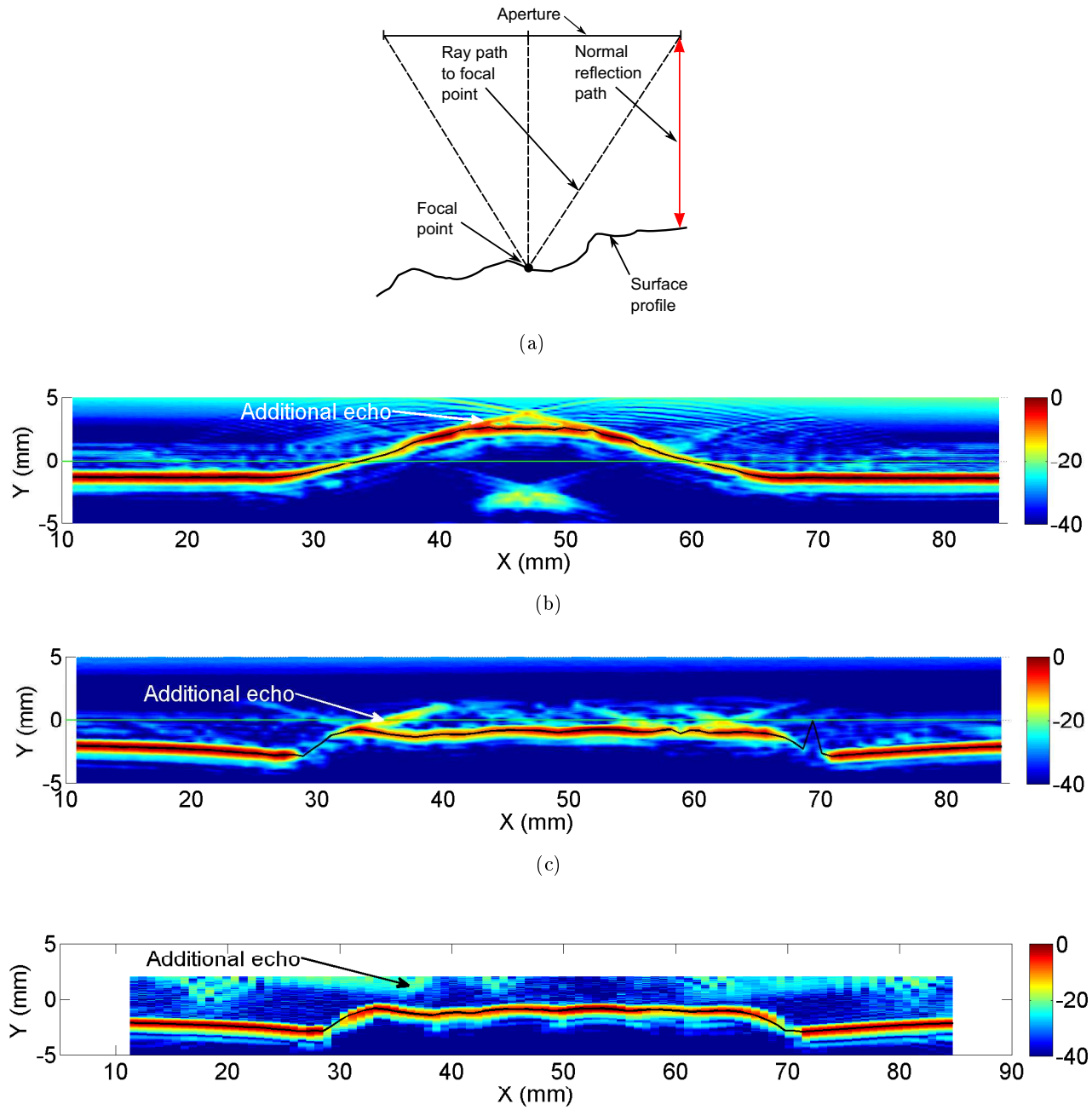

Figure 7.2.7: The problems associated with large aperture sizes and focused beams a) a diagram that presents the kind of experimental arrangement that causes the problem b) a sample B-scan generated using a 30 element aperture and the artificial weld cap test piece c) the same results from the welded test piece d) a TFM image of the welded test piece surface. The extra echoes are marked on each of the B-scans, and the black line represents the surface profile extracted from the results. The colour scale is in decibels.

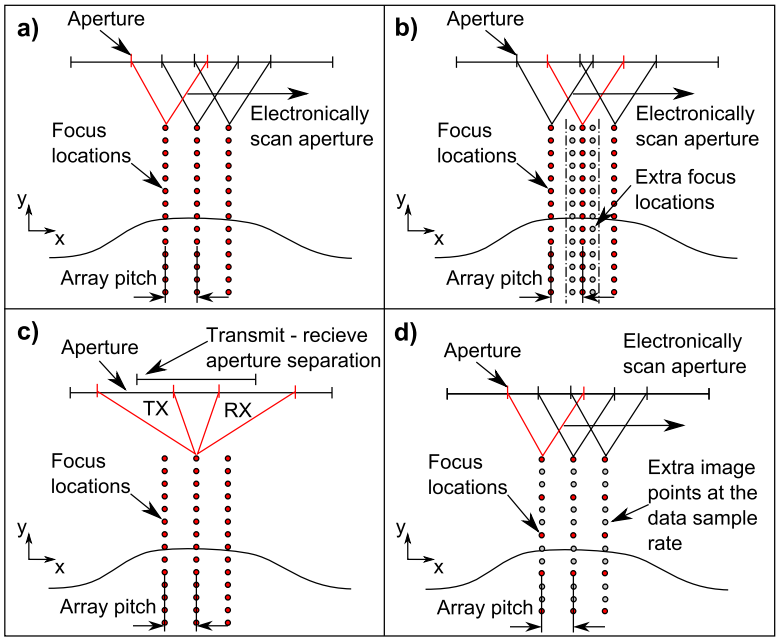

Figure 7.2.8: A series of diagrams explaining the variations of TFM used for surface profile measurements: a) 0 degree beam angle and electronic scanning b) extra imaging points in X c) transmit-receive aperture separation d) extra image points in Y (TFMe).

higher resolution in the surface profile measurement in X. Plot c) demonstrates the same case as a) but with a transmit and receive aperture separated by a number of elements. This method may help to mitigate the problems previously discussed where large array apertures generate high amplitude signals early in the time base, due to normally incident pulse-echo reflections on the interface. Separating the transmit and receive apertures removes the normal incidence pulse-echo signals as pulse-echo A-scans are no longer used during image formation. Plot d) uses the same arrangement as a) but additional image points between the focal points.

One of the main disadvantages of the TFM is the computation burden required to implement the image formation. Conventionally focused B-scans rely on the fact that the beam produced by the transducer results in a region either side of the focal point where the beam is sensitive to reflectors, known as the depth of field. This principle can be applied to TFM imagery to reduce the computational cost of the method. Figure 7.2.8 plot d) demonstrates the case where zero degree beams are generated by a sub-aperture which is electronically scanned along the array. The array is focused at a number of depths, but there are extra image points between the focal points. The resolution of the extra points is driven by the sample period used to collect the data, and the wave velocity. The extra image points are formed by calculating the delay law for a particular image point and locating the data point in the experimental data that corresponds to that point. A number of data points either side of this point are then used to build the amplitude of the extra image points. This is effectively building a short processed A-scan for each focal point in-line with the method employed for a conventional focused beam. This variant of the TFM will be referred to as the Total Focusing Method Extra (TFMe). The process to calculate the amplitudes of the points in the short A-scan,P_E, is described by the following equation:

$$P_E = \sum_{i,j=1}^{AP} FMC_{i,j,\tau-E:\tau+E} \tag{7.2.8}$$

where E is the number of extra image points, and other symbols retain their previous meaning. The number of extra image points, E, possible before any overlap in space with other image points is:

$$E = \frac{Y_R}{2s} \tag{7.2.9}$$

where Y_R is the resolution in Y of the TFM imaging grid, or the vertical distance between consecutive focus locations. The separation in space between the extra points can be calculated for a zero degree beam thus:

$$s = \frac{c.T}{2} \tag{7.2.10}$$

All of the imaging methods discussed have been applied to the experimental results recorded on the artificial weld cap test piece, and can be seen in Figure 7.2.9. In plot a) the B-scan produced using a conventionally focused 0 degree beam is presented. The extracted surface profile is shown by the black line. The B-scan shows a high amplitude response from the surface of the test piece. The signal amplitude decays on the side of the weld cap as much of incident beam is reflected away from the aperture. Signal clarity is also lost on the top of the weld cap as the interface is several mm from the depth of focus. This result is the baseline against which the TFM based results are evaluated.

The most basic TFM case is presented in plot b). The results are similar to the focused B-scan but the interface signal amplitude is more consistent, especially on the sides of the weld cap. This causes the extracted surface profile to exhibit a smoother variation. The result when using extra imaging points in X are very similar, and demonstrates that improved spatial resolution in X is not required for a smoothly varying interface such as this.

The results from the last two TFM methods contain the signals present before the interface echo, as previously discussed. The image produced using transmit-receive aperture separation, shown in plot d), does not contain these signals. However, the interface signal amplitude decays on the sides of the weld cap significantly more than the previous TFM results. This is likely to be due to the fact that this method relies on a wider portion of the element's directivity pattern where the sensitivity is lower. This result may make the method unsuitable for use with surfaces with abrupt changes in profile, and the benefits of the technique are minimal as the surface profile algorithm appears robust against extra signals in the gate. The technique also lowers the coverage of the surface profile provided by the array.

The final image, plot e), has been generated using the TFMe approach using a grid resolution of 2 ppmm. The image is also identical to the image produced using standard TFM and a grid resolution of 20 ppmm. This demonstrates that the depth of field produced by the array is large enough that increasing the distance between focal point in Y by a factor of 10 has a minimal effect on the image produced. This technique is very promising for the 0 degree case as there is minimal computation cost in calculating the co-ordinates of the extra image points. For conventional TFM images where the beam angle is constantly changing, the co-ordinate calculation is more time consuming as the beam angle is different for every image point. Thus this technique would only be attractive when the TFM image resolution is high enough that the extra computation cost required for TFMe image co-ordinates is significantly smaller than the cost of implementing the full TFM. A comparison of computation times has been carried out to demonstrate this point and the results are presented in Table 7.2.1. The results show that the computation of delay laws (including image coordinates) is negligible in comparison to the time required to process the FMC data to form the image. For TFMe this process takes approximately

Table 7.2.1: TFM computation times for imaging grids of equal size to those shown in Figure 7.2.8. Ry is the vertical resolution of the imaging grid in points per mm.

Method	Ry (pts per mm)	AP	Computation times		
			Delay laws	Image formation	Extrapolated time for typical inspection
TFM	20	20	1.5 s	33.2 s	2 h 19 m
TFMe	2	20	0.2 s	13.8 s	58 m
TFMe	20	20	1.5 s	121.5 s	8 h 28 m

60 % of the time required for TFM at higher resolution. The results can be extrapolated to a typical weld inspection of a pipe that requires surface profile mapping. Assuming an outer diameter of 400 mm and a circumferential scan step of 5mm the total TFM computation time is estimated to be 2 h 19 m, and 58 m for TFMe.

The following section discusses the results from all surface profile measurement methods and presents the results of a quantitative analysis of errors relative to the CMM results.

7.2.3 Experimental results

All of the ultrasonic methods of surface profile measurement discussed have been applied to both test pieces, and a quantitative analysis of the measurement error has been made relative to the CMM results. The ultrasonic and CMM results have been manually aligned with one another, and measurement errors have been calculated by comparing the surface height values at the same locations. The CMM results were collected at very high spatial resolution (1 micrometer), in contrast the ultrasonic results are typically limited in resolution in X by the array pitch. For a zero degree array angle this means a resolution in X of only 0.75 mm. To allow a results comparison at the same locations, the CMM results were interpolated to find the surface height at the X locations of the ultrasonic results.

The measurement error was calculated as the difference in surface height of the two methods. The Root Mean Squared (RMS) error was then calculated across the entire surface profile. For the machined test piece the comparison was only made at one Y location, whilst comparisons were made at four Y locations along the welded test piece (details can be seen in Figure 7.2.2). For the welded test piece the RMS error was calculated over all four surface profiles. A complete summary of the results is shown in Table 7.2.2, this includes results using an angled array.

The results from the plane beam show that as predicted the measurement error increases with increasing aperture size. The RMS error is higher for the welded test piece, this is due to higher errors in the weld toe. Regardless of the aperture size used, the errors are so high that this technique is unsuitable. The results for the focused beams are significantly better than those for the plane beam. For both test pieces using a zero degree array angle the measurement error is lowest for an aperture size of 10 elements, and increases for aperture sizes above and below this. As previously discussed this is caused by the degree of focusing achieved by the array combined with errors in the surface profile extraction due to unintended signals in the A-scan. The results using an angled array to measure the artificial weld cap show that the measurement error is lowest for an aperture size of 20 elements. This is likely to have been caused by the increasing water path as the aperture is scanned along the

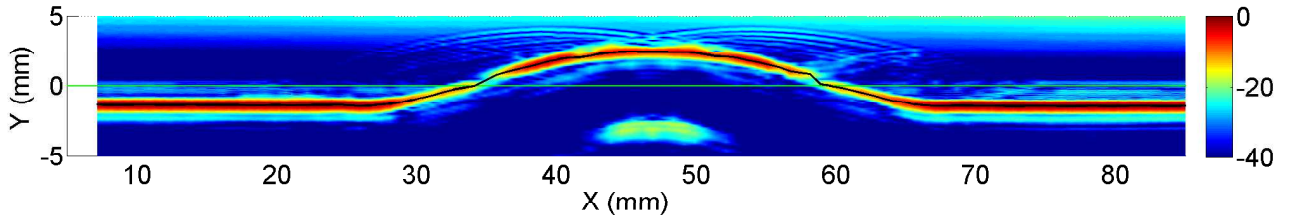

(a)

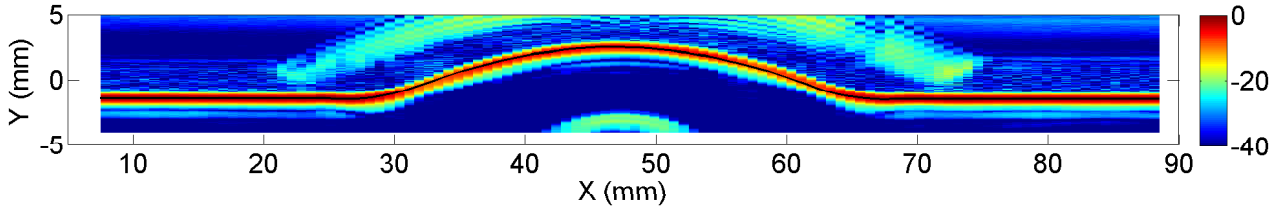

(b)

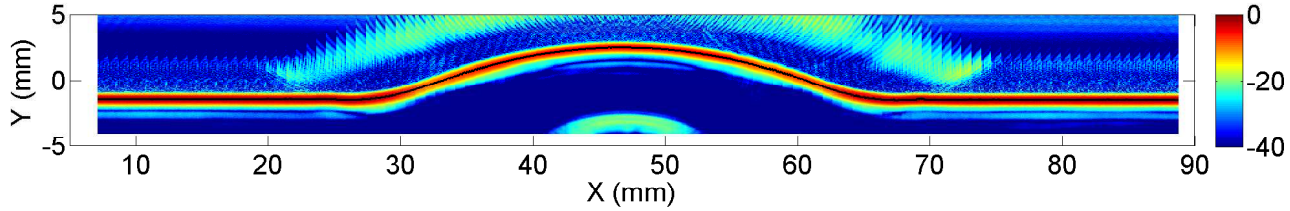

(c)

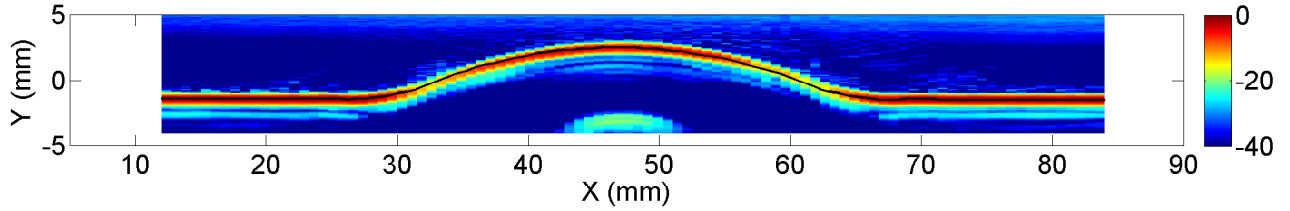

(d)

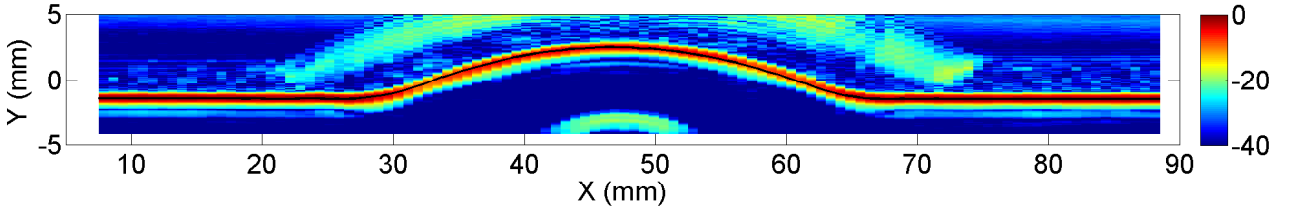

(e)

Figure 7.2.9: Example B-scans produced using conventionally focused beams and the methods described in Figure 7.2.8 using a 20 element aperture a) 0 deg focused B-scan focused at 0 mm depth b) Electronically scanned TFM using a resolution of 20 ppmm c) extra image points in X d) transmit-receive aperture separation by 12 elements, and image resolution of 10 ppmm e) extra image points in Y (TFMe) using a resolution of 2 ppmm. The black line represents the surface profile extracted from the results. The colour scale is in decibels.

Table 7.2.2: A summary of the comparison between ultrasonically measured surface profile and the results from a CMM machine. For the TFM results Ry is the vertical resolution of the imaging grid in points per mm, and TXRX is the separation between the transmit and receive apertures in elements.

Array angle (deg)				0	7	0
Beam type	Aperture (elements)	Ry (pts per mm)	TXRX (elements)	Artificial weld cap		Welded test piece
				RMS measurement error (mm)		
0 degree, plane	5	-	-	0.13	0.36	0.27
	10	-	-	0.31	0.30	0.31
	20	-	-	0.68	0.65	0.55
0 degree, focused	5	-	-	0.18	0.39	0.16
	10	-	-	0.10	0.19	0.14
	20	-	-	0.15	0.06	0.18
	30	-	-	0.18	0.13	0.38
TFM	20	5	-	0.11	0.08	0.12
	20	10	-	0.09	0.05	0.10
	20	20	-	0.09	0.04	0.10
	30	5	-	0.09	0.09	0.21
	30	10	-	0.09	0.05	0.12
	30	20	-	0.10	0.05	0.12
TFMe	20	2	-	0.07	0.04	0.09
	20	5	-	0.08	0.03	0.10
	20	10	-	0.07	0.04	0.10
	30	2	-	0.08	0.04	0.21
	30	5	-	0.09	0.04	0.17
	30	10	-	0.08	0.04	0.12
TFM + TXRX separation	20	10	6	0.07	-	0.11
	20	10	2	0.07	-	0.13
	20	10	12	0.09	-	0.12
	30	10	6	0.09	-	0.14
	30	10	2	0.08	-	0.14
	30	10	12	0.07	-	0.12

array. The increased path means that 10 elements are no longer able to focus at the interface, hence measurement accuracy is decreased.

The results from the TFM based imaging methods are presented for a number of imaging grid resolutions, apertures sizes, and transmit-receive apertures separations. The results show that for an aperture size of 20 elements all of the TFM based algorithms consistently outperform the zero degree focused beam by a small margin. For an aperture size of 30 elements the measurement error increases for the welded test piece; this is also true when a transmit-receive aperture is used on the welded test piece. This result suggests that the higher surface roughness of the welded test piece reduces the accuracy of these algorithms. The weld cap on the welded test piece is much flatter than the machined block, which has a continuously changing curvature. This appears to increase the problems in the weld toe area of the surface profile due to high amplitude normal reflections from the interface, as previously discussed in section 7.2.2. The gradient of the surface at the weld toes is also much higher than the artificial weld cap, further decreasing measurement accuracy as most of the energy is reflected away from the active aperture in the array. Inspection of the results using transmit-receive aperture separation suggests that the results are more consistent, but any gains in accuracy in these areas of the surface profile are eroded by a small decrease in overall accuracy.

The most impressive results from the TFM based methods are those when using extra imaging points. The results show that decreasing the vertical imaging grid resolution as low as 0.5 mm does not adversely affect measurement accuracy at a data sample rate of 25 MHz; this sample rate results in a separation of the extra imaging points of only 0.03 mm. These results show that the depth of field achieved by the array is large enough that results are not adversely affected when using a coarse focusing grid. The reduction in TFM image generation is significant, especially for large scanned data sets. A comparison of computation times has shown that for a typical inspection the time required for the surface profile imaging could be reduced from over 2 hours to approximately 1 hour by using TFMe rather than higher resolution TFM. The TFMe technique can be applied to standard TFM imagery, however the benefits in computation time are reduced as the beam angle is not fixed. Hence image coordinate calculation is significantly more computationally expensive as the beam angle must be calculated for each point in the focusing grid.

Example surface profiles from the welded test piece can be seen in Figure 7.2.10, and corresponding measurement errors can be seen in Figure 7.2.11. The results show that all ultrasonic measurement methods exhibit the highest measurement error in the toe of the weld. The profiles from the focused beam are very similar to those measured using TFM based approaches, although the measurement error is marginally higher away from the weld toes. However, the advantage of the TFM methods is that they are far less sensitive to the imaging parameters e.g. aperture size. The results from the angled array show that the optimum aperture size used to generate the focused B-scan has increased from 10 to 20 elements relative to the results from a zero degree array angle. The RMS measurement error changes from 0.19 to 0.06 mm for apertures sizes of 10 and 20 elements respectively when using an angled array. Conversely the TFM results were consistently able to match the best focused beam results without changing imaging parameters. The measurement error from the angled array data is consistently lower for all methods relative to the zero degree array angle data because the experimental arrangement reduces the parasitic effect of high amplitude normal incidence echoes.

Based on this body of evidence, the TFMe is recommended as the best method for surface profile measurement. This approach offers the best balance between measurement accuracy, processing speed,

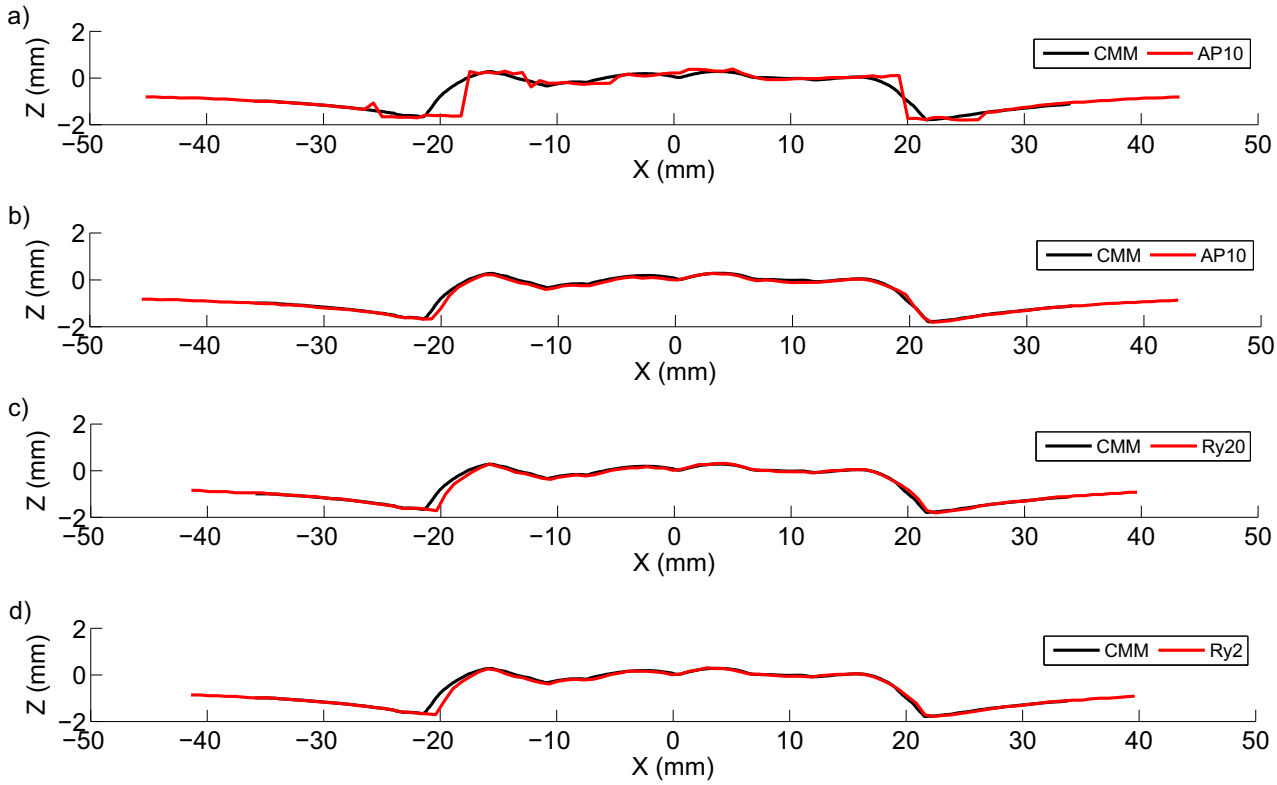

Figure 7.2.10: Example surface profiles from the welded test piece. Unless otherwise stated imaging parameters are given in the plot legend. a) plane 0 degree beam b) focused zero degree, c) 0 degree TFM (AP20), and d) 0 degree TFM with extra imaging points in Y. The CMM result is the black line and the ultrasonic results are the red lines.

and robustness to changes in imaging parameters. Now that the achievable accuracy of surface profile measurement is understood, evidence of the effect that amplifier saturation has on surface profile measurement accuracy must be investigated.

7.2.3.1 The effect of data saturation

The most commercially attractive way of implementing an inspection system utilising surface profile adaptation is to acquire a single set of FMC data that is used for both surface profile measurement and subsequently inspection using the measured surface profile. This necessitates beam forming in both the water above the component and in the component itself. To maximise the dynamic range available in the component a large gain value must be used as the transmission coefficient between water and metals is very low, and the amplitudes of the ultrasonic waves generated by a single element are very low. The consequence of this approach is that the surface echo is saturated in the unprocessed FMC and this will therefore have some impact on the peak detection used to record the surface profile.

The effect of data saturation has been investigated by artificially adding gain to the FMC data collected on the artificial weld cap and comparing the surface profiles extracted from the data. Data collected with a zero and eight degree array angle has been processed. In each case the data was collected with a pulser voltage of 200 V and an amplifier gain such that the pulse-echo surface echoes on all array elements were below 80 % of the dynamic range of the amplifier (26 and 35 dB for 0 and 8 deg array angles respectively). Artificial gain has been added to the data by multiplying all the time

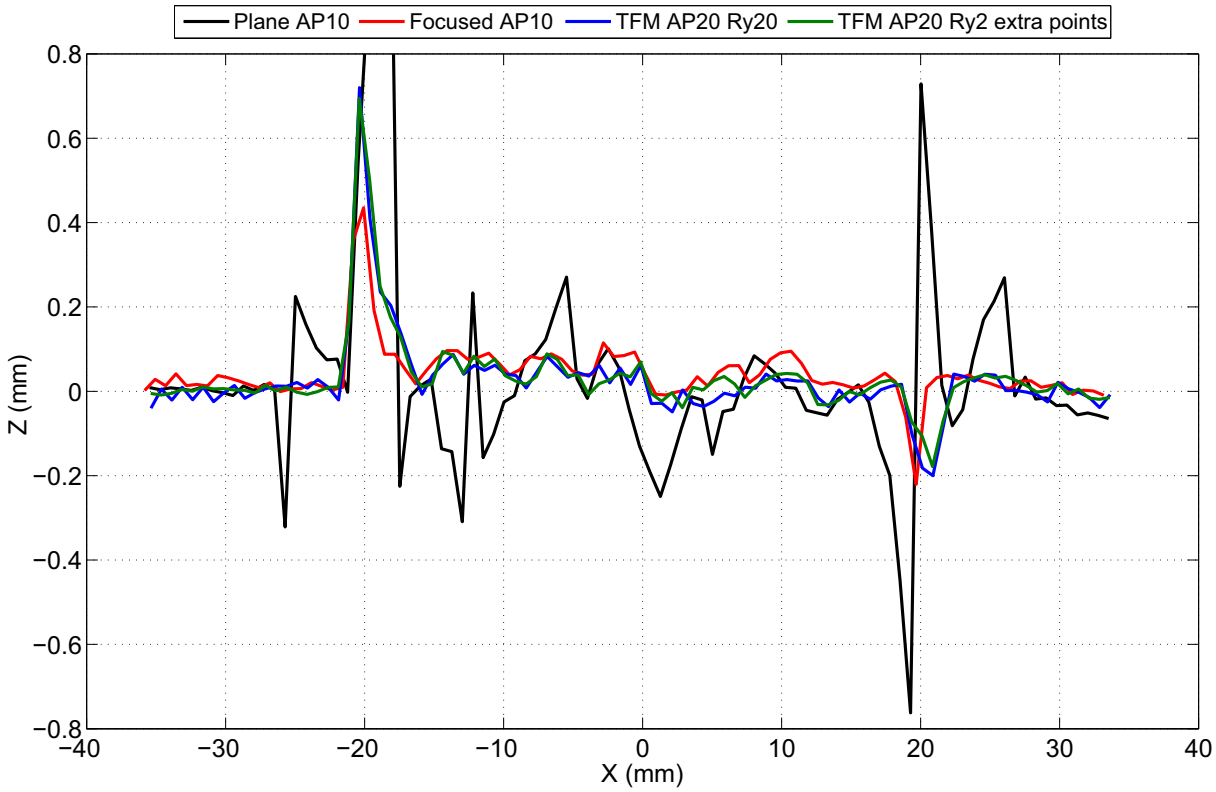

Figure 7.2.11: Example surface profile measurement errors from the welded test piece. Imaging method and parameters are given in the plot legend.

traces by a factor and then setting any value outside of the Analogue to Digital Converter (ADC) range to the appropriate value e.g. 0 and 4095 for 12 bit ADC resolution, or -2047 and 2048 for signed integer values.

The errors in measured surface profile relative to the CMM data are presented in Figure 7.2.12 and the RMS error across the profile is shown in Figure 7.2.13. The plots show that for increasing levels of data saturation the measurement error increases, and the largest increase is on the sides of the weld cap where the signal amplitude is lowest. The performance is generally lower when using a 0 degree array angle, and increasing data saturation causes an increasing level of constant measurement error across the profile. This is not observed when the array is angled, but a general increase in the error of the sides of the weld is seen. To put the result into context at a sample frequency of 25 MHz a 0.1 mm error is equivalent to approximately 3 time samples.

The RMS error does not reach 0.1 mm for the angled array until an artificial gain factor of 6, which is equivalent to a data collection gain of 53 dB. FMC data is normally collected with typical element sizes at a gain value in the region of 40-50 dB. This result suggests that it is possible to extract accurate surface profiles using saturated data, but the amount of saturation should be minimised and an angled array helps as much of the ultrasound skips away from the array when it is reflected off the surface of the steel.

a)

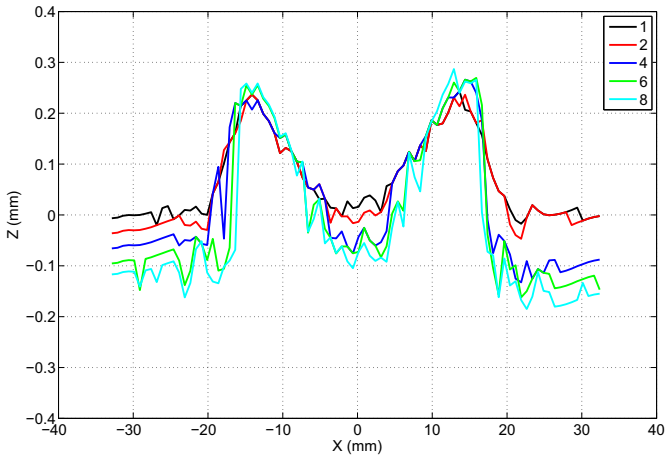

b)

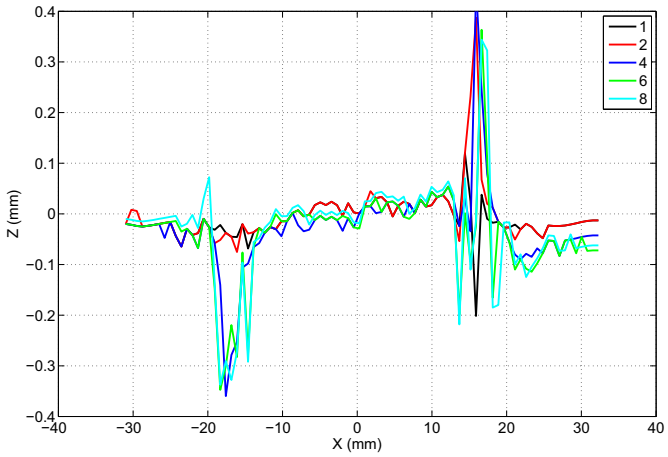

Figure 7.2.12: The errors in surface profile measurement due to increasing levels of amplifier saturation of the data from the artificial weld cap test piece a) 0 deg array angle b) 8 deg array angle. The plot legends show the artificial gain factors used.

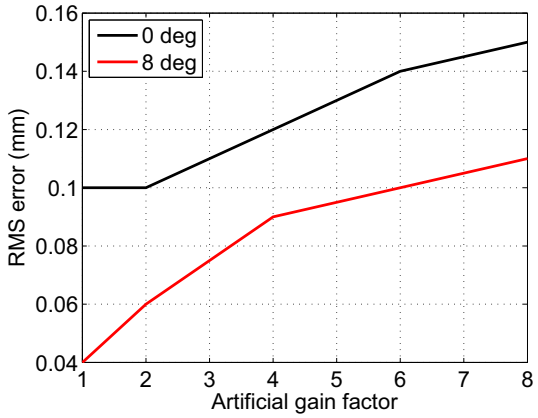

Figure 7.2.13: The RMS errors in surface profile measurement across the entire profile due to increasing levels of amplifier saturation for a zero and eight degree array angle.

7.3 The effect of surface profile measurement inaccuracies

When beam-forming though an irregular interface between two materials it is necessary to employ delay laws which are adapted to the interface in question. For this project an array is used to measure the geometry of the top surface of a component to allow adapted delay laws to be calculated. It follows that any error present in the measured surface profile introduces errors in the delay law which degrade beam quality. Therefore, an important step in the application of conformable array technology is the selection of bounding values of the essential parameters which govern the effectiveness of the ultrasonic inspection. Within these boundaries the array is able to produce a beam of sufficient quality for an inspection to be carried out; outside of these boundaries the inspection performance will have degraded to a point where performance is no longer adequate.

The previous section has investigated the measurement performance which is achievable using a number of different imaging methods. This section will investigate the effect that surface profile measurement errors have on inspection performance via modelling of the ultrasonic beam.

7.3.1 Modelling approach

The investigation has been carried out using a two dimensional beam model that has been reported previously in Chapter 5, with some minor additions to the model. Modifications to the model include the calculation of the local surface normal at the point where a ray transitions between material one and two. This enables the transmission coefficient and effective propagation distance to be calculated for smoothly varying irregular surface profiles. The model structure after alterations is shown in Figure 7.3.1.

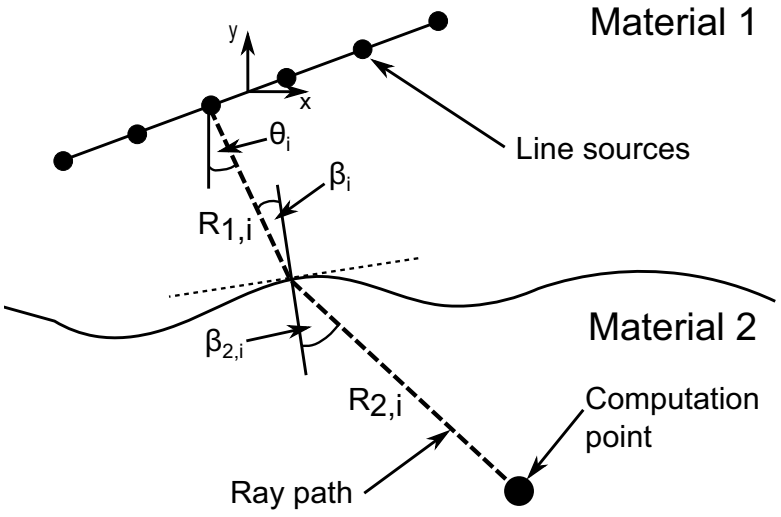

Figure 7.3.1: The structure of the beam model used for this study.

The model has been used to investigate the effect of measurement inaccuracies for three different beams, three different surface profiles, and three different centre frequencies. The irregular surface profiles used are shown in Figure 7.3.2, and the modelled arrays are the same as those used in chapter 5.2, shown in Table 5.3.1. The selected surface profiles are designed to span a range of complexity from a flat interface at one end of the spectrum, increasing in complexity to a artificial weld cap with

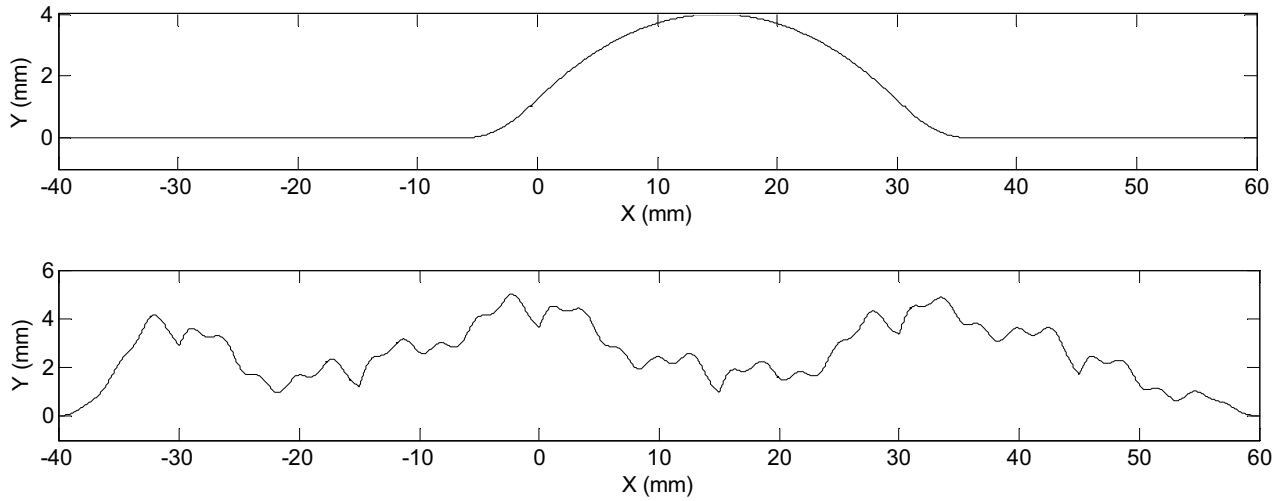

Figure 7.3.2: Plots of two of the surface profiles used in this study: a) artificial weld cap, b) wavy surface. The graphs are not to scale.

smoothly varying profile (and of the same geometry as the machined test piece in section 7.2), and finally increasing in complexity again to a wavy surface with extreme surface variation that has been generated using a summation of sinusoidal waves. The modelled beam types are designed to span a range representative of what may be used if the technology were deployed in the field. The selected beams are zero and 60 degree longitudinal waves (0L and 60L), and a 45 degree shear wave (45T). All of the beams are focused at a depth of 30 mm. The 2D ultrasonic field for all of the beam types have been simulated for the three different surface profiles, when using the correct surface profile to produce adapted delay laws. The results can be seen in Figure 7.3.3.

The simulated fields demonstrate that there is a significant reduction in beam quality when changing the surface profile from a flat interface, to a weld cap, to a wavy surface. One of the reasons for this behaviour is that the changes in surface normal due to the irregular surface cause a change in transmission coefficient. The change in transmission coefficient effectively introduces variation in element sensitivity into the system. The deterioration in performance from the flat interface is greater for the wavy surface profile than for the weld cap profile. This is due to the fact that the standard deviation of the wavy surface is much higher than that of the weld cap. This means that the surface normal varies much more over the range of the surface profile that the ultrasound from each array element will propagate through, and thus a greater variation in transmission coefficient is observed.

The images produced for Figure 7.3.3 have been produced using a single depth focusing algorithm. This means that the inspection is only optimised at a single depth in material two, and as a result the beam is heavily distorted in the first 20 mm of material two. The field presented in plot g) in Figure 7.3.3 shows that there are two additional focus spots introduced into the field before the intended focal point. This type of beam artefact would make the interpretation of inspection results difficult unless a number of different beams were used to cover the depth range that required inspection. A better approach would be to use an imaging method that optimises the image at all depths, e.g.the Total Focusing Method (TFM) and associated approaches [4, 49]. As the primary application of conformable array technology for this project is weld inspection, ultrasonic inspection methods that utilise a fixed beam angle are the most appropriate. For example, the ATFM algorithm is an implementation of the TFM which uses a defined beam angle [49].

The simulation results have demonstrated that the inspection of components with an irregular surface profile is challenging when the exact profile is known. In practice a measurement of a component's surface profile will be used to update delay laws. This measurement will have an accuracy that will cause a corresponding error in the calculated delay laws. The magnitude of the error that can be tolerated before an unacceptable reduction in beam quality must be known. This has been investigated by performing a Monte Carlo simulation for all combinations of beam type, surface profile, and array specification. In previous studies Monte Carlo simulations have been performed by using a random number generator to assign variations to element performance, e.g. element sensitivity. For this study, the varied parameter in the Monte Carlo simulations will be surface profile measurement error. A measurement error taken from a normal distribution has been added to the entire surface profile used to calculate delay laws. The model will produce 1000 realisations of the predicted field for each simulation group. The simulation group is defined by the size of the maximum surface profile measurement error (Mv) that can be assigned by the random number generator. The measurement error is set such that each time the model is run a normal distribution of error is set across the entire surface profile that varies between +/- the maximum error (Mv). The results are compared to the ultrasonic field predicted using no measurement error.

Once the model is run for a number of simulation groups the results are processed, and a limit on surface profile measurement accuracy is estimated. The methodology used is discussed in the next section.

7.3.2 Methodology for results analysis

The results of studies investigating the effect of variations in phased array element performance in chapter 5 have shown that the characteristic of the ultrasonic beam most affected is the enlargement or creation of artefacts in the ultrasonic field. A change to the ultrasonic field due to the introduction of a beam artefact is referred to as a change in the background level. Examples of possible beam artefacts that may increase the background level are the enlargement of, or creation of sidelobes, and raising of the background amplitude of the ultrasonic field. This study will use the change in background level as a metric for classifying the degree of beam degradation caused by surface profile measurement error.

The purpose of this investigation is to estimate the accuracy with which the surface profile must be known in order to beam-form through an interface, and generate a beam of sufficient quality. Analysis of results from simulations has shown that results are well separated if the standard deviation of measurement error for the complete surface profile is plotted against the change in background level. As the Mv value is increased the standard deviation of measurement error increases, as does the mean and standard deviation of change in background level. A line of best fit must then be added to the plot to enable the standard deviation of measurement error that results in a change in background level of 2 dB to be predicted. A full explanation of the significance of a value of 2 dB can be found in chapter 5, but put simply a change in background level of 2 dB results in a minimum amplitude separation of 8 dB between the main beam and any beam artefacts. As the model is simulating the free field, a 8 dB separation would result in a 16 dB separation in the pulse-echo case. This method of results analysis is based on the approach suggested in BSEN 12668 part 2: 2010 [6], a standard for the assessment of single element probes.

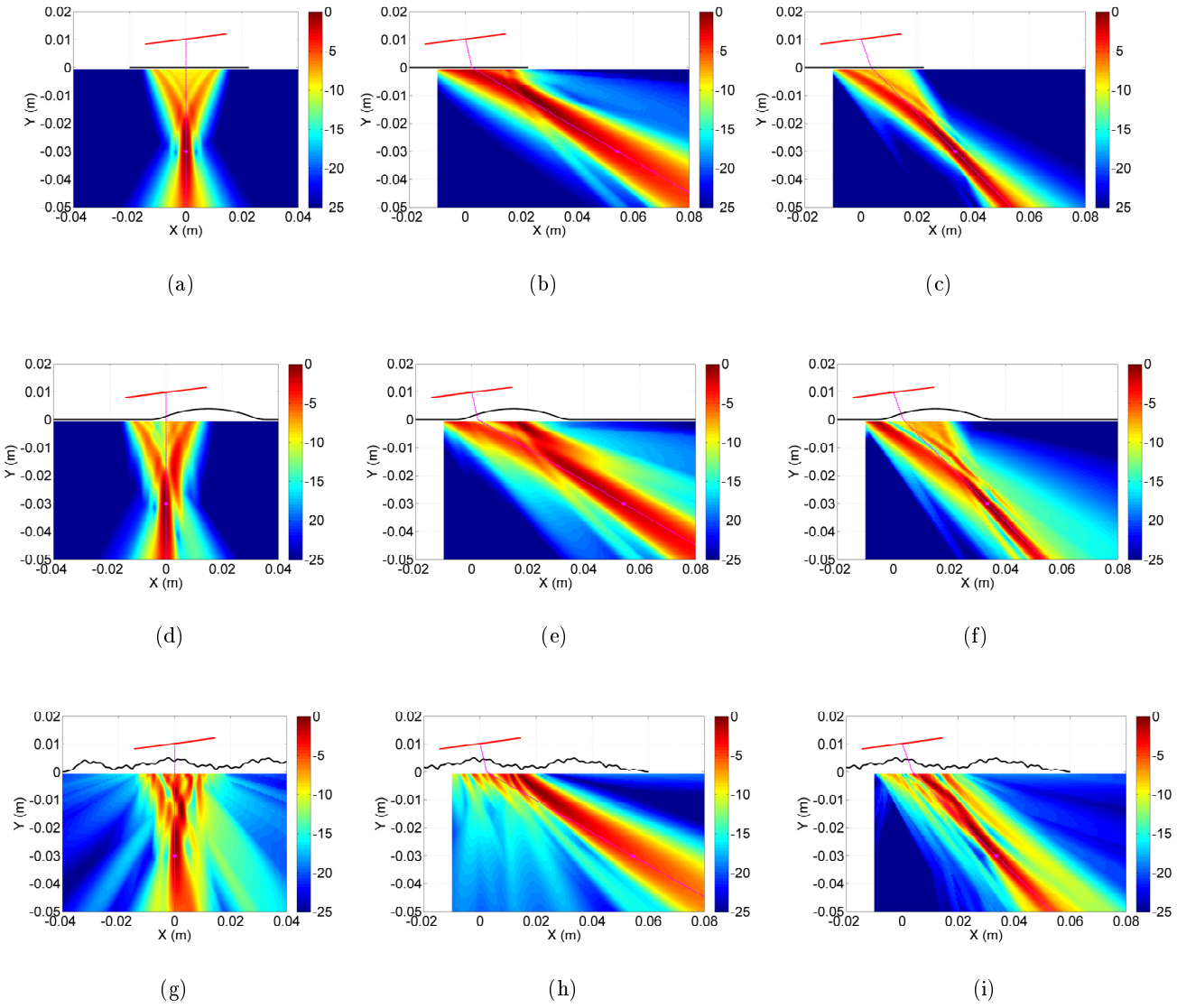

Figure 7.3.3: Beam plots of the three different interfaces at a centre frequency of 2 MHz using the following beam types: 0 and 60 degree longitudinal, and 45 degree shear wave. All beams are focused at 30 mm depth in material two using knowledge of the surface profile in each case. a) - c) flat interface, d) - f) artificial weld cap, g) - i) rough surface based on a summation of sine waves. In each case the colour scale is in decibels.

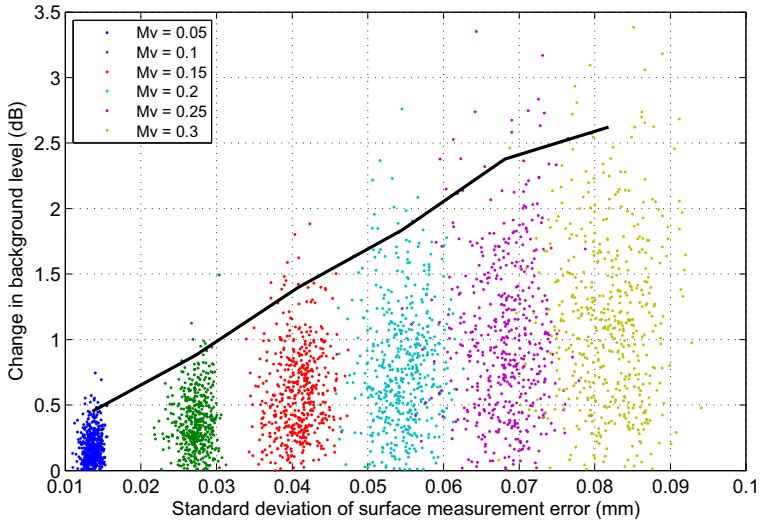

Figure 7.3.4: Sample results with a line of best fit added.

The same method for fitting a profile to the results as presented in chapter 5 is used. An example result can be seen in Figure 7.3.4. The same analysis process can be performed on the delay law errors that are introduced into each simulation as a result of the surface profile measurement error. This means presenting the results from the Monte Carlo simulations by plotting the standard deviation of delay law error taken over the array, against the change in background level. Figure 7.3.5 presents a sketch of a typical result. This plot can be used to predict a limiting value of standard deviation of delay law error using the same method as previously described.

The next section presents the results of applying both methods of analysis for all combinations of beam type, surface profile, and array specification.

7.3.3 Simulation results

The profiles extracted for the variation of change in background level with the standard deviation of surface measurement error can be seen in Figure 7.3.6 for a centre frequency of 2 MHz, and profiles for other centre frequencies can be seen in chapter 9.3 Appendix. The estimated limits of maximum measurement error and standard deviation of delay law error that have been extracted from these profiles for all centre frequencies, and can be seen in Table 7.3.1.

The results summary shows that the maximum tolerable measurement error remains approximately constant for the flat and artificial weld cap surface profiles at a single centre frequency, regardless of beam type. The wavy surface requires greater measurement accuracy; this is thought to be a result of the higher complexity of the surface with respect to the flat and weld cap surface profiles. For all surface profiles the required measurement accuracy increases with increasing probe centre frequency.

Previous work [109] has shown that the effect of the introduction of phase errors into a phased array system is frequency dependent, and the product of probe bandwidth and timing error (Bt_0) should remain constant. This work also demonstrated that to maintain a minimum of 8 dB amplitude separation between the main beam and any beam artefact the value of Bt_0 should be kept below 0.050 for focused beams. To relate the results from this study with the previous results, Bt_0 values have

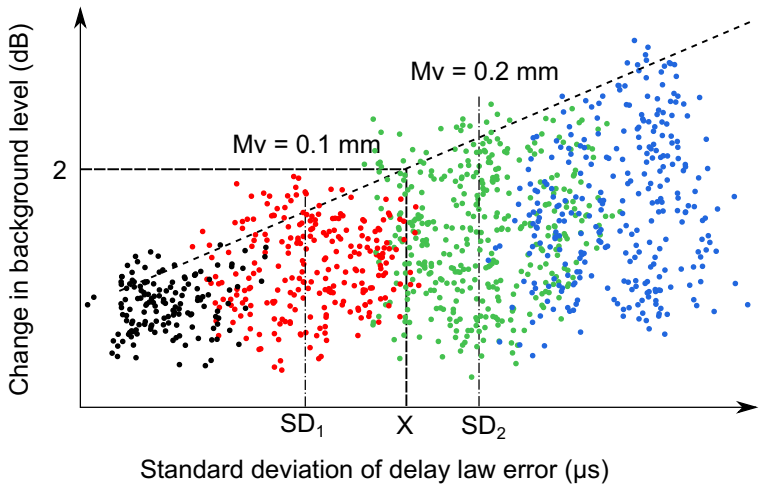

Figure 7.3.5: A sketch demonstrating the method used to find the 2 dB limit. $SD_{1/2}$ are the mean standard deviation values for simulation groups using a maximum variation (M_V) of 0.1 and 0.2 mm.

been calculated for this study by converting the maximum measurement error values to time using the longitudinal wave velocity. A second value has also been calculated based on the delay law standard deviation. Since the effect of surface profile measurement errors is the introduction of delay law errors into the system, it would be expected that the limiting Bt_0 value would remain constant for all centre frequencies. The Bt_0 values are reported in Table 7.3.1 .

The mean limiting value of Bt_0 is 0.045 for the flat and weld cap surface profiles for all beam types, with an associated standard deviation of 0.007. The wavy surface profile exhibits a much smaller limiting mean Bt_0 value of 0.025, with an associated standard deviation of 0.007. This result demonstrates good agreement with previous work for the flat and weld cap surface profiles. The limiting measurement error for the wavy surface is significantly lower than for the other surface profiles, but this is intuitive as the complexity of the wavy surface is much higher. The results in Table 7.3.1 also show that the limiting Bt_0 value is higher at 2 MHz than at the results at 5 and 7.5 MHz. One possible explanation for this behaviour is that the wavy surface contains features that only become significant when the wavelength of the ultrasound is of the same order. It could be possible that at a centre frequency of 2 MHz the majority of excited wavelengths are not influenced by the fine detail in the profile, but are significant at the higher frequencies.

The Bt_0 values calculated using the limiting standard deviation of delay law values also show good agreement for the flat and weld cap surface profiles for all beam types, although there is greater spread in the results than those calculated using the measurement error. Again the limiting values are lower for the wavy surface, and the Bt_0 value is also higher for the results at 2 MHz. One possible explanation for the greater spread in the results is that the method used to predict the limiting standard deviation of delay law error is less accurate. To convert the results from the standard deviation of delay law error to a maximum delay law error the same interpolation method is used as for measurement error. The difference between the two cases is that there is significantly more spread in the standard deviation of delay law error, to the extent that the results from different simulation groups (and therefore Mv values) can overlap, this is demonstrated by Figure 7.3.5. This means that the assumption that the mean result from each simulation group is proportional to the Mv value is less accurate.

a)

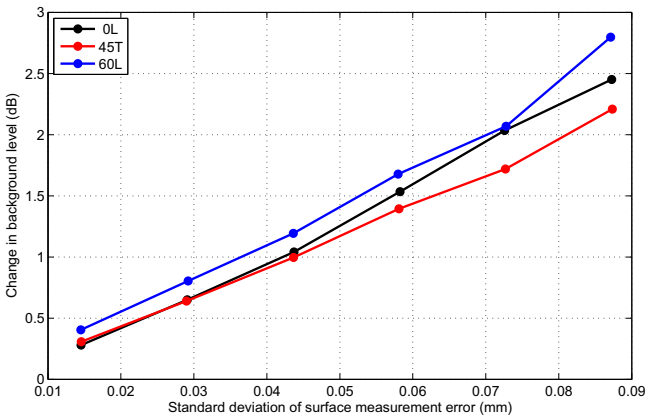

b)

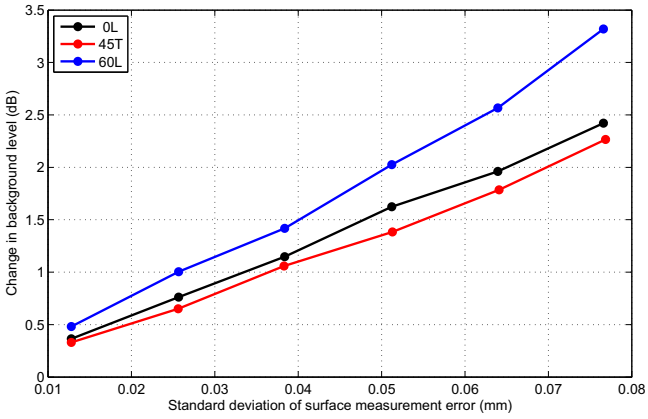

c)

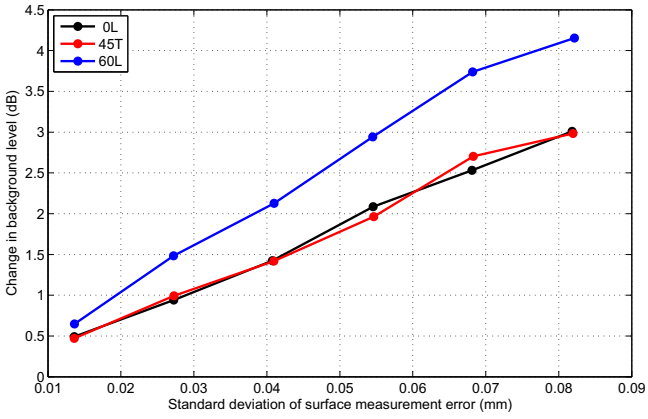

Figure 7.3.6: The results of analysing the Monte-Carlo simulation results for zero and 60 degree longitudinal beams (0L and 60L) and a 45 degree shear wave (45T) at a centre frequency of 2 MHz for a) a flat interface b) the artificial weld cap c) the wavy surface.

Table 7.3.1: Results summary for maximum surface profile measurement error (Mv), associated standard deviation of delay law error (DL), and Bt_0 values based on the maximum measurement error (and DL error). The results have been calculated on the basis of allowing a minimum of 8dB between the amplitude of beam artefacts and the main lobe.

Surface	Flat interface			Weld cap			Wavy surface		
Beam	Mv (mm)	DL (ns)	Bt_0 $(\times 10^{-3})$	Mv (mm)	DL (ns)	Bt_0 $(\times 10^{-3})$	Mv (mm)	DL (ns)	Bt_0 $(\times 10^{-3})$
Frequency	2 MHz								
0L	0.25	15.4	42.8(15.4)	0.25	14.3	44.2(14.2)	0.19	12.7	33.6(12.7)
45T	0.28	14.5	48.4(14.5)	0.27	13.3	47.3(13.3)	0.20	11.2	35.2(11.2)
60L	0.24	16.8	41.9(16.8)	0.20	12.8	34.4(12.8)	0.14	10.7	24.3(10.7)
Mean	**0.26**	**15.6**	**44.4(15.6)**	**0.24**	**13.4**	**42.0(13.4)**	**0.18**	**11.5**	**31.0(11.5)**
Frequency	5 MHz								
0L	0.13	8.5	56.0(21.2)	0.09	5.5	39.8(13.8)	0.05	.7	22.3(9.2)
45T	0.11	6.1	47.9(15.2)	0.12	5.9	51.6(14.6)	0.06	3.7	26.8(9.3)
60L	P.11	7.4	42.8(18.4)	0.08	5.6	35.8(13.9)	0.04	3.2	16.3(7.9)
Mean	**0.11**	**7.3**	**48.9(18.3)**	**0.10**	**5.6**	**42.4(14.1)**	**0.05**	**3.5**	**21.0(8.8)**
Frequency	7.5 MHz								
0L	0.07	4.9	46.2(18.4)	0.06	3.7	38.7(13.7)	0.03	2.5	22.2(9.3)
45T	0.08	4.5	52.0(17.0)	0.08	3.8	53.1(14.1)	0.04	2.4	25.7(9.2)
60L	0.06	4.5	38.1(17.0)	0.06	3.8	37.7(14.4)	0.03	2.2	16.4(8.2)
Mean	**0.07**	**4.7**	**45.4(17.5)**	**0.07**	**3.8**	**43.2(14.1)**	**0.03**	**2.4**	**21.4(8.9)**

7.3.3.1 Application to a realistic weld cap

The results clearly show that as the complexity of the surface profile increases from flat, to weld cap, to wavy surface the maximum M_V value decreases. The corresponding maximum delay law error remains approximately constant across the different surface profiles. This result means that it is not possible to define a minimum required tolerance for surface profile measurement as the limit will be dependent on the surface profile in question. However, it is unlikely that a surface profile as complex as the wavy surface would be inspected using a conformable array. A far more likely surface profile is the type of profile seen on the welded test piece used in section 7.2. To demonstrate how sensitive this type of profile is to measurement accuracy, and how it compares to the three profiles considered so far, Monte Carlo simulations have been performed at 2 MHz using the three beam types considered previously.

As before the ultrasonic field has been calculated for the three different beam types using the correct surface profile, the results can be seen in Figure 7.3.7. Results have been generated with the model configured such that the centre of the array is centred on the weld toe, and with the array located 20 mm to the right over the weld cap. The configuration with the array centred on the weld toe should produce the highest sensitivity to surface profile measurement errors as the surface gradient is highest at this point, and the experimental trials have also shown that this is the location where the largest measurement errors are likely to be encountered. The results from the array located above the weld cap will demonstrate any increase in sensitivity to surface profile measurement accuracy caused by the weld toe.

The profiles produced from the Monte Carlo results are shown in Figure 7.3.8, and maximum Mv values and associated Bt_0 values can be seen in Table 7.3.2. The results show that with the array over the weld toe the weld cap profile is slightly more sensitive to measurement errors than is the case for the wavy surface. The results with the array over the weld cap show an increase in mean Mv value of almost 30 % relative to the configuration with the array centred over the weld toe. The link between beam deterioration and surface profile complexity is not clear.

7.3.4 Discussion

The results demonstrate that the sensitivity of a given surface to measurement error is influenced by several parameters. Several metrics for classifying surface types will be investigated.

Comparing the limiting values of standard deviation of delay law error across all surface profiles shows that the number remains in the region of 11-17 ns. This parameter appears to be the essential parameter, but as discussed previously the calculation of it is not as accurate as the calculation of the maximum measurement error. From these results it is not clear why the realistic weld cap profile is more sensitive to measurement error than the wavy surface.

One possible explanation for the sensitivity of the realistic weld cap is that the variation in transmission coefficient due to changes in surface normal orientation is more extreme than the other profiles. This hypothesis has been investigated through the use of ray tracing. The angle between the local surface normal and the ray connecting each array element to all points along the surface profile has

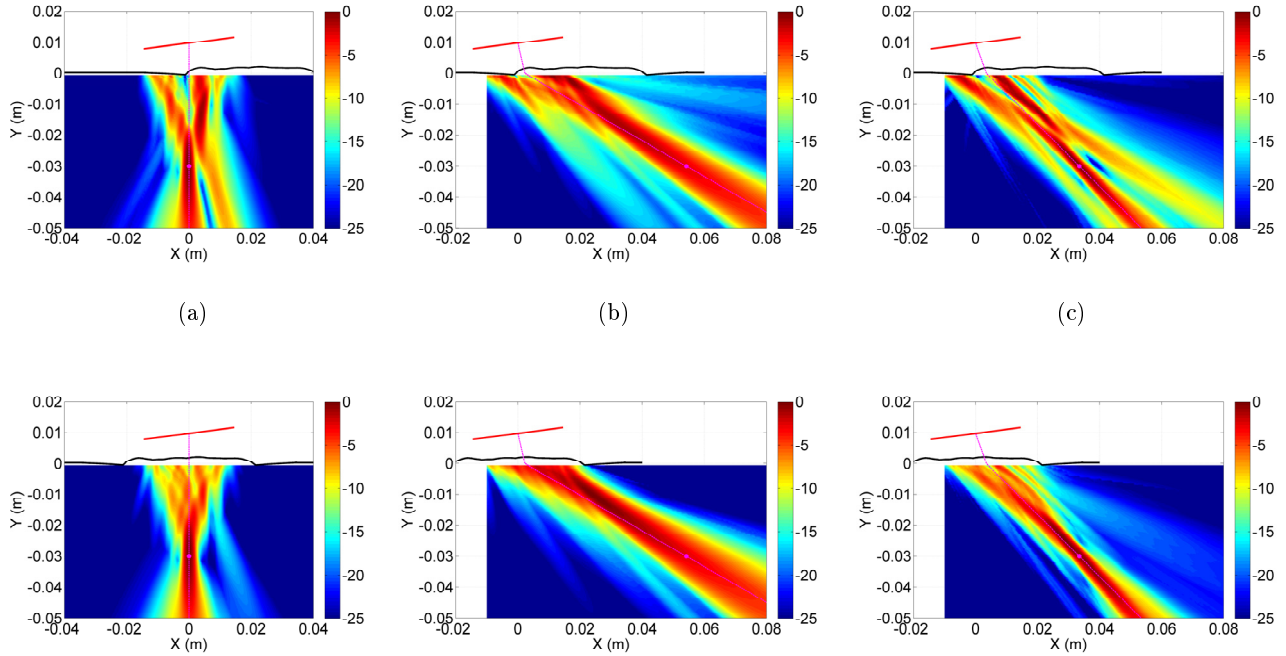

Figure 7.3.7: Beam plots of the realistic weld cap profile at a centre frequency of 2 MHz using the following beam types: a) & b) 0 and 60 degree longitudinal, and c) 45 degree shear wave. All beams are focused at 30 mm depth in material two using knowledge of the surface profile. Results d) - f) are repeat simulations with the array located 20 mm further to the right. In each case the colour scale is in decibels.

Table 7.3.2: Results summary for the realistic weld cap surface profile for maximum surface profile measurement error (Mv), associated standard deviation of delay law error (DL), and Bt_0 values based on the maximum measurement error (and DL error). The results have been calculated on the basis of allowing a minimum of 8dB between the amplitude of beam artefacts and the main lobe.

Surface	Realistic weld cap			Realistic weld cap - array offset by 20mm		
Beam	Mv (mm)	DL (ns)	Bt_0 $(\times 10^{-3})$	Mv (mm)	DL (ns)	Bt_0 $(\times 10^{-3})$
Frequency	2 MHz					
0L	0.13	11.7	22.6(11.7)	0.19	16.3	33.2(16.3)
45T	0.17	12.4	29.4(12.3)	0.25	16.8	43.3(16.8)
60L	0.15	15.1	26.6(15.1)	0.18	16.5	30.4(16.5)
Mean	**0.15**	**13.1**	**26.2(13.0)**	**0.21**	**16.5**	**35.6(16.5)**

a)

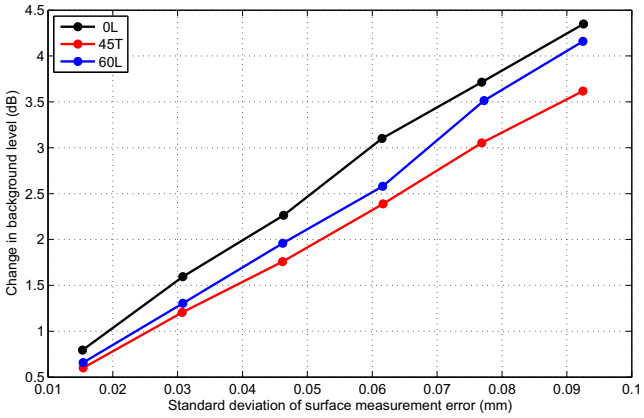

b)

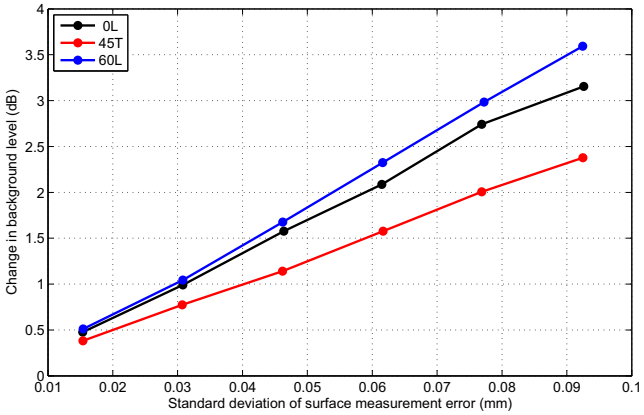

Figure 7.3.8: The results of analysing the Monte-Carlo simulation results for a zero and 60 degree longitudinal beams (0L and 60L) and a 45 degree shear wave (45T) at a centre frequency of 2 MHz for the realistic weld cap profile a) the array centred on the weld toe, b) the array centred 20 mm to the right of the weld toe

been calculated. This information is then used to compute a local transmission coefficient, and the standard deviation of the transmission coefficients not equal to zero is calculated for each element. This number represents the level of variation in transmission coefficient encountered by the ultrasound generated by each element. The results are presented for all surface types in Figure 7.3.9. The plots demonstrate that whilst the results for the realistic weld cap exhibit a higher level of variation than for all the other surfaces bar the wavy surface, the increase in variation is not sufficient to explain the sensitivity to measurement error.

A second possible explanation for the deterioration in performance is the phase variation introduced into the system by the surface profile. The array can be adapted to a given surface profile by using ray tracing to determine the ray path between each element and the focal location. These solution are only valid for rays drawn from the centre of the elements to the focal location. For a system with a flat interface the variation in ray path for locations on the element surface close to the element centre is smooth, and as a result the element will produce a broad arc of ultrasound that propagates close to the desired focal location. The phase differences introduced by the differences in ray path are small relative to the length of the tone burst emitted by the element; hence the summation of the ultrasound generated by each element in the array will lead to a single maximum close to the focal location, assuming the array produces no grating lobes.

For the same system imaging through an irregular surface the magnitude of the maximum is reduced, and the location may be altered. The ray tracing is still valid for a solution between the centre of each element and the focal location, but the variation in ray path for locations on the element surface not at the element centre may no longer be smooth. Variations in local surface normal cause the ultrasound from each element to be refracted over a greater angular range, and in extreme cases only part of the ultrasound may be transmitted into the component at all. This leads to less ultrasound from each element passing close to the focal location, and a greater variation in phase. The summation of the ultrasound from each array element leads to less constructive interference, and the variation in the refraction of the ultrasound from each element can lead to secondary maxima formation. The reduction in performance means that the array is more reliant on the component of each element's directivity pattern that is selected by the ray tracing, hence delay law errors can more easily degrade beam quality.

To quantify the effect of changes in surface orientation for a given surface profile a measure of surface roughness can be used. The same ray tracing method as used to quantify the variation in transmission coefficient is used to locate areas of the surface profile utilised by each array element. The surface roughness is calculated, using equation (7.3.1), using the method outlined in Figure 7.3.10.

$$R_a = \frac{\sum_{i=1}^{i=n} |y| - \sum_{i=1}^{i=n} y/n}{n} \tag{7.3.1}$$

where y is the vertical coordinate of the surface profile, and n is the number of points used to calculate the surface roughness. The travel time between each element and the focal location via each point on the surface profile is calculated. Points on the profile where the travel time is within 4 cycles at the centre frequency of the array, and the angle to local normal is less than the critical angle, are used to calculate the local surface roughness for each element.

The surface roughness value is a measure of the variation in the profile used by each element. Results for all three beam types for all surface profiles can be seen in Figure 7.3.11. The analysis shows that

the high gradient of the realistic weld cap at the weld toe causes a large rise in surface roughness relative to all the other surface profiles considered. This helps to explain why the results from the Monte Carlo study of the realistic weld cap show a higher sensitivity to measurement error than those for the wavy surface. In practice the wavy surface is so extreme that it is likely that the surface could not be ultrasonically measured to the required accuracy, and the predicted performance using no measurement error is also very poor.

The modelled performance on the four different surface profiles has shown that a measurement accuracy of 0.15 mm is sufficient to maintain beam quality. The range of surface profiles covers a broad range from flat to extreme wavy surfaces. The experimental trials reported in the previous section have demonstrated that a 2 MHz array can be used to measure surface profile to an accuracy of 0.1 mm using a focused beam. However, analysis of results has shown that errors up to 1 mm in magnitude can be encountered when the surface gradient is high. The sample containing a realistic weld cap has areas of the surface profile where the gradient is extremely high, and this geometry is typical of the type of weld at which this technology would be targeted. However, ray tracing, presented in Figure 7.3.12, shows that the weld toe area is not relied upon to calculate delay laws so larger measurement error in this area of the profile can be tolerated. This statement assumes that the measured surface profile does not contain any large positive peaks. If the opposite is true, the measurement error will affect the delay laws as the higher velocity of steel would cause the Fermat minimum time algorithm to return incorrect solutions. As a result the surface profile should be filtered to remove any large peaks.

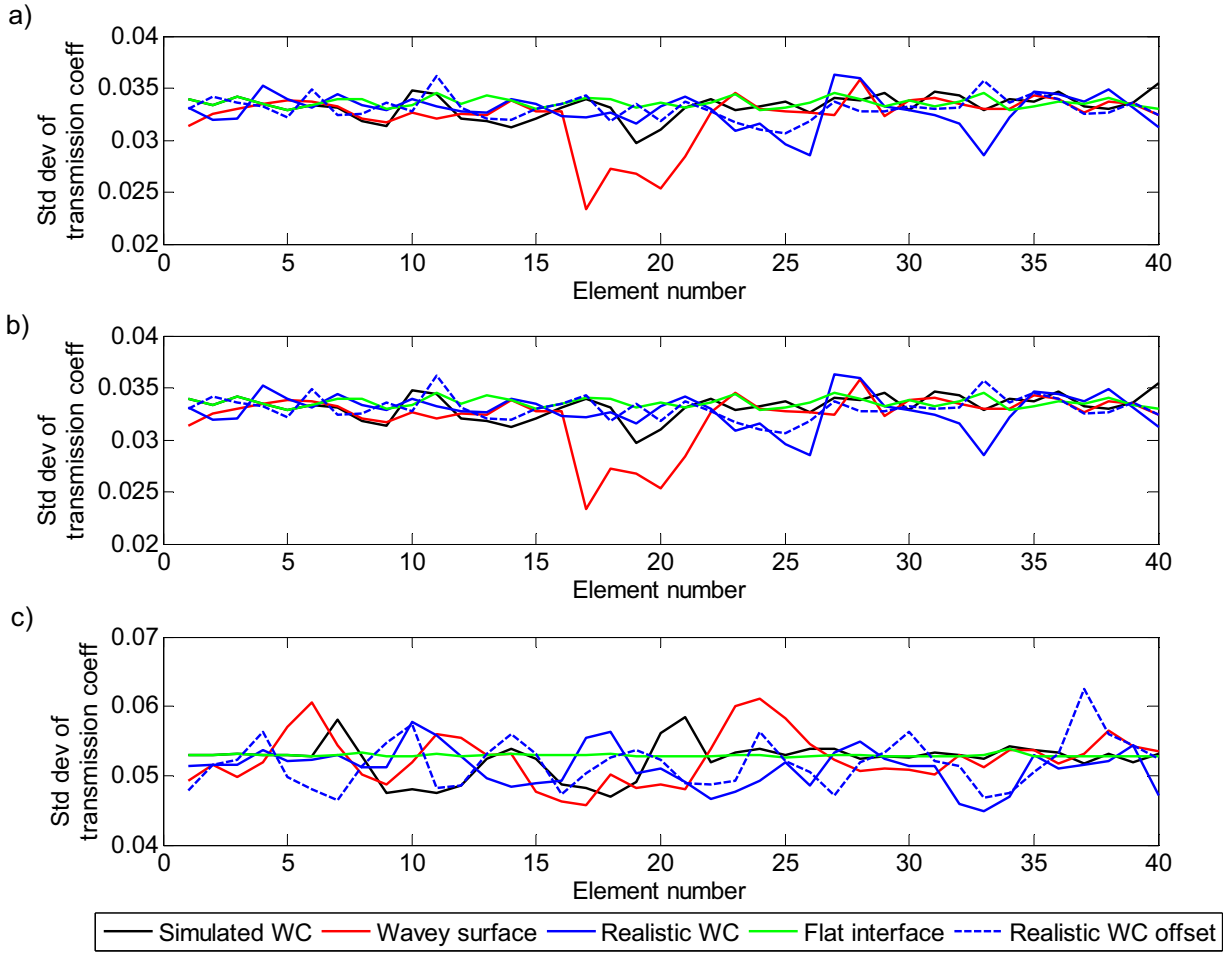

Figure 7.3.9: Plots of the standard deviation in local transmission coefficient for each array element for the following beam types a) 0L b) 60L c) 45T.

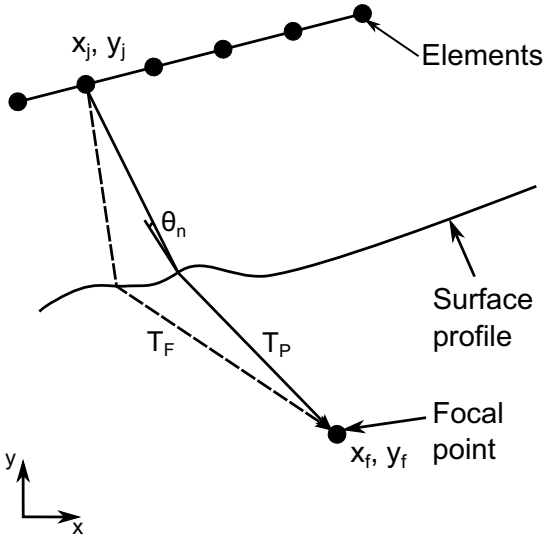

Figure 7.3.10: The method used to calculate local surface roughness. $T_{F/P}$ are the ray paths for the Fermat minimum time solution and the point on the surface profile in question.

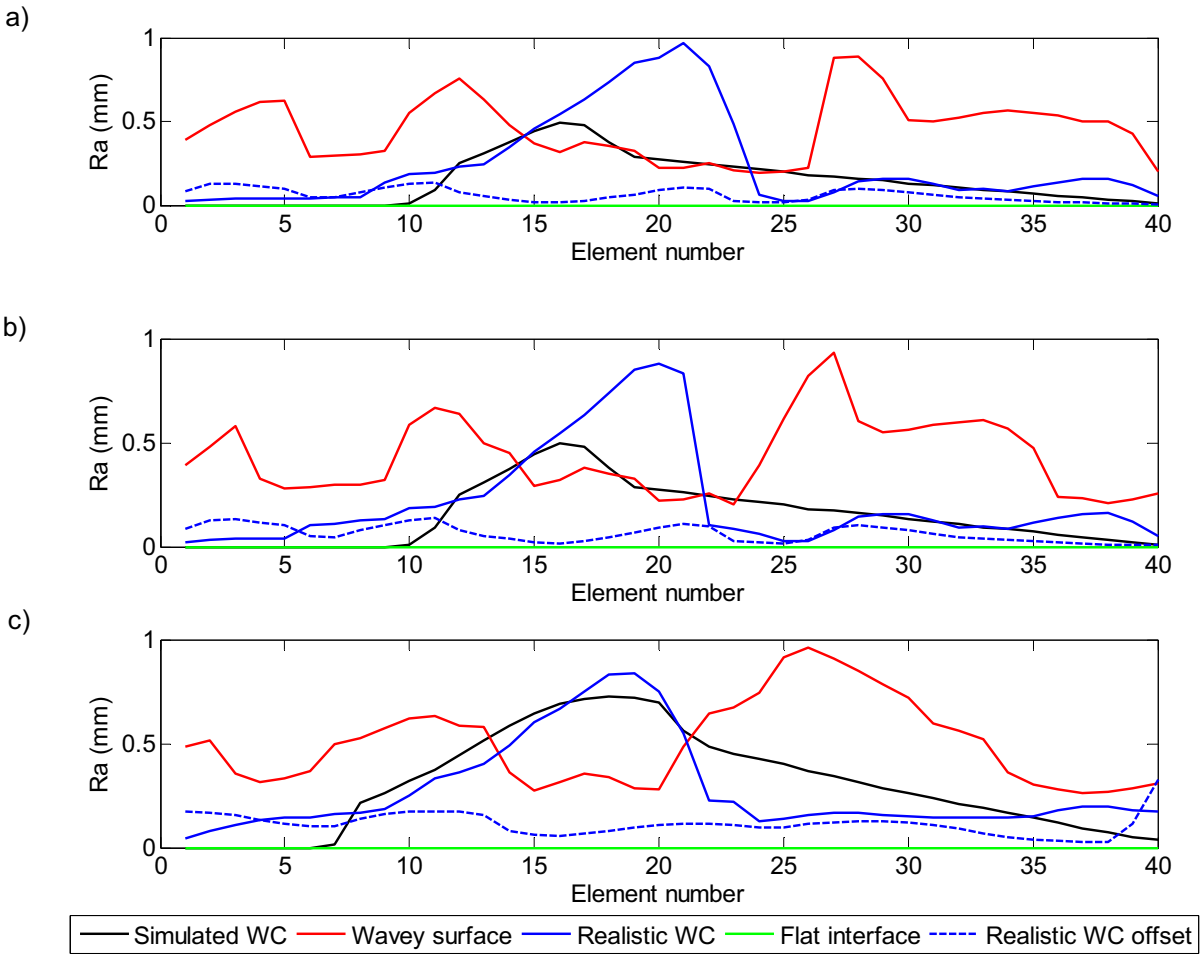

Figure 7.3.11: The variation in surface roughness (Ra) of the surface profiles utilised by each array element, for three beam types a) 0L b) 60L c) 45T.

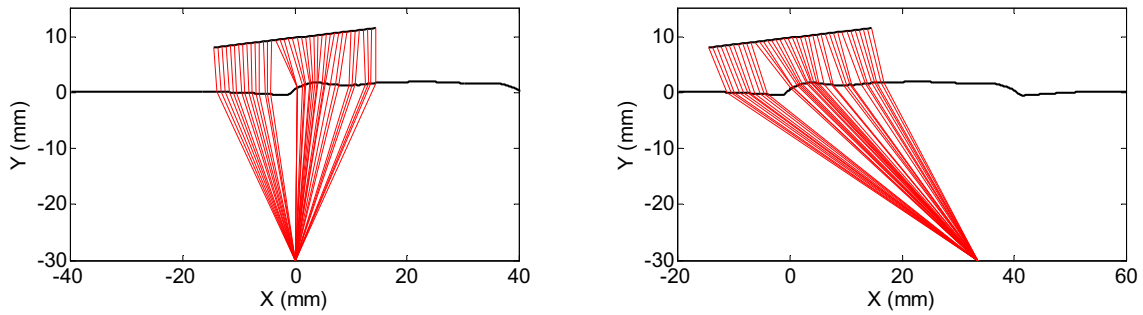

(a) (b)

Figure 7.3.12: The results of ray tracing for the realistic weld cap, for beam types a) 0L and b) 45T.

7.4 Summary

This study aimed to demonstrate that an array can be used to measure the surface geometry of a component and that this information can be used to enable beam forming in the component. This has been achieved by experimental demonstration of the measurement performance on two test pieces. These results have then been compared with a series of results from Monte Carlo modelling that demonstrate the measurement accuracy that must be achieved in order to guarantee that there is a minimum amplitude separation of 8 dB, in the free field, between the main beam and any beam artefacts. This value is based on a reduction of the 10 dB recommended by BSEN 12668 part 2: 2010 [6].

The experimental trials have demonstrated the accuracy to which a 2 MHz array can be used to measure surface geometry in immersion, using processing methods of increasing complexity. These results have shown that conventionally focused beams are able to measure surface profile to an accuracy of 0.1 mm, and better in some cases. Focused beams have also been found to be sensitive to the parameters used to form the beam, some of which would not be known for an uncharacterised surface. As a result, the TFM is suggested as the most appropriate imaging approach, specifically TFMe as it offers an excellent balance between processing time and performance for this application. However, no methods have been found for measuring surface profile where the surface gradient is very high. In these areas measurement errors of the order of 1 mm can be encountered, but ray tracing has shown that the weld toe is not used for delay law correction providing that the results do not contain large peaks or discontinuities.

The experimental results have also shown that accurate surface profiles can be measured when using data where the echoes from the surface of a component have saturated the amplifier. However, measurement errors increase with increasing levels of saturation, thus it should be minimised where possible. An angled array is also better suited to collect data to be used for surface profile measurement and inspection as much of the ultrasound is skipped away from the array, hence for a given level of gain the level of amplifier saturation is lower for an angled array.

The modelling results have shown that for a variety of surface profiles a measurement accuracy of 0.15 mm is required to maintain beam quality at a centre frequency of 2 MHz. The results have also been shown to be similar to those suggested by the results in chapter 5.2 for phase errors in array systems, and the frequency dependence of the results has also been demonstrated. No single parameter has been found for predicting the sensitivity of a given surface profile to measurement errors, but surfaces containing areas of high gradients have been shown to be more sensitive than smoothly varying surfaces.

In conclusion this study has proven that an array can measure a surface profile accurately enough to enable a high quality beam to be produced in the component under inspection. This approach is ideally suited to smoothly varying surfaces, and is also suitable for application to rougher surfaces provided that performance is demonstrated on a case-by-case basis.

8 Conclusions

The broad aim of this thesis has been to investigate the effect of variations in array inspection system parameters on inspection performance, and to use this understanding to develop a means of calibrating a FMC based inspection in an industrially practical way. The approach taken has been to first understand the key parameters that must be controlled, their typical experimental variation, and to then develop practical tolerances based upon evidence produced from modelling. This work has primarily focused on linear wedge mounted arrays, but has also considered conformable/immersion arrays. These items are of considerable interest to Rolls-Royce, and the development of a complete calibration framework is one of the final barriers to the transition of a FMC based inspection system to technology readiness level six and deployment in a production environment.

8.1 Review of thesis

In chapter 1 I have outlined how my Engineering Doctorate fits into Rolls-Royce, and how the technological requirements of the company have driven my research, and technology transfer. I have discussed how my research links with existing inspection frameworks and current practice with the NDE department within Rolls-Royce Submarines.

Chapter 2 introduces the fundamental principles on which conventional ultrasonic inspection are based. Single element probe inspections are discussed, and the benefits of phased array technology are summarised. FMC technology is introduced and the current state of research is reviewed. This chapter summarises current FMC based inspection technology, as these needs drive the requirements of a calibration routine targeted at FMC applications. This includes FMC imaging methods, defect characterisation, and conformable phased array technology.

The main research theme of my doctorate has been the identification, and investigation into, the essential parameters that dictate array performance. This task has required a significant amount of modelling. Chapter 3 reviews methods of modelling ultrasonic transducers, and their individual advantages and disadvantages. A modelling method is selected on the basis of a balance between model speed and accuracy. The development of a plane strain array beam model is discussed, and the results of a validation programme against an established commercial modelling package and experiment are presented. The chosen modelling method is shown to be sufficiently accurate whilst offering low enough computation times to allow Monte Carlo modelling to be practical on a high specification desktop PC.

One of the essential parameters that dictate array performance is the directivity pattern exhibited by the elements that compose the array. Initial experimental trials revealed that transducer models commonly applied to small array elements were inaccurate. The models were initially identified as a standard against which directivity patterns could be compared as part of a calibration routine, although this proved unnecessary as directivity patterns were proven to be consistent and uncoupled from element sensitivity. This also raised the broader question of the effect that modelling inaccuracies

have on array models. Chapter 4 reviews methods of modelling array elements, compares results with experimental measurements, and proposes a more accurate approach. However, the final section demonstrates that the improved models actually result in little change to the ultrasonic field produced via an aperture of array elements, when beam forming. This chapter justifies the use of the piston source approximation for array elements, despite the inaccuracies on an element scale.

The calibration framework developed for the calibration of FMC systems is presented in chapters 5 and 6. The first stage of calibration is an array integrity check that measures element performance. Chapter 5.2 introduces the modelling and results analysis methodology, based on a Monte Carlo type approach, designed to reveal the dependence of array performance on element sensitivity and phase. The results of this are used to define pass-fail criteria for the array integrity check. Once an array has passed this check the performance of the array must be monitored throughout the inspection. Chapter 6 reports the development and verification by modelling and experiment of a combined probe check. The combined probe check monitors the amplitude and timing of an echo stationary in time, to monitor performance. The reflection from the array's wedge to component interface has been selected as the most appropriate signal to use. Results show that temperature variation affects results more than variation in element performance. As a result a means of detecting and correcting for wave velocity shift due to temperature variation, is proposed.

The final stage of calibration is to set inspection sensitivity relative to calibration reflectors; this is also reported in chapter 6. A high resolution scan of a calibration block is recorded such that the data can be processed post inspection, and the data used to record normalisation amplitudes and DAC curves for any conceivable beam type. An automated means of data analysis is demonstrated that allows DAC curves to be implemented as artificial gain in post processing on a per aperture basis. This allows B-scan images generated via electronic scanning to be viewed at a constant known sensitivity. An application of this technique to a realistic application is also presented.

The calibration framework presented in chapters 5 to 6 focuses on FMC systems using a rigid wedge. Conformable arrays are of interest to Rolls-Royce and must be accommodated. The conformable array option selected by Rolls-Royce uses a water filled wedge encapsulated with a flexible membrane. This system effectively provides a portable immersion transducer where irregular surfaces are accommodated via alteration of the water path between the array and the top surface of the component. The accuracy of the delay law corrections used to accommodate the irregular geometry is defined by the accuracy to which the surface location is known. This introduces an extra parameter into the inspection system that must be controlled. Chapter 7 reports the development of acceptance criteria for surface profile measurement accuracy using an extension to the model discussed in previous chapters.

8.2 Review of findings

The main areas of focus of this thesis are the modelling of ultrasonic arrays, the identification of the essential system parameters that define performance, and subsequently the required level of parameter control. The application of this theoretical work is the development of an inspection calibration framework that is both rigorous and practical to implement in an industrial environment. In this section the main findings of the thesis will be reviewed.

8.2.1 Ultrasonic array modelling

One of the fundamental components of an array beam model is the mathematical construct chosen to represent the behaviour of an individual array element. To save computation time an analytical solution to the diffraction behaviour of a single element is often selected. For example, the solution to the pressure variation with respect to the angular location relative to an element surface normal via the Rayleigh integral. This technique allows an array of elements to be modelled provided that the point of interest is outside of the near field of an individual array element, at low computation cost relative to modelling each element individually. Clearly the accuracy of the chosen solution affects the accuracy of the complete model.

Experimental comparisons with commonly used solutions to the pressure field produced by a single array element showed poor agreement. The investigation into the cause of this has shown that array elements that are considered small, e.g. a width smaller than the wavelength at the transducer's centre frequency, are poorly described by solutions arrived at by assumption of piston behaviour. An improved modelling approach based on a crude approximation of the pressure variation across the element provides good agreement with experiment. However, the transition point from piston like behaviour cannot be located without further data points. This work has not been completed as comparisons between array models built on the assumption of piston like behaviour and one using the improved modelling technique shows that errors are limited in the normal operating range of the array. Based on this conclusion the use of an array beam model using the piston assumption was considered justified.

The semi-analytical ultrasonic array model reported in this thesis was selected on the basis of its flexibility, and speed. The validation cases compared against CIVA demonstrate that the model is able to accurately predict the pressure field produced by an aperture of phased array elements. The advantage of this modelling technique is its simplicity.

8.2.2 The effects of phased array element performance variation

The ultrasonic modelling tools developed during the course of my doctorate were developed to allow large scale parametric studies to be conducted. The goal was to identify the key parameters that affect array system performance, and the type of alterations that the variation in these parameters has on the field produced by an array. Previous work on this subject by Lancee et al [92, 94] focused on the acoustic application of phased arrays for a medical application. This work considered the variation in element sensitivity and phase, including the development of a novel method of identifying the major artefact present in an echodynamic. The work reported by Steinberg [96] on the effect of phase errors inherent to digital phased array equipment was found to be directly relevant to this work. The analysis tools developed by these authors were used to assess the results generated by the beam model developed for this project, but the results were analysed using metrics defined in existing standards used for conventional single element ultrasonic inspections. This approach has produced tolerance bands for the uniformity of array element performance that enables phased array system performance to be ensured without performing measurements of specific beam types.

The modelling work has also been extended to conformable phased array, and the effect of surface profile measurement accuracy has been considered. This work is based upon the same method of analysis developed for variations in element performance, but uses a version of the beam model modified to consider irregular interfaces. The results have also been used to define acceptable tolerances on

surface profile measurement accuracy. These tolerances have defined the most appropriate imaging methods for measuring surface profile. The results have also shown that although beam forming can be conducted through an irregular interface at a particular point, beam quality is badly degraded away from this depth. Hence it is appropriate that imaging techniques that are optimised over the complete imaging area should be used, e.g. the TFM or ATFM.

8.2.3 A calibration routine for FMC

The ultimate goal of this thesis is the development of a means of calibrating phased arrays systems that enables the full flexibility of FMC to be unlocked. The modelling tools and results discussed above were crucial elements of this work, as they provide the basis for many of the developed procedures. The complete calibration routine uses a simple element performance check to ensure array integrity. A novel means of monitoring element performance is then used that has been developed to detect and correct the effects of wave velocity variation due to small temperature changes. Finally a combined equipment check is used to more completely test system performance than the array integrity check, whilst providing the operator with a more tangible output that is compatible with established tolerances on variations in system performance during the course of an inspection.

This capability is highly attractive for industrial application of FMC based inspections as it enables an array transducer to be checked via a small number of automated checks that require little user intervention, and have little impact on inspection duration. A method of relating results to known calibration reflectors has also been developed. A worked example has been presented that demonstrates how FMC technology can be used to successfully detect a defect in a realistic industrial application. Modelling tools were also used to inform the selection of imaging parameters used to size the defect with two separate techniques.

8.3 Future work

8.3.1 FMC inspection within Rolls-Royce Submarines

Following the completion of the work reported in my thesis the project to deliver a FMC based inspection software platform continues. The project is scheduled to continue for several months. During this time all of the software tools developed in Matlab for the FMC calibration framework will be implemented in C for inclusion in the software platform. As part of this integration the entire calibration process will record an auditable record of the inspection. For example, the initial array integrity check result will be recorded and the results incorporated into the inspection data such that dead elements are automatically accommodated by the FMC processing code. The combined probe and equipment check algorithms will be included in the data acquisition software and the user forced to calibrate and recalibrate throughout the inspection.

The focus of the project is no longer the inspection of components with irregular surface geometries with UT in lieu of Radiographic Testing (RT). The results of cost-benefit analysis have shown that the inspection of un-dressed pipe butt welds using a membrane type device is not viable at present due to access limitations reducing the number of candidate welds, and current working practices in the submarines production line. For this technology to be deployed it is also necessary for the development of ultrasonic specific acceptance criteria. Current acceptance criteria for radiography are designed to ensure good workmanship rather than a completely defect free structure. For example, no crack like

defects are acceptable under the ASME boiler and pressure vessel code. In practice the radiographic techniques used to inspect components would likely not detect small benign cracks. However, ultrasonic inspection is far more sensitive to planar flaws which complicates the situation. ASME code cases exist for the use of UT in lieu of RT on nuclear plant, but no amendments have yet been approved by US and UK safety regulators.

While the specific application chosen for the membrane probe is not being carried forward, the FMC inspection platform development will be completed. The aim is to develop the software to a point where all the functionality is present to allow a FMC implementation of automated ultrasonic inspections that are currently carried out with multiple single element probes. The software will also include TFM and ATFM processing functionality.

Once complete the FMC software will be taken through a TRL 6 gate. Successful completion of this review will enable the software to be applied on a component inspection. The first application is intended to be the Manufacturing Acceptance Inspection (MAI) of a butt weld in a thick sectioned ferritic pressure vessel. The inspection will be conducted in a factory environment. Despite the simple geometry of this application there will be many other challenges, such as data storage. The inspection of a vessel several metres in circumference and several hundred millimetres thick is anticipated to generate in excess of 50 Terabytes of data that must be stored for the life of the component (25 - 50 years).

8.3.2 The future of FMC inspection

In my opinion there are several barriers to the wide spread adoption of FMC inspection technology:

- Better application specific demonstration of the benefits of FMC technology compared to conventional phased array
- Purpose designed hardware and software
- Commercial experience of applying FMC inspection and internationally agreed standards

Chpater 2 discussed the background of ultrasonic inspection and discussed current and recent developments in phased array technology, in particular FMC data processing. Many of the developments discussed, e.g. derivatives of the TFM algorithm, scattering matrices etc, have been demonstrated on a small number of test pieces. More widespread evaluation of this technology against the performance of conventional phased array inspection methods will help to demonstrate to end users and the manufacturers of NDE equipment that the investment in FMC technology is worthwhile. For the output of this type of evaluation to yield maximum benefit the comparison should be conducted using a realistic test piece and a fully proceduralized inspection, that must detail inspection calibration and defect reporting and sizing criteria. Ideally the inspection should be conducted along side a conventional phased array inspection and should be carried out by experienced operators and data analysts.

For FMC technology to become routinely used by industry the development of a complete inspection platform is required, with a software solution that incorporates all aspects of the inspection process from calibration to data interpretation. The design of such a system will vary depending on the application. For example high speed data acquisition and data reprocessing is of interest to the nuclear industry, while the ability to view real time TFM imagery and conventional phased array imagery using the parallel processing power of Graphical Processing Unit (GPU), or hardware speed of Field

Programmable Gate Arrays (FPGAs), would be of interest to the manual phased array inspection market. Whatever the solution, hardware and software must be developed that are designed with the data volumes and processing requirements of FMC base inspection in mind. Particularly for applications where the FMC data will be retained for long periods of time, application of existing lossless data compression methods should be utilised to reduce the quantity of storage required.

Finally the last and probably most important obstacle for FMC technology is commercial experience of applying FMC technology and the development of standards. As with most new technologies, widespread adoption does not normally happen until a number of applications of the technology have successfully been applied and international standards are agreed. This is often achieved by a small number of large organisation that have the resources to risk the development of an unknown technology and justify its use without agreed standards in place. Conventional phased array technology was introduced to NDE by using arrays to replicate well known inspection methods, whilst benefiting from improved inspection speed and data display. This phased method of introduction has the benefit of less risk but the disadvantage of a slower transition to inspection design with arrays in mind. Consequently the development of array specific inspection standards has been relatively slow. This type of introduction of FMC technology is unlikely to happen as there are few benefits of this approach, instead it is more likely that FMC technology will be first deployed to solve a small number of difficult inspection problems, and the technology will slowly flow down to more generic inspection activities. The speed at which this transition happens will likely be governed by how effectively the benefits of FMC technology are communicated to end users and manufacturers of ultrasonic inspection equipment. However, once the technology is better understood, standards are in place, and FMC specific inspection hardware is widespread I believe the technology will largely replace conventional array inspection. FMC will become the basis of acquiring array data, and flexible hardware and software will be used to deploy a variety of imaging methods, including conventional beam types. Methods such as the TFM will simply become imaging tools that the user can choose from a range of methods to suit a specific role.

8.4 Publications

The main areas of novel work associated with my doctorate are the development of a calibration routine for FMC capture, the model based studies into the effects of phased array element performance and surface profile measurement accuracy, and the modelling of array elements. This work and the development of tools for industrial deployment have been presented at several international conferences, and published in proceedings and journals:

- D. Duxbury, J. Russell, M. Lowe, "Designing a Calibration Full Matrix Capture (FMC) based Inspection", In D.E. Chimenti D.O. Thompson, editor, Review of Progress in Quantitative Non-destructive Evaluation, volume 30, pp 851-858, American Institute of Physics, 2010.

- D. Duxbury, J. Russell, M. Lowe, "A Calibration Routine for Full Matrix Capture (FMC)", *Proceedings of the 9th International Conference on NDE in Relation to Structural Integrity for Nuclear and Pressurised Components*, *In Press*, 2013.

- D. Duxbury, J. Russell, and M. Lowe. "The Effects of Variation in Phased Array Element Performance". *Ultrasonics*, volume 53, pp 1065-1078, 2013.

- D. Duxbury, J. Russell, and M. Lowe. "Accurate Two Dimensional Modelling of Piezo-composite Array Transducer Elements". *NDT&E International*, volume 56, pp 17-27, 2013.
- J. Russell, R. Long, D. Duxbury, and P. Cawley, "Development and implementation of a membrane-coupled conformable array transducer for use in the nuclear industry", *Insight*, volume 54, pp 386-393, 2012.

Bibliography

[1] Safety of Nuclear Power Plants: Design, 2000.

[2] Safety Assessment Principles for Nuclear Facilities, Revision 1, 2006.

[3] C.D. Bell, C.T. Watson, J. Howson, and A.W. Walker. Safety Classification Informed Structural Integrity Assessment of Nuclear Plant Components. In *Proceedings of the ASME 2010 Pressure Vessel & Piping Division / K-PVP Conference*, 2010.

[4] C. Holmes, B.W. Drinkwater, and P.D. Wilcox. Post-Processing of the Full Matrix of Ultrasonic Transmit-Receieve Array Data for Non-Destructive Evaluation. *NDT & E International*, 38:701–711, 2005.

[5] J. Russell. The Development and Implementation of Advanced Ultrasonic Phased Array Technology. *EngD thesis, Imperial College London*, 2010.

[6] British and European standard : Non-Destructive testing - Characterization and Verification of Ultrasonic Examination Equipment - Part 2: Probes (BSEN12668-2:2010).

[7] British and European standard: Non-destructive testing - Characterization and Verification of Ultrasonic Examination Equipment - part 3: Combined Equipment (BSEN12668-3:2004).

[8] P. Cawley. Non-Destructive Testing - Current Capabilities and Future Directions. *Proceedings of the Institute of Mechanical Engineers, Part L: Journal of Materials Design and Applications*, 215:213–223, 2001.

[9] J. Krautkramer and H. Krautkramer. *Ultrasonic Testing of Materials*. Springer-Verlag, London, 4th edition, 1990.

[10] D. Kalkhof, W. Gorner, C.H. Schurig, and C.H. Muller. Detection of Defects in Austenitic Piping and Welds of Nuclear Power Plant Components by Ultrasonics. *International Journal of Pressure Vessels and Piping*, 39:279–291, 1989.

[11] R.J. Hudgell, G.M. Worrall, J. Ford, and B.S. Gray. Ultrasonic Characterisation and Inspection of Austenitic Welds. *International Journal of Pressure Vessels and Piping*, 39:247–263, 1989.

[12] A.W. Eberhand. On the State of the Art of the Inspection of Austenitic Welds with Ultrasound. *International Journal of Pressure Vessels and Piping*, 39:227–246, 1989.

[13] G.D. Connolly. Modelling of the Propagation of Ultrasound Through Austenitic Steel Welds. *PhD thesis, Imperial College London*, 2009.

[14] J.L. Rose. *Ultrasonic Waves in Solid Media*. Cambridge University Press, Cambridge, 1999.

[15] A. Scuster. *An introduction to the Theory of Optics*. E. Arnold, 1904.

[16] R/D Tech Inc. *Introduction to Phased Array Technology Applications*. R/D Tech Inc, Quebec, Canada, 2004.

[17] A.C. Whittle. Preliminary Steps to Validate a Beam Model for Ultrasonic Phased Arrays. *Insight*, 48(4):221–227, 2006.

[18] M. Berke and T. Ballenger. Phased Array Technology for Standard Ultrasonic Testing. *Insight*, 48:218–220, 2006.

[19] B.W. Drinkwater and P.D. Wilcox. Ultrasonic Arrays for Non-Destructive Evaluation: A Review. *NDT & E International*, 39(7):525–541, 2006.

[20] S. Yang, B. Yoon, and Y. Kim. Using Phased Array Ultrasonic Technique for the Inspection of Straddle Mount Type Low-Pressure Turbine Disk. *NDT & E International*, 42:128–132, 2009.

[21] S. Song, H.J. Shin, and Y.H. Jang. Development of an Ultrasonic Phased Array System for Non-Destructive Test of Nuclear Power Plant Components. *Nuclear Engineering and Design*, 214:151–161, 2002.

[22] P.D. Wilcox, C. Holmes, and B.W. Drinkwater. Exploiting the Full Data set from Ultrasonic Arrays by Post-Processing. *AIP Conference Proceedings*, 820:845–852, 2006.

[23] C.L. Morgan. B-scan & Real-Time Ultrasound in the Antepartum Diagnosis of Conjoined Twins & Pericardial Effusion. *American Journal of Roentgenology*, 130:578, 1978.

[24] R.C. Michell and P.J. Bradley-Watson. The Detection of Fetal Meningocele and Meningoencephalocele by Ultrasound B-scan Ultrasound. *Journal of Clinical Ultrasound*, 3:307–308, 1975.

[25] R.C. Oeftering. LEW16189. In *NASA Technical Briefs*. NASA, 1997.

[26] J.H. Friedl, T.A. Gray, P. Khandelwal, and T. Dunhill. Ultrasonic Phased Array Inspection of Seeded Titanium Billet. *AIP Conference Proceedings*, 700:809–816, 2004.

[27] V. Lupien. Phased Array Ultrasonic Probe Design: From Art to Science through Optimization. *AIP Conf. Proc*, 700:809–816, 2005.

[28] O. Oralkan. Volumetric Ultrasound Imaging using 2-D CMUT Arrays. *IEEE Transactions on Ultrasonics Ferroelectrics and Frequency Control*, 50:1581–1594, 2003.

[29] S. W. Smith, H.G. Pavey, and O.T. von Ramm. High Speed Ultrasound Volumetric Imaging System-Part I: Transducer Design and Beam Steering. *IEEE Transactions on Ultrasonics Ferroelectrics and Frequency Control*, 38:100–108, 1991.

[30] G.R. Lockwood and F.S. Foster. Optimizing the Radiation Pattern of Sparse Periodic Two-Dimensional Arrays. *IEEE Transactions on Ultrasonics Ferroelectrics and Frequency Control*, 43:15–19, 1996.

[31] S. Mondal, P.D. Wilcox, and B.W. Drinkwater. Design of Two-Dimensional Ultrasonic Phased Array Transducers. *Transactions of the ASME Journal of Pressure Vessel Technology*, 127:336–344, 2005.

[32] J.E. Kirkebo and A. Austeng. Improved Beam Forming using Curved Sparse 2D Arrays in Ultrasound. *Ultrasonics*, 46:119–128, 2007.

[33] R. E. Davidsen, J. A. Jensen, and S.W. Smith. Two-Dimensional Random Arrays for Real Time Volumetric Imaging. *Ultrasonic Imaging*, 16:143–163, 1994.

[34] A.A. Austeng and S. Holm. Sparse 2D Arrays for 3D Phased Array Imaging - Design Methods. *IEEE Transactions on Ultrasonics Ferroelectrics and Frequency Control*, 49:1073–1086, 2002.

[35] A. Velichko and P.D. Wilcox. Strategies for Ultrasound Imaging using Two Dimensional Arrays. *AIP Conference Proceedings*, 1211:887–894, 2010.

[36] A. Velichko and P.D. Wilcox. Defect Characterization Using Two Dimensional Arrays. *AIP Conference Proceedings*, 1335:835–842, 2011.

[37] A.S. Birks and R.E. Green. *Nondestructive Testing Handbook: Volume 7 Ultrasonic Testing.* American Society of Nondestructive Testing, second edition, 1991.

[38] R. Long, J. Russell, and P. Cawley. Ultrasonic Phased Array Inspection using Full Matrix Capture. *Insight*, 54:380–385, 2012.

[39] J.C. Collingwood. Nuclear NDT development at Harwell. *NDT International*, 20:33–41, 1987.

[40] L.N.J. Poulter. Signal Processing Methods Applied in the Ultrasonic Inspection of PWR Inlet Nozzles. *NDT International*, 19:141–144, 1986.

[41] P.D. Wilcox, C. Holmes, and B.W. Drinkwater. Advanced Reflector Characterization with Ultrasonic Phased Arrays in NDE Applications. *IEEE Transactions on Ultrasonics Ferroelectrics and Frequency Control*, 54:1541–1550, 2007.

[42] P.D. Wilcox, C.H. Holmes, and B.W. Drinkwater. Enhanced Defect Detection and Characterisation by Signal Processing of Ultrasonic Array Data. In *ECNDT*, 2006.

[43] A.J. Hunter, B.W. Drinkwater, and P.D. Wilcox. The Wavenumber Algorithm: Fast Fourier-Domain Imaging using Full Matrix Capture. *AIP Conference Proceedings*, 28:856–863, 2009.

[44] A.J Hunter, B.W. Drinkwater, and P.D. Wilcox. The Wavenumber Algorithm for Full Matrix Imaging using an Ultrasonic Array. *IEEE Transactions on Ultrasonics Ferroelectrics and Frequency Control*, 55:2450–2640, 2008.

[45] British and European standard: Non-Destructive Testing of welds - Ultrasonic testing - Characterisation of Indications in Welds (BSEN ISO 23279:2010).

[46] C. Holmes, B.W. Drinkwater, and P.D. Wilcox. Advanced Post-Processing for Scanned Ultrasonic Arrays: Application to Defect Detection and Classification in Non-Destructive Evaluation. *Ultrasonics*, 48:636–642, 2008.

[47] A. Tweedie, R.L. O'leary, G. Harvey, A. Gachagan, C. Holmes, P.D. Wilcox, and B.W. Drinkwater. Total Focussing Method for Volumetric Imaging in Immersion Non Destructive Evaluation. In *IEEE Ultrasonics Symposium Proceedings*, pages 1017–1020, 2007.

[48] J. Zhang, B.W. Drinkwater, and P.D. Wilcox. Defect Characterization Using an Ultrasonic Array to Measure the Scattering Coefficient Matrix. *IEEE Transactions on Ultrasonics Ferroelectrics and Frequency Control*, 55:2254–2265, 2008.

[49] R. Long, P. Cawley, and J. Russell. Ultrasonic Phased Array Inspection of Flaws on Weld Fusion Faces using Full Matrix Capture. In D.E. Chimenti D.O. Thompson, editor, *Review of Progress in Quantitative Nondestructive Evaluation*, volume 28, pages 848–855, Portland Oregon, USA, 2008. American Institute of Physics.

[50] J. Russell, R. Long, D. Duxbury, and P. Cawley. Development and Implementation of a Membrane-Coupled Conformable Array Transducer for use in the Nuclear Industry. *Insight*, 54:386–393, 2012.

[51] S. Chatillion, G. Cattiaux, M. Serre, and O. Roy. Ultrasonic Non-Destructive Testing of Pieces of Complex Geometry with a Flexible Phased Array Transducer. *Ultrasonics*, 38:131–134, 2000.

[52] O. Roy, S. Mahaut, and O. Casula. Control of the Ultrasonic Beam Transmitted Through an Irregular Profile using a Smart Flexible Transducer: Modelling and Application. *Ultrasonics*, 40:243–246, 2002.

[53] A.J Hunter, B.W. Drinkwater, and P.D. Wilcox. Autofocusing Ultrasonic Imagery for Non-destructive Testing and Evaluation of Specimens with Complicated Geometries. *NDT & E International*, 43(2):78–85, 2010.

[54] R. Long and P. Cawley. Phased Array Inspection of Irregular Surfaces. In D.E. Chimenti D.O. Thompson, editor, *Review of Progress in Quantitative Nondestructive Evaluation*, pages 814–821. American Institute of Physics, 2007.

[55] A.J. Hunter, B.W. Drinkwater, and P.D. Wilcox. Least-Squares Estimation of Imaging Parameters for an Ultrasonic Array Using Known Geometric Image Features. *IEEE Transactions on Ultrasonics Ferroelectrics and Frequency Control*, 58:414–426, 2011.

[56] P.R. Stepanishen. The Time-Dependant Force and Radiation Impedance on a Piston in a Rigid Infinite Planar Baffle. *Journal of the Acoustic Society of America*, 49:841–849, 1971.

[57] R.K. Chapman. A System Model for the Ultrasonic Inspection of Smooth Planar Cracks. *Journal of Nondestructive Evaluation*, 9:197–210, 1990.

[58] J.W. Goodman. *Introduction to Fourier Optics*. Goodman & Company Publishers, 2005.

[59] A.L. Lopez-Sanchez, H.J. Kim, W.L. Schmerr, and A. Sedov. Measurement Models and Scattering Models for Predicting the Ultrasonic Response from Side-Drilled Holes. *Journal of Nondestructive Evaluation*, 24:83–96, 2005.

[60] R.K. Chapman. Ultrasonic Scattering from Smooth Flat Cracks: an Elastodynamic Kirchhoff Diffraction Theory. *CEGB report NWR/SSD/84/0059/R*, 1984.

[61] B. Delannoy, H. Lasota, C. Bruneel, R. Torguet, and E. Bridoux. The Infinite Planar Baffles Problem in Acoustic Radiation and its Experimental Verification. *Journal of Applied Physics*, 50(8):5189–5195, August 1979.

[62] J.A. Jensen and N.B. Svendsen. Calculation of Pressure Fields from Arbitrarily Shaped, Apodized, and Excited Ultrasound Transducers. *IEEE Transactions on Ultrasonics Ferroelectrics and Frequency Control*, 39:262–267, 1992.

[63] A. Lhemery, P. Calmon, I. Lecoeur-Taibi, R. Raillon, and L. Paradis. Modelling Tools for the Ultrasonic Inspection of Welds. *NDT & E International*, 33:1279–1290, 2000.

[64] T.P. Lerch and L.W. Schmerr. Ultrasonic Beam Models: An Edge Element Approach. *Journal of the Acoustic Society of America*, 104:1256–1265, 1998.

[65] L.W. Schmerr. A Multigaussian Ultrasonic Beam Model for high performance simulations on a personal computer. *Materials Evaluation*, 58:882–888, 2000.

[66] H. Kim, L.W. Schmerr, and A. Sedov. Generation of the Basis Sets for Multi-Gaussian Ultrasonic Beam Models - An Overview. *Journal of the Acoustic Society of America*, 119:1971–1978, 2006.

[67] D. Ding, Y. Zhang, and J. Liu. Some Extensions of the Gaussian Beam Expansion: Radiation Fields of the Rectangular and the Elliptical transducer. *Journal of the Acoustic Society of America*, 113:3043–3048, 2003.

[68] X. Zhao and T. Gang. Nonparaxial Multi-Gaussian Beam Model and Measurement Models for Phased Array Transducers. *Ultrasonics*, 49:126–130, 2009.

[69] R. Huang, L.W. Schmerr, and A. Sedov. Modeling the Radiation of Ultrasonic Phased-Array Transducers wih Gaussian Beams. *IEEE Transactions on Ultrasonics Ferroelectrics and Frequency Control*, 55:2692–2702, 2008.

[70] CIVA. *EXTENDE*. Batiment Erable, 86 rue de Paris, 91 400 Orsay, France, 2012.

[71] J.A. Johnson, N.M. Carlson, and D.M. Tow. Ray trace calculations of ultrasonic fields. *Research in Nondestructive Evaluation*, 37:27–39, 1991.

[72] Extende. *CIVA Validation evidence*. www.extende.com/validation-2, 2012.

[73] P. Crowther. Practical Experience of Phased Array Technology for Power Station Applications. *Insight*, 46(9):525–528, 2004.

[74] A.E. Weyman. *Principles and Practise of Echocardiography*. Lea and Febiger, Philadelphia, 1994.

[75] J. Dybedal, A. Lovik, and K.A. Ingebrigtsen. A High Resolution Sonar for Sea-Bed Imaging. *Ultrasonics*, 23(2):71–76, 1985.

[76] S. Wooh and Y. Shi. Three-Dimensional Beam Directivity of Phase-Steered Ultrasound. *Journal of the Acoustic Society of America*, 105:3275–3282, 1999.

[77] A.R. Selfridge, G.S. Kino, and B.T. Khuri-Yakub. A Theory for the Radiation Pattern of a Narrow-Strip Accoustic Transducer. *Applied Physics Letters*, 37(1):35–36, July 1980.

[78] P. Gendreu, M. Fink, and D. Royer. Optical Imaging of Transient Acoustic Fields Generated by Piezocomposite Transducers. *IEEE Transactions on Ultrasonics Ferroelectrics and Frequency Control*, 42(1):135–143, 1995.

[79] S. Wooh and Y. Shi. Influence of Phased Array Element Size on Beam Steering Behavior. *Ultrasonics*, 36:737–749, 1998.

[80] S. Wooh and Y.Shi. Optinum Beam Steering of Linear Phased Arrays. *Wave Motion*, 29:245–265, 1998.

[81] G.E. Tupholme. Generation of Acoustic Pulses by Baffled Plane Piston. *Journal of the Acoustic Society of America*, 16:209–224, 1969.

[82] P.R Stepanishen. Transient Radiation from Pistons in an Infinite Planar Baffle. *Journal of the Acoustic Society of America*, 49:1627–1638, 1970.

[83] N. Felix, D. Certon, E. Lacaze, M. Lethiecq, and F. Patat. Experimental Investigation of Cross-Coupling and its Influence on the Elementary Radiation Patter in 1D Ultrasound Arrays. In *IEEE Ultrasonics symposium*, 1999.

[84] N. Felix, D. Certon, L. Ratsimandresy, M. Lethiecq, and F. Patat. 1D Ultrasound Array: Performance Evaluation and Characterization by Laser Interferometry. In *IEEE Ultrasonics Symposium*, pages 1191–1194, 2000.

[85] Polytech. *OFV 505*. www.polytec.com, 2012.

[86] N. Lamberti. Radiation Pattern Distortion Caused by the Interelement Coupling in Linear Array Transducers. In *IEEE Ultrasonics Symposium*, pages 1071–1075, 1999.

[87] D. Robertson, G. Hayward, A. Gachagan, J. Hyslop, and P. Reynolds. Comparison of Mechanical Cross Talk in Single Crystal and Ceramic Periodic Piezoelectric Composite Arrays. In *IEEE Ultrasonics Symposium*, pages 1668–1671, 2003.

[88] D.H. Turnbull and F.S. Foster. Beam Steering with Pulsed Two-Dimensional Transducer Arrays. *IEEE Transactions on Ultrasonics Ferroelectrics and Frequency Control*, 38(4):320–333, July 1991.

[89] D.H. Turnbull and F.S. Foster. Fabrication and Characterization of Transducer Elements in Two-Dimensional Arrays for Medical Imaging. *IEEE Transactions on Ultrasonics Ferroelectrics and Frequency Control*, 39(4):464–475, 1992.

[90] T.P. Pialucha. The Reflection Coefficient from Interface Layers in NDE of Adhesive Joints. *PhD thesis, Imperial College London*, 1992.

[91] J. Krautkramer and H. Krautkramer. *Ultrasonic Testing of Materials*. Springer-Verlag, London, 4th edition, 1990.

[92] C.T. Lancee, J.M. Vissers, S. Mientki, C.M. Ligtvoet, and N. Bom. Influence of Amplitude Errors on Beam-Steered Phased Arrays. *Ultrasonics*, 25:147–153, 1987.

[93] C. Nageswaran. Coping with Failed Elements on an Array: A Modelling Approach to the Technical Justification. *Insight*, 52:372–379, 2010.

[94] C.T. Lancee, J.M. Vissers, S. Mientki, C.M. Ligtvoet, and N. Bom. Influence of Phase Errors on Beam-Steered Phased Arrays. *Ultrasonics*, 25:154–159, 1987.

[95] J. Zhang, B.W. Drinkwater, and P.D. Wilcox. Effects of Array Transducer Inconsistencies on Total Focusing Method Imaging Performance. *NDT & E International*, 44:361–368, 2011.

[96] B.D. Steinberg. Digital Beamforming in Ultrasound. *IEEE Transactions on Ultrasonics Ferroelectrics and Frequency Control*, 39(6):716–721, November 1992.

[97] Ake Bjorck. *Numerical Methods for Least Square Problems*. Society for Industrial Mathematics, 1996.

[98] D. MacDonald. Procedure for Examination of Reactor Piping Using Phased Array Ultrasound. Technical report, Electric Power Research Institute (EPRI), Palo Alto, California, USA, 2002.

[99] L. Azar, Y. Shi, and S.C. Wooh. Beam Focusing Behavior of Linear Phased Arrays. *NDT & E International*, 33:189–198, 2000.

[100] G. Maes, J. Berlanger, J. Landrum, and M. Dennis. Appendix VIII Qualification of Manual Phased Array UT for Piping. *Insight*, 48(4):240–244, 2006.

[101] N.Bilaniuk and G.S.K Wong. Erratum: Speed of Sound in Pure Water as a Function of Temperature. *Journal of the Acoustic Society of America*, 93(3):1609–1612, 1993.

[102] E.L. Kaplan and P. Meier. Nonparametric Estimation from Incomplete Observations. *Journal of the American Statistical Association*, 53:457–481, 1958.

[103] D.R. Cox and D. Oakes. *Analysis of Survival Data*. Chapman & Hall, London, 1984.

[104] M. Greenwood. *The Natural Duration of Cancer (Report on Public Health and Medical Subjects No. 33)*. His Majesty's Stationery Office, 1926.

[105] M.S. Greenwood, J.R. Skorpik, J.A. Bamberger, and R.V. Harris. On-line Ultrasonics Density Sensor for Proces Control of Liquids and Slurries. *Ultrasonics*, 37:159–171, 1999.

[106] Kobold. *HND-T105 with HND-TF03 probe*. www.kobold.com, 2012.

[107] G.H. Hunter and T.G. Fenney. Computer Graphics for Ultrasonic Data Interpretation. In *IEEE Colloquium on Digital Signal Processing and Display Techniques for Ultrasonics*, pages 8/1–8/3, 1988.

[108] A.H. Harker, J.A. Ogilvy, and J.A.G. Temple. Modeling Ultrasonic Inspection of Austenitic Welds. *Journal of Nondestructive Evaluation*, 9:155–165, 1990.

[109] D. Duxbury, J. Russell, and M. Lowe. The Effects of Variation in Phased Array Element Performance. *Ultrasonics*. In Press.

9 Appendix

9.1 Array beam model development

Additional amplitude comparisons against the CIVA modelling package and experiment

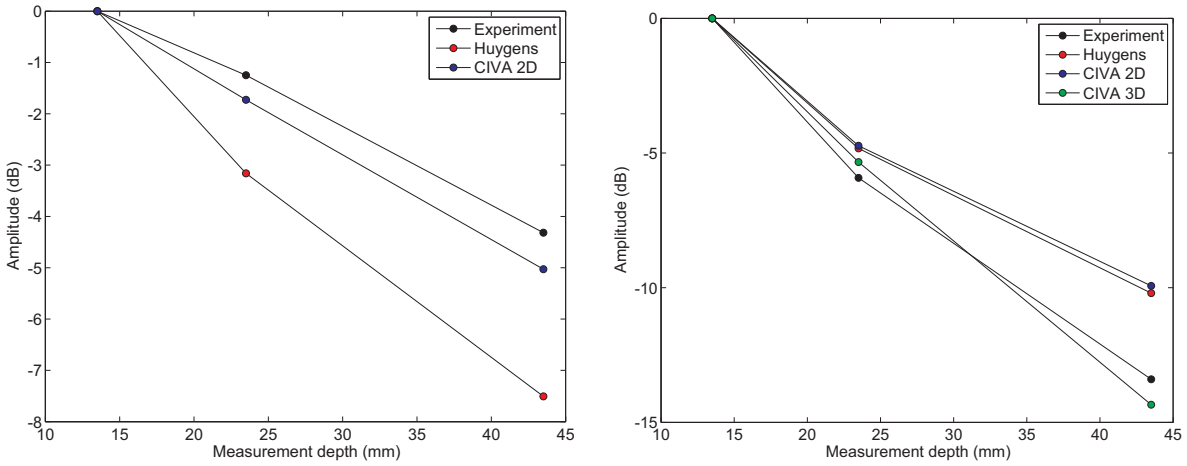

(a) (b)

Figure 9.1.1: A comparison of predicted amplitude variations of CIVA and the Huygens model against experimentally measured values a) focused 0 degree longitudinal wave b) focused 70 degree transverse wave.

9.2 A calibration routine for FMC

9.2.1 Temperature insensitive firing delay shift measurement

The errors in measured velocity shift associated with the simulation results presented in Figure 6.1.6 are presented in Figure 9.2.1. The results in plot a) have been produced when no velocity shift has been applied and therefore represents the combined numerical noise of the simulation and velocity shift detection algorithm.

The effect of the number of element groups, TXRX separation, and amplifier gain can be seen in Figure 9.2.2.

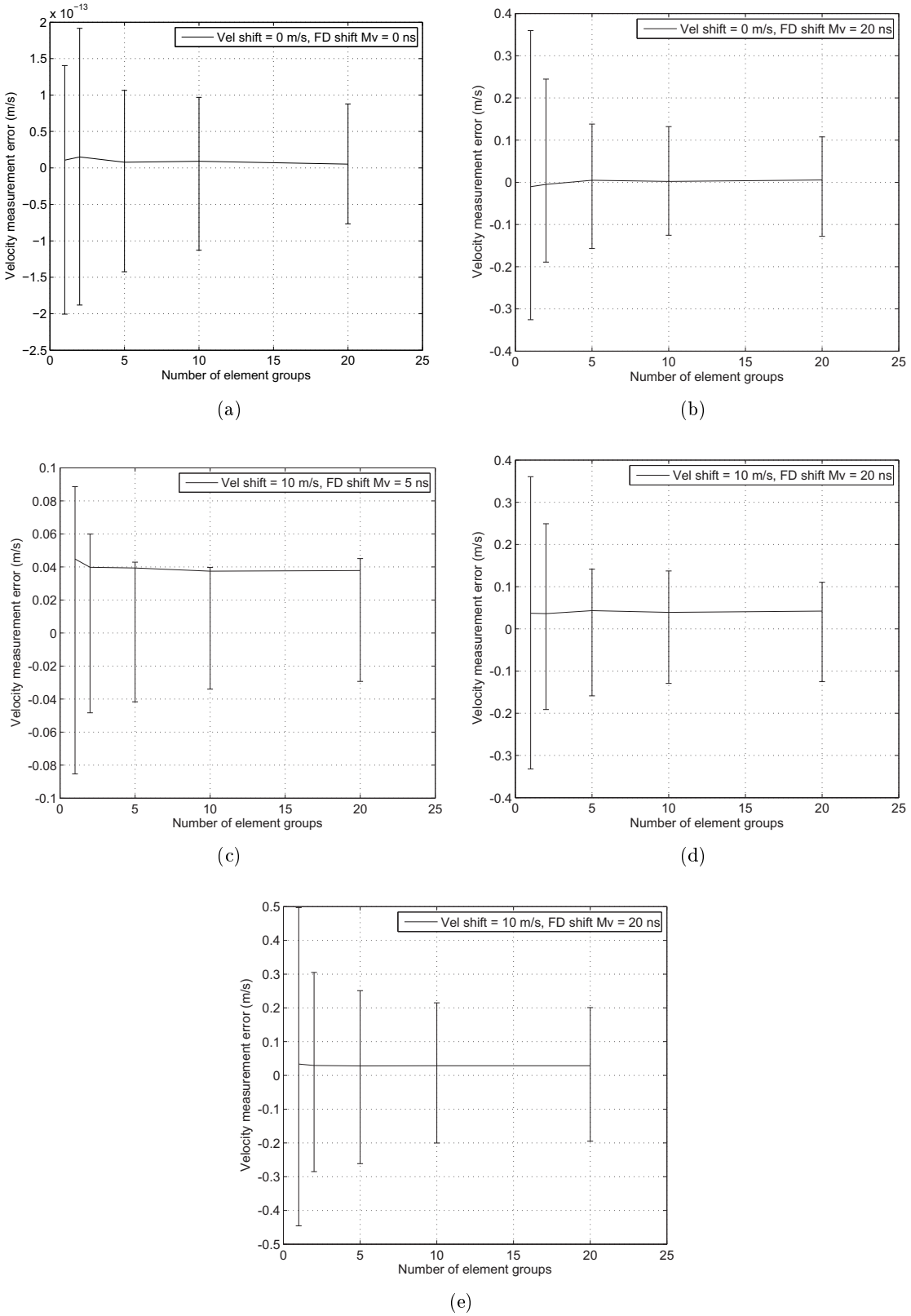

Figure 9.2.1: The error in measured velocity shift predicted via Monte Carlo simulation using array specification A: a) velocity shift = 0 m/s, FD shift Mv = 0 ns, b) velocity shift = 0 m/s, FD shift Mv = 20 ns, c) velocity shift = 10 m/s, FD shift Mv = 5 ns, d) velocity shift = 10 m/s, FD shift Mv = 20 ns, e)velocity shift = 10 m/s, FD shift Mv = 20 ns. In results a) - d) 10 % of the array is affected by FD shift, in case e) 20 % is effected. In all cases a maximum FD value of 25 ns has been applied, and the FD shift has been measured using a TXRX separation of 10 elements. In each case 300 simulations have been completed for each element group size.

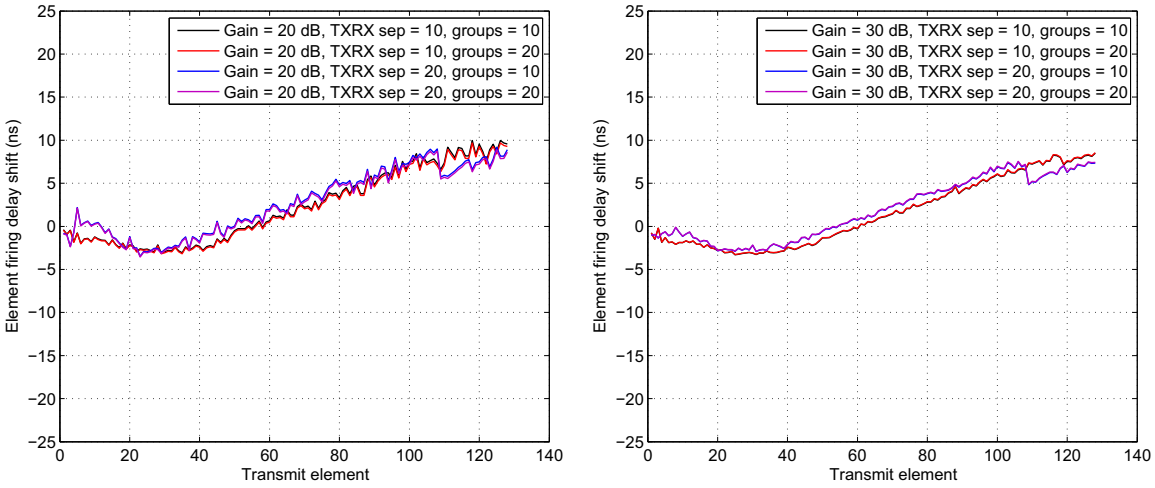

(a) (b)

Figure 9.2.2: Measurements of FD shift between T1 and T4 using different numbers of groups, TXRX separations, and amplifier gain levels a) gain = 20 dB, b) gain = 30 dB.

9.3 The effect of surface profile measurement inaccuracies

Figures 9.3.1 and 9.3.2 contain the profiles extracted from the Monte Carlo results at array centre frequencies of 5 and 7.5 MHz respectively.

a)

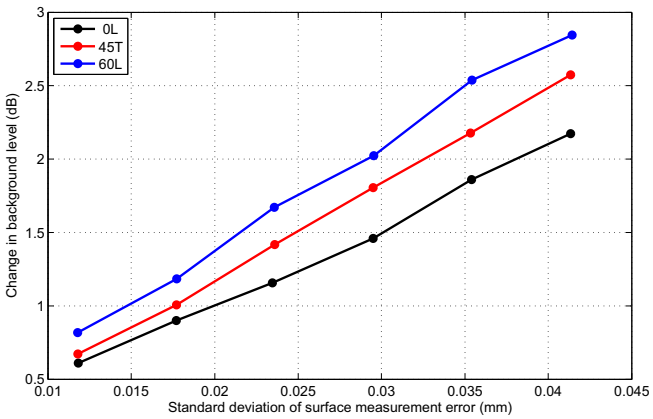

b)

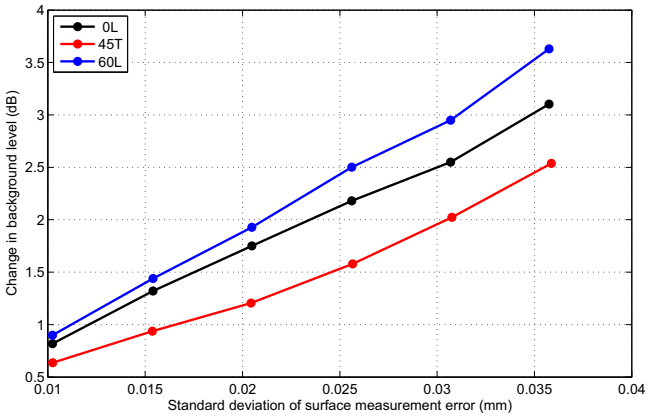

c)

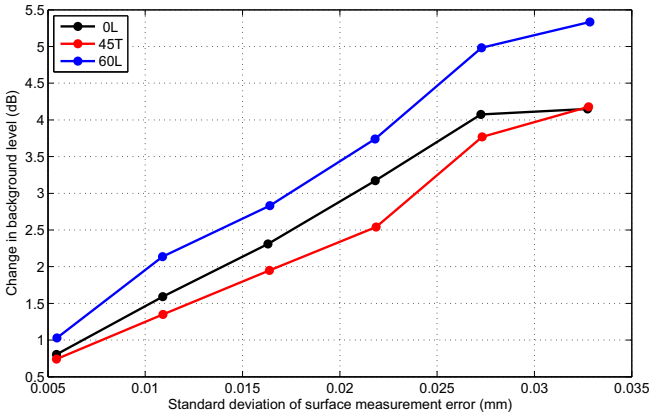

Figure 9.3.1: The results of analysing the Monte-Carlo simulation results for zero and 60 degree longitudinal beams (0L and 60L) and a 45 degree shear wave (45T) at a centre frequency of 5 MHz for a) a flat interface b) the artificial weld cap c) the wavey surface.

a)

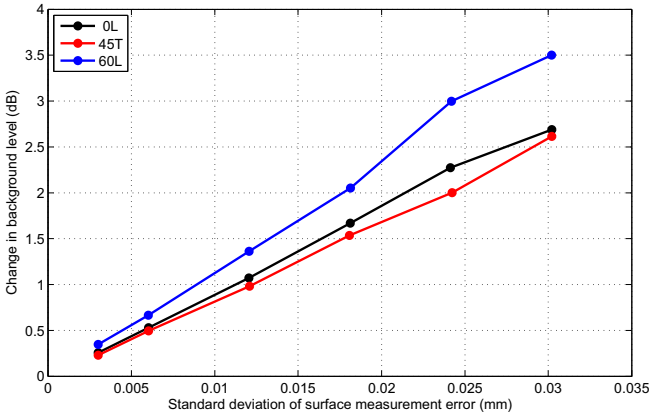

b)

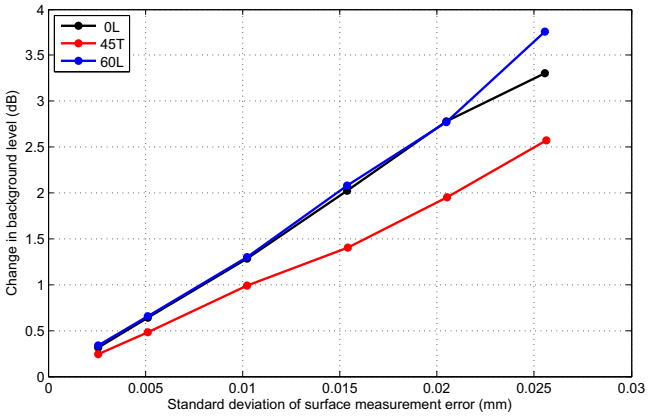

c)

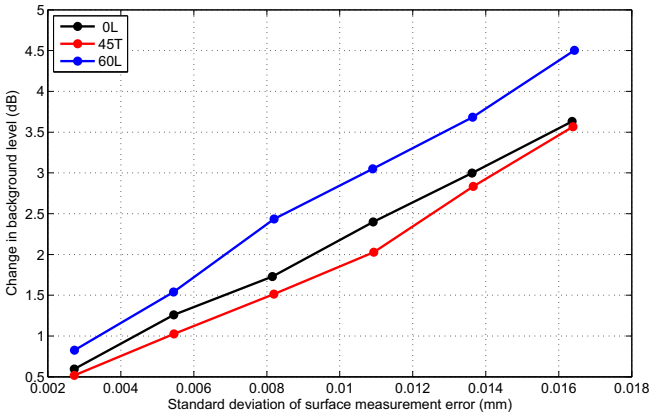

Figure 9.3.2: The results of analysing the Monte-Carlo simulation results for zero and 60 degree longitudinal beams (0L and 60L) and a 45 degree shear wave (45T) at a centre frequency of 7.5 MHz for a) a flat interface b) the artificial weld cap c) the wavey surface.